# IMPROVING THE SEISMIC ISOLATION FOR THE AEI 10 m PROTOTYPE

Von der Fakultät für Mathematik und Physik
der Gottfried Wilhelm Leibniz Universität Hannover
zur Erlangung des Grades

**Doktor der Naturwissenschaften**
**Dr. rer. nat.**

genehmigte Dissertation
von

**Dipl.-Phys. Gerald Bergmann**

2018

REFERENT:
Prof. Dr. Karsten Danzmann

KORREFERENT:
Prof. Dr. Kenneth A. Strain

KORREFERENT:
Prof. Dr. Michèle Heurs

TAG DER DISPUTATION:
20.04.2018


Diese Arbeit wurde angefertigt am
Max-Planck-Institut für Gravitationsphysik (Albert-Einstein-Institut)
und Institut für Gravitationsphysik, Leibniz Universität Hannover,
Callinstraße 38, 30167 Hannover

# ABSTRACT

The first detection of gravitational waves (GWs) on September 14, 2015 as well as the subsequent observations brought forth a new era in astronomy, which offers new insights into the nature of the universe. Future GW observatory networks, with even higher sensitivity, will make GW observations a routine occurrence.

Test facilities, such as the AEI 10 m prototype, provide an environment for developing novel technologies for these future detectors. The AEI 10 m prototype offers a low noise environment, ideal for performing high precision physics, such as measurements at and below the standard quantum limit (SQL) of interferometry, a regime so far largely unexplored. At low frequencies, seismic noise is a major limitation for ground-based GW detectors, where isolation from environmental vibration is crucial. This thesis presents the performance analysis of and improvements to the AEI 10 m prototype Seismic Attenuation System (AEI-SAS).

The fundamental resonance frequencies of optic suspensions of the AEI 10 m prototype are between 0.5 Hz and 30 Hz, a frequency band in which efficient vibration reduction is essential. Three individual AEI-SAS units provide vibration isolation to the three optical tables which support the suspensions and other optical mechanics of the AEI 10 m prototype. This system decouples the payload from ground vibration in six degrees of freedom by means of low fundamental resonance frequencies and a low active-bandwidth isolation scheme. The scheme employs Inverted-Pendulum (IP)-legs to provide horizontal vibration attenuation and Geometric Anti-Spring (GAS)-filters to provide vertical isolation.

Two AEI-SAS units were assembled and implemented in the AEI 10 m prototype. A detailed analysis of these units revealed their mechanical limitations. Internal resonances, in particular, severely reduced their isolation performance above 8 Hz. As a solution, several design improvements, such as an additional well damped isolation stage, inertial damping structures, a new IP-leg design, and a stiffer GAS-filter support structure were suggested in the scope of this work. The former two improvements were implemented in the first two AEI-SAS units. The third AEI-SAS unit employs all the improvements listed above. A revised GAS-filter tuning technique further improved its high vertical isolation performance at frequencies above 30 Hz.

Performance tests of the first two AEI-SAS units now show improvement in passive isolation from ground motion by a factor of about 400 in the horizontal direction at 4 Hz and in the vertical direction at 9 Hz. Internal resonances limit the isolation performance above 30 Hz. The amplitude of the internal resonances, however, is reduced by up to a factor of 75 by means of the inertial damping structures. The third AEI-SAS unit's internal modes have been stiffened to a lowest resonance frequency of 54 Hz. The AEI-SAS, therefore, now provides substantial passive isolation at all the fundamental mirror suspension resonances.

The improvement in passive performance allow the implementation of an enhanced active low frequency isolation, since internal resonances strongly influence the control loop design. Active isolation reduces the payload motion efficiently in the frequency band around the AEI-SAS's fundamental resonances. Future upgrades, such as the implementation of horizontal low-noise table top sensors, will further enhance the active performance of all three units. The improvements to the AEI-SAS, developed in the scope of this thesis, have potential benefits for GW detectors and other experiments requiring low seismic noise conditions. The studies presented here influence and guide the design of future vibration isolation systems for high precision measurements in general and ground-based gravitational wave observatories in particular.

# ZUSAMMENFASSUNG

Mit der ersten Gravitationswellendetektion am 14. September 2015 und den folgenden Beobachtungen beginnt eine neue Ära der Astronomie, die neue Erkenntnisse über das Verständnis des Universums verspricht. Ein Netzwerk aus noch empfindlicheren Gravitationswellenobservatorien wird die Häufigkeit der Detektionen stark vergrößern.

Einrichtungen wie der AEI-10 m-Prototyp bieten eine Plattform für die Entwicklung neuer Gravitationswellendetektortechnologien. Der AEI-10 m-Prototyp ist aufgrund des extrem niedrigen Auslenkungsrauschen hervorragend geeignet zur Durchführung von Hochpräzisionsexperimenten. Hierzu zählen unter anderen die Messung und Unterbietung des bisher unerreichten Standardquantenlimits (SQL) der Interferometrie. Die Genauigkeit von Hochpräzisionsexperimenten sowie von Gravitationswellendetektoren ist bei niedrigen Frequenzen durch seismisches Rauschen limitiert. Die Vibrationsisolation dieser Experimente ist daher essenziell. Diese Doktorarbeit beschreibt die Analyse und die Verbesserungen des seismischen Abschwächungs-Systems (SAS) für die AEI 10m Prototyp-Einrichtung.

Die fundamentalen Resonanzen der als Mehrfachpendel aufgehängten Optiken des AEI 10 m Prototyps liegen zwischen 0,5 Hz und 30 Hz, daher ist eine effiziente Rauschreduzierung in diesem Frequenzband unerlässlich. Drei AEI-SAS-Einheiten isolieren die drei optischen Tische, die die optischen Elemente des Prototypen beherbergen, durch die Kombination ihrer niedrigen fundamentalen Resonanzen mit einer aktiven Isolation geringer Bandbreite in allen sechs Freiheitsgraden von Bodenvibrationen. Invertierte-Pendel(IP)-Beine sorgen für die horizontale Schwingungsabschwächung und Geometrische-Antisprungfedern(GAS)-Filter werden für die vertikale Isolation genutzt.

Zwei im Rahmen dieser Arbeit in den AEI-10 m-Prototypen eingebaute AEI-SAS-Einheiten wurden einer detaillierten Untersuchung unterzogen, die insbesondere in dem Frequenzbereich über 8 Hz Limitierungen durch interne Resonanzen aufgezeigt hat. Zur Behebung dieses Problems wurden mehrere Änderungen vorgeschlagen und umgesetzt. Hierzu gehören eine zusätzliche gedämpfte Isolationsstufe, passive Schwingungsdämpfer, ein neues IP-Bein Design und das Versteifen der GAS-Filter-Trägerstruktur. Die beiden erstgenannten Verbesserungen konnten in den ersten zwei AEI-SAS-Einheiten integriert werden. Die dritte AEI-SAS-Einheit beinhaltet alle oben genannten Verbesserungen. Zudem sorgt eine überarbeitete GAS-Filter Justierungstechnik für eine verbesserte vertikale Isolation im Frequenzbereich über 30 Hz. Resultat dieser Änderungen sind eine Verbesserung der passiven Isolation von Bodenbewegungen um einen Faktor von 400 in horizontaler Richtung bei 4 Hz und in vertikaler Richtung bei 9 Hz für die ersten beiden AEI-SAS-Einheiten. Noch immer verringern interne Resonanzen die Isolationsleistung über 30 Hz. Die Amplitude der Eigenresonanzen wurde jedoch durch die Schwingungsdämpfer um den Faktor von 75 reduziert. Die internen Resonanzen des dritte AEI-SAS-Einheit wurden versteift, sodass deren niedrigste interne Resonanzfrequenz nun 54 Hz ist. Damit werden alle Grundschwingungen der Spiegelaufhängungen erheblich von der Bodenbewegung entkoppelt. Die Verbesserung der passiven Isolierung ermöglicht eine Verbesserung der aktiven Isolierung, da interne Resonanzen das Regelkreisdesign stark beeinflussen.

Die aktive Isolierung reduziert effizient die Bewegung der optischen Tische im Frequenzband um die Grundschwingungsfrequenzen des AEI-SAS. Optimierungen wie der Einsatz von horizontalen rauscharmen Tischsensoren werden die aktive Isolation aller drei AEI-SAS Einheiten weiter steigern.

Die Verbesserungen des AEI-SAS, die im Rahmen dieser Doktorarbeit entwickelt wurden, haben das Potential, die Empfindlichkeit von Gravitationswellendetektoren und anderen Experimenten, die ein extrem niedriges Auslenkungsrauschen erfordern, weiter zu verbessern. Die hier vorgestellten Untersuchungen werden darüber hinaus Einfluss auf die Planung und den Bau zukünftiger Schwingungsisolationssysteme haben.

**Key words:** Ground-based gravitational wave detection, AEI 10 m prototype, seismic isolation

**Schlagwörter:** Erdgebundene Gravitationswellenmessung, AEI 10 m Prototyp, Seismikisolation

# ABBREVIATIONS

| Abbreviation | Disambiguation |
|---|---|
| AEI | Max Planck Institute for Gravitational Physics (Albert Einstein Institute) based in Hannover and Golm, Germany |
| AIGO | Australian International Gravitational Observatory |
| AlGaAs | Aluminum Gallium Arsenide |
| Caltech | California Institute of Technology |
| CDS | Control and Data acquisition System |
| CLIO | Cryogenic Laser Interferometer Observatory prototype for KAGRA |
| CoM | Center of Mass |
| CoP | Center of Percussion |
| CoR | Center of Rotation |
| CW | Counter Weights |
| EIB | External Injection Bench |
| ESD | Electro Static Drive |
| GAS | Geometric Anti Spring |
| GEO 600 | GW detector with 600 m arm length in Germany |
| GW | Gravitational Waves |
| HAM | Horizontal Access Module |
| HEPI | Hydraulic External Pre-Isolation system, used at LIGO |
| IP | Inverted Pendulum |
| ITM | Input Test Mass |
| KAGRA | KAmioka, GRAvitational wave detector |

| | |
|---|---|
| LASTI | LIGO advanced systems testing interferometer at MIT |
| LIGO | Laser Interferometer Gravitational-Wave Observatory |
| LVDT | Linear Variable Differential Transformer |
| $M_\odot$ | Solar mass |
| MAS | Magnetic Anti Spring |
| MGAS | Monolithic Geometric Anti Spring |
| MIT | Massachusetts Institute of Technology |
| OL | Optical Lever |
| PEEK | PolyEther Ether Ketone |
| rms | Root-Mean-Square |
| SAS | Seismic Attenuation System |
| SPI | Suspension Platform Interferometer |
| SQL | Standard Quantum Limit |
| TAMA 300 | Japanese GW detector with 300 m arm |
| Virgo | GW detector with 3 km arm length based in Italy |

# CONTENTS

# Part I

# INTRODUCTION

# 1 GRAVITATIONAL WAVES

Accelerated masses emit gravitational waves (GWs), and these can be detected directly [1]. GWs are perturbations in spacetime; their existence was postulated by Albert Einstein in 1916. They are a solution of his field equations [2]. Approximately 100 years later, after decades of intense research and engineering, the second half of the first sentence of this paragraph could be stated. The first directly detected GW signal was measured by the two Advanced LIGO (Laser Interferometer Gravitational-Wave Observatory) detectors (see section 3) on September 14, 2015 [1]. The signal was emitted around $1.4{\times}10^9$ years ago by the inspiral of a pair of black holes that underwent a violent merger. This introductory chapter gives an overview of the first and subsequent GW observations, of how GWs are measured, and of their immense scientific impact. The last section of this introduction focuses on the first detection of a neutron star binary collapse with a GW signal and its electromagnetic counterparts.

## 1.1 MEASURING GRAVITATIONAL WAVES

According to Einstein's theory of general relativity, matter and energy cause spacetime to curve. This curvature gives rise to gravitational interaction. Accelerated masses change the gravitational field dynamically and thereby induce GWs that propagate away from the source at the speed of light. One of the basic properties of GWs is that, when propagating through spacetime, they stretch it in one direction, while contracting it in another. These deformations are transverse to the direction of propagation and can be described as a linear combination of a 'cross' and a 'plus' tensor polarization. By measuring the relative distance between free objects one can, therefore, observe the GW-induced dynamic deformation of spacetime (see figure 1). The amplitude of a GW is written as

$$h_{GW} = \frac{\Delta L_{GW}}{L} \tag{1}$$

and is referred to as *strain*. Here $\Delta L_{GW}$ is the length change between two points in spacetime. The points are separated by the distance $L$.

In principle, GWs are emitted by all accelerated massive objects. However, spacetime is very 'stiff', therefore detecting such signals is extremely challenging and only possible for high-mass sources. For in-

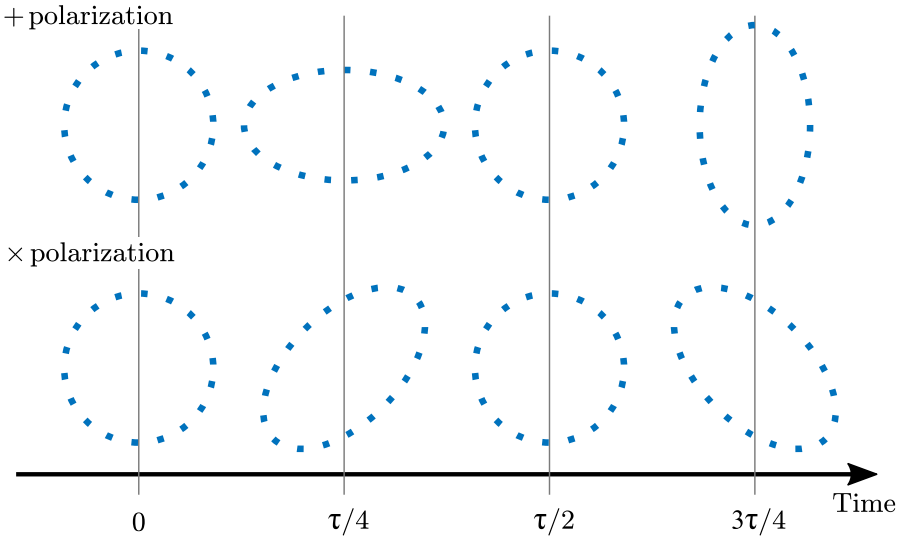


**Figure 1:** The effect of a GW on a ring of freely falling test masses. The figure visualizes the temporal progress of spacetime deformations by a GW with a propagation direction transverse to the paper surface. Here $\tau$ is the period of the GW. Two linear independent patterns of polarizations are shown, referred to as 'cross' and 'plus' polarization. They are related to one another by a rotation of 45°.

stance, the GW strain caused by two stars or black holes with an equal mass orbiting each other is [3]

$$|h_{GW}| \approx \frac{8GMr^2\Omega^2}{Rc^4} \ , \tag{2}$$

where $G$ is the gravitational constant and $M$ is the mass of each object. The two objects orbit each other with a frequency $\Omega$ at a distance of $2r$. The signal is observed at a distance $R$ from the source.

The current ground-based GW detectors have a good sensitivity from about 20 Hz to a few hundred hertz [4]. 20 Hz corresponds to an orbital frequency of 10 Hz. At this frequency, a strain of $h = 10^{-21}$ is well detectable. As an example, a two-mass system in a distance of 16.5 Mpc is considered (this is approximately the distance from our solar system to the Virgo Cluster). Based on Kepler's third law and equation 2 it can be approximated that two objects with a mass of approximately $3\,M_\odot$ would radiate GWs with the corresponding amplitude of $h = 10^{-21}$. Such a system would have an orbital radius of only 600 km, therefore the objects would need to be extremely compact. Only high-density stars, such as neutron stars or black holes, could exist in such low-distance orbits.

In order to detect GW-induced spacetime perturbations, extremely high precision measurement instruments are required. The interference of light is an extremely sensitive technique suitable for this purpose.

In the case of a Michelson interferometer (see figure 2), laser light is split into two beams at a beam splitter. The two partial beams are sent into two usually perpendicular arms. The laser light is reflected by mirrors at the end of the arms and recombined at the beam splitter. By measuring the power of the two returning beams interfering at the photodetector, differential arm length changes can be monitored.

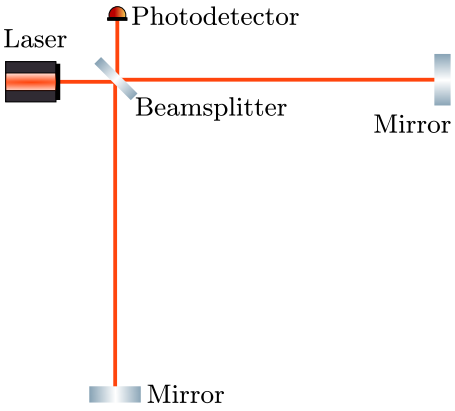


**Figure 2:** Simple Michelson interferometer. The principle of the current GW observatories is based on such an optical layout. If a 'cross' polarized GW propagating in the direction transverse to the paper surface one interferometer arm stretches while the other shrinks. This induces a variation of the optical field at the photodetector. Compared to the optical layout of real GW detectors this sketch is greatly simplified.

Equation 1 shows that the longer the arms the higher the GW-induced differential arm length variation. In the case of the two Advanced LIGO detectors, the arms are 4 km long. Figure 1 depicts that an angle of 90° between the interferometer arms is ideal to sense a GW signal. Such a configuration is, however, insensitive to a signal which stretches and shrinks the two arms in the same way. This is, for instance, the case for a signal rotated by 45° with respect to the signal that has maximal impact on the interferometer.

The figure furthermore illustrates, that the end mirrors, or test masses, must be free falling. In the case of a ground-based detector, this is hardly possible. Mounting the mirror on a three-dimensional spring, however, provides a good approximation for a free test mass far above the resonance frequency of such a mechanical harmonic oscillator. Suspending the test masses has the further advantage that the suspension system decouples the interferometer from environmental disturbances, such as seismic motion. This thesis discusses techniques for the isolation from environmental vibrations in detail.

In a kilometer-scale GW detector, reaching the sensitivity of $h = 10^{-21}$ requires detecting a differential mirror displacement of $10^{-18}$ m. Reaching such a sensitivity is extremely challenging and requires advanced noise reduction techniques. Starting in the 1970s GW detector technology was developed in prototype facilities such as the LIGO ad-

vanced systems testing interferometer (LASTI) at the Massachusetts Institute for Technology, the Caltech 40 m prototype [5], the Garching 30 m prototype [6] and the Glasgow 10 m prototype [7]. The construction of LIGO as the first km-scale GW detector began in 1994. It took more than 20 years until the first GWs were directly observed.

Interferometric GW detectors have very limited directional sensitivity. One detector is therefore not sufficient to obtain information about the location of the GW source. A signal measured independently by multiple detectors far apart helps to distinguish it from noise. At the time of writing, four observatories have been operated simultaneously (LIGO Livingston, LIGO Hanford, Virgo, and GEO 600).

## 1.2 THE FIRST DIRECT OBSERVATION OF GRAVITATIONAL WAVES

After 5 years of intense upgrading of the LIGO observatories from so-called enhanced detectors to advanced detectors, it was planned to start the first official observation run on September 18, 2015 [8]. Four days earlier, both LIGO detectors were fully functional but officially still being commissioned in an 'engineering mode', when the distance between the suspended mirrors of the LIGO Livingston detector oscillated by an amplitude of approximately $10^{-18}$ m. About 7 milliseconds later the same pattern was observed by the LIGO Hanford detector, which is approximately 3000 km away. This pattern turned out to be a GW event and is referred to as GW150914.

The data recorded by the detectors was analyzed on computer clusters at the Albert Einstein Institute (AEI), the Massachusetts Institute of Technology (MIT) and the California Institute of Technology (Caltech) [9]. These automated data pipelines determined the optimal fitting template for the data. The signal appeared above the background detector noise only for approximately 0.45 s, but the signal-to-noise ratio of 24 and the consistency with the theoretical model, deduced from general relativity were both high enough that a significance greater than 5.1 $\sigma$ could be stated. This was determined by studying the sensor behavior over 16 days of data, recorded before and after the signal was measured. In the following months, instrumental and environmental disturbances were exhaustively analyzed. These investigations showed that the GW150914 signal was not caused by any of the regarded noise sources [10]. As a consequence, the collaboration published the first observation of GWs on February 11, 2016 [1].

The modeled time series, as well as the recorded signal of GW150914, are shown in figure 3. It shows the characteristic shape of a GW signal from a compact binary source. The sinusoidal waveform with a slowly increasing amplitude is emitted during the *inspiral* phase of two massive objects. Due to the emitted energy, the orbit of the system shrinks and the angular velocity and thereby the GW frequency increases. The last

phase of the inspiral sees a drastic increase of the signal amplitude. It is followed by the collision of the two objects, called *merger*. During this merger the GW amplitude peaks. The remnant object's oscillations emit GWs with an amplitude that decays in a relatively short time. This last phase is referred to as a *ringdown*.

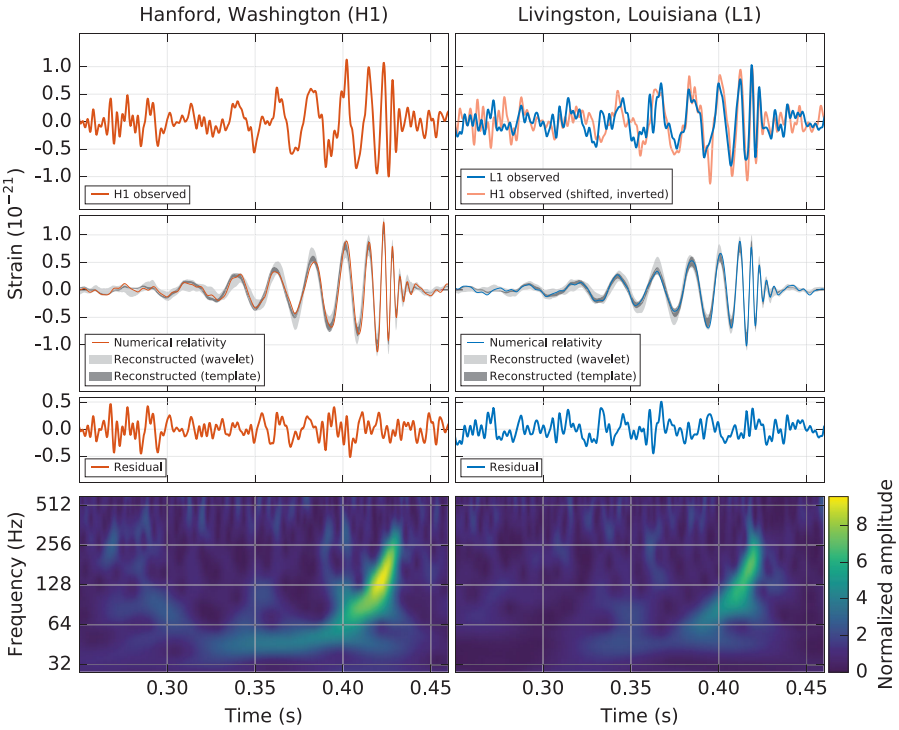


**Figure 3:** Time series of the GW signal from the GW150914 event. The left column shows the modeled and recorded H1 (LIGO Hanford), and the right column the L1 (LIGO Livingston) data. All data is filtered by a bandpass filter with corner frequencies of 35 Hz and 350 Hz. Both measured time series are compared in the upper right figure. The H1 data is shifted by 6.9 ms and inverted, in order to compensate for the difference in signal arrival time at, and orientation difference between, the two detectors.
The second row of the figure shows the waveform of a fitted numerical relativity model, projected on each detector (solid lines); furthermore, the 90 % credible regions for two independent waveform reconstructions are shown in light and dark gray. Further information about these models can be found in ref. [11], [12] and [9].
The difference between the measured data and predicted curve is shown in the third row.
The last row shows the spectral representation of the measured data, illustrating that the signal frequency increases over time.
This figure is taken from ref. [1].

In order to obtain the parameters of a GW source, the measured waveform is matched with a numerical relativity model. This model includes variables such as the distance from the source, the corresponding redshift of the signal, the masses of the system, the size of the two

orbiting objects, the spin and the source direction. For GW150914, the uncertainty of the latter is rather high since only the two LIGO detectors were online and sensitive enough to detect the signal. The source's angular location is determined by the time difference between the detections in the two detectors and by the angular sensitivity distribution of the observatories. A third observatory greatly increases the accuracy of the source localization.

The system's masses can be constrained by their *chirp mass*, which is a function of the signal's frequency and its time derivative. The observed frequency, however, scales with the redshift. It is a measure of the source's velocity and is determined by the distance the signal traveled through spacetime. The distance between source and observer is deduced from the amplitude of the signal and the model of the source, as shown in the greatly simplified example in section 1.1.

The mass of the two objects involved in GW150914 was determined to be approximately $36\,M_\odot$ and $29\,M_\odot$ (see table 2). From the masses of the system and the orbital radius right before the merger, one can conclude that the signal originated from two black holes which merged into a remnant black hole. The mass of the remnant was estimated to be $62\,M_\odot$. The energy radiated by the system is hence equivalent to $3\,M_\odot$. Most of it was released in the very last cycles of the system. The relatively high amplitude of the signal and the fact that the frequency band of the waveform in the few hundred milliseconds around the merger matched the sensitivity of Advanced LIGO, made the detection possible.

The observation of GW150914 did not only confirm the theory of general relativity. The detection furthermore proved that binary black hole systems exist and that such systems merge within the age of the universe. This can be seen as the inauguration of the new field of GW-astronomy.

The LIGO-Virgo Collaboration (LVC) published the detection results on 11 February 2016. Amongst numerous recognitions of single members of or the entire collaboration, the 2017 Nobel Prize in Physics was awarded to Rainer Weiss, Barry Barish and Kip Thorne 'for decisive contributions to the LIGO detector and the observation of GWs' [13].

## 1.3 FOLLOW UP DETECTIONS OF BLACK HOLE BINARY GW SIGNALS

The first observational run (O1) of the Advanced LIGO detectors lasted four months and ended on January 19, 2016. In this time period, not only GW150914, but two more events were detected. Parameters of all events detected so far are listed in table 2.

On October 12, 2015, a signal with a relatively low statistical significance of $1.7\,\sigma$ was observed. Due to the comparably low probability (87 %) of being of astrophysical origin, the signal is treated as a trig-

ger rather than a GW event. It is referred to as LIGO-Virgo Trigger LVT151012 [14].

A second black hole merger was observed on December 26, 2015. The distance of the source of this event was comparable to GW150914. The estimated masses, however of the GW151226 black holes were much smaller; therefore the signal's frequency right before the merger was relatively high 450 Hz and the inspiral signal was visible relatively long in the LIGO detection band (1 second) [15].

| Event | Type | Distance [Mpc] | Redshift | Primary mass [$M_\odot$] | Secondary mass [$M_\odot$] | Radiated energy [$M_\odot c^2$] | Remnant mass [$M_\odot$] | Final spin |
|---|---|---|---|---|---|---|---|---|
| GW150914 | BH-BH | $420^{+150}_{-180}$ | $0.09^{+0.03}_{-0.04}$ | $36.2^{+5.2}_{-3.8}$ | $29.1^{+3.7}_{-4.4}$ | $3.0^{+0.5}_{-0.4}$ | $62^{+3.7}_{-3.1}$ | $0.68^{+0.05}_{-0.06}$ |
| LVT151012 | BH-BH | $1000^{+500}_{-500}$ | $0.2^{+0.09}_{-0.09}$ | $23^{+18}_{-6}$ | $13^{+4}_{-5}$ | $1.5^{+0.3}_{-0.4}$ | $35^{+14}_{-4}$ | $0.66^{+0.09}_{-0.10}$ |
| GW151226 | BH-BH | $440^{+180}_{-190}$ | $0.09^{+0.03}_{-0.04}$ | $14.2^{+8.3}_{-3.7}$ | $7.5^{+2.3}_{-2.3}$ | $1.0^{+0.1}_{-0.2}$ | $20.8^{+6.1}_{-1.7}$ | $0.74^{+0.06}_{-0.06}$ |
| GW170104 | BH-BH | $880^{+450}_{-390}$ | $0.18^{+0.08}_{-0.07}$ | $31.2^{+8.4}_{-6.0}$ | $19.4^{+5.3}_{-5.9}$ | $2.0^{+0.6}_{-0.7}$ | $48.7^{+5.7}_{-4.6}$ | $0.64^{+0.09}_{-0.20}$ |
| GW170608 | BH-BH | $340^{+140}_{-140}$ | $0.07^{+0.03}_{-0.03}$ | $12^{+7}_{-2}$ | $7^{+2}_{-2}$ | $0.85^{+0.07}_{-0.17}$ | $18.0^{+4.8}_{-0.9}$ | $0.69^{+0.04}_{-0.05}$ |
| GW170814 | BH-BH | $540^{+130}_{-210}$ | $0.11^{+0.03}_{-0.04}$ | $30.5^{+5.7}_{-3.0}$ | $25.3^{+2.8}_{-4.2}$ | $2.7^{+0.4}_{-0.3}$ | $53.2^{+3.2}_{-2.5}$ | $0.70^{+0.07}_{-0.05}$ |
| GW170817 | NS-NS | $40^{+8}_{-14}$ | $0.008^{+0.002}_{-0.003}$ | $1.36 - 1.60$ | $1.17 - 1.36$ | $> 0.025$ | | |

**Table 2:** Parameters of the GW events measured so far [1, 4, 14–18]. The masses displayed for the GW170817 event are based on a model assuming low component spins. Such a model matches earlier observations of binary neutron stars. The nature of the remnant of GW170817 is still subject of discussion.

About ten months after the Advanced LIGO detectors were shut down for maintenance and minor improvements the second observation run (O2) began on November 30, 2016. On August 1, 2017, the Advanced Virgo detector joined O2. The systems went offline for further improvements as scheduled on August 25, 2017. During the second observation run, three binary black hole mergers were observed. Moreover, the first GW signal of a binary neutron star collapse was detected a few days before O2 ended (see section 1.4).

The first event measured in O2 was GW170104. With a distance to the source of $880^{+450}_{-390}$ MPc it is the farthest event that has been observed so far [16].

The lightest and closest black hole merger detected with GW detectors corresponds to GW170608. X-ray binaries with a similar size

were observed optically. This allows the comparison of x-ray and GW observations [17].

Shortly after the Advanced Virgo detector started taking scientific data, a third binary black hole collision, called GW170814, was detected in O2. The participation of three detectors enabled an estimation of the polarization of the GWs. Furthermore, a far better identification of the source's location can be deduced from the data measured by the LIGO-Virgo antenna network [4]. The area of the sky region was estimated to be $60\,\mathrm{deg}^2$. For the two LIGO detectors alone, this region would be about 20 times larger. This constraint on the sky location greatly increases the chance for astronomers to detect electromagnetic counterparts to the GWs. The first of such multi-messenger detection is described in the following section.

## 1.4 FIRST MULTI-MESSENGER DETECTION OF A NEUTRON STAR BINARY COLLAPSE

On August 17, 2017, the LIGO-Virgo observatory network detected a further GW signal, shortly before the end of O2 [18]. 1.7 seconds later, a short $\gamma$-ray burst was detected independently by the Fermi and the INTEGRAL satellites [19].

The GW170817 waveform was quite different from those detected before. Whereas the black hole binary signals lasted for less than 2 seconds in the measurement band of the detectors, the latest event's waveform was visible for approximately 100 seconds. The frequency of the signal swept from approximately 24 Hz to a few hundred Hertz in the typical chirp pattern of a compact binary collapse. The waveform suggests that it originates from the collision of two neutron stars with a total mass of the system of approximately $3\,\mathrm{M}_\odot$. The distance from the source was estimated to be $40^{+8}_{-14}$ Mpc (further parameters of the event are shown in table 2).

The difference in the signal's arrival time at the three GW detectors allowed the localization of the source within a sky region of $28\,\mathrm{deg}^2$. With this directional information, multiple telescopes detected signals which were associated with the GW signal GW170817, even though the estimations of this sky map took a few hours due to technical difficulties. These electromagnetic counterparts of the GW signal were detected in a wide frequency band, covering gamma rays, X-rays, ultraviolet, visible, infrared and radio waves [20]. No neutrino signal consistent with GW170817 was detected [21].

With these electromagnetic signals, the source of the event was located in the galaxy NGC 4993. The observation supports the theory that heavy elements, such as gold and platinum, are formed when two neutron stars merge. The merger rate deduced from the event and the estimate of mass ejected by the collision even suggest that neutron star mergers produce the major part of heavy elements in the universe.

The immense scientific significance of GW170817 is reflected in the additional information gained from the detection. This includes a new way to determine the expansion rate of the universe, in other words, the Hubble constant. It is estimated from the GW luminosity distance and the recession velocity, which is the rate at which astronomical objects move away. The recession velocity is deduced from the redshift of the electromagnetic signal.

The result is in good agreement with excising measurements, while being completely independent of them [22]. Further detections of similar systems will decrease the error bars on the Hubble constant.

The multi-messenger measurement of GW170817 did not only prove the theory of general relativity by being fully consistent with it. Moreover, it proves experimentally the connection between $\gamma$-ray burst, transient astronomical events called kilonovae, and neutron star mergers [20].

Further exciting physics, such as the investigation of the speed of gravity and tests of the equivalence principle, can be explored by comparing GW signals and $\gamma$-rays emitted by the same source [19].

GW measurements as an integral part of multi-messenger astronomy have opened a new window to learn more about the universe. Objects such as pulsars and events such as supernovae have high potential to be detected soon. The GW detectors' performance will, therefore, be further improved and new detectors will be included in the antenna network within this decade. Novel techniques need to be developed and tested in order to increase the sensitivity of the detectors and to overcome even largely unexplored limitations such as the standard quantum limit (SQL) of interferometry. The AEI 10 m prototype, which is discussed in this thesis, will pioneer in such investigations; however, the low frequency sensitivity of the experiments performed at the AEI 10 m prototype facility, as well as all current ground-based GW detectors, are limited by environmental vibrations. These are for the most part seismic motion. A substantial seismic vibration reduction is needed in order to provide the low displacement noise environment required for such experiments. This thesis discusses the low frequency Seismic Attenuation System employed in the AEI 10 m prototype, the AEI-SAS. The presented improvement techniques do not only enable high precision measurements at AEI 10 m prototype, but they have the potential to be adapted for the current GW detector's seismic isolation systems. The detailed analysis of the AEI-SAS and its individual components, furthermore, influences the development and design of new vibration isolation systems, which will increase the GW measurement band.

# 2 MOTIVATION AND STRUCTURE OF THIS THESIS

As motivated in section 1, further performance improvement of current GW detectors and the developments of new observatories is required to increase the GW detection rate. This will provide completely new insights into the universe. These techniques are developed in test facilities such as the AEI 10 m prototype. It provides an extremely low noise environment which also enables the setup of high precision experiments, apart from testing improvements for GW detectors. An overview of the AEI 10 m prototype is given in chapter 4.

For the AEI 10 m prototype as well as for ground-based GW detectors environmental vibrations is the natural dominant noise source at low frequencies. Developing techniques to mitigate the influence of this seismic noise, therefore, is an essential task for such experiments.

The Seismic Attenuation System for the AEI 10 m prototype, the AEI-SAS, is an integral part of solving this task. It is supposed to decouple numerous present and future experiments from vibrations caused by seismic and anthropogenic ground motion, as well as from structural acoustics. The system furthermore compensates for low frequency drifts and provides a high position adjustment range. Its original design is presented in ref. [23] and [24]. Developing improvements for the isolation performance allows the realization of more sensitive experiments. The same techniques can furthermore be applied in other vibration cancellation systems. An overview of such devices is given in chapter 3. Insights gained by characterizing the AEI-SAS lead to a better design for new isolation systems. The Advanced Virgo GW detector now employs a suspended external injection bench which is based on the AEI-SAS design (see section 3.6.2). System designs related to the AEI-SAS are furthermore proposed as noise cancellations for third generation GW detectors [25] as well as for high precision devices outside the field of GW physics. The design of the vibration isolation system for the very long baseline atom interferometers (VLBAI), for instance, was strongly influenced by the experience with the AEI-SAS [26].

## 2.1 INTRODUCTION: WHY DOES THE AEI-SAS NEED IMPROVEMENT

There are restrictions to the AEI-SAS on both ends of the frequency band. At low frequencies, the passive isolation window is confined by the AEI-SAS's fundamental resonances. At high frequencies internal resonances and the CoP plateaus of the Inverted Pendulum (IP)-legs and Geometric Anti-Spring (GAS)-filters limit the passive isolation win-

dow. On that account, an improved technique for the GAS-filters' CoP and resonance frequency tuning, internal resonance frequency shifting, and damping, as well as the active isolation, are discussed. A good understanding of the system and its limitations is necessary for the development of such improvements. Part II of this work, therefore, analyzes the AEI-SAS in detail.

In this introduction, the necessity and benefits of performance improvements are briefly discussed.

### 2.1.1 *High frequency isolation limits: internal resonances and CoP plateau*

The AEI-SAS's purpose is to provide low frequency vibration isolation for the AEI 10 m prototype experiments. Ideally, above a relatively low frequency resonance the transmissibility of ground motion to payload motion rolls of with $f^{-2}$ (see section 6.1). There are two main limits that typically let real systems deviate from the ideal passive isolation of a harmonic oscillator at high frequencies:

- The moment of inertia of a massive spring and the corresponding center of percussion effect (discussed in section 7.1.3 in more detail) limits the isolation of AEI-SAS-like systems above about 10 Hz (depending on the resonance frequency) to a constant value (depending on the CoP tuning).
- The components and the support structure of the isolation system are not ideally stiff but bend dynamically. The resulting oscillations are referred to as internal resonances. In particular, the spring components are not ideally uni-directional but show a certain compliance in all degrees of freedom. The systems are typically designed such that internal resonances are at much higher frequencies than the fundamental resonances of the system.

Accordingly, the isolation window of a vibration isolation system spans in between the fundamental resonance frequencies and the internal resonance frequencies. Typically, low fundamental resonance frequencies cause relatively low internal resonance frequencies[1]. A very simple illustration is the example of a simple pendulum. The fundamental resonance frequency of a pendulum is inversely proportional to the square root of the pendulum string's length; however, since the string material has a finite stiffness, the vertical bounce mode frequency decreases in the same way. Violin mode frequencies decrease with pendulum string length as well [27][2].

1 Certainly, internal resonances can be caused by other reasons as well. For instance, in the case of the vertical spring-box modes not only the vertical compliance of the IP-legs but also the insufficient stiffening of the support structure causes relatively low internal resonance frequencies (see section 11.3).

2 The same holds true for the example of an idealized IP-leg: A higher payload mass reduces the fundamental resonance frequency (see equation 37) but also reduces the

Hence, the design of a vibration attenuation systems needs to be carefully adapted to the frequency window that requires isolation. In terms of the AEI 10 m prototype's Standard Quantum Limit (SQL) interferometer the measurement frequency window (around 200 Hz) is decoupled from ambient motion by the triple stage mirror suspension system (see section 4.1.3). Thus, the suspension system is designed in such a way that its fundamental resonances (including vertical bounce) are below 30 Hz and the lowest violin modes will be at approximately 1 kHz.

The AEI-SAS is, for the main part, designed to pre-isolate the mirror suspensions mounted on the optical table at their fundamental resonances frequencies in order to reduce their rms motion. Their resonance frequencies range from 0.63 Hz to 27.3 Hz. The lowest frequency corresponds to the longitudinal swing mode of the 850 g triple suspensions (e.g. the frequency reference cavity), the highest frequency is the lowest stage roll mode frequency of the SQL mirrors [28, 29]. The latter value is based on a model and might differ slightly in reality.

At the lower end of the frequency band payload motion reduction is achieved by active control. Above 3 Hz the AEI-SAS's performance relies purely on passive isolation.

The lowest of the original design AEI-SAS internal resonances were as low as 13 Hz and 17 Hz, due to the relatively low horizontal compliance of the GAS-filters and the corresponding differential spring-box-payload oscillation (discussed in section 11.2). The next highest set of internal resonances between 30 Hz and 35 Hz arises from an interaction between the low vertical stiffness of the original IP-legs and the bending of the spring-box (discussed in section 11.3).

These internal resonances are within, or close to, the suspensions' resonance frequency band and the amplitude of individual modes used to be even higher than ground motion at the same frequency. Thus, the AEI-SAS's original design required extensive improvements in order to serve its purpose of pre-isolating the mirror suspensions.

Low internal resonance frequencies furthermore limit the active isolation abilities as they strongly influence the loop design. Unity gain frequency and the steepness of the control filters need to be chosen, such that no gain peaking at internal resonances occurs.

Although internal resonances cannot be eliminated completely, design changes to mitigate their harm are required. In general, there are two options to achieve this: the first one is to dampen the modes (reduce their peak height), the second one is to stiffen the system (shift them to higher frequencies), in order to widen the isolation window. Increasing the internal resonance frequencies usually also reduces the rms motion coupled to the payload since the ground motion decreases with higher frequencies.

---

frequency of its bounce mode. The vertical stiffness of a realistic IP can nevertheless be increased without influencing the horizontal stiffness, as described in section 13.

Different techniques that employ both options, stiffening, and damping, were investigated theoretically and tested experimentally in the AEI-SAS. The techniques and the resulting improvements are discussed in chapter 11 to 15.

### 2.1.2 *Low frequency active control*

Below its eigenfrequencies, a purely passive isolation system cannot provide any vibration attenuation. It even enhances the ground motion on and around its fundamental resonance frequency (see section 6.1). The AEI-SAS has 6 fundamental resonances corresponding to the 6 (rigid body) degrees of freedom. Depending on the choice of the coordinate system the motion in the different direction is partially coupled. The AEI-SAS's principal axes do not coincide exactly with the Cartesian coordinate system, due to imperfections in the mechanical tuning. Thus, cross-coupling between the individual degrees of freedom reduces the performance, particularly in the frequency band of the fundamental resonances (see chapter 9).

Reducing the quality factor by passive viscous damping (relative to ground) would lower the amplitude at the resonance at the cost of reducing the steepness of the transmissibility roll-off to $f^{-1}$ (compare to section 6.1). The fundamental resonances of the AEI-SAS are furthermore strongly excited as they are in the frequency band of the microseismic peak, a maximum of ground motion amplitude (see section 4.1.2.1). This is a strongly motivating the suppression of the payload motion below the ground motion, also at low frequencies.

The AEI-SAS is equipped with a set of sensors and actuators (see section 5.2). They read out the payload motion and feed an actuation force back to minimize this motion, originally to dampen the fundamental modes. The sensors and actuators can however also be used to suppress the payload motion below the ground motion at low frequencies. The active isolation of the AEI-SAS is discussed in section 16.

## 2.2 THESIS STRUCTURE

Part I of this thesis gives an introduction to the field of GW astronomy. It thereby motivates the necessity of GW detector improvements and the need of vibration isolation. It furthermore gives an overview of the vibration isolation methods used in GW detectors and emphasizes their similarities to and differences from the AEI-SAS. The introductory part of this thesis ends with a discussion of the AEI 10 m prototype as a testbed for GW detector improvements and a facility for high precision experiments.

The second part (II) of this thesis describes the working principle of the AEI-SAS. Its individual components are analyzed and a general

introduction to passive vibration isolation is given. This part discusses potential performance limitations and the risk of hydrogen embrittlement in GAS-filter blades. It finishes with a detailed characterization of the AEI-SAS's performance, which is compared to other state of the art vibration isolation systems.

Part III of this thesis discusses the development of the AEI-SAS improvements. It introduces an enhanced method of GAS-filter tuning, followed by an analysis of the AEI-SAS's internal resonances. Techniques for the mitigation of these parasitic modes are described and characterized in detail. This part furthermore elucidates the AEI-SAS's active control strategy and reports its current status. A discussion of a proceeding in the case of a GAS-filter failure finalizes the main part of this thesis. The results from this work are applied to develop a draft of a possible new isolation system design for the AEI 10 m prototype.

The work of this thesis is summarized in part IV, which also gives a brief outlook on followup work.

The low noise environment provided by the AEI-SAS enables electrostatic actuation of the SQL interferometer test masses with a rather simple capacitor design. The discussion of this system's realization is not directly related to the main part of this thesis and therefore subject of the appendix A. It presents a finite element simulation based electrostatic drive (ESD) design as a preparation for the realization of such a system.

# 3

# VIBRATION ISOLATION FOR GRAVITATIONAL WAVE DETECTORS

In this chapter the vibration isolation systems operating in interferometric GW detectors of past and present are discussed. The detectors treated in the following are:

- **Tama 300**, the former Japanese GW detector with a 300 m baseline length. It is located at the Mitaka campus of the National Astronomical Observatory of Japan (NAOJ). Construction started in 1995 and data was recorded between 1999 and 2004 [30]. Thereby TAMA 300 was the first online interferometric GW detector.

- The construction of **GEO 600**, too, began in 1995. This 600 m baseline length GW detector is operated since 2002. It is located in Ruthe near Hannover, Germany [31]. GEO 600 is operated by a joint Center of Gravitational Physics of AEI and Leibniz Universität Hannover, together with the universities of Glasgow and Cardiff [32].

- The construction of the Laser Interferometer Gravitational-Wave Observatory (**LIGO**) started as early as 1994. It consists of two 4 km arm length interferometric GW detectors, one located in Hanford, Washington, one in Livingston, Louisiana. LIGO started taking data in 2002 [33]. From the beginning it was planned to construct first a simpler, less sensitive interferometer called initial LIGO and than upgrade it to a much more sensitive Advanced LIGO [34]. As the first detector of the 2nd generation to come online Advanced LIGO was the first observatory to directly detect a GW signal in September 2015 (see section 1.2).

- The **Virgo** interferometer is a 3 km arm length GW detector located in Cascina near Pisa, Italy [35]. Its construction started in 1996 and was finished in 2003. After a commissioning phase, the first data was taken together with LIGO and GEO 600 between May and October 2007 [36]. In 2012 Virgo started updating the detector to a 2nd generation GW observatory. In August 2017 Advanced Virgo joined Advanced LIGO in the second Advanced Detector Observing Run O2 (see section 1.3).

- The Kamioka Gravitational Wave Detector (**KAGRA**), formerly called the Large Scale Cryogenic Gravitational Wave Telescope (LCGT), is a Japanese GW detector currently being constructed in the Kamioka mine [37]. It is the first GW detector underground

and the first with cryogenic test masses. The initial phase operation of a 3 km baseline length interferometer has been completed. In 2018 the first cryogenic operation is expected, followed by observing runs with a full interferometer in the 2020s [38].

Further future ground-based detectors such as LIGO India [39] or the Einstein Telescope [40] are not discussed here, since their seismic isolation is either (in the case of LIGO India) identical to already existing systems or only proposed, but not yet built and tested.

In addition to the operating vibration isolation systems the geometry and performance of prototypes related to the AEI-SAS are summarized in this chapter, too (without any claim to completeness).

Both passive and active systems will be discussed. Passive systems refer to low fundamental resonance frequencies, low active bandwidth systems, while active systems have high fundamental resonance frequencies and a high active bandwidth.

The advantages and disadvantages of passive systems over active systems are summarized by Stochino et al. [41].

A summary of the evolution of low resonance frequency vibration isolation systems is given at the beginning of this chapter with a 'family tree' of these devices. This will show the chronological order and development steps. The vibration isolation systems are discussed in more detail below.

This chapter will show, that vibration isolation systems in GW detectors have many similarities. This suggests, that the studies and improvements of isolation limitations in the AEI-SAS could be applicable for other systems, too, in order to improve their performance. It furthermore quotes the isolation performance of the different systems. These numbers are more for the characterization, rather than for the comparison of the individual devices, since they are designed for different purposes, e.g. pre-isolation, test mass isolation or the isolation auxiliary systems.

## 3.1 LOW RESONANCE FREQUENCY VIBRATION ISOLATION SYSTEMS FAMILY TREE

This section briefly describes the evolution of low resonance frequency vibration isolation system for GW detectors, without claiming completeness. The subject of this overview are systems which are incorporating isolation components closely related to those integrated into the AEI-SAS. Low resonance frequency vibration isolation systems such as the X-pendulum [42], the folded pendulum [43], the Scott-Russell horizontal isolator [44], the torsion crank vertical isolator [45], and the AIGO High Performance Compact Vibration Isolation System [46] are not regarded.

Figure 4 illustrates this evolution as a family tree. The origin from which the single drawings of the systems were taken and the year the

isolation systems were published are listed in the following paragraph. The evolution of this systems is summarized below.

- Horizontal **IP-leg isolation stage** [47] published in 1993;
- **Blade springs with MAS** [48] published in 1997;
- **Superattenuator** [49] preliminary design published in 1987 [50], performance published in 2005;
- **GAS-filter** [51], feasibility study published in 1999 [52];
- **LIGO-SAS** [51] published in 2000 [53]
- **TAMA-SAS** [54], published in 2002;
- **HAM-SAS** [55], first results published in 2006 [56];
- **AEI-SAS** [57], design and preliminary results published in 2012 [23];
- **EIB-SAS** [58] installed at Virgo in 2011 published in 2012;
- **MultiSAS** [59] installed at Virgo in 2014;
- **KAGRA-SAS** [60] basic principle approved in 2002 [61], Installation of the suspension system at the Kamioka site ongoing at the time of writing this thesis [38].

### 3.1.1 *Evolution of low resonance frequency vibration isolation system*

In 1993 Pinoli et al. [47] reported the performance of inverted pendulums as horizontal vibration isolators. They were chosen as the horizontal pre-isolation stage for Virgo's test masses. A first multistage pendulum isolation for Virgo was proposed in 1987 by Fabbro et al. [50]. The vertical performance of the Superattenuator was improved by lowering the blade spring filter resonance frequency with magnetic anti springs. The results of the same were published in 1997 by Beccaria et al. [48]. A geometry close to the current Superattenuator was proposed in the same year by Holloway [62]. The Superattenuator is described in more detail in section 3.2.

As a passive suspension system and an alternative to LIGO's passive isolation stack [63] the SAS was proposed in 2000 by Bertolini et al. [53] (for clear distinction from the other SASs this system is here referred to as LIGO-SAS). Although similar in design to the Superattenuator, it features GAS-filters as cascaded vertical isolation stages instead of blade springs with MAS. A feasibility study of the GAS-filters was published in 1999 by Bertolini et al. [52].

Even though the LIGO-SAS was discarded as an isolation system for LIGO the design was modified and implemented in TAMA 300 as the

TAMA-SAS, introduced by Takamori et al. in 2002 [54]. More information can be found in section 3.4.

Components of the LIGO-SAS were furthermore used to design a vibration isolation system to support the optical benches in Advanced LIGO's HAM chambers. In contrast to the systems listed above, the HAM-SAS supports the payload from below. First results of this system were presented by Bertolini et al. in 2006 [56]. The HAM-SAS is described in more detail in section 3.5.1.

Although not implemented in Advanced LIGO, the HAM-SAS design was improved and adapted as pre-isolation for the AEI 10 m prototype, the AEI-SAS. The system was first mentioned in 2010 [64].

Further minor modifications led to the EIB-SAS, an out of vacuum isolation system for Advanced Virgo's external injection bench. The requirements on this system are more relaxed compared to the AEI-SAS. It was introduced in 2012 by Beker et al. [58] and is described in more detail in section 3.6.2.

The geometry of the multiSAS is similar to the TAMA-SAS. However, building the EIB-SAS at Nikhef allowed the multiSAS (which were built at Nikhef, too) to benefit from this experience. First results were published in 2013 by Beker [59]. The multiSAS is described in more detail in section 3.6.1.

The KAGRA-SAS is the latest youngest vibration isolation system for GW detectors. It is currently being installed at the KAGRA site [38]. Its structure resembles the Superattenuators 8 horizontal and 6 vertical low frequency stages (an additional vertical stage is part of the cryogenic test mass). However, the KAGRA-SAS features components that have proven themselves in the other systems here presented, namely GAS-filters and short IP-legs. A difference to its predecessors is that the KAGRA-SAS's test mass will be cooled to cryogenic temperature in order to reduce thermal noise. The KAGRA-SAS is described in more detail in section 3.6.3.

## 3.2 VIRGO'S SUPERATTENUATOR

The first species in the family of passive isolation systems in GW detectors is Virgo's Superattenuator [50, 65]. It is basically a multi-stage coupled harmonic oscillator, where each stage provides both horizontal and vertical isolation.

Early prototypes led the way to the current system. The first prototype was a seven-fold pendulum. Each pendulum stage consists of a gas spring (not to be confused with the GAS-filters) for vertical isolation [66]. Additional Magnetic Anti Springs (MAS) lowered the vertical gas-spring resonance frequencies below 2.5 Hz [67]. These basically consist of a set of magnets fixed to a frame and a second set of magnets mounted to the structure suspended by the spring. The polarity of the

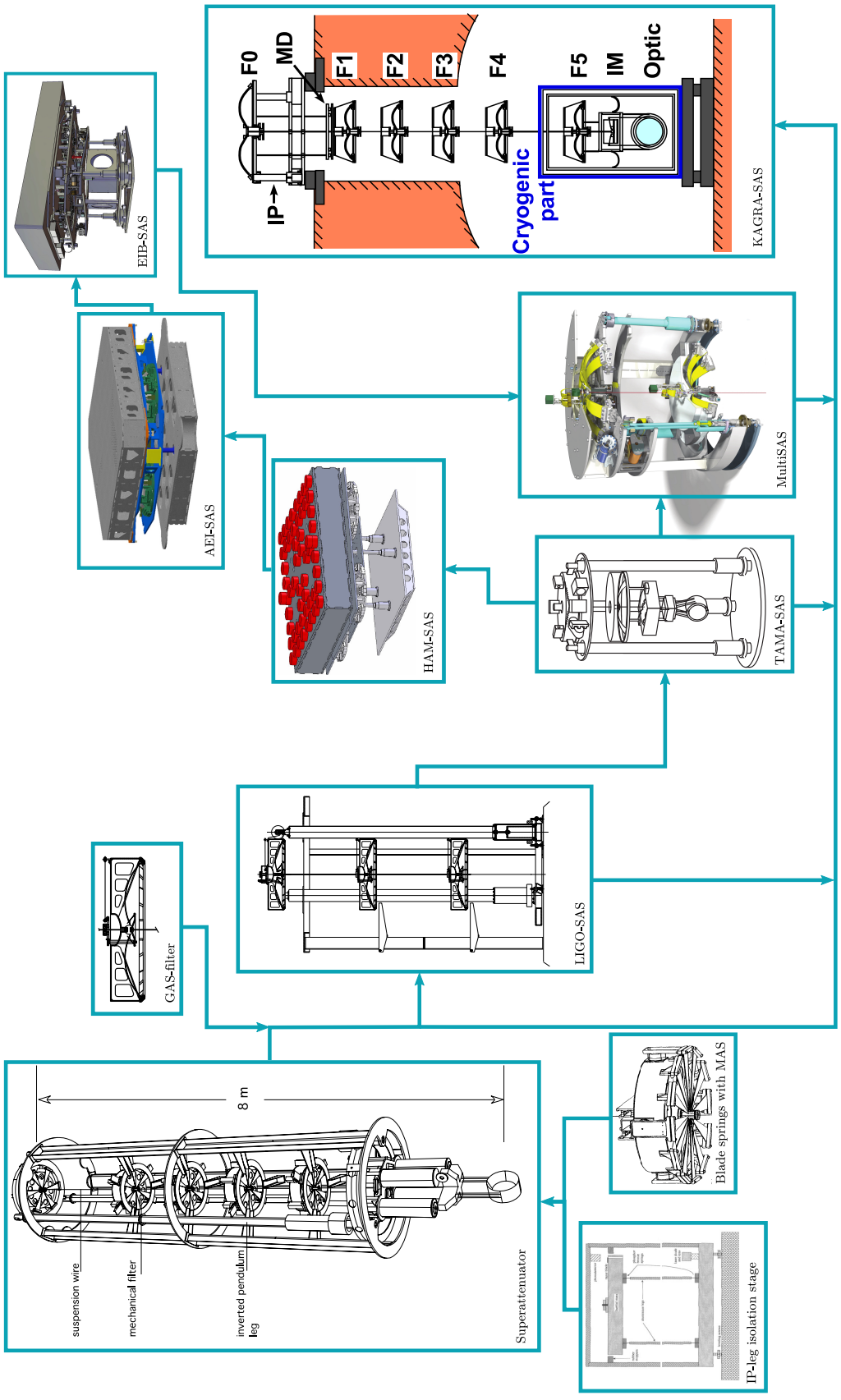


**Figure 4:** Low frequency vibration isolation system family tree. The origin of the drawings and the year the systems were published is listed above in section 3.1.

magnets is aligned such that repulsive force is counteracting the spring force.

The Superattenuator design installed in Virgo is a progression of these prototypes. It consists of a primary low frequency IP-leg isolation stage and a cascade of six vertical filters, which provide horizontal and vertical isolation (see figure 4). The payload is suspended from the last filter. It consists of an upper mass (called the marionette), which supports the interferometer mirror and a reference mass. The reference mass acts as a reaction mass for the actuators controlling the mirror position [65].

A first IP-leg isolation stage prototype for GW detectors was investigated by Pinoli et al. in 1993 [47]. The Superattenuator IP-leg pre-isolation stage was then presented by Losurdo et al. [68]. These 6 m high IP-legs achieves an isolation of approximately $5.6 \times 10^{-4}$ at 1 Hz due to a horizontal resonance frequency of 30 mHz. They, however, suffer from rather low frequency internal resonances.

The vertical gas-filters of the early design were discarded in favor of an arrangement of metal blades. These circular arranged, triangular blades are pre-bent such that they are approximately flat when under load. Again, additional MASs were used to reduce the vertical resonance frequencies of the system, such that the highest vertical resonance frequency of the Superattenuator is at approximately 2 Hz [48]. A technical drawing of such a filter is part of figure 4. In order to achieve low creep noise maraging steel was chosen for the filter blade material [69, 70] and is used as spring material in many related systems ever since.

For low frequency control, the Superattenuator is equipped with a set of sensors and actuators, similar to those used in later systems like the AEI-SAS [71].

As a result of the Superattenuator's outstanding performance, it was retained in the Advanced Virgo design, whereas other upgraded detectors required newly designed seismic isolation [72]. Only minor design changes to the Superattenuator were necessary [73], such as:

- Stiffening the central tube of the IP-legs by machining it from one piece, rather than bolting multiple pieces together. The 'monolithic' IP-legs increased its bending ('banana') mode frequency from approximately 10 Hz to above 20 Hz.

- The installation of piezo actuators below the foundation ring which the IP-legs are mounted on, in order to allow tilt control of the entire isolation system.

### 3.3 GEO 600's VIBRATION ISOLATION SYSTEMS

GEO 600's vibration isolation relies on a passive pre-isolation stage and a triple suspension system. The pre-isolation stage consists of a

rubber layer that supports an stainless steel layers. This passive stage is mounted on top of an active piezo stage, equipped with geophones for active control. However, the active part has not been operated long term due to technical problems. These stacks are encapsulated in stainless steel bellows to prevent contamination of the vacuum system. This rather simple system provides vertical isolation of approximately $1 \times 10^{-1}$ and approximately $3.2 \times 10^{-2}$ in horizontal directions at 50 Hz [74]. A technical drawing of GEO 600's isolation system is shown in figure 5

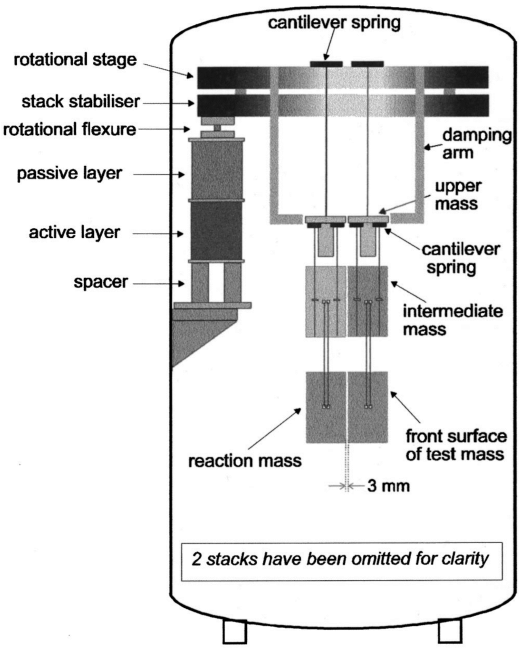


**Figure 5:** Technical drawing of GEO 600's vibration isolation system. This figure was taken from [74].

Three of these stainless steel-rubber stacks carry each a triple suspension system, which support the test masses as the lowest pendulum stage. These optics are suspended by fibers from the penultimate mass. The test mass, the fibers, and the penultimate mass are made from fused silica in order to reduce suspension thermal noise. GEO 600 was the first GW detector realizing this so-called monolithic suspension [74, 75], a feature later applied in other detectors.

A model of GEO 600's vibration isolation performance is shown in figure 10. The high frequency performance is briefly compared to the initial LIGO vibration isolation in section 3.5.

## 3.4 THE TAMA-SAS

Seismic isolation for TAMA 300 underwent many changes before the final TAMA-SAS was designed and implemented. A first isolation system installed in TAMA 300 was a stack of rubber and steel plates, similar

in design but softer than the GEO 600 isolation stack [76]. It was found to provide insufficient attenuation. Thus, it was discarded in favor of a commercial system which itself performed unsatisfyingly. A passive system based furthermore on a two-dimensional X pendulum was proposed and tested by Barton et al. [77]. Unwanted low frequency internal resonances, cross-coupling, and a challenging resonance frequency tuning led to replacing this system by the TAMA-SAS.

The TAMA-SAS was developed by a collaboration of Caltech and TAMA researchers, starting in 2000. The design of the system is based on the LIGO-SAS prototype experiments [53, 61, 78]. The goal was to obtain a system which meets TAMA's requirements and is more compact and simpler than the Virgo's Superattenuator while maintaining its strong points. These are the completely passive attenuation at high frequencies, which provides high reliability, combined with the low frequency active control [79].

The main improvement of the TAMA-SAS over the Superattenuator is the monolithic geometric anti-spring (MGAS)-filters [80]. They are a progression of the GAS-filters introduced by Bertolini et al. [52]. The principle of GAS-filters is discussed in chapter 8.

Similar to the Superattenuator the system is pre-isolated by an IP-leg stage. It supports a cascade of two MGAS-filters, suspended in series and providing vertical isolation. From the lower filter, the payload is suspended. The payload itself is a multi-stage pendulum suspended from four mini-GAS-filters embedded in the platform suspended from the lower MGAS-filter. These four vertical attenuators support an intermediate stage for eddy-current damping of the payload motion. The test mass and the recoil mass are hanging from this intermediate mass [81]. A technical drawing of the TAMA-SAS is shown in figure 4.

Even though the IP-legs are shorter compared to the Superattenuator (2.5 m) they were tuned to a horizontal resonance frequency below 100 mHz. With an MGAS-filter's resonance frequency below 500 mHz two of these have the isolation performance of three Superattenuator filters. This enabled an isolation factor at the mirror of $1 \times 10^{-12}$ at a few hertz [61]. The modeled performance of the TAMA-SAS, including the payload, is shown in figure 10. Four SAS towers for the test-mass mirrors were sequentially installed from 2005 to 2006 in TAMA 300 [81].

## 3.5 LIGO'S VIBRATION ISOLATION SYSTEMS

In the initial LIGO design, seismic isolation was rather rudimentary compared to the state of the art Advanced LIGO system. The mirrors were suspended as a single stage pendulum which was pre-isolated by a stack of four masses supported by rubber damped springs, similar to the passive GEO 600 pre-isolation stage. The design was published in 1996 by Giaime et al. [63]. The modeled performance of this system is compared to other isolation systems in figure 10.

Even though GEO 600 suspends their optics from a triple suspension the high frequency performance (in terms of test mass motion) of the initial LIGO and the GEO 600 system is very similar at high frequencies. The reason for it is, that initial LIGO's pre-isolation stack contributes strongly to the high frequency isolation with attenuation factors up to $1 \times 10^{-7}$ in the horizontal directions and $2.9 \times 10^{-6}$ in the vertical direction at 100 Hz [63].

Strong micro seismic motion and relatively high traffic noise compromised the duty cycle of the Livingston detector, which led to the design and implementation of active Hydraulic External Pre-Isolators (HEPI). This system provides the DC-actuation range necessary to compensate for environmental disturbances [82]. Each HEPI system supports a total mass of 6400 kg, actively pre-isolating it in 6 degrees of freedom between 100 mHz and 10 Hz [83].

In 2005, a newly designed isolation system, based on the passive components of the LIGO-SAS [53] (compare to section 3.4), was suggested as a platform for the HAM (horizontal access module) vacuum chambers [56]. However, after only 8 months of testing it was discarded in April 2007 in favor of the active/passive HAM-ISI. The reasons given for this decision were that

- Not all isolation requirements were met
- The active control system was not tested at that time
- Stability issues were not studied
- The interaction with suspensions to be mounted on the platform was not tested experimentally

A longer characterization time could probably have answered those questions [84].

Both systems, HAM-SAS and the HAM-ISI are briefly discussed in the following subsections, since they are strongly related to the AEI-SAS. The HAM-SAS is the direct ancestor of the AEI-SAS and the HAM-ISI is the operating system best comparable to the AEI-SAS, while based on a different mechanical approach. A feature common to AEI-SAS, HAM-SAS and HAM-ISI is, that they support an approximately 1-ton optical bench from below by one isolation stage in horizontal and one in the vertical direction. Furthermore, all three systems are designed to operate in ultra high vacuum. Apart from the HEPI a completely redesigned isolation system for Advanced LIGO replaced the initial LIGO system. The new systems can be summarized as:

- HEPI is located externally to the vacuum system and forms the first stage of vibration isolation.
- The next one or two stages are referred to as the Internal Seismic Isolation (ISI) systems. They are contained within the vacuum

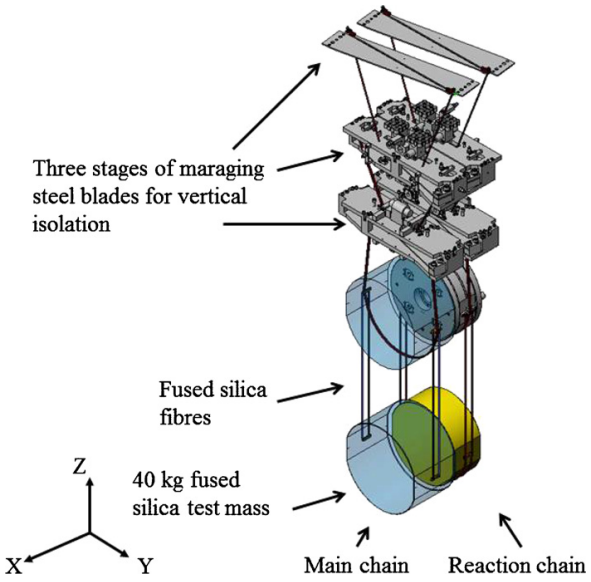


**Figure 6:** Drawing of quadruple pendulum with quadruple reaction pendulum suspended behind it.
This figure is taken from [85].

system. The test mass, beam splitter and transmission monitor suspensions are supported by inverted optics tables which have two in-vacuum stages, housed in the BSC chambers. All other interferometer elements are supported by HAM-ISI units, discussed in more detail below. They are basically optics tables installed on a one-stage ISI systems, housed in smaller Horizontal Access Modules (HAM) vacuum chambers [86].

- The optics are suspended as multi-stage pendulums from the ISI. The number of horizontal and vertical isolation stages depends on the requirements. The most sophisticated suspension system supports the 40 kg test masses and their reaction masses. Four horizontal and three vertical stages provide a longitudinal noise floor better than $10^{-19}\,\mathrm{m}/\sqrt{\mathrm{Hz}}$ at 10 Hz[1]. The suspension system's design is based on the GEO 600 suspensions and was developed at the University of Glasgow [85]. Accordingly the design resembles the AEI 10 m prototype's SQL suspensions, particularly due to the monolithic last pendulum stage. A drawing of the quadruple pendulum suspension is shown in figure 6

This way the optics are isolated by up to seven stages in the horizontal direction and up to six stages in the vertical direction in case of the interferometer's core optics. The performance of the full test mass suspension system is shown in figure 10.

1 In Advanced LIGO the monolithic stage is not counted as a fourth vertical isolation stage, even though the bounce mode is relatively low.

### 3.5.1 *The HAM-SAS*

The HAM-SAS was designed as a cost-effective, simple and reliable vibration isolation solution for the Advanced LIGO's auxiliary optics. The concept and first measurements of this one stage horizontal and one stage vertical attenuator was published in 2006 by Bertolini et al.[56].The system was proposed as a low natural resonant frequencies, low-bandwidth control systems alternative to the high natural resonant frequencies, high-bandwidth control systems provided by the HEPI-ISI baseline [87].

Even though the original HAM-SAS design is purely based on passive mechanical oscillators to fulfill the Advanced LIGO requirements it left space to upgrade the system by active components.

The HAM-SAS's structure resembles strongly the AEI-SAS (see figure 4). A horizontal stage, the spring-box, is supported by four IP-legs, which are mounted on a baseplate. This baseplate interconnects the HAM-SAS to the vacuum chamber. The spring-box, in turn, houses four GAS-filters which are supporting the optical table [55].

In order to lower the CoP effect (see section 7.1.4) the weight of the 448 mm long legs was reduced to 300 g. Already without CoP compensators an isolation plateau of approximately $1 \times 10^{-4}$ was achieved. CoP compensators were included in the design but not tested [41].

Figure 7 shows the horizontal performance measured in the test lab (gray) and the projection of the system's transmissibility on the seismic noise at the LIGO Livingston site (black) compared to requirements on a HAM chamber isolation system. It shows that most of the requirements are achieved. Only at low frequencies (below 800 mHz) and at an amplitude peak between 10 Hz and and 20 Hz the horizontal payload motion is to high. The authors argued, that this preliminary result was achieved after very short commissioning time. Finer tuning of the filters as well as implementation of all subsystems should make the complete fulfillment of the requirement possible [41].

For thorough investigations of the origin of the amplitude peak between 10 Hz and and 20 Hz the tight schedule did not leave any time. Preliminary tests of damping the suspected tilt correcting springs and the corresponding wires showed a small effect on the resonance [88][2]. However, the AEI-SAS shows resonances in the same frequency band. They could be identified as the differential, mainly horizontal oscillation of spring-box and the table top, due to the horizontal compliance of the GAS-filters. How these modes were studied and how their effect is mitigated is discussed in chapter 11 and 12.

2 This is the reason why the AEI-SAS does have high internal resonance frequency blade springs functuning as tilt stabilization. They are connected by wires tuned to 170 Hz to the central column (see section).

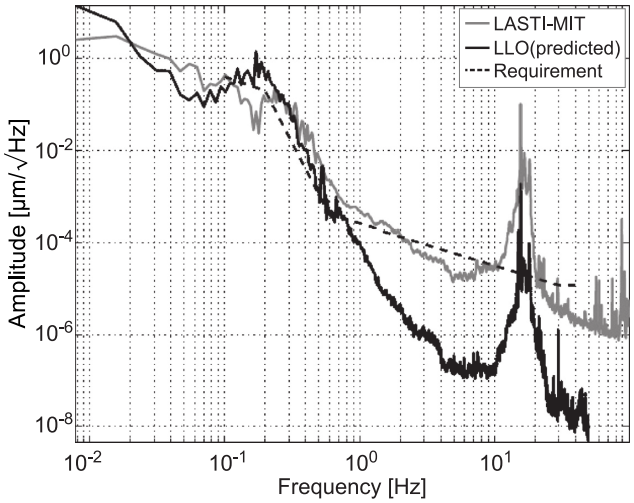


**Figure 7:** HAM-SAS: Measured and predicted performance compared to the requirements. The data plotted in gray shows the HAM-SAS performance measured in the LASTI lab. The data shown in black is the projection of the gray data to the ground motion at the LIGO Livingston observatory
This figure is taken from [41].

### 3.5.2 *The HAM-ISI*

The HAM-ISI vibration isolation approach is different to one of the HAM-SAS (or other SASs) in the sense that not the mechanical oscillator properties but active feedback provide the attenuation at low frequencies. However, at high frequencies also this system's vibration decoupling relies on passive isolation.

Similar to the other systems, the HAM-ISI attenuates ground motion in six degrees of freedom by one oscillator stage in horizontal and one in the vertical direction and it is designed compatible for the use in ultra-high vacuum. Vertical isolation is provided by three triangular maraging steel blade. The payload is suspended from them by three flexure rods which provide horizontal isolation. All six degrees of freedom's fundamental resonances are tuned to frequencies between 900 mHz and 1.8 Hz. Due to the relatively high fundamental resonances the HEPI pre-isolation stage is needed in order to achieve a DC dynamic range of the order of millimeters.

The payload of the HAM-ISI mainly consists of a 2 m wide hexagonal optical table. A drawing of the system is shown in figure 8. The whole structure is stiffened thoroughly so that the lowest internal resonances of the system are at frequencies above 100 Hz. However, mechanical resonances of the support structures above 10 Hz are reported by Matichard et al [90] and shown in figure 9.

The HAM-ISI is equipped with an arrangement of high precision motion sensors and actuators. As in the AEI-SAS they are used to reduce the payload motion around and below the fundamental resonance

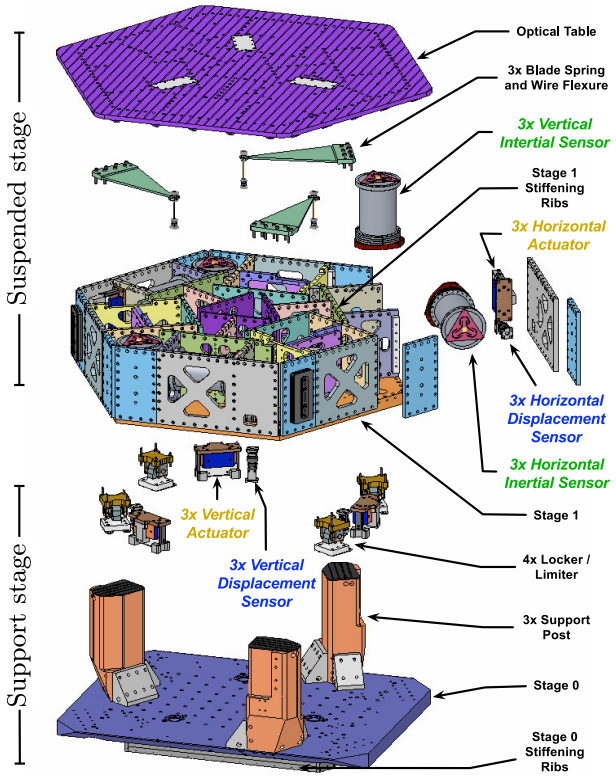


(a)

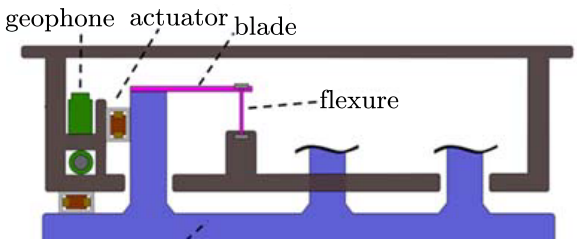


(b)

**Figure 8:** (a)Technical drawing of the HAM-ISI. A thoroughly stiffened hexagonal optical bench is suspended from three blade springs by three flexure rods. The signal from inertial and displacement sensors is used to actively control the suspended stage by means of three vertical and three horizontal actuators.
This figure is taken from [89].
Figure (b) is taken from [90] and shows a schematic drawing of the HAM-ISI.

frequencies. However, due to the higher resonance frequencies the HAM-ISI's control is designed for a much larger bandwidth, namely a unity gain frequency of approximately 25 Hz. The control noise is therefore ultimately limiting the vibration isolation performance in this frequency band, whereas the AEI-SAS's performance is determined by its passive performance above about 3 Hz in the vertical direction [90]. A typi-

cal performance of the system is shown in figure 9. In section 9.1 the AEI-SAS's and the HAM-ISI's performance is directly compared.

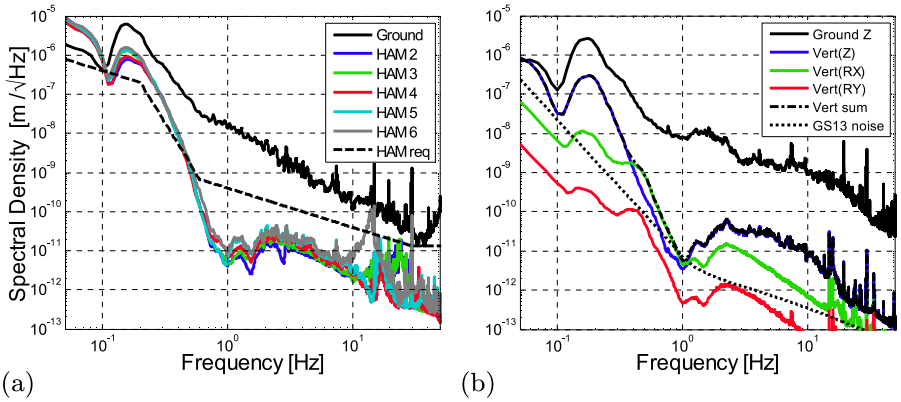


**Figure 9:** HAM-ISI performance. The ground motion at the site (black) is compared to the HAM-ISI payload motion. The dashed line represents the requirement for the system. These figures are taken from [90].

(a) x-direction motion of all 5 HAM-ISI units of one LIGO detector. The features above 10 Hz are related to the mechanical resonances of the support structures.
(b) Estimation of the vertical suspension point motion of the suspensions mounted on the HAM-ISI.

The concept of the HAM-ISI was first tested at Stanford University by Lantz et al. and the results of this technology demonstrator were presented in 2005 [91]. It bases on a system proposed in 1997 by Newell et al. [92].

After the HAM-ISI design was favored over the HAM-SAS one unit was installed in 2008 in both LIGO detectors. It was used for enhanced LIGO, the intermediate step between Initial LIGO and Advanced LIGO. The results obtained with these two prototypes were published by Kissel in 2010 [89]. In the following years the system was improved and 15 platforms were produced for Advanced LIGO [90].

## 3.6 ADVANCED VIRGO'S AUXILIARY ISOLATION SYSTEMS

Improvements in vibration isolation was not only required for the main optical components of the advanced GW detectors, but also for the auxiliary optics. For Advanced Virgo, this was realized by suspending five in vacuum optical benches, each from a so-called MultiSAS. An out of vacuum isolation system is supporting the External Injection Bench (EIB) and is referred to as EIB-SAS. Both systems were constructed at Nikhef and consist of similar components, arranged in different geometries for different purposes. The EIB-SAS design started in 2010, whereas the construction of the MultiSAS started in 2011 [93].

### 3.6.1 *The MultiSAS*

The design of the MultiSAS is reminiscent of the TAMA-SAS (without test mass). As the AEI-SAS, the MultiSAS is designed to operate in ultrahigh vacuum. A double stage vertical attenuation, realized by two GAS-filters, is supported by three IP-legs. Together with the two conventional pendulum stages (where the second GAS-filter and the bench are the pendulum masses) they provide a triple stage horizontal attenuator. The limited space in the MiniTower vacuum chambers only allowed for shorter IP-legs (440 mm long). However, they could easily be tuned down to about 100 mHz and have the advantage of higher internal resonances compared to the longer IP-leg designs used in the Superattenuator, the LIGO-SAS or the TAMA-SAS.

The largest upper GAS-filter is tuned to approximately 200 Hz, the smaller lower filter is tuned to approximately 300 mHz. The tilt modes of the suspended optical bench are tuned to around 200 mHz to decouple these modes from the horizontal pendulum modes of the chain. This system achieves vertical ground motion suppression of more than $1 \times 10^{-5}$ while horizontal isolation in excess of $1 \times 10^{-7}$ is predicted above 10 Hz [59]. The horizontal performance is planned to be measured by advanced horizontal accelerometers with optical readout developed at Nikhef. They will be able to measure in the vicinity of the fm/Hz regime from 10 Hz onwards [94].

A further unique feature of the MultiSAS is a multi-channel feedback approach using a Kalman state observer to improve the low frequency active control [93].

As well as the other isolation systems presented here the MultiSAS's isolation window is limited at high frequencies by internal resonances. Tilt and bounce modes of the upper stage on the IP-legs appear above 50 Hz [59] (compare to the AEI-SAS's vertical spring-box modes discussed in chapter 11.3).

### 3.6.2 *The EIB-SAS*

The EIB-SAS design is very similar to the one of the AEI-SAS. The most obvious difference is the rectangular shape of the optical bench. It was chosen due to the space requirements on the EIB. A further major difference is that the EIB-SAS operates in air and thus has lower requirements on the choice of employed materials or cleanliness.

The isolation system itself consists of an IP-leg stage supporting a vertical stage, which includes three GAS-filters. GAS-filters and IP-legs feature CoP compensators. The vertical fundamental resonance of the system is tuned to 390 mHz, the horizontal resonance frequency is adjusted to 220 mHz. This way the EIB requirements are met while having a more robust system in terms of vertical temperature drifts (compare to section 8.1.4) or recovery of working position after adjusting optics

on the bench [95]. As in the AEI-SAS, low frequency active isolation improves the EIB-SAS's performance around its fundamental resonance frequencies.

In the configuration described above the system provides more than $1 \times 10^{-2}$ of isolation above 10 Hz in 6 degrees of freedom [96].

### 3.6.3 *The KAGRA-SAS*

The most sophisticated design in the seismic attenuation system family at present is probably the KAGRA-SAS, more precisely KAGRA's type A suspension. However, it relies on the techniques proven in its predecessor. The system is designed to attenuate the already relatively low ground motion in the Kamioka mine (approximately $10^{-11}$ m/$\sqrt{\text{Hz}}$ at 10 Hz), which is the KAGRA site, by a factor of at least $1 \times 10^{-8}$ at 10 Hz. This performance is required to isolate the cryogenic test masses of the interferometer. A system consisting of 8 horizontal and 6 vertical stages was therefore designed. It has some similarities to Virgo's Superattenuator, inasmuch as an IP-leg stage is supporting a chain of 6 vertical low frequency filters, arranged as an approximately 13 m long cascaded pendulum (see figure 4). The major difference is that the vertical filters are GAS-filters with center of percussion tuning instead of blade springs with MAS. The resonance frequency of the highest and largest GAS-filter, called filter 0, is modeled to be as low as 60 mHz while the lower standard GAS-filters are tuned to 250 mHz [97]. A further difference is the shorter (472.5 mm) long IP-legs, similar to the multiSAS.

With this configuration an overall vibration isolation factor of $1 \times 10^{-14}$ in the horizontal direction and $1 \times 10^{-13}$ in the vertical direction at approximately 4 Hz is expected. That is approximately 8 magnitudes better than the requirements at 10 Hz mentioned above. This safety margin is prudent since internal resonances above 50 Hz degrade the isolation performance [60]. Furthermore, an isolation performance reduction due to mechanical links for cooling the test mass is expected. This mechanical shortcut is included in the model shown in figure 10 [98].

KAGRA-SAS's IP-legs are standing on the solid rock-floor of a tunnel drilled above the main tunnel in which the interferometer is located. This horizontal pre-isolation stage is tuned to 100 Hz.

A challenging task is to include the cryogenic test mass in the isolation system, which itself contains a 7th vertical isolation stage [60].

The requirements in terms of seismic isolation for the beam splitter, the signal recycling cavity and the power recycling cavity are more relaxed than for the test mass. The beam splitter and signal recycling cavity require a vibration attenuation of $1 \times 10^{-6}$ at 10 Hz, the power recycling cavity requires $1 \times 10^{-4}$ at 10 Hz. It is provided by so-called type B and a type Bp suspensions. These systems are basically type A suspensions reduced in highs and isolation stages. The type B suspen-

sion features an IP-leg stage and three GAS-filters. For the type Bp suspension two GAS-filters suffice. Instead of an IP-leg stage they are mounted on a motorized stage called the traverser.

The test masses are suspended from all these suspension types. The suspensions consist of intermediate mass, recoil masses and the optic. Thereby the design is similar to Superattenuator and TAMA-SAS' test masses and it allows actuation of the optics.

At the time this thesis is written the installation of the KAGRA-SAS is ongoing [38].

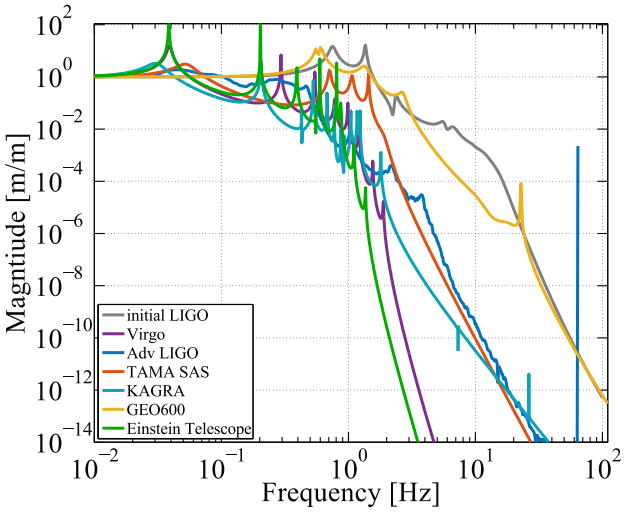


**Figure 10:** Comparison of the interferometer optic isolation of initial LIGO [63], Virgo and Advanced Virgo [99–101], TAMA (with SAS) [61], GEO 600 [102, 103], Advanced LIGO [87], KAGRA [104] and the Einstein Telescope [25]. In the KAGRA case, the mechanical links for cooling (included) are expected to limit the isolation performance above 1 Hz.
This composition of isolation system performances is taken from [105].

# 4

# THE AEI 10 M PROTOTYPE

Detecting GWs requires extremely low-noise detectors. The techniques to mitigate the various noise sources and to achieve the required sensitivity were developed in multiple test facilities before they were implemented in the GW detectors. These GW detector prototypes are for instance the Garching 30 m prototype [6], the Glasgow 10 m prototype [7], the LASTI at the Massachusetts Institute for Technology, the Caltech 40 m prototype at [5], the cryogenic laser interferometer observatory (CLIO) project [106], and the Albert-Einstein-Institute (AEI) 10 m prototype [64].

The first main objective of the AEI 10 m prototype is an experimental setup for measurements at the SQL of interferometry (discussed in section 4.1.1). It is a macroscopic quantum mechanical effect that will limit the sensitivity of GW detectors in the near future; therefore, after characterizing the SQL, the interferometer setup will be modified in order to test techniques to overcome this limit. Among other techniques, new frequency dependent squeezing [107] can be investigated in the AEI 10 m prototype.

An overview of the AEI 10 m prototype and its individual components is the subject of this chapter. Furthermore, a brief outline of the SQL-interferometer and the relevant noise sources is given.

This test facility was designed to provide a low-noise environment for testing GW detector technology and to probe the limits of high-precision interferometry. In particular, the system is designed such that classical noise sources (see section 4.1.2 ) have a lower amplitude than the quantum noise. That allows studding the SQL (see figure13). The AEI 10 m prototype is located in a dedicated hall at the Max Planck Institute for Gravitational Physics (Albert Einstein Institute) in Hanover, Germany. The experiments are set up in a large vacuum envelope, which is located in the basement of the lab (see figure 11). The ground floor provides space for auxiliary experimental setups and assembly areas, such as a clean room tent for building and testing the AEI-SAS (see chapter 5)

A crucial element of the AEI 10 m prototype design is isolation from environmental vibrations. The vacuum envelope ($100\,\mathrm{m}^3$, $10^{-7}$ hPa) shields the entire apparatus against acoustic coupling. The AEI-SAS isolates all essential components from vibrations caused by seismic and anthropogenic ground motion, above approximately 0.1 Hz. Two out of three AEI-SAS units are installed and operating at the time of writing. A third AEI-SAS unit was used to test mechanical design improvements. These are discussed in detail in this work. The third AEI-SAS unit will be implemented in the vacuum system in spring 2018.

The AEI-SAS supports the optical tables on which the experiments are set up. It provides an approximately $3\,m^2$ platform and therefore enough space and versatility to perform different experiments with extremely low noise requirements in the AEI 10 m prototype infrastructure.

Further experiments such as a thermal noise interferometer (discussed in detail in ref. [28]) are being built in parallel to the SQL interferometer in the AEI 10 m prototype. The low noise environment of the facility is furthermore suitable for less complex experimental setups. The characterization and improvement of motion sensors, for instance, was undertaken as a side project [108].

In addition to the low noise experiments, novel techniques are being developed and tested both for upgrades to Advanced GW detectors as well as for future observatories such as the Einstein Telescope [40]. A slightly modified version of the AEI-SAS, for instance, is implemented in the Advanced Virgo observatory as the EIB-SAS (see section 3.6.2). The concept of the Suspension Platform Interferometer (SPI) could also be applied for length stabilization in ground-based GW detectors. In this chapter, the individual components of the AEI 10 m prototype are outlined. Furthermore, it gives a brief overview of the SQL-interferometer and the relevant noise sources.

## 4.1 THE SQL INTERFEROMETER

As mentioned above, the first goal of the AEI 10 m prototype is setting up an interferometer to reach and surpass the SQL [109] with 100 g mirror masses. This is promising not only for exploring and, subsequently, overcoming limits of GW detectors but also in terms of observing the macroscopic object's dynamics dominated by quantum mechanical effects.

A simplified version of the SQL interferometer's optical layout is shown in figure 12. The SQL amplitude spectral density for this interferometer configuration is approximately $10^{-19}\,m\,Hz^{-1/2}$ at 200 Hz. The margin between the sum of the classical noise contributions and the SQL is expected to be at least a factor of 2.5 lower [110]. The optical design chosen for the SQL interferometer is discussed in detail in ref. [111].

One of the first challenges is the reduction of the coating thermal noise. The beam size on the arm cavities mirrors is therefore chosen to be relatively large. This, however, reduces the stability of the cavities. Before setting up the full interferometer a single arm test will provide experience with such a fragile system and will lead to suitable control schemes. Furthermore, the performance of the novel electrostatic drive (ESD) design for test mass actuation is investigated in this setup(see section 4.1.3 and the appendix chapter A).

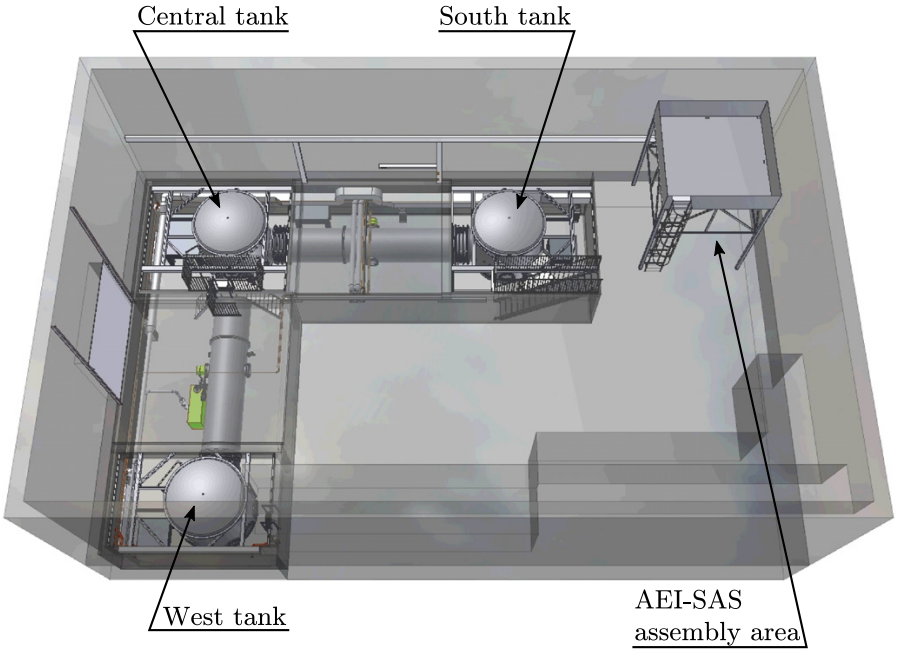


**Figure 11:** Rendered image of the AEI 10 m prototype hall. The L-shaped vacuum tank is located in the lab's basement. The ground floor provides space for preparing the individual components of the experiments. The structure in the upper right corner of the image is the assembly area for the AEI-SAS.

### 4.1.1 *The Standard Quantum Limit*

In the absence of classical noise sources, the sensitivity of an interferometer is limited by quantum noise. The quantum noise can be described as divided into two noise sources: shot noise and radiation pressure noise. Both effects originate from the coupling of the light's quantum fluctuations into the output signal of the interferometer. It therefore results from the uncertainty of the photon rate on the photodiode. In that sense shot noise is a readout noise.

The shot noise amplitude spectral density, written in the dimensionless differential arm length unit $h = \Delta L/L$ is [3]

$$h_{sh} = \frac{1}{L}\sqrt{\frac{\hbar c \lambda}{2\pi P_{in}}} \ . \tag{3}$$

Here $L$ is the interferometer's arm length, $\Delta L$ is the time evolving difference in the arm lengths, $c$ is the speed of light, $\lambda$ is the light's wave length and $P_{in}$ is the light input power of the interferometer. Shot noise only relates to the uncertainty of the photon ratio and it is frequency independent.

Radiation pressure noise can be understood as the back-action noise of the suspended mirrors, induced by the momentum transfer of the

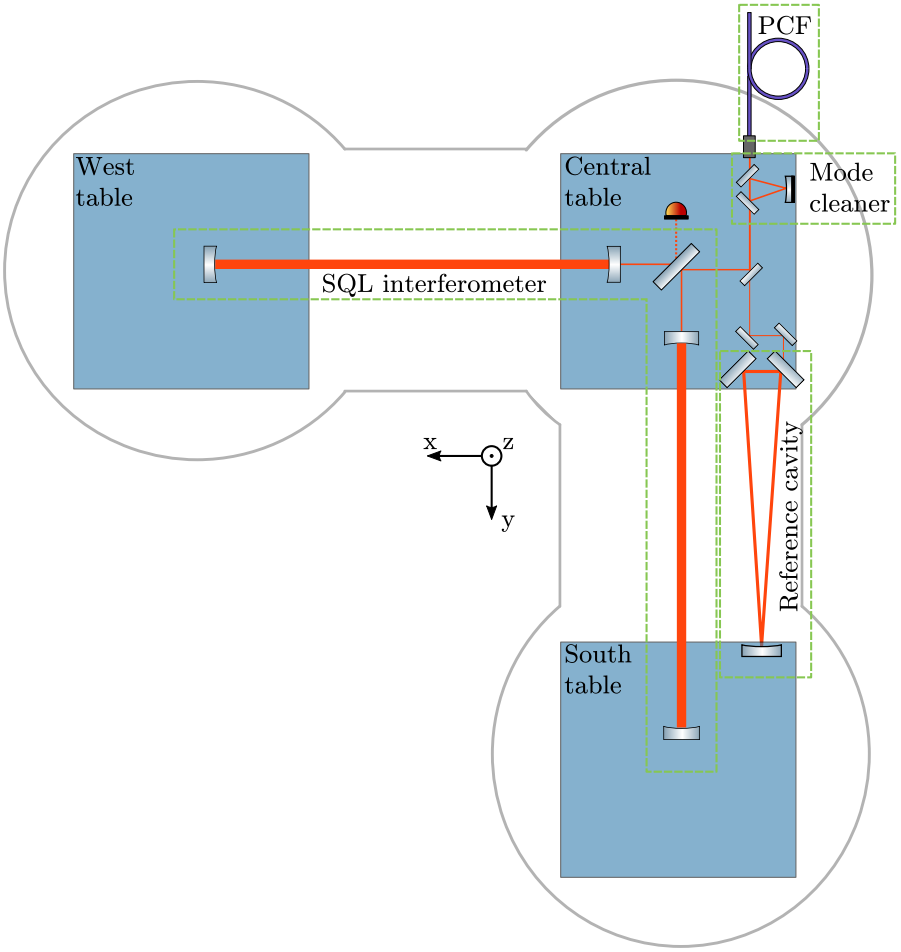


**Figure 12:** Simplified optical layout of the SQL interferometer experiment. The 1064 nm laser light is coupled through a photonic crystal fiber (PCF) in the vacuum system. Behind a mode cleaner, the laser beam is split. A fraction of the light is coupled into the frequency reference cavity. The major part of the light is coupled into the SQL interferometer. It is a Michelson interferometer with approximately 11.4 m long Fabry-Pérot arm cavities.

reflected stochastically distributed photons. Expressed as amplitude spectral density it is

$$h_{rp} = \frac{1}{m f^2 L}\sqrt{\frac{\hbar P_{in}}{2\pi^3 c\lambda}} \ , \tag{4}$$

approximated for free-falling interferometer mirrors with a mass $m$. The force on the mirrors due to the stochastically distributed photons is frequency independent, however, the inertia of the test mass mirrors introduces the $f^{-2}$ dependence of the displacement measurement.

The total quantum noise of the interferometer is the incoherent sum of shot noise and radiation pressure noise:

$$h_q = \sqrt{h_{sh}^2 + h_{rp}^2} \ . \tag{5}$$

Since radiation pressure noise is proportional to power, whereas shot noise is inversely proportional, the standard quantum limit of interferometry is determined by finding the quantum noise's minimum at each frequency by variation of $P_{in}$. It is accordingly:

$$h_{SQL} = \frac{1}{\pi L f}\sqrt{\frac{\hbar}{m}} \ . \tag{6}$$

According to equation 6, a GW detector with low quantum noise limitations is achieved with long arms and high mirror masses (Advanced Virgo and Advanced LIGO use 40 kg test masses on kilometer scale arms). The SQL interferometer, however, is designed to be dominated by quantum noise. Relatively light mirrors were therefore chosen as test masses. In order for quantum noise to dominate the interferometer across a wide band, the challenging task is to reduce all classical noise sources below quantum noise. A brief outline of the relevant noise sources is given in the following section. The techniques employed in the AEI 10 m prototype to reduce these noise sources are summarized in the sections below.

### 4.1.2 *Classical noise sources*

The signal in an interferometric measurement is the optical intensity variation caused by the variable to be measured. This variable is usually the relative interferometer arm length change, primarily induced by, in the case of the SQL interferometer, quantum fluctuations. The optical signal is usually converted into a readout electrical signal. Noise sources usually cannot be canceled completely. However, suppressing them to a level well below the signal is one major challenge in the field of high precision physics.

Noise sources can be classified into two categories:

- Noise sources that change the mirror surface position such as suspension thermal noise, coating thermal noise, thermal drift, noise of the control system, acoustic noise, seismic noise and the radiation pressure noise (if not treated as the signal).
- Noise sources that influence the length measurement, such as laser frequency and laser power noise, optical path length fluctuations due to residual gas in the vacuum system, and shot noise (if not treated as the signal, as in the case of the SQL-interferometer).

Perturbations such as acoustic noise or noise due to air currents are suppressed by operating the AEI 10 m prototype experiments in vacuum. Techniques to mitigate the other relevant noise sources are discussed in the following section.

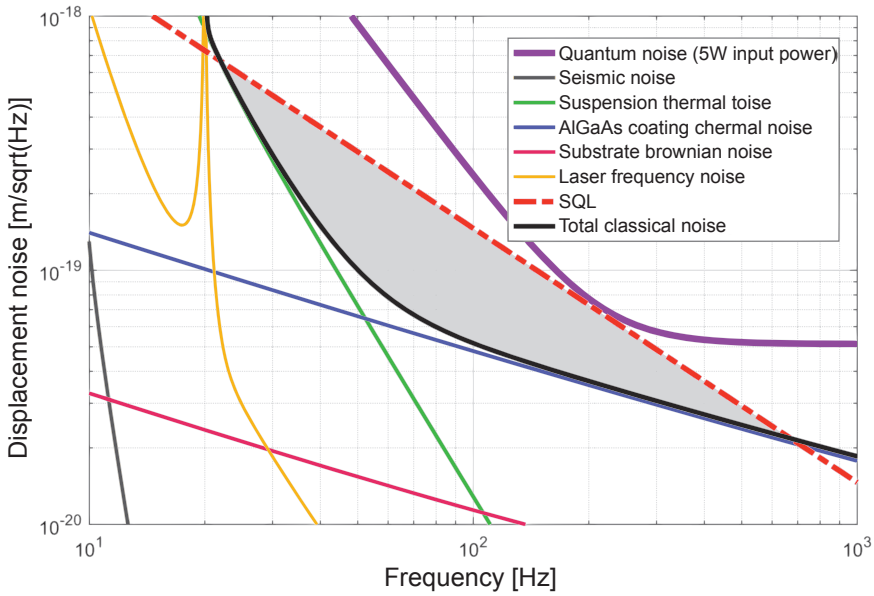


**Figure 13:** Noise budged of the SQL interferometer. The experiment will be purely quantum noise limited over a wide frequency band, since all classical noise sources are suppressed well below the quantum noise. The shaded area in the plot represents the clearance between classical noise and the SQL (black) [112].

The noise budget of the SQL-interferometer is shown in figure 13. Due to the SQL experiment's intended measurement band and sensitivity requirements, seismic noise is a particular challenge, therefore a brief overview of its origin and shape is given here.

#### 4.1.2.1 *Seismic noise*

At low frequencies ground-based GW detectors as well as the AEI 10 m prototype experiments are limited by vibrations of the ground. Whereas GW detectors are designed for long duty cycles, the AEI 10 m prototype experiments can be performed in normal or low noise periods; therefore, only the ambient seismic noise is of interest for this system. Temporary, loud events such as earthquakes, high traffic or construction work are not regarded. Also very low frequency motion as it is induced, for instance, by tidal forces between moon and earth, are due to its rather short baseline less dominant in the AEI 10 m prototype compared to GW detectors. Figure 14 shows a typical amplitude spectral density of the ambient seismic motion at the AEI 10 m prototype. Below 0.1 Hz the horizontal motion measurement is limited by ground tilt that couples in the STS-2 seismometer (see section 5.2). This tilt coupling is briefly discussed in section 9.1.2. The vertical motion measurement is not affected by this effect. Between 0.1 Hz and 0.3 Hz the seismic spectrum in figure 14 forms local maxima in all three degrees of freedom. The orientation of the coordinate system is displayed in figure 12. The

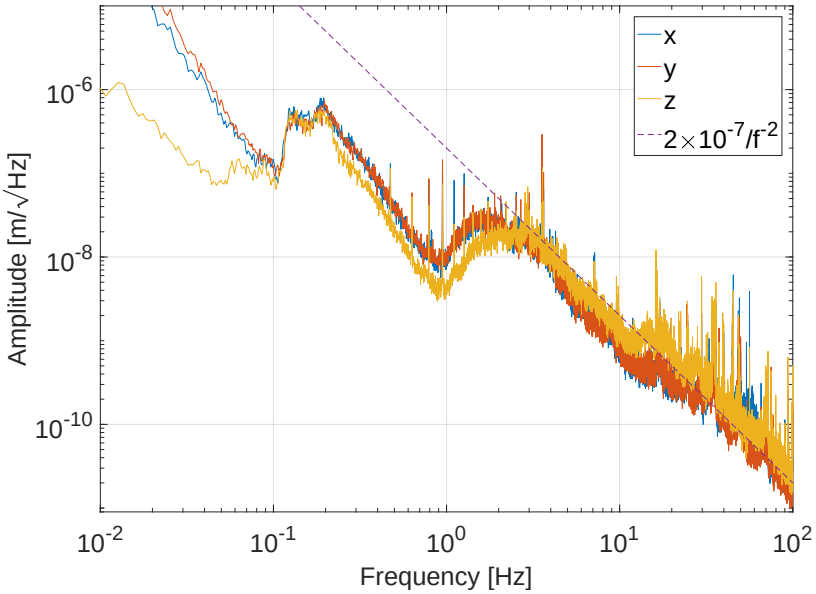


**Figure 14:** Measurement of the seismic motion at the AEI 10 m prototype. The data is recorded with the STS-2 seismometer, which is located in the basement on the ground, next to the central tank of the AEI 10 m prototype vacuum system.

motion at this so-called microseismic peak [113] is caused by environmental disturbances. Sea waves excite the ground by pressing against the sea floor and the shore. Furthermore, wind contributes to ground motion in this frequency band. It couples to the ground by exciting trees and buildings oscillations. The microseismic peak amplitude is therefore strongly depended on the weather conditions.

The structure above 1.5 Hz in the seismic spectrum is referred to as the anthropogenic noise peak. This motion is caused by people walking by, traffic and industry. Anthropogenic activities also cause the dominant tilt motion which couples into the horizontal signal below 0.1 Hz. This man-made noise is significantly lower on weekends, at night or on holidays than during working hours. At the AEI 10 m prototype the anthropogenic noise is dominant up to approximately 30 Hz, therefore sensitive measurements are usually recorded overnight. GW detectors are usually located far away from areas with high population density or industry in order to minimize this disturbance.

Above a few hertz, the seismic motion rolls off with a slope of approximately $f^{-2}$, as shown in the plot.

A detailed discussion of the seismic noise at the AEI 10 m prototype can be found in [28].

### 4.1.3 *SQL interferometer suspensions*

The dominating classical noise source at low frequencies are ground vibrations, as discussed above. The SQL interferometer optics are isolated by up to four stages from this ambient motion. The first stage is the AEI-SAS, which is the major subject of this work. It provides pre-isolation for all in-vacuum optics at low frequencies. However, in the measurement frequency band, the arm cavity optics require a much higher vibration attenuation. Each mirror is therefore suspended as a three-stage pendulum. Figure 15 shows a photograph of the input test mass's (ITM) suspension. The suspension system was developed at the University of Glasgow. The assembly, modifications and the implementation in the AEI 10 m prototype is done in Hanover.

The upper cross-shaped mass is suspended from steel wires, which are attached to maraging steel blade springs. These blades are connected to an aluminum frame which is mounted on top of the optical table. A further set of blade springs inside the upper mass supports the penultimate mass. The mirror is the lowest mass. Figure 15 shows the version of the suspension setup used for the single arm test. In this case, the penultimate mass is a donut-shaped aluminum structure and the test mass is supported by steel wire slings. The wires are not visible in the photograph since they are covered by safety structures called fiber guards. For the SQL interferometer, this lower stage will be replaced by a monolithic penultimate mass-mirror construction. They will be interconnected by four fused silica fibers of 20 µm diameter, in order to reduce the suspension thermal noise [64]. Due to their vertical elasticity, the fibers provide a third vertical isolation stage with a resonant frequency below 20 Hz.

In order to reduce the coating thermal noise, the SQL interferometer mirror surfaces will be made of an aluminum gallium arsenide (AlGaAs) coating. Its crystalline structure has a significantly lower mechanical loss than conventional coatings such as the amorphous silica/tantala [114].

The cavities are controlled by voice coil actuators, actuating on the upper mass and the penultimate mass. An ESD provides fast and low noise actuation directly on the test mass in the beam direction. The consideration of this structure by finite element analysis can be found in the appendix A. A hierarchical control scheme is considered for the SQL interferometer control. The coarse DC positioning will be provided by the AEI-SAS. At low frequencies, the control signal will be fed back to the upper and penultimate mass, whereas the ESD is used for high frequency control.

**Figure 15:** Photograph of the ITM suspension. The mirror is suspended as a three stage pendulum with ultimately three vertical stages. The figure shows the suspension setup for the single arm test. In the final SQL interferometer version the lower stage (intermediate mass to test mass) will be replaced by a monolithic stage.

## 4.2 STABILIZING THE LASER

For experiments at the SQL, a high intensity and extremely stable laser is required. The AEI 10 m prototype is equipped with a laser system that supplies approximately 35 W light power at a wavelength of 1064 nm. A highly stable seed beam from a monolithic non-planar ring oscillator (NPRO) with an output power of 2 W is therefore enhanced by four amplifier stages [115]. About 10 W of laser light is coupled inside the vacuum system via a photonic crystal fiber. In this way, the light is decoupled from vibrations of the laser bench positioned out of the vacuum system. Furthermore, the fiber operates as a passive mode cleaner. The laser beam's mode shape behind the fiber provides approximately 99 % overlap with the fundamental Gaussian mode [116]. The second stage of laser light preparation is the active mode cleaner. It is rigidly mounted on the central table and thereby benefits from the vibration isolation provided by the AEI-SAS. The mode cleaner is discussed in detail in [28] and [117].

The laser power is controlled with a shot noise limited multi photodetector sensing scheme providing an extremely low intensity noise [118].

**Figure 16:** Photograph of frequency reference cavity suspension system for the two central table mirrors.

The laser frequency is stabilized by the frequency reference cavity. It is a triangular optical resonator with a round trip length of 21.2 m. The three mirrors are distributed on the central and the south table, as depicted in figure 12. These 850 g test masses are each suspended as a three-stage pendulum with two vertical stages. Figure 16 shows a photograph of the two suspended mirrors located on the central table. Suspending the mirrors provides an extremely low noise length reference above the suspension system's fundamental resonances. The frequency reference cavity thereby provides laser frequency stability from approximately 20 Hz to 1 kHz. The aspired sensitivity is are $10^{-4}\,\mathrm{Hz}\,\mathrm{Hz}^{-1/2}$ at 20 Hz and $10^{-6}\,\mathrm{Hz}\,\mathrm{Hz}^{-1/2}$ at 1 kHz. A more detailed discussion of the frequency reference cavity can be found in ref. [28].

## 4.3 OPTICAL MOTION SENSORS

The optics of the single arm test (see section 4.1) and the frequency reference cavity (see section 4.2) are both distributed over the central and south table and the SQL-interferometer will populate all three tables. At high frequencies, the vibration isolation systems (AEI-SAS and suspensions) suppress the mirrors' motion sufficiently. However, at low frequencies, the mirror motion is dominated by the motion of the individual optical tables. The table motion, in contrast, is dominated by ground motion and, if locally controlled, at some frequencies by

sensor noise (compare to chapter 16). Even though the ground motion is usually coherent over 10 m below a few hertz [59], the three table top setups do not necessarily move in common. In particular, ground tilt is locally different and it is translated to horizontal table top motion, illustrated in figure 106 in chapter 16.

Low frequency differential table oscillations are a huge impediment for operating the optical systems. In order to mitigate this relative motion the AEI-SAS is equipped with a Suspension SPI. This system reads out the inter-table motion. This error signal is fed back to the actuators of the south and west table such that they follow the central table at low frequencies. This way the three tables form a rigid platform in the beam direction.

A simplified illustration of the SPI is shown in figure 17. Two heterodyne Mach-Zehnder interferometers sense the relative table motion. A phase meter reads out the photodiode signals and provides dynamic range larger than the maximum table top displacement in the longitudinal direction[1]. Outside the vacuum system the SPI 1064 nm laser beam is split into two paths. Both beams are modulated by acousto-optic modulators near 80 MHz, with a heterodyne frequency difference of ±15 kHz. The laser light is coupled through optical fibers into the vacuum system via fiber couplers. Fiber couplers, as well as all central table optics, are bonded to a baseplate made from a type of glass with an ultra-low thermal expansion coefficient, in order to improve the low frequency performance of the system [119].

The SPI link to the south table is, as of the time of writing, installed and operating; the west table SPI will be installed when the west SAS is implemented in the AEI 10 m prototype.

Originally it was planned to use the SPI not only for sensing the relative table displacement in the longitudinal directions but also the rotational degrees of freedom, except the roll motions around the longitudinal axes. However, the rather poor sensitivity in the rotational degrees of freedom led to a different sensing approach, namely the optical levers (OLs).

The basic principle of the OLs is rather simple. A collimated laser beam shines from the center of one table top on a quadrant photodiode on the next tabletop. Tilt motion of the laser source is translated to displacement of the beam on the photodiode. The approximately 10 m lever arm enhances the beam motion, such that the motion of the second table is negligible in first order. Thus, the OLs provide low noise, high bandwidth inertial tilt signals of the SAS. The performance of the SPI and the OL are expected to be published in 2018.

Currently, one OL is installed on the south and one on the central table respectively. They sense the central and south table's rotational motion about the x-axis (rx) and about the vertical axis (rz). Two

1 'Longitudinal' in each arm indicates the direction along the arm from the central tank to the south table (y-direction) and to the west (x-direction).

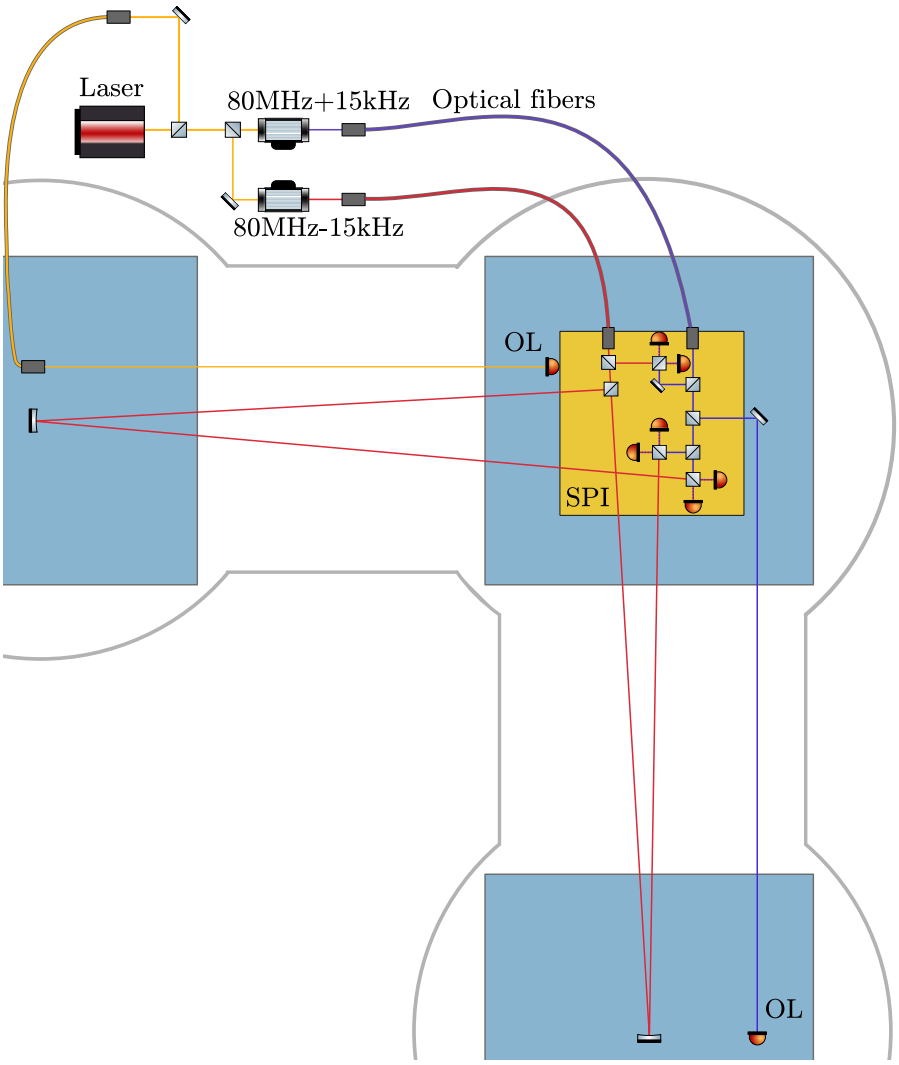


**Figure 17:** Simplified optical layout of the SPI and the OLs. Light from a 1064 nm NPRO laser is modulated by two AOMs. It is coupled through optical fibers in the vacuum tank. The SPI measures the differential table motion with two heterodyne Mach-Zehnder interferometers. A third interferometer represents the power and frequency control of the SPI laser. OLs are installed in parallel to the SPI in order to measure the table's tilt motion. In this figure, two out of four OLs are illustrated. In reality, a collimated laser beam shines from the west to the central table (illustrated), one from the central to the west table (not illustrated), one from the central to the south table (illustrated) and one from the south to the central table (not illustrated). Laser light from the in-vacuum SPI setup is used for the central table OLs. The south and east table OL light is coupled through two extra fibers in the vacuum tank. The optical layout is vastly simplified in this illustration for the sake of clarity.

further OLs will be installed on the west and the central table in order to provide a control signal for the rotational motion about the y-axis (ry) of west and central SAS and the rz motion of the west AEI-SAS

unit. The control signals for the other degrees of freedom are provided by local motion sensors. These sensors are introduced in section 5.2, the AEI-SAS control scheme is summarized in section 16.

# Part II

# THE AEI-SAS AND ITS WORKING PRINCIPLE

# 5

# THE AEI-SAS

The AEI-SAS isolates all essential components of the AEI 10 m prototype from vibrations caused by seismic and anthropogenic ground motion and from structural acoustics. Two AEI-SAS units are installed and operating and a third AEI-SAS unit has been used to test mechanical design upgrades. It will be installed in the vacuum system in spring 2018. A CAD drawing of the AEI-SAS in the vacuum system and a photograph of one AEI-SAS unit is shown in figure 18.

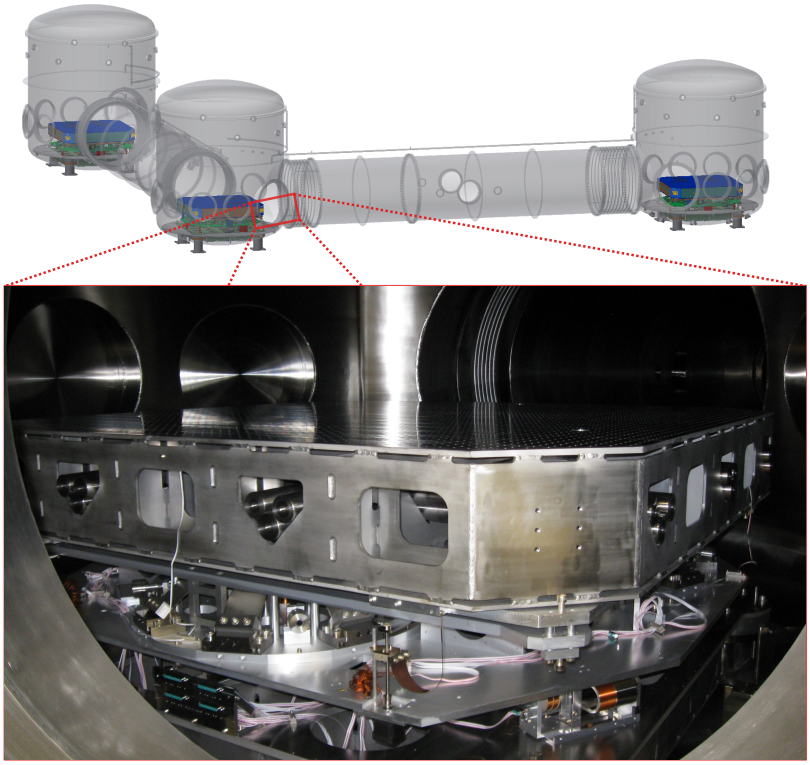

**Figure 18:** The AEI-SAS in the AEI 10 m prototype vacuum system. The upper part of the figure illustrates the three AEI-SAS units in the south, central, and west tank (from left to right). The photograph shows the AEI-SAS unit in the central tank shortly after its installation. At the time of writing the optical table is populated with experimental components, as shown in figure 15 and 16.

The 1.75 m×1.75 m optical table isolated by an AEI-SAS unit offers a spacious platform to perform various high precision experiments. In particular, the design of the mirror suspensions for the SQL-interferometer and the frequency reference cavity rely on pre-isolation at their fundamental resonances (between 0.6 Hz and 28 Hz). An overview of these

subsystems is given in section 4.1.3 and 4.2. This isolation of the suspension point reduces the total actuation forces required to control the suspended mirrors, enabling the use of low-noise actuators that meet the SQL-interferometer's noise requirements.

The AEI-SAS design bases on the HAM-SAS (see section 3.5.1). It is adapted and improved for the AEI 10 m prototype application.

An adapted version of the AEI-SAS, the EIB-SAS, is used to isolate injection optics at Advanced Virgo. The EIB-SAS has higher fundamental resonant frequencies compared with the AEI-SAS. This is tolerable due to the relatively relaxed noise requirement. This increases stability at the expense of isolation performance. An overview of the EIB-SAS design is given in section 3.6.2.

This chapter discusses the design and the individual components of the AEI-SAS. Parts of this chapter were published in ref. [57].

## 5.1 MECHANICAL DESIGN OF THE AEI-SAS

The AEI-SAS is composed of two stages: a horizontal isolation stage based on three IP-legs, and a vertical isolation stage with three GAS-filters [23].

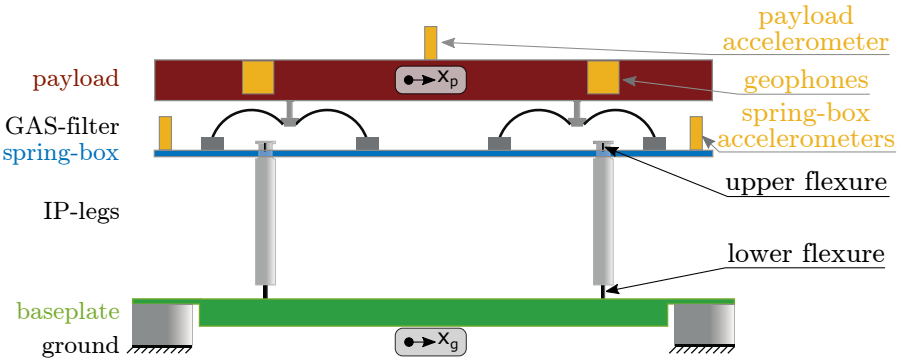


**Figure 19:** Simplified sketch of the original AEI-SAS design: The payload is supported by three GAS-filters providing vertical isolation. The diagram shows an unfolded version, but in reality, the GAS filters are nested inside an aluminum structure, the spring-box, within the horizontal stage (see figure 20). The spring-box is supported by three IP-legs providing horizontal isolation. The bottom of the IP-legs is connected via flexures to the baseplate. This baseplate is rigidly connected to the 'feet' of the vacuum tank. Three vertical geophones are installed inside the payload. Horizontal motion is sensed by three custom-made accelerometers [120] that are placed on the spring-box. An auxiliary horizontal accelerometer is installed on top of the payload.

Each AEI-SAS unit supports a payload of approximately 900 kg. This includes a 530 kg, 1.75 m×1.75 m stainless steel breadboard with an internal honeycomb structure. The breadboard is mounted on the three GAS filters. Each GAS filter consists of a crown-shaped assembly of eight maraging steel blades [121]. These blades are bent and fastened

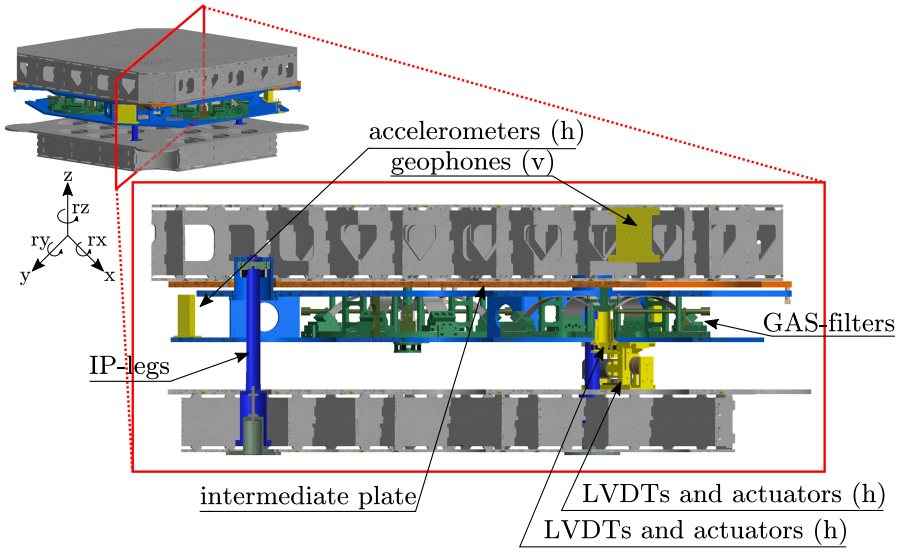


**Figure 20:** CAD model of the AEI-SAS: A section view shows the structure of the individual isolation stages and the location of the single components. For simplicity components as the motorized springs and the tilt stabilization are not shown in this model. This figure shows the original version of the AEI-SAS with the old IP-legs and a rigid intermediate plate to payload connection.

to a central key-stone that supports the table top. Compression of opposing blades against each other introduces negative stiffness along the vertical axis, lowering the effective spring constant [52, 80].

The spring-box is suspended by means of 3 mm thick and 25 mm long cylindrical maraging-steel flexures connected to the top of the IP-legs on their other side. The leg itself is an aluminum tube with 1 mm wall thickness. The horizontal restoring force is provided by a 10.6 mm thick and 60 mm long maraging-steel flexure connecting the IP-leg to the baseplate at the bottom (see figure 19 and 20). The AEI-SAS's baseplate is bolted to the inside of the rigid 'feet' of the vacuum tank. On the outside, these feet are bolted to the 80 cm thick concrete foundation of the lab.

Above the individual resonance frequencies, the AEI-SAS decouples the payload from ground motion in 6 degrees of freedom. Table 1 shows the resonance frequencies of the AEI-SAS and the corresponding masses [24] and moments of inertia. The displayed values vary during commissioning of the system. The resonance frequencies of the horizontal degrees of freedom are tuned by mass adjustment. All three moments of inertia depend on the mass distribution of the payload, which will vary, due to changing experiments in the AEI 10 m prototype. Fairly high tilt stiffness is ensured in rx and ry for stability reasons.

The individual components and their mechanical properties are described in the following. Its masses are listed in table 4. The working principles of the IP-legs and the GAS-filters are described in more detail in chapter 7 and 8.

| Direction | Resonance frequency [Hz] | Mass [kg] |
|---|---|---|
| x | 0.16 | 1231 |
| y | 0.16 | 1231 |
| z | 0.27 | 900 |
| | | Moment of inertia [kg m$^2$] |
| rx | 0.4 | 260 |
| ry | 0.4 | 260 |
| rz | 0.1 | 598 |

**Table 3:** Resonance frequencies, and corresponding masses [24] and moments of inertia of the AEI-SAS. Figure 20 shows the corresponding coordinate system. The moments of inertia are determined with respect to the principal axes of either the payload (for rx and ry) or the payload and the spring-box (rz). Note that the rx and ry axes do not coincide with the principle axes of the AEI-SAS.

A more detailed description of the AEI-SAS and its instruments can be found in ref. [23].

This thesis discusses design changes which were made to improve the AEI-SAS's performance. In the following, it is distinguished between the original design and the new design, which mainly includes the new, symmetric IP-legs (see chaper 11.3), the improved spring-box stiffening (see chaper 14), its mode damping (see chapter 15), and the fluorel stage (see chapter 12).

### 5.1.1 *The baseplate*

The AEI-SAS's baseplate is the link between the vacuum system and the IP-legs. It consists of a relatively stiff stainless steel structure. In its four corners a 17 mm thick upper plate is bolted to the inside of the vacuum tank's feet. The baseplate is leveled by shims which are placed in between the baseplate corners and the vacuum tank's feet. The height of those shims is individually determined for each AEI-SAS in order to compensate for the local unevenness of the ground and the vacuum tank's feet.

In order to lower the total height of the AEI-SAS, the second plate is mounted 196 mm below the upper plate. The IP-leg stands are bolted to this lower plate. Upper and lower plate are interconnected by a stiffening structure. The whole baseplate assembly is welded to increase

| **Components** | **Component mass [kg]** | **sum [kg]** |
|---|---|---|
| Baseplate | 490 | |
| Horizontal motorized springs | 15 | |
| Horizontal LVDT/actuator pairs | 15 | |
| IP-legs | 24 | |
| **Total base platform** | | 544 |
| GAS-filters | $3 \times 50$ | |
| Lower spring-box plate | 99 | |
| Upper spring-box plate | 64 | |
| Vertical motorized springs | 10 | |
| Original stiffening plates | 5 | |
| Accelerometers | 3 | |
| **Total spring-box** | | 331 |
| Optical table | 530 | |
| Ballast rods | 220 | |
| Intermediate plate | 115 | |
| Vertical geophones (in cans) | 30 | |
| Tilt stabilization column | 5 | |
| **Total optical bench** | | 900 |
| **Total AEI-SAS** | | 1775 |

**Table 4:** Mass estimation of the AEI-SAS. The values are taken from the CAD-model. Bolts, nuts and washers are not included in this model [24].

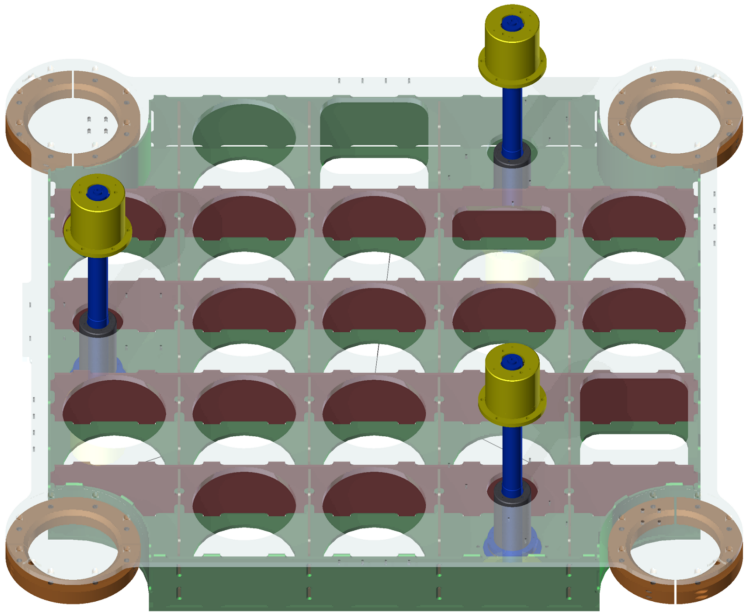

**Figure 21:** CAD model of the AEI-SAS's baseplate with IP-legs. The upper plate is displayed transparently to illustrate the stiffening assembly and the folded structure of the baseplate. The copper rings in the four corners are shims which are the link between baseplate and vacuum tank.

its stiffness. Figure 21 shows a CAD drawing of the baseplate with the IP-legs. The holes in the top and the bottom plate reduce the weight of the structure. The three IP-leg stands are covered by the IP-leg's center of percussion tuning structure.

Figure 22 shows a finite element simulation of the baseplate's static deformation due to the weight of the isolation system. The stiffening structure prevents a significant deformation of the whole structure. However, the area where the IP-leg's bases are bolted to the lower plate deform. That causes a vertical lowering and tilt of this area. The top

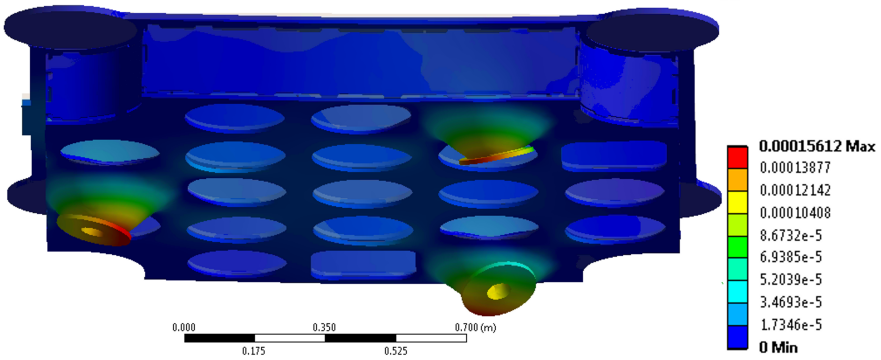


**Figure 22:** Finite element model of the AEI-SAS's baseplate. The CAD model used for this simulation was simplified and features the stainless steel baseplate structure which is rigidly connected to the IP-leg stands. A force of 12312 N, corresponding to the isolation system's mass, acts vertically on the top of the three stands. The baseplate is fixed in its four corners. The exaggerated deformation illustrates the static deformation of the structure. Even though the whole structure hardly bends, the connection areas between the baseplate and the stand arch. The color scale in the figure represents the total deformation in meters.

of the IP-legs, if not interconnected with each other by the spring-box, would accordingly be displaced by

$$\vec{P}_{IP1} = \begin{pmatrix} 1.95 \times 10^{-4}\,\mathrm{m} \\ -5.38 \times 10^{-7}\,\mathrm{m} \\ -1.47 \times 10^{-4}\,\mathrm{m} \end{pmatrix}, \quad \vec{P}_{IP2} = \begin{pmatrix} -1.56 \times 10^{-4}\,\mathrm{m} \\ -3.03 \times 10^{-4}\,\mathrm{m} \\ -1.17 \times 10^{-4}\,\mathrm{m} \end{pmatrix}$$

and (7)

$$\vec{P}_{IP3} = \begin{pmatrix} -1.69 \times 10^{-4}\,\mathrm{m} \\ 3.12 \times 10^{-7}\,\mathrm{m} \\ -1.19 \times 10^{-4}\,\mathrm{m} \end{pmatrix},$$

Where $\vec{P}_{IP_1}$, $\vec{P}_{IP_2}$ and $\vec{P}_{IP_3}$ are the positions of the top of the IP-legs. IP1 is the IP-leg on the left, IP2 and IP3 follow counterclockwise[1]. The resulting lateral payload displacement in the x and y direction is

$$\vec{P}_p = \begin{pmatrix} -1.30 \times 10^{-4}\,\mathrm{m} \\ -8.68 \times 10^{-6}\,\mathrm{m} \end{pmatrix} . \tag{8}$$

The payload tilts by approximately 30 µrad in the rx-direction and by about 2 µrad in the ry-direction. These static deformations can easily be compensated by the motorized springs and voice coil actuators (see section 5.2). So far no AEI-SAS performance aggravation due to this static deformation has been observed. However, for further analysis of the system these simulations might be of interest.

### 5.1.2 *The spring-box*

The spring-box is the horizontal stage of the AEI-SAS. It is horizontally isolated by the IP-legs and it houses the three GAS-filters. The spring-box consists of an upper and a lower aluminum plate. These plates are vertically separated by 134 mm. Stiffening plates interconnect the upper and lower plate (see figure 23). Holes in the stiffening structure reduce the weight and enable visible and manual inspection of the inner spring-box components.

The IP-legs are connected to the upper plate via a bell-shaped structure. The lower plate supports the GAS-filters on which the payload rests. This sandwich-like structure of the assembly reduces the total height of the AEI-SAS. This way the center of mass of the payload is lowered.

The horizontal motion sensors are located in the spring-box. The three accelerometers (see section 5.2.2) are mounted on the outer rim of the lower spring-box plate. They are placed on the extended lines from the vertical center axis of the AEI-SAS to the IP-legs. The horizontal LVDTs and collocated Actuators (see section 5.2.3) are mounted on the same lines, slightly closer to the center axis of the AEI-SAS. The inner coil of each horizontal LVDT and actuator magnet are rigidly connected to the lower spring-box plate, the LVDTs' sensing coil and the actuator coil are bolted to the baseplate of the AEI-SAS.

The horizontal motorized blades (see section 5.2.5) are situated between IP-legs and the vertical central AEI-SAS axis. Such as the LVDTs they are mounted in between lower spring-box plate and baseplate.

The two spring-box plates are relatively soft. In combination with the mass of three GAS-filters, this leads to parasitic low frequency spring-box bending modes. The frequencies of these oscillations are

1 These are the coordinates of the south table. The central table is rotated by −90°, thus, the vector components change accordingly.

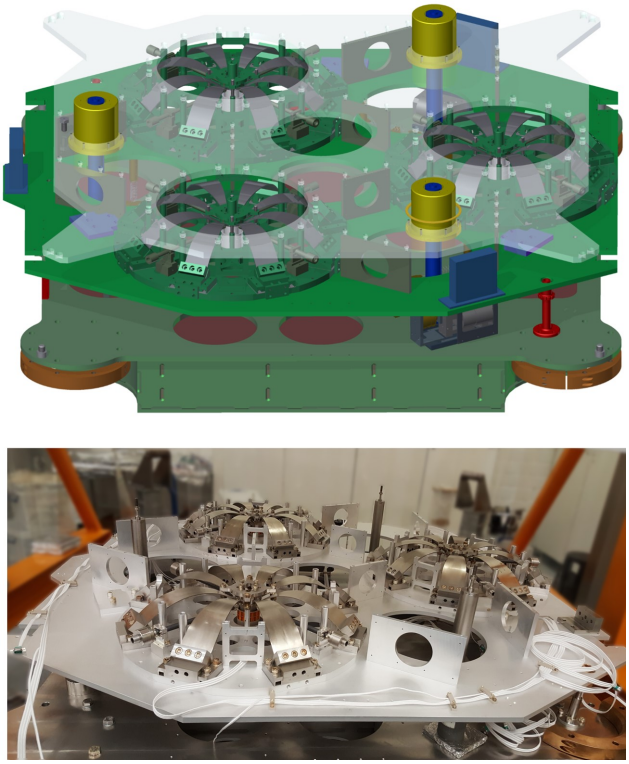

**Figure 23:** CAD model and photograph of the spring-box (without upper plate). The displayed CAD model represents the original design. The upper spring-box plate is displayed transparently. The photograph shows the third AEI-SAS unit during the assembly. In the displayed state it features the original stiffening structure and the new symmetric IP-legs. The cables for the actuators and sensors are in place.

further reduced by the vertically relatively soft IP-legs such that the lowest resonance frequency of these modes is at approximately 30 Hz. The original stiffening plates hardly provide sufficient support. These modes, as well as possible improvements, are discussed in chapter 11.3.

### 5.1.3 *The tabletop*

The payload of the AEI-SAS consists of a squared optical bench made from stainless steel and an aluminum plate referred to as intermediate plate (see figure 24). This plate supports the tilt stabilization.

A raster of M8 threads in the surface of the upper plate of the optical bench enables populating it with varying experiments. The upper plate and a lower plate are connected by a honeycomb shaped stiffening structure. A finite element simulation of a simplified optical bench shows, that the structure provides a rigid platform up to the lowest internal resonance frequency of 175 Hz (see figure 25). At such high frequencies the interferometer mirrors are sufficiently decoupled from the AEI-SAS by the mirror suspensions (see section 4.1.3). The system

**Figure 24:** Photograph of the AEI-SAS including the payload. The figure shows the third AEI-SAS unit during characterization of the improvements. It is suspended in the shaker stand. The table top is placed on three fluorel pads (not visible). They are placed on the intermediate plate. The corners of this structure are visible in the photograph. They feature the upper part of a vertical clamping structure (M8 bolts in the corners, below the optical table).

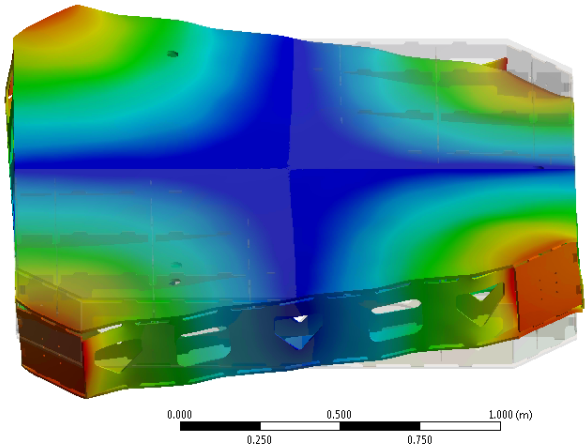


**Figure 25:** Finite element model of the simplified AEI-SAS's optical bench. The figure shows the mode with the lowest resonance frequency of the free optical bench. In reality, the structure is supported by three fluorel pads. Compared to the stainless steel structure these rubber pads are negligibly soft, thus, the system is simulated without constraints in order to obtain its elastic modes. The honeycomb-shaped plate structure inside the optical bench stiffens it efficiently. Accordingly, the displayed mode has a resonance frequency as high as 175 Hz. That is in a frequency band which is high enough for the optics to be sufficiently isolated by the mirror suspensions.

is modeled without rigid constraints, since, in reality, the optical bench is placed on soft fluorel pads (see section 12). At high frequencies the stiffness of the pads is negligible.

Those fluorel pads are placed on top of the intermediate plate, which itself is rigidly connected to the GAS-filter's keystones. In the original design, the optical table and the intermediate plate were rigidly con-

nected. In order to decouple the spring-box from the payload, this rigid connection was replaced by fluorel pads. Furthermore, the relatively soft intermediate plate is damped and decoupled from the payload by this rubber stage. This is discussed in more detail in chapter 11.

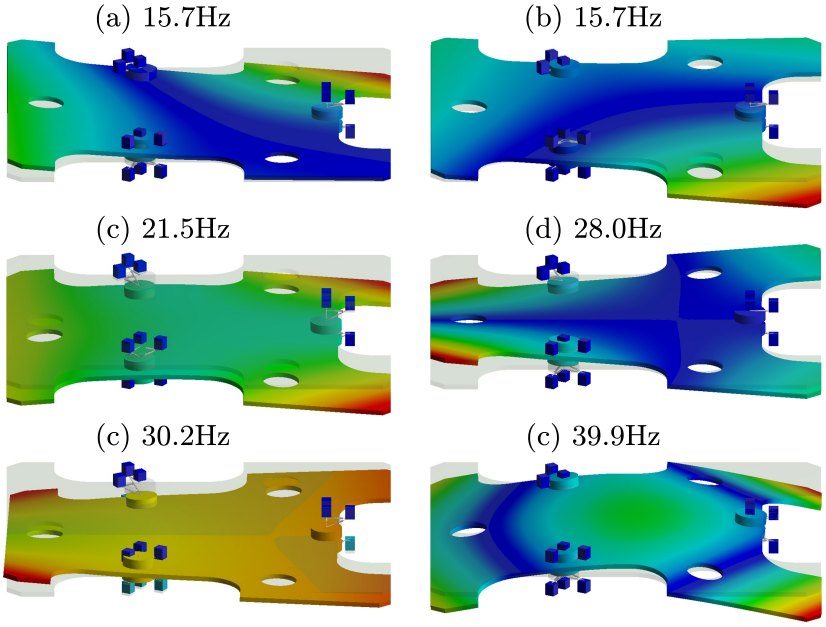


**Figure 26:** Finite element modal analysis of the intermediate plate. The figure shows the mode shape of the intermediate plate's 6 internal resonances with a resonance frequency below 50 Hz. The structure is supported by 6 sets of springs (compare to figure 118). The three sets of springs connected to the bottom side of the structure represent the GAS-filters stiffness matrix, the three connected to the upper side represent the fluorel stage stiffness matrix. The parameters of these matrices are derived in section 11.2.2 and 12.1. The colors in the picture represent the relative displacement from no displacement (blue) to high displacement (red).
For each of the displayed mode shapes the fluorel pads are deformed during the oscillation. Thereby these modes should be sufficiently damped. Thus, they were not identified experimentally, yet.

The intermediate plate is included in the AEI-SAS design to support the tilt stabilization. This subsystem's purpose is to prevent the AEI-SAS from instability in pitch and roll (rx and ry). The fundamental resonance frequencies of those degrees of freedom are strongly dependent on the payload's moment of inertia, e.i. its vertical mass distribution. Since the AEI 10 m prototype is designed for being a versatile testbed for varying experiments, the tilt stabilization should account for a potentially relatively high moment of inertia.

Due to its large horizontal dimensions and low thickness, the intermediate plate is relatively soft and its eigen-resonances are a potential hazard for the AEI-SAS performance. Figure 26 shows a finite element simulation of the intermediate plate's 6 lowest frequency bending modes

which are in a band between 15 Hz and 50 Hz. Also above 50 Hz there are numerous bending modes which are not shown here. The plate is constrained by a set of springs which represent the GAS-filter and the fluorel pads. In this simplified simulation those springs interconnect the intermediate plate to a spring-box plate and a tabletop plate. The modeled geometry is discussed in more detail in section 12.2.

A significant simulation of the original AEI-SAS design, where the optical bench was directly placed on top of the intermediate plate, is hardly possible since the contact points to the optical table are not well defined, yet have a strong influence on the mode frequency. It is likely though, that intermediate plate modes limited the old design's isolation performance. The intermediate plate modes, however, have not been identified in the AEI-SAS's performance, not in the original design nor in the new setup. In the old design they might have been covered by high amplitude horizontal and vertical spring-box modes (see chapter 11 and 11.3). In the new design, the fluorel pads dissipate the energy of the intermediate plate modes. The resonances are strongly therefore damped. However, they might be visible in the third AEI-SAS unit, where the vertical spring-box modes are shifted to higher frequencies. If intermediate plate modes will become harmful in any way they can easily be damped by installing additional soft but lossy springs between the corners of the table top and the intermediate plate.

## 5.2 SENSORS AND ACTUATORS

The AEI-SAS provides passive vibration isolation for the payload above its fundamental resonance frequencies. Additionally, several sensors and actuators are installed in the system to sense and control the payload position actively. Furthermore, the three translational degrees of freedom of the ground motion are sensed by a commercial Streckeisen STS-2 triaxial broadband seismometer [122]. It is located on the laboratory floor next to the central tank of the AEI 10 m prototype vacuum chamber. The various inertial and relative in-vacuum sensors and the actuators are briefly discussed in this section. The location of sensors and actuators in the AEI-SAS are shown in figure 20.

### 5.2.1 *Geophones*

Three commercial geophones, arranged in a triangle, sense the inertial vertical payload motion. Geophones are in principle damped harmonic oscillators. The device's frame velocity with respect to the test mass is red out by converting mechanical motion into an electrical signal. This is depicted in figure 27. A mass (blue) is mounted on a spring, in parallel to a damping unit. A magnet (red) is connected to the mass. It is moving inside a coil (green), inducing a current proportional to the

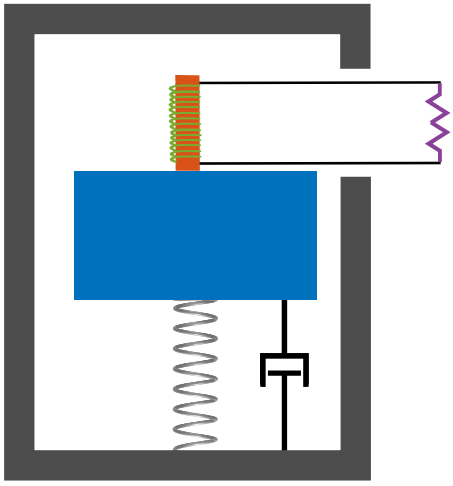

**Figure 27:** Simplified illustration of a geophone. The velocity of a damped harmonic oscillator with respect to the device's frame is measured by a contactless magnet (red) coil (green) configuration. The induced current is read out by electronics (purple). This way the frame's velocity can be measured with respect to an, at high frequencies, approximately inertial reference.

relative velocity. The current is converted to a voltage by the readout electronics (purple).

In the original AEI-SAS configuration, L-22D geophones were used as vertical inertial sensors. However, due to their better performance, the AEI-SAS was equipped with additional L-4C geophones. Both types of geophones are products from Sercel [123]. The performance of the geophones was measured in huddle tests and the results were published in ref. [108]. Figure 28 shows a comparison of both geophone's sensitivities. It is clearly visible, that over the whole frequency band of interest (0.01 Hz to 100 Hz) the L-4C performs better than the L-22D. The L-4Cs is successfully used for vertical and tilt inertial control of the AEI-SAS (see section 16).

Both types of geophones are not made for the use of a clean vacuum environment, therefore they have to be housed in airtight envelopes. A custom made housing was designed for the new L-4C geophones. It is much lighter than the old design for the L-22Ds and it can easily be retrofitted to the optical tables without major reconstructions [124].

### 5.2.2 *Accelerometers*

Three custom made, monoaxial accelerometers sense the inertial horizontal motion of the system. They are placed close to the edges of the spring-box. As well as the other sensors the accelerometers are arranged in an equilateral triangle.

In principle, an accelerometer is a low resonance frequency driven harmonic oscillators. It is designed as a folded pendulum, where a test

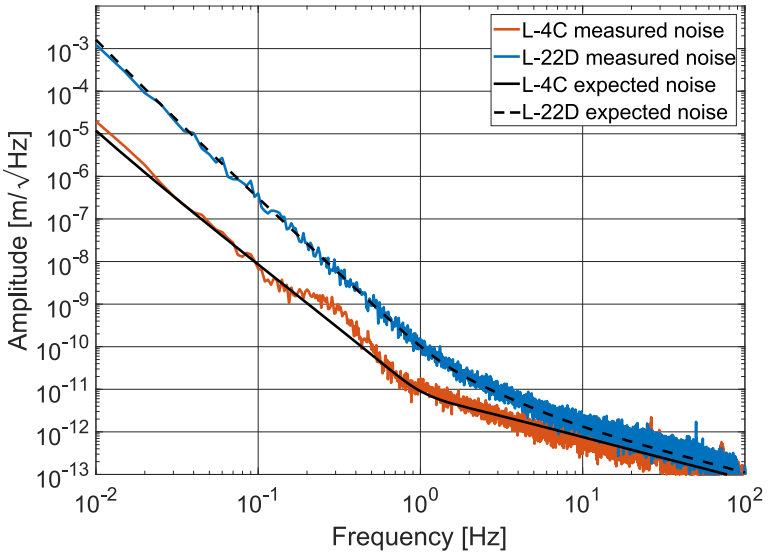


**Figure 28:** Geophone noise curve. This figure shows the performance of L-22D (blue) and L-4C (red) geophones, measured in a huddle tests. The solid black line represents the theoretical L-4C noise floor model. It is limited by Johnson noise and the voltage noise of the operational amplifier. The amplitude of these two noise contributions is almost equal over the regarded frequency band.
The L-22D performance is limited by operational amplifier voltage noise and Johnson noise at low and high frequencies. Around its resonance frequency (2 Hz) thermal suspension noise is limiting. The L-22D noise model is represented by the dashed black line.
This figure is taken from [108].

mass with a tunable center of mass is on one side suspended from a pendulum, on the other side it is supported by an inverted pendulum. By adjusting the horizontal position of the test mass's center of mass the pendulum or the inverted pendulum gains larger influence and the fundamental resonance of the system is increased or decreased. The AEI-SAS accelerometers are tuned to approximately 0.3 Hz. This is a good compromise between a high sensitivity, due to a low resonance frequency, and a reasonably stable system. The test mass position is red out by miniature LVDTs. They have a higher sensitivity and a smaller dynamic range as the relative payload sensors discussed in section 5.2.3. This reduced measurement amplitude is tolerable since the motion of the system is controlled by feeding back the LVDT signal to a voice-coil actuator. The feedback signal is processed by a digital CDS (Control and Data acquisition System) controller.

The AEI-SAS accelerometers' mechanical design is similar to the monolithic accelerometers used in TAMA300 [120]. A photograph of the device is shown in figure 29.

The sensitivity of the AEI-accelerometers is currently being analyzed. Preliminary experimental results suggest that the AEI-SAS active iso-

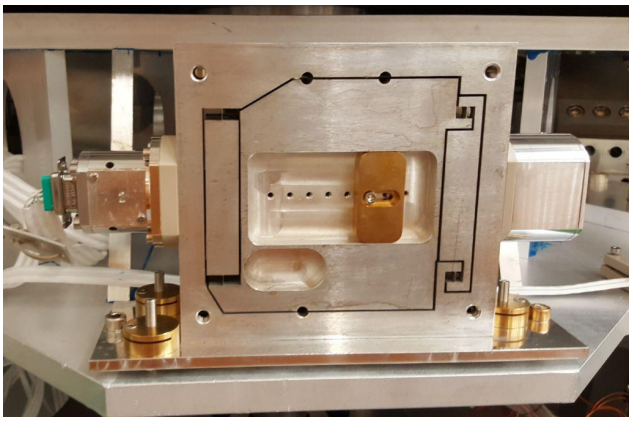

**Figure 29:** Photograph of an AEI-SAS accelerometer. A test mass is suspended on the left by a pendulum and it is supported on the right by an inverted pendulum structure. Such a type of suspension is referred to as Watt's linkage. The whole geometry is cut from one piece of aluminum in order to reduce the pendulum and inverted pendulum flexure's thermal noise. The bronze piece bolted to the test mass is for adjusting its center of mass horizontally and thereby tune the fundamental resonance frequency of the system. LVDT, actuator magnet, and coils are mounted to the payload and the frame from the side. They are not visible in this photograph.

lation performance is limited by the noise floor of the accelerometers' noise floor [125].

Due to the limited performance of the accelerometers, it is planned to install a set of three horizontal L-4C geophones in each isolation platform. They have a sensitivity comparable to the vertical L-4Cs (see figure 28).

### 5.2.3 *Relative motion sensors*

The relative displacement of the payload with respect to the ground is measured by Linear Variable Differential Transformers (LVDTs) [126]. They are monoaxial contactless displacement sensors with a dynamic range of about 20 mm and a sensitivity of $8\,\mathrm{nm\,Hz^{-1/2}}$ [24]. An LVDT consists of two coaxial coil systems, an inner excitation coil, and two rigidly connected outer sensing coils. The excitation coil is driven with a 15 kHz sine wave and thereby generates a magnetic field. The excitation coil is bolted to the payload, the sensing coils are fixed to the ground.

The two sensing coils are electrically connected in series and wound in opposite directions. Thereby the currents in the two coils induced by the excitation coil's magnetic field cancel each other out if the excitation coil is centered between the two sensing coils. If the coils shift against each other along their common axis a sensing signal proportional to the relative displacement is induced in the sensing coil pair.

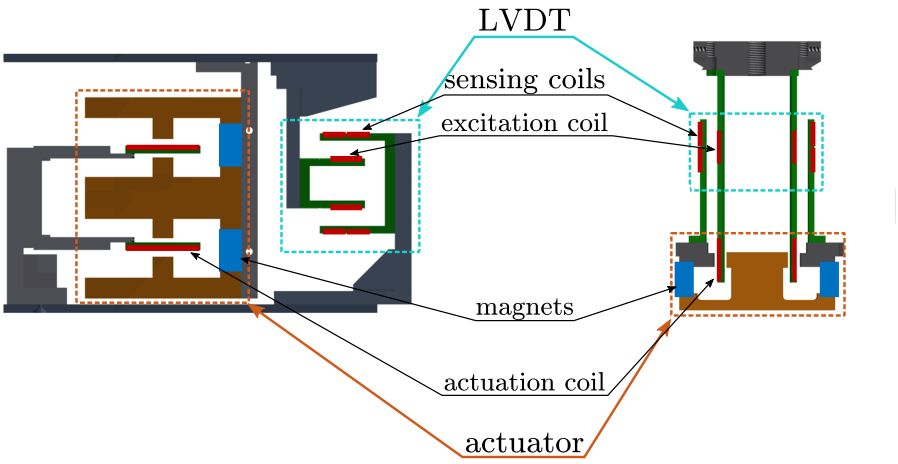


**Figure 30:** Section view of a horizontal (left) and a vertical (right) LVDT-actuator pair. The top of the horizontal LVDT-actuator system is bolted to the lower spring-box plate, the bottom part is fixed to the baseplate. The gray upper part of the vertical LVDT-actuator system is the GAS-filter's keystone. The bottom part is bolted to the lower spring-box plate.

The AEI-SAS is equipped with three horizontal and three vertical LVDTs. The horizontal LVDTs' excitation coils are rigidly connected to the lower spring-box plate, the sensing coils are fixed to the baseplate. Seen from the vertical central axis of the AEI-SAS they are located right behind the IP-legs. The sensing coils of the vertical LVDTs are bolted to the bottom of the GAS-filter keystones. The actuation coils are connected to the lower spring-box plate. This way they are decoupled from horizontal differential ground-payload motion. Figure 30 shows a section view of a horizontal and a vertical LVDT.

### 5.2.4 *Voice-coil actuators*

Each LVDT is co-located with a voice-coil actuator, as shown in figure 30. This way the feedback signals act on payload contactless and with low noise. Each actuator consists of an actuation coil and a magnetic steel structure, magnetized by a set of neodymium magnets. The actuation coil is connected to the baseplate, the magnetic structure is connected to the lower spring-box plate in case of the horizontal actuator. The vertical actuation coil is wound on the same structure as the LVDT's excitation coils. As mentioned above, this structure is bolted to the keystone. The vertical actuator magnet structure is connected to the lower spring-box plate. The basic principle of the actuators is described in ref. [127]. The vertical actuators provide a force of $7\,\mathrm{N\,A^{-1}}$, the horizontal provide $5\,\mathrm{N\,A^{-1}}$ [24]. The maximum current of the horizontal coils is approximately $\pm 0.07\,\mathrm{A}$. Accordingly, the maximum force in this direction is $0.3\,\mathrm{N}$. In the vertical direction, the maximum current is approximately $0.2\,\mathrm{A}$ and the maximum force is accordingly $1.4\,\mathrm{N}$ per

actuation coil. This way the dynamic range is approximately ±500 µm in the transversal directions.

### 5.2.5 *Motorized springs*

Additional to the very precise voice-coil actuators, which have a relatively low dynamic range, the AEI-SAS is equipped with a set of motorized spring actuators. They have a large linear dynamic range of the order of millimeters and are used for rough pre-positioning of the payload. With these actuators, small mass changes of the payload or thermal drifts can be compensated.

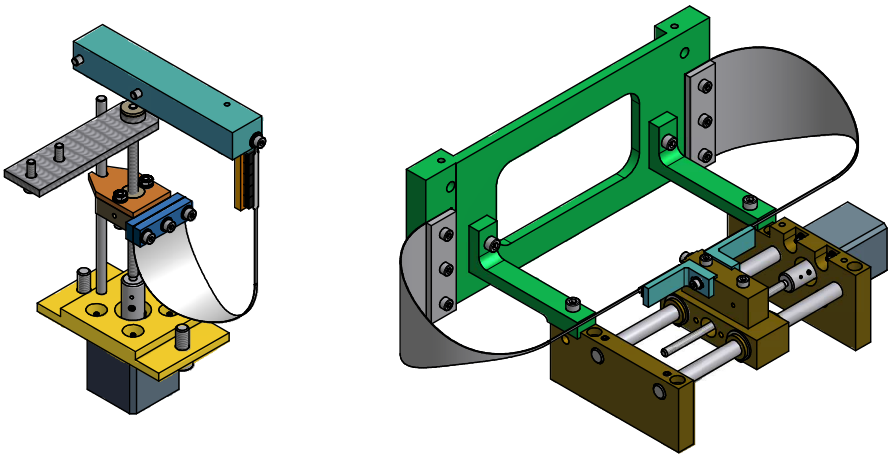

**Figure 31:** Technical drawing of the vertical (left) and horizontal (right) motorized springs. The horizontal motorized spring illustration includes a clamping structure (green) interconnecting the spring-box connection plate (also green) and the stepper motor mount (brown). This component is only installed during installation of the motorized springs. It is removed when the system is operated.

As shown in figure 31 the vertical motorized springs are soft blade springs mounted on a sled. The sled is shifted vertically by rotating a threaded rod. A vacuum compatible stepper motor drives this threaded rod. Stepper motor and threaded rod are mounted between the spring-box plates. The tip of the bent blade spring is connected to the intermediate plate. Since the blades mechanically shortcut the GAS-filters they are designed to be very soft. Reducing the dummy mass on the table top compensates for the additional force between spring-box and payload.

The horizontal motorized springs are designed in a similar way. Here the additional force, however, cannot be compensated by a mass change. Two blades are therefore mounted symmetrically to a plate which is bolted to the lower spring-box plate. In the horizontal motorized springs, the blade tips are mounted on a sled driven by a stepper motor. This part of the structure connects rigidly to the baseplate.

These blades are furthermore relatively soft to reduce mechanical shortcutting.

Both, horizontal and vertical motorized springs feature eddy current damping units in order to mitigate the effect of the blade spring's internal resonances.

Three horizontal and four vertical motorized springs enable payload positioning in six degrees of freedom at DC. Seen from the AEI-SAS's center the horizontal motorized springs are located in front of the LVDT's, in one line with IP-legs and the LVDTs. The vertical motorizes springs are situated in the four corners of the optical table.

The stepper motors are operated separately from the AEI-SAS's feedback system. The relatively noisy stepper motors would compromise the AEI-SAS's performance. However, after the payload position has been roughly aligned, the voice coil actuators are taking over fine adjustment. The stronger motorized springs are than only needed if environmental changes, as for instance temperature fluctuations, change the system strongly.

# 6 PASSIVE VIBRATION ISOLATION

Vibration isolation techniques can be divided into two groups: active isolation and passive isolation. Active isolation is based on measuring and actively counteracting the payload motion. Passive isolation systems make use of the principle of mechanical harmonic oscillators and their second order low pass behavior. The AEI-SAS employs both passive and active isolation. As summarized in chapter 5, active isolation minimizes payload motion below and at the fundamental AEI-SAS resonances. At higher frequencies, the system attenuates ground motion purely passively. Various other systems using these techniques are described in chapter 3. In this chapter, the principle of passive isolation is introduced.

## 6.1 THE HARMONIC OSCILLATOR AS A MECHANICAL PASSIVE ISOLATOR

A simple mechanical harmonic oscillator ideally consists of a spring and a mass. A force is acting on the mass through a spring. This force is proportional to the displacement of the mass with respect to the system's equilibrium position. If the spring is on one end connected to the ground, which is moving with $\vec{x}_g$, and on the other end to the mass, which is moving with $\vec{x}$, the force acting on the mass is

$$\vec{F}_{osc} = -k(\vec{x} - \vec{x}_g) \ . \tag{9}$$

In case of a pendulum and a spring-mass system, the restoring force can be provided by gravity [128]. Figure 32 shows a more comprehensive model of a one-dimensional mechanical harmonic oscillator. It includes both, viscous damping and structural damping. The viscous damping force is proportional to the velocity. In this case, it is represented by a dashpot between ground and mass. Energy dissipation due to internal friction in the spring material is usually referred to as structural damping. The phase lag of the mass motion $x$ with respect to the ground motion resulting from the internal loss in the spring material can be described as $i\phi$, the imaginary part of the complex spring constant $k_s = k(1 + i\phi)$. The structural damping is frequency independent and is defined as the phase angle in radians. The resulting force from this inelasticity is proportional to the spring deflection and is in phase with the velocity [3].

Owing to the fact the AEI-SAS is operated in vacuum conditions, the energy dissipation is dominated by structural damping. viscous damping, nevertheless, plays a role when the vacuum system is vented

and, more importantly, in the active control, which is based on velocity damping (See chapter 16).

The equation of motion of a damped, one-dimensional harmonic oscillator is

$$F_{osc} = m\ddot{x} = -k_s(x - x_g) - \gamma(\dot{x} - \dot{x}_g) \ , \tag{10}$$

where $\gamma$ is the viscous damping coefficient.

### 6.1.1 *Transmissibility of an harmonic oscillator*

The capability of passive vibration isolation of mechanical harmonic oscillators is best displayed as the transmissibilty of ground motion to mass motion. It follows from the Fourier transform of equation 10

$$\omega^2\tilde{x} - \left(\omega_0^2(1 + i\phi) + i\frac{\gamma}{m}\omega\right)(\tilde{x} - \tilde{x}_g) = 0 \tag{11}$$

as

$$T(\omega) = \frac{\tilde{x}}{\tilde{x}_g} = \frac{\omega_0^2(1 + i\phi) + i\frac{\gamma}{m}\omega}{\omega_0^2(1 + i\phi) - \omega^2 + i\frac{\gamma}{m}\omega} \ , \tag{12}$$

where $\omega = 2\pi f$ is the angular frequency[1]. The spring constant $k$ and the mass $m$ are substituted with the resonance frequency

$$\omega_0^2 = \frac{k}{m} \ . \tag{13}$$

Figure 33 shows the amplitude and phase of the transmissibility with dominant structural damping (red, yellow, purple and green) and dominant viscous damping (blue). Both cases clearly show that above the resonance frequency, the motion of the mass falls off rapidly with respect to the ground motion. This is the isolation frequency band of a harmonic oscillator. The mass follows ground motion at frequencies far below the resonance frequency of the mass. At the resonance frequency, the amplitude depends on the damping factor. If the damping is low, the maximum amplitude of the oscillation is approximately equal to the mechanical quality factor Q. For a purely viscous damping, it is

$$Q_v = \frac{m\omega_0}{\gamma} \ , \tag{14}$$

for a purely structural damping it is

$$Q_s = \frac{1}{\phi} \ . \tag{15}$$

1 Here the theory is derived using the more general angular frequency $\omega$. For the description of experiments it is more convenient to use the ordinary frequency $f$.

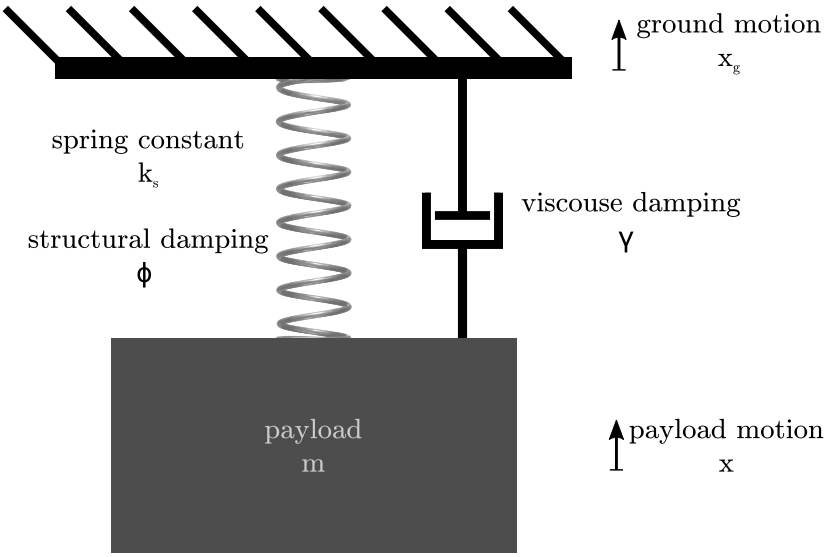


**Figure 32:** One-dimensional harmonic oscillator. A mass is suspended from a spring with a spring constant and structural damping. In parallel a dashpot is damping the oscillation.

The harmonic oscillator is critically damped with $Q = 1/2$ and overdamped with $Q < 1/2$. In those cases, the suspended mass motion does not exceed the ground motion at the resonance frequency.

The transmissibility of the structurally damped harmonic oscillator rolls of with $\omega^{-2}$ above the resonance frequency, whereas the viscously damped system's transmissibility bends up to a $\omega^{-1}$ slope at the corner frequency

$$\omega_v = \omega_0 Q_v \ . \tag{16}$$

This is due to the dashpot configuration shown in figure 32, which damps the mass against the moving ground. At high frequencies, i.e. high velocity, the damping force is high and motion is coupled through the dashpot onto the mass. A dashpot in between the mass and something inertially quiet would keep the second order filter properties of a free harmonic oscillator while reducing the resonance amplitude. The inertial control, discussed in chapter 16, makes use of this technique.

The lower plot in figure 33 represents the phase lag between suspension point motion and mass motion and can be written down as the angle between the real and the imaginary part of $T$ from equation 12:

$$\Phi = \arctan\frac{\mathrm{Im}(T)}{\mathrm{Re}(T)} \tag{17}$$

Below the resonance frequency, suspension point and mass are moving approximately in phase. At the resonance, the phase lag is $-90°$ and falls off to $-180°$ at high frequencies for an undamped harmonic oscillator. The phase of a viscously damped oscillator approaches $-90°$ in

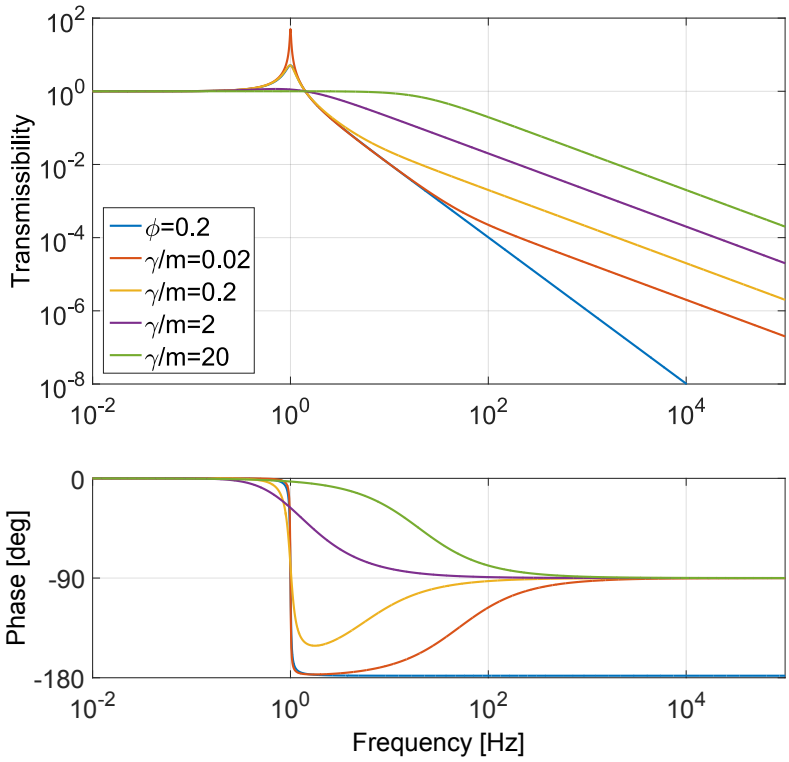


**Figure 33:** Amplitude and phase of the transmissibility of a damped harmonic oscillator from suspension point motion to payload motion (compare to equation 12). The blue line represents a purely structural damped system ($\phi = 0.2$, $\gamma = 0$), whereas the other lines show the transmissibility of viscously damped systems ($\phi = 0$). An overdamped (green), a critically damped (purple), and two underdamped systems (red and yellow) are plotted in this figure.

the frequency band where the viscous force dominates over the spring force.

### 6.1.2 *Frequency response of a harmonic oscillator*

In the model, discussed above, the damped harmonic oscillator was actuated by ground motion through the spring. If it is driven by an external force $F_{ext}$, which is acting directly on the mass, and the motion of the mass is dominated by this force and not by the ground motion, the equation of motion is

$$m\ddot{x} = F_{ext} - k_s x - 2\pi\gamma\dot{x} \ . \tag{18}$$

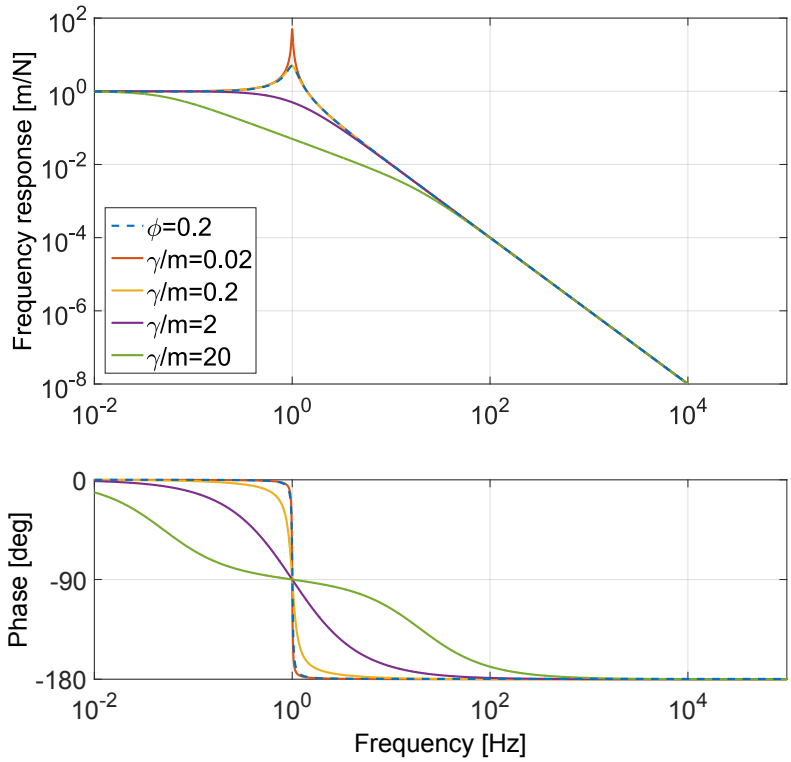


**Figure 34:** Amplitude and phase of the frequency response function of a driven harmonic oscillator (equation 19). The response function is plotted for a structurally damped oscillation (dashed blue line) and 4 viscously damped cases (compare to figure 33).

The resulting frequency response function is defined similarly to the transmissibility function and derived from the Fourier transform of equation 18 as

$$R(\omega) = \frac{\tilde{x}}{F_{ext}} = \frac{1}{\omega_0^2(1+i\phi) - \omega^2 + i\frac{\gamma}{m}\omega} \quad , \tag{19}$$

Where the parameters are derived in the same way as for equation 12. Unlike the amplitude of the transmissibility, the amplitude of the frequency response rolls of with $\omega^{-2}$ for structural and viscous damping. Accordingly the phase converges towards $-180°$. Figure 34 shows the phase and amplitude of $R(\omega)$ for the same viscous and structural damping factors as it is shown in figure 33.

### 6.1.3 *Maximum amplitude versus resonance frequency*

While the maximum of the frequency response function of an undamped harmonic oscillator coincides with the resonance frequency $\omega_0$, it decreases below it for viscously damped systems. The location of the maximum of purely structural damped systems, however, is independent of

the damping factor. The maximum frequency $\omega_{maxR}$ as a function of the quality factor $Q_v$ is

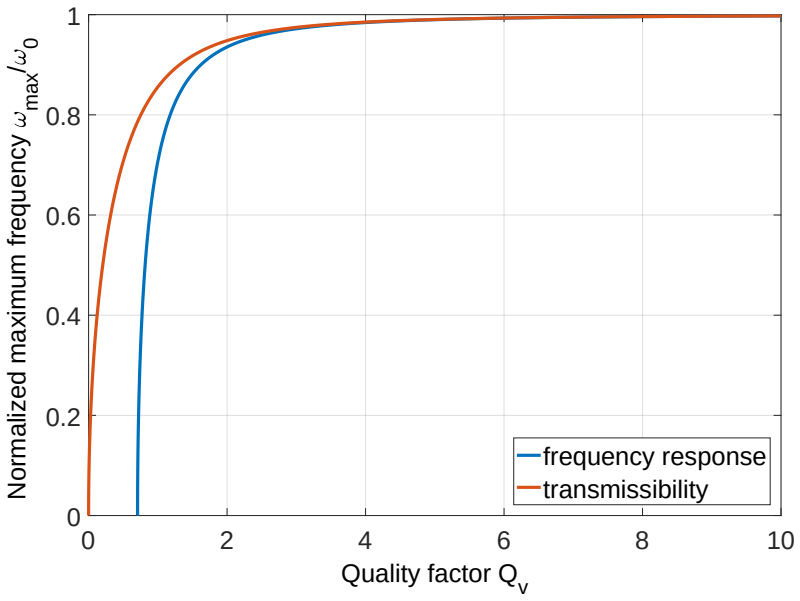


**Figure 35:** Normalized frequency of the maximum of the frequency response and the transmissibility amplitude as a function of the quality factor. The frequency with a maximum amplitude of a viscously damped oscillator $\omega_{maxT}$ and $\omega_{maxR}$ varies from the resonance frequency $\omega_0$. At a quality factor of $Q_v = \sqrt{1/2}$ the amplitude maximum of the frequency response is 0. Below that value the frequency response amplitude is strictly decreasing. The transmissibility maximal amplitude frequency is higher than the one of the frequency response. It exist also for critical and overdamped harmonic oscillators. The two plotted lines correspond to equation 20 and equation 21.

$$\omega_{maxR} = \frac{\sqrt{Q_v^2 - \frac{1}{2}}}{Q_v}\omega_0 \ . \tag{20}$$

Figure 35 illustrates this relation. It shows, that for a high quality factor the frequency response amplitude's maximum is approximately equal to the resonance frequency, whereas it decreases to $\omega_{maxR} = 0$ at a quality factor of $Q_v = \sqrt{1/2}$.

Unlike the frequency response amplitude, the transmissibility amplitude has a maximum for all quality factors $Q_v > 0$. The frequency of the maximum $\omega_{maxT}$ is derived from the absolute value of equation 12. It is

$$\omega_{maxT} = Q_v\omega_0\sqrt{\sqrt{1+\frac{2}{Q_v^2}}-1} \ . \tag{21}$$

# 7 INVERTED PENDULUM LEGS

As briefly discussed in chapter 5, the horizontal passive isolation of the AEI-SAS is based on three Inverted-Pendulum (IP)-legs. Their advantage over conventional horizontal isolation systems, such as regular pendular, is that extremely low resonances can be achieved with a very compact system.

Each IP-leg consists of an aluminum tube, which is resting on a cylindrical flexure, connecting the leg to the ground (see figure 36). This lower flexure provides a restoring force of the IP-leg. The vertical stage of the AEI-SAS is suspended by a thin flexure from the top of the aluminum tube. This upper flexure simply functions as a joint.

The name 'inverted pendulum' might be misleading since unlike a common inverted pendulum the IP-legs are stable systems. The inverted pendulum effect is rather used to counteract a flexure's restoring force and therefore tune the IP-leg close to instability, i.e. to a low resonance frequency.

A key component of the improved AEI-SAS, described in this work, is the new symmetric IP-legs. In this chapter, the design of the old IP-legs is described. They are installed in the first two AEI-SAS units and their geometry is similar to the IP-legs used in related systems such as Virgo's EIB-SAS, the Superattenuator or the KAGRA-SAS (see chapter 3). The symmetric IP-legs are designed for the third, improved AEI-SAS unit. They are described in chapter13.

## 7.1 WORKING PRINCIPLE OF THE IP-LEG

The goal of passive seismic isolation systems in the field of gravitational wave physics is to achieve very low resonance frequencies in order to obtain low frequency seismic attenuation. The fundamental resonance frequency of a regular pendulum depends on the length of the pendulum wire. To achieve a resonance frequency of 0.1 Hz, a pendulum length of approximately 25 m would be required. Such dimensions are hardly feasible in a regular lab space. A better alternative for a horizontal low frequency isolator is IP-legs. They are much more compact than a regular pendulum (the AEI-SAS's IP-legs are approximately 0.5 m high), can carry a high-mass payload and their resonance frequency can be tuned below 0.1 Hz.

The IP-legs can be described as a combination of a spring component and an adjustable anti-spring component. The restoring force of the spring is given by the lower flexure, the anti-spring force originates from gravity acting on the payload (see figure 36). If the mass of the payload

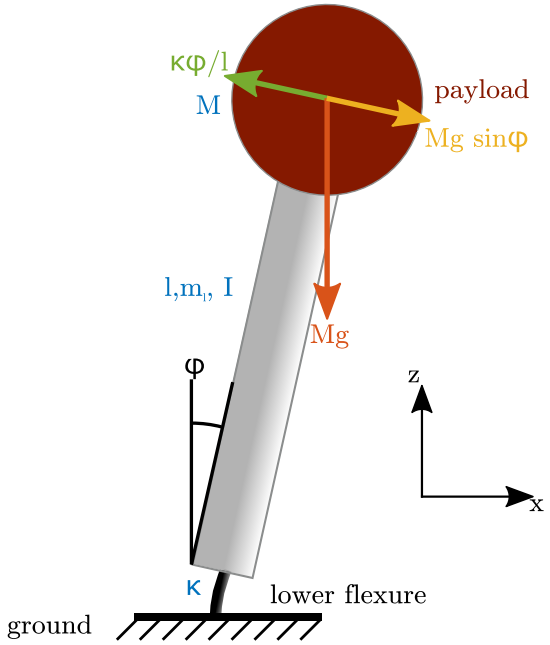


**Figure 36:** Simplified IP-leg: A rigid rod is supporting the payload. A flexure on the bottom of the rod is providing the restoring force and preventing the system from falling over. The restoring force resulting from the lower flexure is shown in green, the force resulting from gravity is shown in yellow. A very low resonance frequency can be achieved by increasing the payload mass M until the system is almost instable.

is too high, the anti-spring dominates the system and it becomes the eponymous unstable inverted pendulum.

### 7.1.1 *Fundamental resonance of the IP-leg*

The principal of the horizontal stage is best described in a simplified two-dimensional model of a single IP-leg [129]. The leg, carrying a point-mass-payload, is assumed to be mass-less. Furthermore, the length of the flexure is assumed to be 0 hence the pivot point of the system is right above the ground. The fundamental resonance frequency of the IP-leg can be derived from the equation of motion of the payload which is derived in the following.

The torque on the leg caused by the lower flexure's angular stiffness $\kappa$ is:

$$\tau = -\kappa\varphi \ , \tag{22}$$

where $\varphi$ is the displacement angle of the IP-leg. The resulting force on the payload is

$$F_{\text{flex}} = -\frac{\kappa\varphi}{l} \ , \tag{23}$$

with $l$ being the length of the IP-leg. The inverted pendulum force $F_g$ is counteracting the flexure force and is the projection of the gravitational force acting on the payload

$$F_g = Mg\sin\varphi \ , \tag{24}$$

Where $M$ is the payload mass and $g$ is the gravitational acceleration. The equation of motion of the payload follows as

$$M\ddot{x} = F_g + F_{flex} \ . \tag{25}$$

The angular displacement of the IP-leg can be approximated to a small angle with $\varphi \approx \sin\varphi = x/l$. Inserting this in equation 25 leads to

$$\ddot{x} = \left(\frac{g}{l} - \frac{\kappa}{Ml^2}\right) x \ . \tag{26}$$

From equation 9 and 13 the resonance frequency $f_{IP}$ of an IP-leg can be derived to

$$f_{IP} = \frac{1}{2\pi}\sqrt{\frac{\kappa}{Ml^2} - \frac{g}{l}} \ . \tag{27}$$

Figure 37 shows a plot of the resonance frequency as a function of the payload mass. Below 100 mHz the slope decreases strongly. An IP-leg tuned to this frequency range is very sensitive to mass change and can become instable due to a small mass mismatch. That is one reason why the horizontal resonance frequency of the AEI-SAS is tuned only down to 100 mHz.

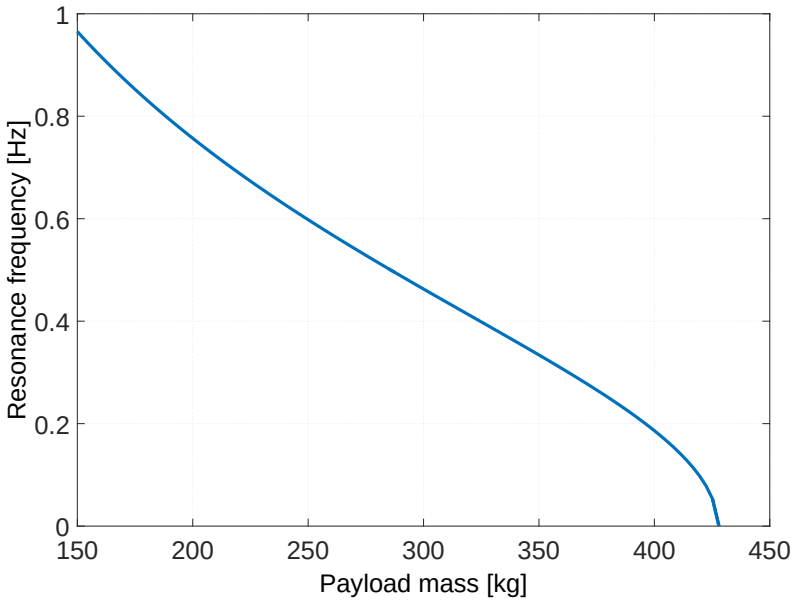


**Figure 37:** IP-leg fundamental resonance frequency as a function of the payload mass.

### 7.1.2 *Maximum load of an IP-leg*

| Parameter | Value | Description |
|---|---|---|
| $l_{leg}$ | 0.4335 m | length of the rigid part of the IP-leg |
| $E$ | 186 GPa | Young's modulus of maraging steel [70] |
| $l_{flex}$ | 0.06 m | length of the IP-leg's lower flexure [24] |
| $d_{flex}$ | 0.0108 m | thickness of the IP-leg's lower flexure [24] |
| $l_{uflex}$ | 0.025 m | length of the IP-leg's upper flexure [24] |
| $d_{uflex}$ | 0.003 m | thickness of the IP-leg's upper flexure [24] |
| $\kappa$ | 2070 Nm | angular stiffness of the IP-leg [24] |

**Table 5:** IP-leg parameters (compare to figure 36).

Equation 27 shows that by increasing the payload mass, the resonance frequency decreases down to a point where $f_{IP} = 0\,\text{Hz}$ and the system becomes instable. The maximum mass that can be stably supported by an IP-leg is

$$M_{max} = \frac{\kappa}{g l} \quad . \tag{28}$$

To calculate the maximal load that can be supported by the vertical stage of the AEI-SAS, the angular stiffness and the IP-leg length need to be determined. The realistic geometry of the IP-legs is discussed in section 7.1.6. The angular stiffness of the lower flexure can be approximated as the angular bending stiffness of a cylinder,

$$\kappa = \frac{E I_y}{l_{flex}} = \frac{E \pi d_{flex}^4}{64 l_{flex}} \approx 2070\,\text{Nm} \quad , \tag{29}$$

with the moment of inertia of a cylinder $I_y = \pi d^4/64$ [130] and the parameters from table 5.
In the simplified IP-leg model the effective length does not coincide with the realistic length of the rigid leg. The effective length of the IP-leg is the distance between the point where the horizontal force induced by the payload is acting on the upper end of the leg and the bending

point of the lower flexure. This bending point can be deduced from the Euler-Bernoulli beam theory, which states, that the deflection of a beam follows

$$\frac{d^2w}{dz^2} = w''(z) = -\frac{M_b(z)}{EI} \ , \tag{30}$$

where $w''(z)$ is the second derivative of the deflection of the beam $w(z)$ at the position $z$. $M_b(z)$ is the bending moment along the beam and I is the moment of inertia of the beam's cross section perpendicular to the $z$-axis. The lower flexure is assumed to be a one-dimensional cantilever beam, fixed at its lower end ($z = 0$) and bend by a force $F_b$ acting horizontally on the upper end of the flexure ($z = l_{flex}$). The deflections are assumed to be small and the cantilever length is assumed to be much longer than its cross section dimensions. The bending moment of such a configuration is $M_b(z) = F_b(z - l_{flex})$ [131]. After integrating equation 30 and inserting the boundary conditions ($w(0) = 0$ and $w'(0) = 0$) it leads to the bending curve

$$w(z) = \frac{F_b z^2(3l_{flex} - z)}{6EI} \ . \tag{31}$$

The vertical position of the bending point of the IP-leg follows as

$$z_b = \frac{1}{3} l_{flex} \ . \tag{32}$$

$z_b$ is the vertical component of the intersection of the $z$-axis and the tangent line of $w(l_{flex})$.

The upper flexure is only 25 mm long and stressed in tension, thus, the point where the payload force is acting on the IP-leg can be assumed to be at the contact position between upper flexure and the IP-leg cap (compare to figure 44). The total effective IP-leg length is

$$l = l_{leg} + \frac{2}{3} l_{flex} = 493.5\,\text{mm} \ , \tag{33}$$

where $l_{leg}$ is the length of the rigid part of the IP-leg, namely the length of the aluminum tube, the upper foot of the lower flexure, and a part of the IP-leg cap. Inserting these values in equation 28 results in the maximum payload mass per IP-leg to be $M_{max} = 428\,\text{kg}$. The payload mass for the whole AEI-SAS with three IP-legs is accordingly 1284 kg. This value differs from the estimation in ref. [24], due to a more precise way of obtaining the IP-leg length. The real AEI-SAS is obviously not loaded to the maximum payload mass, which would result in an unstable system. When comparing this very simple model to the real payload mass, not the maximum mass but the mass of a system with a resonance frequency of approximately 0.1 Hz needs to be regarded. According to equation 27, three IP-legs support 1258 kg.

This differs only approximately 2% from the payload mass of the real system shown in table 4.

### 7.1.3 *IP-leg with finite mass*

The calculations above describe a highly simplified model of the IP-leg. The leg itself is assumed mass-less, and the center of mass (CoM) is the geometrical center of the payload. For small deflections, this system is described by a simple harmonic oscillator (see section 6.1). As it is shown in this and the following sections, by taking the mass of the IP-leg itself into account, its high frequency isolation performance differs from the one of a simple harmonic oscillator.

| **Parameter** | **Value** | **Description** |
|---|---|---|
| $l$ | 0.4935 m | effective length of the IP-leg |
| $M$ | 419 kg | payload mass which leads to a fundamental resonance frequency of 0.1 Hz |
| $m$ | 0.2 kg | IP-leg mass |
| $I$ | $4.06 \times 10^{-3}$ kg m$^2$ | moment of inertia about the center of mass of the IP-leg |
| $\varphi$ | | deflection angle of the IP-leg |
| $x, z$ | | payload position |
| $x_l, z_l$ | | position of the IP-legs's center of mass |
| $x_0, z_0$ | | position of IP-leg pivot point ($\frac{1}{3} l_{flex}$ above the flexure-ground connection) |

**Table 6:** Parameters for the simplified two-dimensional IP-leg model.

The model sketched in figure 36 is described by the Lagrangian

$$L = K - U \ , \tag{34}$$

with the kinetic energy $K$ and the potential energy $U$ [132]. Those energies can be described as

$$\begin{aligned} K &= K_{payload} + K_{leg} \\ &= \frac{1}{2}\left(M\left(\dot{x}^2 + \dot{z}^2\right) + m\left(\dot{x}_l^2 + \dot{z}_l^2\right) + I\dot{\varphi}^2\right) \end{aligned}$$

and (35)

$$\begin{aligned} U &= U_{payload} + U_{leg} + U_{flex} \\ &= Mgz + mgz_l + \frac{1}{2}\kappa\varphi^2 \quad . \end{aligned}$$

The parameters used in this model are defined in tabel 6 and illustrated in figure 36. The sketch shows, that the variables are constrained as follows:

$$\begin{aligned} x_l &= \frac{1}{2}(x + x_g) \\ z_l &= \frac{1}{2}z \\ \sin\varphi \approx \varphi &= \frac{x - x_g}{l} \\ z &= l\cos\varphi \end{aligned} \tag{36}$$

Inserting this in $K$ and $U$, and neglecting the vertical velocities due to small deflections, gives

$$K = \frac{1}{2}M\dot{x}^2 + \frac{1}{8}m(\dot{x} + \dot{x}_g)^2 + \frac{I}{2l^2}(\dot{x} - \dot{x}_g)^2$$

and (37)

$$U = gl\left(M + \frac{m}{2}\right)\cos\left(\frac{x - x_g}{l}\right) + \frac{1}{2}\kappa\left(\frac{x - x_g}{l}\right)^2 \quad .$$

Figure 38 shows a plot of the potential energy for different payload masses. It illustrates that the potential is approximately parabolic shaped for a stable loaded IP-leg (with the masses $M_4$ and $M_5$). $M_3$ is the maximum payload mass (when omitting the IP-leg mass of $m = 0.2\,kg$) for which the potential is flat around the equilibrium position $x_g = 0$. For higher masses the system becomes bistable. In reality, the rising potential flanks caused by the quadratic behavior of $U_{flex}$ do not matter since the flexures would break due to the stress of such a deflection.

The equation of motion of the payload of the massive IP-leg is derived from the Euler-Lagrange equation

$$\frac{d}{dt}\frac{\partial L}{\partial \dot{x}} = \frac{\partial L}{\partial x} \tag{38}$$

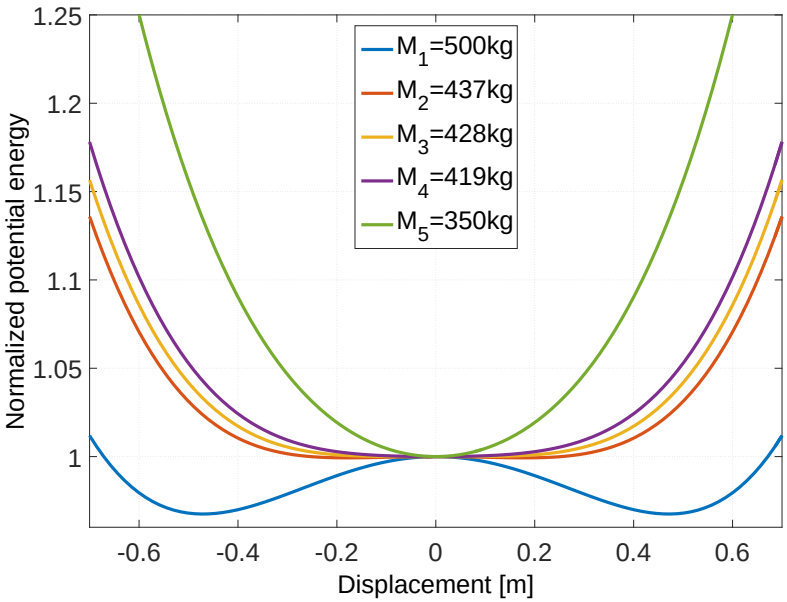


**Figure 38:** Potential energy of an IP-leg: The figure shows plots of equation 37 for varying payload masses. $M_3$ represents the maximum Payload mass (compare to section 7.1.2). In this configuration the potential is flat around the equilibrium position $x_g = 0$. For higher masses the system is bistable, for lower masses it is stable. $M_4$ is the theoretical payload mass by which a horizontal resonance frequency of 0.1 Hz is achieved.

$$\left(M + \frac{m}{4} + \frac{I}{l^2}\right)\ddot{x} + \left(\frac{m}{4} - \frac{I}{l^2}\right)\ddot{x_g} = -\left(\frac{\kappa}{l^2} - \frac{g}{l}\left(M + \frac{m}{2}\right)\right)(x - x_g) \quad . \tag{39}$$

From the equation of motion the effective spring constant and the fundamental resonance frequency of the system can be deduced. Equation 39 can be written as $M_{eff}\ddot{x} = -k_{eff}x$ respectively $\ddot{x} = \omega_0^2 x$ when the ground motion is assumed to be $x_g = 0$. The effective spring constant is then calculated from

$$k_{eff} = \frac{\kappa}{l^2} - \frac{g}{l}\left(M + \frac{m}{2}\right) \tag{40}$$

and the fundamental resonance frequency

$$\omega_0 = \sqrt{\frac{k_{eff}}{M + \frac{m}{4} + \frac{I}{l^2}}} \quad . \tag{41}$$

The moment of inertia of the IP-leg can be approximated to the moment of inertia of a thin cylinder with $I \approx ml^2/12$ [130]. That assumption simplifies the resonance frequency to

$$\omega_0 = \sqrt{\frac{k_{eff}}{M + \frac{m}{3}}} \ . \tag{42}$$

Usually the mass of the IP-leg is small with respect to the payload mass and the resonance frequency can be approximated as shown in equation 27 with $\omega_0 \approx 2\pi f_{IP}$.

In order to obtain more information about the frequency dependent behavior of a massive IP-leg, the transmissibility function is again considered. The Fourier transform of equation 39 leads to

$$(\omega_0^2 - \omega^2)\tilde{x} - (\omega_0^2 + \beta_h\omega^2)\tilde{x}_g = 0 \ , \tag{43}$$

with

$$\beta_h = \frac{\frac{m}{4} - \frac{I}{l^2}}{M + \frac{m}{4} + \frac{I}{l^2}} \approx \frac{1}{2}\frac{m}{3M + m} \ . \tag{44}$$

The transmissibility function is obtained directly from equation 43 as

$$T_{IP} = \frac{\omega_n^2 + \beta_h\omega^2}{\omega_n^2 - \omega^2} \ . \tag{45}$$

Here the fundamental frequency $\omega_0$ can be replaced by the complex natural frequency

$$\omega_n^2 = \omega_0^2(1 + i\phi) \tag{46}$$

to include energy dissipation through structural damping (see section 6.1).

The amplitude and the phase of the transmissibility function are shown in figure 39 (blue). It is compared to a simple harmonic oscillator with the same structural damping factor (red dashed line).

The amplitude of $T$ converges to $|\beta_h|$ (gray dashed line) for $\omega \to \infty$. In the case of an ideal harmonic oscillator with a massless spring or suspension wire, $\beta_h$ equals 0. That means that at high frequencies the node of the oscillation is at the position of the payload's CoM thus it is decoupled from the ground motion. This is discussed in more detail in section 7.1.4.

The CoM of a harmonic oscillator with a suspension system having finite inertia, however, is shifted in the direction of the suspension point. Hence, at $\omega = \infty$ the oscillator does not move around the payload's CoM but around a point between the CoM of the whole suspension and the CoM of the payload, the Center of Percussion (CoP) (see section 7.1.4 and [68, 121]). The transmissibility function reaches a plateau with the value of $|\beta_h|$, which is represented by the gray dashed

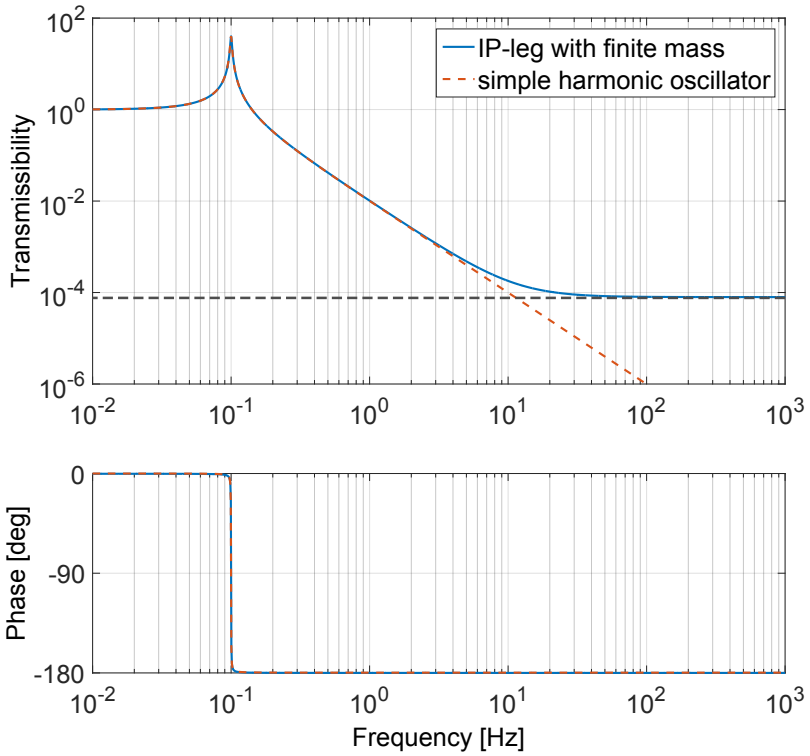


**Figure 39:** Transmissibility of an IP-leg with finite mass compared to a simple harmonic oscillator. Both models employ a structural damping factor of $\phi = 0.025$. The transmissibility amplitude of both models converges against $|\beta_h|$ at high frequencies (gray dashed line). For the simple harmonic oscillator $|\beta_h|$ is 0 because its spring is massless (see equation 44 and 45). Hence, the still point of the high frequency oscillation is the CoM of the payload. The isolation performance of a harmonic oscillator with a finite spring mass is limited, since at high frequencies it oscillates about a point between the CoM of the payload and the CoM of the leg, referred to as the center of percussion.

line in figure 39. An IP-leg mass of $m = 0.2\,\mathrm{kg}$ and a payload mass of $M_4 = 419\,\mathrm{kg}$ lead to a high frequency isolation of

$$\beta_h = 7.9 \times 10^{-5} \quad . \tag{47}$$

In reality a much lower isolation value is achieved (compare to [24]), probably due to the inhomogeneous mass distribution of the IP-leg. This explains the need of CoP tuning, discussed in section 7.1.5.

The corner frequency of the plateau is

$$\omega_c = \frac{\omega_o}{\sqrt{\beta_h}} \quad . \tag{48}$$

The values used in this model lead to a corner frequency of

$$f_c = 11.3\,\mathrm{Hz} \quad . \tag{49}$$

This is the intersection of the red dashed line and the gray dashed line in figure 39.

### 7.1.4 *The center of percussion effect*

As we have seen in the previous section, the CoP effect limits the isolation performance of massive harmonic oscillators such as the IP-leg or the GAS-filter (see section 10.2.3) at high frequencies.

A simple way to understand the CoP effect is the picture of a simple, two-dimensional, rigid beam which can rotate about a pivot point (see figure 40 and [133]). The beam has a mass $m$, a length $l$ and the pivot point's distance to the CoM is $a$. A force $F_p$ acting perpendicular to the beam through the pivot point causes the CoM to move with the velocity $v_{CoM}$. This force can be written as

$$F_p = m\dot{v}_{CoM} \ . \tag{50}$$

Due to the beam's inertia, the force also causes a rotation of the beam. The corresponding torque with respect to the CoM is

$$\tau = F_p a = I\dot{\omega}_{CoM} \ , \tag{51}$$

where I is the moment of inertia about the CoM and $\omega_{CoM}$ is the angular velocity. If the force would act on the CoM, the beam would only translate, if it would act far away from the CoM the beam would mainly rotate around its CoM.

The position on the beam, where the translational and the rotational velocity cancel each other is referred to as the center of percussion which is located at a distance $b$ from the CoM[1]. It can be obtained by deriving the velocity in each distance $z$ from the CoM. It is the deviation of the translational velocity $v_{CoM}$ and the velocity induced by the rotation around the CoM $v_{rot}$

$$\begin{aligned} v_{CoM} &= \frac{1}{m}\int F_p dt \\ v_{rot} &= \omega_{CoM} z = \frac{az}{I}\int F_p dt \\ v_z &= \left(\frac{az}{I} - \frac{1}{m}\right)\int F_p dt \ . \end{aligned} \tag{52}$$

The CoP is at the position $b$ at which the velocity $v_z$ equals zero

$$b = \frac{I}{ma} \ . \tag{53}$$

1 In the literature often the point where the external force is acting on the body is called CoP. Since the two points are interchangeable and here the point where the external force acts are fixed, and the force-free point is depended on the given parameters, the latter point is called CoP

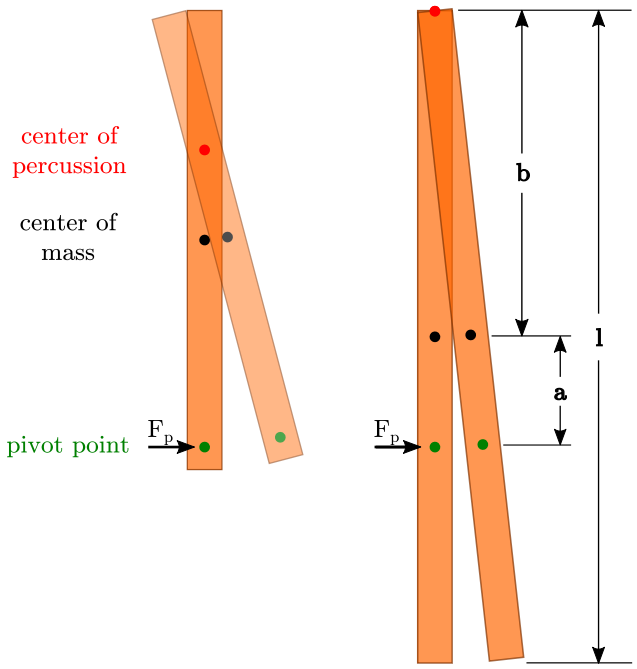


**Figure 40:** Illustration of the center of percussion effect: A rigid beam is fixed in a horizontally displaceable pivot point (green). When a horizontal force acts on this pivot point the beams reaction can be described by two motions: the CoM translates horizontally and, due to the Inertia of the beam, rotates about the CoM. Those two motions cancel each other in the CoP (red). The CoP can be shifted upwards by extending the beam beneath the pivot point. The CoP tuner of the GAS-filters and the IP-legs are working similarly.

In the case of the IP-leg, the CoP should be shifted to the top end of the beam, while the pivot point remains in position. For a beam with uniform mass distribution, the mass density is $\rho = m/l$. That results in a moment of inertia of $I = ml^2/12$. In order to shift the CoP to the top end of the beam, while keeping the distance $R$ between the pivot point and the beam's top, the beam can be extended beneath the pivot point as shown in figure 40. The required beam length is

$$l_t = \frac{3}{2}R \ . \tag{54}$$

If the force acting on the beam causes a horizontal, high frequency, the sinusoidal motion of the pivot point, then, in first order, the beam is rotating about the CoP. This decouples the pivot point motion from the CoP motion.

In terms of the IP-leg, the shifting of the center of percussion can certainly be solved more elegantly by changing the mass distribution of the leg, instead of just increasing the length.

### 7.1.5 *Center of percussion tuning for the IP-legs*

| Parameter | Value | Description |
|---|---|---|
| $M_{cw}$ | variable | counter weight mass |
| $m_{bell}$ | 0.45 kg | bell mass |
| $l_{bell}$ | 0.172 m | height of the bell |
| $l_{b1}$ | 0.1115 m | distance from pivot point of the IP-leg to counter weight |
| $l_{b2}$ | 0.062 m | distance from pivot point of the IP-leg to effective CoM of the bell |
| $m_{b2}$ | 0.117 kg | effective mass of the bell |
| $m^*$ | 0.236 kg | effective mass of the leg |
| $I_{bell}$ | $1.8 \times 10^{-3}$ kg m$^2$ | moment of inertia of the bell |
| $x_{cw}, z_{cw}$ | | position of the counter weight's center of mass |
| $x_{bell}, z_{bell}$ | | position of the bell's CoM |

**Table 7:** center of percussion tuning parameters. (compare to figure 42)

As previously described, the isolation performance at high frequencies can be improved by modifying the mass distribution of the oscillator and shifting the CoM closer to the suspension point, thus, lowering $|\beta_h|$. In the case of the IP-legs, this is done by adding mass below the pivot point (i.e. the lower flexure) of the leg on a bell-shaped structure (see figure 44). The counter weight can be adjusted in increments of 137 g.

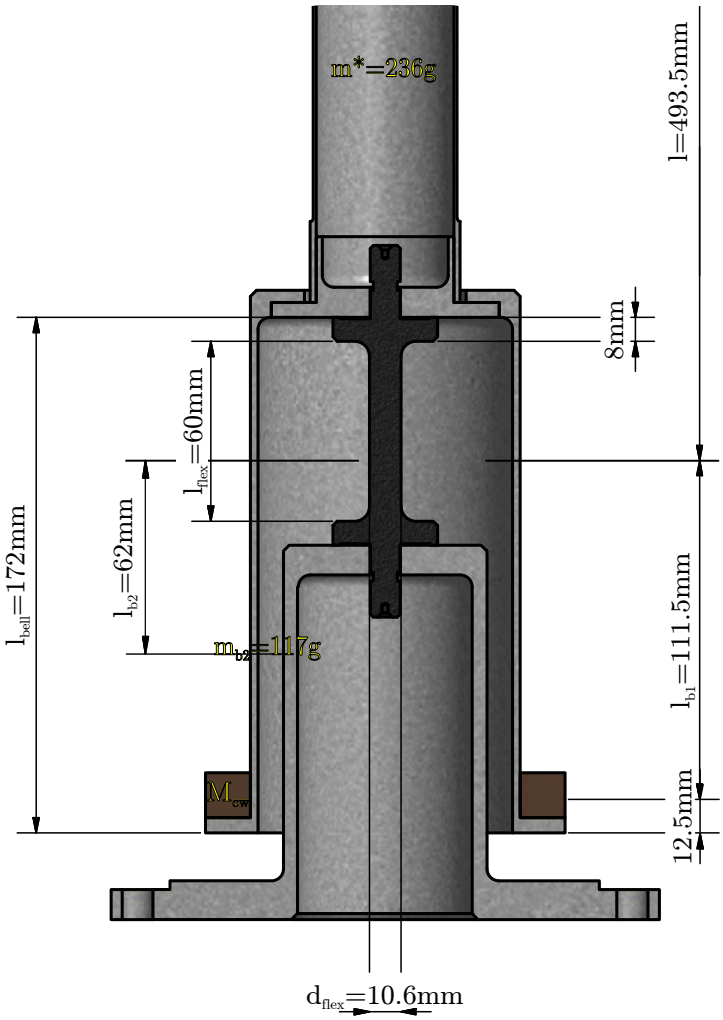


**Figure 41:** Geometry and dimension of the CoP tuning structure. This figure shows the lower part of the IP-leg (compare to figure 44). Illustrated are the dimensions used in the simplified two-dimensional IP-leg model. These unintuitively appearing dimensions $(l, l_{b1}, l_{b1})$ and masses $(m^*, m_{b2})$ are chosen with respect to the IP-leg's pivot point, which is located at $\frac{1}{3}$ of the flexure height.

Adding the CoP tuning structure to the IP-leg model expands the potential and the kinetic energy in equation 35 by four terms

$$\begin{aligned} K_{cw} &= \frac{1}{2} M_{cw} (\dot{x}_{cw}^2 + \dot{z}_{cw}^2) \\ K_{bell} &= \frac{1}{2} m_{b2} (\dot{x}_{bell}^2 + \dot{z}_{bell}^2) + \frac{1}{2} I_{bell} \dot{\varphi}^2 \\ &\text{and} \\ U_{cw} &= M_{cw} g z_{cw} \\ U_{bell} &= m_{b2} g z_{bell} \end{aligned} \tag{55}$$

with the constrains

$$\begin{aligned}
x_{cw} &= x_g - \frac{l_{bell} - \frac{2}{3}l_{flex} - (8+12.5)\times 10^{-3}\,m}{l}(x - x_g) \\
&= \left(1 + \frac{l_{b1}}{l}\right) x_g - \frac{l_{b1}}{l} x \\
x_{bell} &= x_g - \frac{l_{bell} - \frac{2}{3}l_{flex} - 8\times 10^{-3}\,m}{2l}(x - x_g) \\
&= \left(1 + \frac{l_{b2}}{l}\right) x_g - \frac{l_{b2}}{l} x \\
z_{cw} &= (l_{bell} - \frac{2}{3}l_{flex} - (8+12.5)\times 10^{-3}\,m)\cos\varphi \approx l_{b1}\cos\left(\frac{x - x_g}{l}\right) \\
z_{bell} &= \frac{1}{2}(l_{bell} - \frac{2}{3}l_{flex} - 8\times 10^{-3}\,m)\cos\varphi \approx l_{b2}\cos\left(\frac{x - x_g}{l}\right) \quad .
\end{aligned} \tag{56}$$

All parameters can be found in table 12 and figure 41. The lengths $l_{b1}$ and $l_{b2}$ are taking in to account, that the bell is not connected to the leg at the pivot point, but $\frac{2}{3}l_{flex} + 8\times 10^{-3}\,m$ above, due to geometrical restrictions. $l_{b1}$ is the length from the IP-leg's pivot point to the CoM of the counter weights and $l_{b1}$ measures the distance between the pivot point and the CoM of the reduced bell. The corresponding masses are derived from the ratio of the lengths with

$$\begin{aligned}
m_{b2} &= \frac{2l_{b2}}{l_{bell}} m_{bell} \approx 0.117kg \\
&\text{and} \\
m^* &= m + m_{bell} - m_{b2} \approx 0.236kg \quad ,
\end{aligned} \tag{57}$$

where $m^*$ is the corrected mass of the leg.

The equation of motion following equations 38, 39 and 55 is modified to be

$$\begin{aligned}
&\left(M + \frac{m^*}{4} + \frac{I}{l^2} + M_{cw}\left(\frac{l_{b1}}{l}\right)^2 + m_{b2}\left(\frac{l_{b2}}{l}\right)^2 + \frac{I_{bell}}{l^2}\right)\ddot{x} \\
&+ \left(\frac{m^*}{4} - \frac{I}{l^2} - M_{cw}\frac{l_{b1}}{l}\left(1 + \frac{l_{b1}}{l}\right) - m_{b2}\frac{l_{b2}}{l}\left(1 + \frac{l_{b2}}{l}\right) - \frac{I_{bell}}{l^2}\right)\ddot{x}_g \\
&= -\left(\frac{\kappa}{l^2} - \frac{g}{l}\left(M + \frac{m^*}{2}\right) - M_{cw}g\frac{l_{b1}}{l^2} - m_{b2}g\frac{l_{b2}}{l^2}\right)(x - x_g) \quad .
\end{aligned} \tag{58}$$

Analogous to section 7.1.3 this leads to a transmissibility function

$$T_{cw} = \frac{\omega_n^{cw\,2} + \beta_h^{cw}\omega^2}{\omega_n^{cw\,2} - \omega^2} \quad , \tag{59}$$

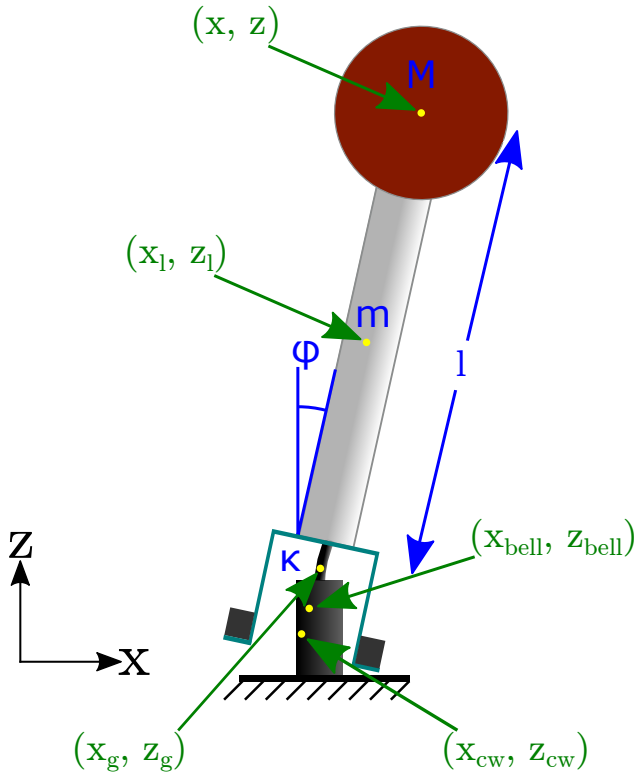


**Figure 42:** Illustration of the IP-leg with CoP tuner for the two-dimensional analytical model. The locations of the Coordinates of the single IP-leg components (payload, leg, CoP tuning bell, counter weights) and the ground are illustrated as yellow dots.

where the parameters $\omega_n^{cw}$ and $\beta_h^{cw}$ are dependent on the CoP tuning with

$$\omega_n^{cw} = \sqrt{\frac{k_{eff}^{cw}}{M_{eff}^{cw}}} \,, \tag{60}$$

$$M_{eff}^{cw} = M + \frac{m^*}{4} + \frac{I + I_{bell}}{l^2} + M_{cw}\left(\frac{l_{b1}}{l}\right)^2 + m_{b2}\left(\frac{l_{b2}}{l}\right)^2 \,, \tag{61}$$

$$k_{eff}^{cw} = \frac{\kappa}{l^2} - \frac{g}{l}\left(M + \frac{m^*}{2} - M_{cw}\frac{l_{b1}}{l} - m_{b2}\frac{l_{b2}}{l}\right) \tag{62}$$

and

$$\begin{aligned}\beta_h^{cw} = \frac{1}{M_{eff}^{cw}}\left(\frac{m^*}{4} - \frac{I + I_{bell}}{l^2} - M_{cw}\frac{l_{b1}}{l}\left(1 + \frac{l_{b1}}{l}\right)\right) \\ - \frac{1}{M_{eff}^{cw}}\left(m_{b2}\frac{l_{b2}}{l}\left(1 + \frac{l_{b2}}{l}\right)\right) \,.\end{aligned} \tag{63}$$

The fundamental resonance frequency is dominated by the payload mass, and $\omega_n^{cw} \approx \omega_n$, since the payload mass is usually much larger than the bell mass, the counter weight mass and the leg mass. The CoP plateau's level $\beta_h^{cw}$, however, is strongly dependent on the bell and the counter weight mass.[2]

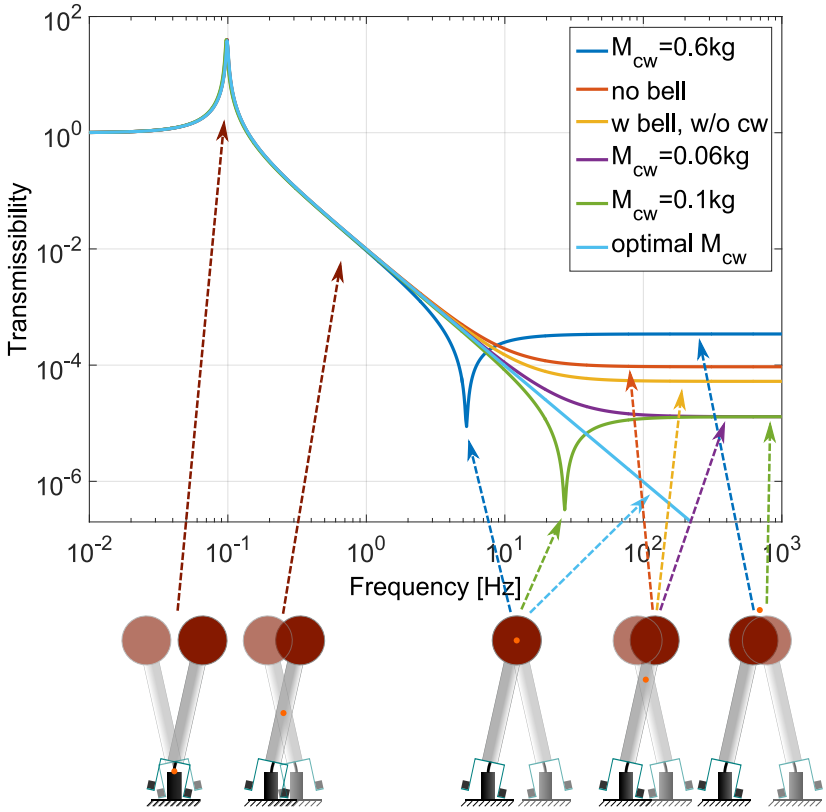


**Figure 43:** Amplitude of the transmissibility function of an IP-leg with CoP tuning (equation 59). The transmissibility is plotted for different tuning settings: Without any CoP tuning (red), this curve is identical with the transmissibility in figure 39. By attaching the 0.45 kg bell to the IP-leg, the CoP plateau decreases to $\beta_h = 5.3 \times 10^{-5}$ (yellow). These systems are both undercompensated. The ideal tuning is achieved with a counter weight mass of approximately $79.6 \times 10^{-3}$ kg (light blue). Examples of good realistic tunings are shown in green and purple. A CoP plateau height of $1.3 \times 10^{-5}$ is achieved with counter weight masses of 0.06 kg and 0.1 kg. A strongly overcompensated system is shown in blue. The drawings beneath the plot depict the CoR (orange dot) of the IP-leg at different frequencies. Note that the amplitude of the IP-leg's payload is depicted equally for all frequencies for the sake of visualization.

2 The values in table 12 and figure 43 and the equations presented in this section vary from those shown in ref. [24] or [129]. That is because here the IP-leg length $l$ is measured from the pivot point in the lower flexure to the upper flexure whereas in the literature the leg length was assumed to be the length of the aluminum tube. The corresponding change in the length of the CoP tuner and mass ratios has a noticeable influence on the horizontal stiffness and the transmissibility function.

Figure 43 shows the amplitude and phase of the transmissibility function for different counter weight masses, including two undercompensated cases, the ideal tuning and three plots of an overcompensated system. In the latter case, the amplitude of the transmissibility shows an antiresonance between the resonance frequency and the CoP plateau. As depicted in figure 43, this behavior can be explained by regarding the z-position of the point the IP-leg is rotating around (here named center of rotation (CoR)) as a function of the frequency. For frequencies $f << f_0$ the payload is moving in phase with the ground and the amplitudes are approximately equal. In this case, the CoR is far below the lower flexure. When the frequency is rising towards the resonance frequency in an underdamped system the payload amplitude is much larger than the ground motion. Thus, for $f = f_0$ the CoR is slightly below the pivot point in the flexure. The CoR converges against the CoP at higher frequencies. In an undercompensated system the CoP is below the payload and the ideally tuned CoP coincides with the CoM of the payload. However, in the case of an overcompensated system, the CoP is above the payload, which means, that, at a certain frequency, the CoR coincides with the payload's CoM. At this frequency, the system is strongly decoupled from the ground motion and the transmissibility forms a notch before it converges against $|\beta_h|$. The notch frequency can be derived from equation 59 and is

$$\omega_{notch} = \frac{\omega_0^{cw}}{\sqrt{-\beta_h^{cw}}} \ . \tag{64}$$

Figure 43 illustrates that the CoP tuning structure itself already causes a good isolation of $|\beta_h| = 5.3 \times 10^{-5}$. As shown above, for an undercompensated system the CoP constant is $\beta_h > 0$, for an overcompensated system it is $\beta_h < 0$ and $\beta_h = 0$ is the ideal tuning. The ideal tuning mass follows as

$$M_{cw}^{ideal} = \frac{l^2 m^* - 6 m_{b2}\left(l_{b2} l + \frac{4}{3} l_{b2}^2\right)}{6 l_{b1}(l + l_{b1})} \approx 79.6 \times 10^{-3}\,\mathrm{kg} \ , \tag{65}$$

where the bell's moment of inertia is approximated to be $I_{bell} \approx \frac{m_{b2} l_{b2}^2}{3}$. Since the ideal counter weight mass $M_{cw}^{ideal}$ is relatively low, the wall thickness of the improved IP-legs for the third AEI-SAS unit is chosen to be thicker. This increases their vertical stiffness. The higher weight can be compensated with a increase in counter weight (see section 13.3).

### 7.1.6 *Geometry of the AEI-SAS's IP-legs*

The geometry of the IP-legs is shown in a CAD drawing in figure 44. The upper and lower flexure is made from Maraging C-250 steel (Marval 18 from [134]). The material was chosen because it combines very high strength (1.94 GPa ultimate tensile strength), very low creep, and a low

loss angle, due to precipitation hardening, a technique to artificially age the steel [24, 68, 69]. The lower flexure is bolted to a foot, which is directly connected to the baseplate of the AEI-SAS. On the upper end, the flexure is bolted to an adapter piece which is carrying the CoP tuning bell and the leg itself a 438 mm wide and 48 mm thick aluminum tube. It is designed to be much stiffer than the lower flexure in the horizontal direction and at the same time lightweight. This is probably a relict from earlier IP-leg designs since the CoP tuning structure could compensate for heavier legs, as shown in section 7.1.5 and 13.3.

The spring-box is suspended from the top of the aluminum tube by the thin upper flexures. Its contribution to the horizontal stiffness of the IP-leg can be neglected and it is designed to serve as a joint between the leg and the horizontal stage. As discussed in section 11.3.1, the upper flexure is relatively soft in the vertical direction, which leads to unwanted low frequency vertical spring-box modes. The adapter part between the upper flexure and the spring-box is a bell-shaped aluminum structure. On its inside, it supports a set of magnets which reduce the amplitude of higher order IP-leg body modes via eddy current damping [135].

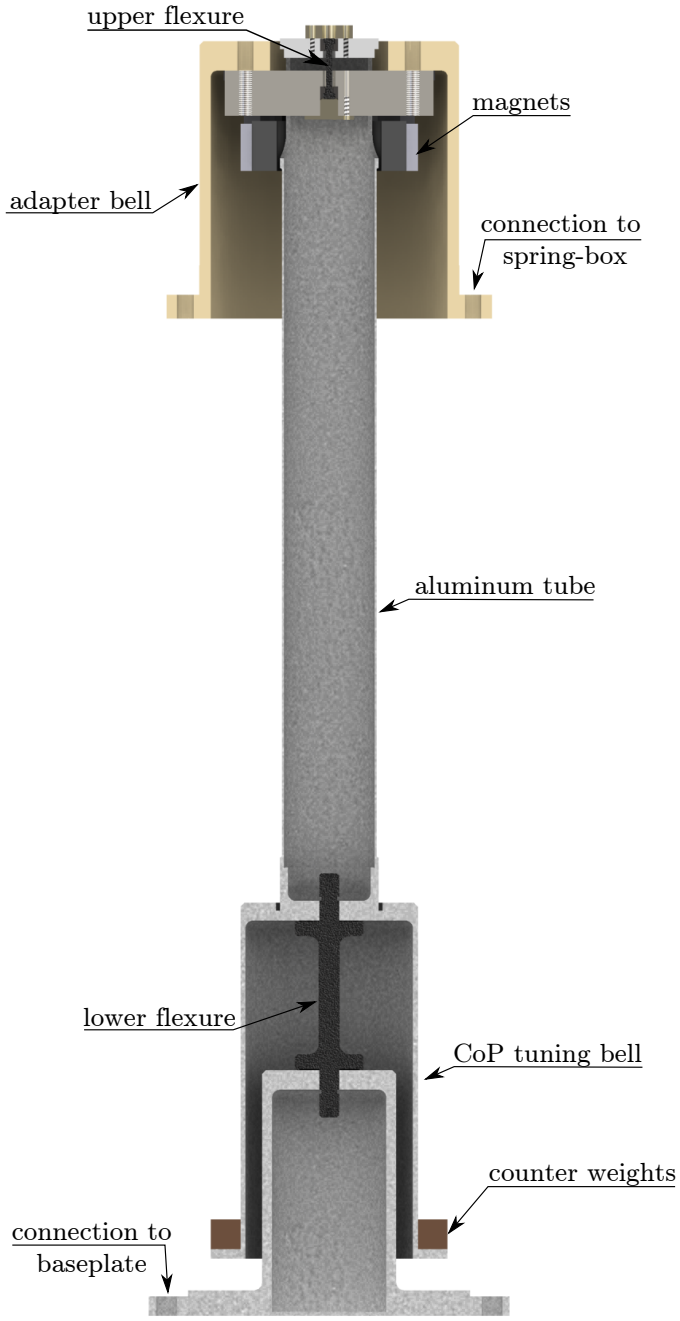


**Figure 44:** Section view of a single IP-leg. The whole leg is placed on a foot, which is the connection to the AEI-SAS baseplate. The dumbbell-shaped lower flexure is bolted on its lower end to the food and on its upper end to the bottom of the leg. The leg itself is an aluminum tube with 1 mm wall thickness. The upper flexure is suspended from a stainless steel cap on the upper end of the aluminum tube. It is a 25 mm long and 3 mm thick maraging steel cylinder with a nail head on the top and the bottom for connecting it to the neighboring parts. The whole payload and the spring-box are suspended from those three upper flexures. The upper spring-box plate is resting on the rim of the upper bell. This bell is supported by a stainless steel bar which is reaching through two windows in the aluminum tube and is suspended from the upper flexure. The upper bell serves the purpose of reducing the total height of the AEI-SAS. The lower end of the IP-leg is surrounded by the lower bell. This structure is used to tune the CoP of the IP-legs. That is achieved, by loading it with counter weights.

# 8

# THE GEOMETRIC ANTI-SPRING-FILTER

As discussed in chapter 7 the AEI-SAS's IP-legs decouple the payload from horizontal ground motion above the systems fundamental resonance frequency of about 0.1 Hz. However, not only horizontal ground

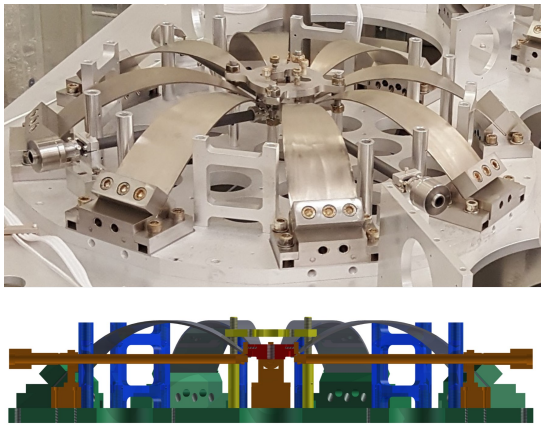

**Figure 45:** Photograph and CAD drawing of an AEI-SAS GAS-filter. The photograph shows the GAS-filter during installation. It is bolted on the lower spring-box plate and surrounded by stiffening plates. The CAD drawing shows a sectional view of the GAS-filter with the CoP compensators in brown and the stiffening posts in blue. The yellow structure in the center is for holding the keystone (red) in position during installation. It is removed when the GAS-filter is under load.

motion but also vertical ground motion couples into the interferometer signal of, for instance, gravitational wave detectors or the AEI 10 m prototype's SQL-interferometer.

Pitch and roll motion of the optical table is translated into horizontal motion of the mirror since the suspension point is far above the rotation axis [1]. Vertical motion couples into the interferometer signal due to the curved interferometer mirrors surface. The laser beams are also not necessarily perfectly perpendicular to the vertical direction, which increases the coupling. Cross coupling from pitch and roll motion to the horizontal degrees of freedom in the mechanics of the AEI-SAS itself furthermore limits the isolation performance (compare to section 9). Hence, low frequency attenuation of vertical, pitch and roll ground motion is crucial for high precision experiments.

The AEI-SAS's vertical, pitch and roll isolation relies on three geometric anti-spring (GAS) filters. As discussed in section 5.1, they are

1 The suspension cages are about half a meter high, mounted on top of the optical table (see figure 16)

housed in the spring-box, which is suspended from the three IP-legs (see figure 20). A photograph and a CAD-drawing of an AEI-SAS GAS-filter is shown in figure 45.

Whereas a regular vertical spring is elongated by about 5 m to achieve a resonance frequency of 300 mHz, GAS-filters are very compact in all three dimensions and can be tuned down to about 200 mHz. Furthermore, they are able to support a high payload mass and can be made from ultra-high vacuum compatible materials.

The feasibility of GAS-filters as vertical low frequency seismic noise attenuators was first studied by Bertolini et al. [52] and a first GAS-filter prototype was tested by Cella et al. [136]. Though the design was improved with time the basic working principle remained and GAS-filters are nowadays employed in many gravitational wave detectors in different configurations, as discussed in chapter 3. Furthermore, GAS-filters are also used in non-isolation applications such as nano-g MEMS accelerometers [137]. Outside the field of gravitational wave physics, high precision measurements require strong attenuation of vertical seismic motion at low frequencies, too. GAS-filter based isolation systems serve this purpose, for instance, to isolate atom interferometers [26, 138].

In this chapter, the working principles of GAS-filters are discussed briefly. A more detailed discussion of the matter can be found in ref. [52] or [79]. Furthermore, a short summary and discussion of recently occurring incidents of GAS-filter blade cracking in systems similar to the AEI-SAS are discussed. Hydrogen embitterment is believed to cause those material failures [139].

## 8.1 WORKING PRINCIPLE OF THE GAS-FILTER

The basic concept of a GAS-filter is to use regular blade springs to support the payload mass and reduce the resonance frequency by introducing a force acting against the direction of the regular spring force. This principle was already used in Virgo's magnetic anti-spring filters, where a magnetic force is counteracting the blade's spring force if the payload deflects from the equilibrium position [48, 140]. Magnetic anti-springs are very effective but require quite complex mechanics. They are strongly sensitive to temperature changes since they are made from components with different thermal behaviors. Furthermore, they require cumbersome tuning mechanisms and may induce unwanted couplings to external electromagnetic fields [52].

The GAS-filter's anti-spring force does not result from magnetism but from a geometrical arrangement of blade springs which compresses two opposing blades against each other. This introduces a force which is counteracting the regular spring force. A linearized model of this anti-spring effect is discussed in the following section.

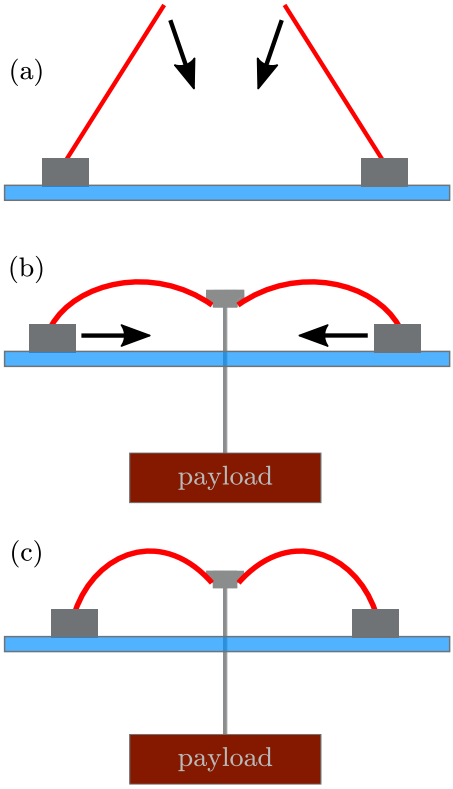


**Figure 46:** Simplified GAS-filter assembly sketch.
(a) The straight GAS-filter blades (red) are clamped to feet which are mounted on the baseplate. The blade tips are bent down to the center.
(b) The tips are bolted to the keystone and a dummy payload of about 300 kg is suspended from it.
(c) By shifting the blade feet inwards the blades are compressed against each other. This introduces an anti-spring force and lowers the GAS-filters resonance frequency (compare to figure 47).

The blades are manufactured flat and bent under load like a fishing rod. Figure 46 depicts the process of how a GAS-filter is assembled. This helps to understand the concept of the system:

- The blades are bolted to the rim of the filter's baseplate.
- They are bent to a central keystone, which is interconnecting all eight blades.
- For the assembly and tuning of the GAS-filter, a dummy mass is suspended from this keystone (later the keystone supports the AEI-SAS's payload from below). This mass keeps the keystone at its working point [2] and the blades bent.
- The vertical stiffness in this working point is now lowered by compressing the blades against each other. The assembly of a GAS-filter is described in more detail in the appendix C, the GAS-filter tuning is described in section 10.2.

2 Here the distinction is made between the working point and the equilibrium position. The equilibrium position is the vertical keystone position in which the vertical GAS-filter force and gravity cancel each other. This position is naturally a function of the payload mass (see section 8.1.2). The working point is the particular equilibrium position in which the horizontal springs from the linearized GAS-filter model have no vertical component (see section 8.1.1). This position is given determined by the geometry.

### 8.1.1 *Linearized GAS-filter model*

The principle of a GAS-filter can be understood by a simplified, linearized model. However, in order to design a GAS-filter a deeper understanding of the blade geometry and properties is necessary. An analytical model of the blades has been developed by Cella et al [80] and a detailed description of finite element analysis of the blade is discussed in ref. [95].

For the work described in this thesis, only the linear behavior of the GAS-filter around its working point is of interest. It can be described as a payload mass $m_p$ suspended from a vertical spring. Two horizontal springs are connected to the mass. They are compressed against each other [88].

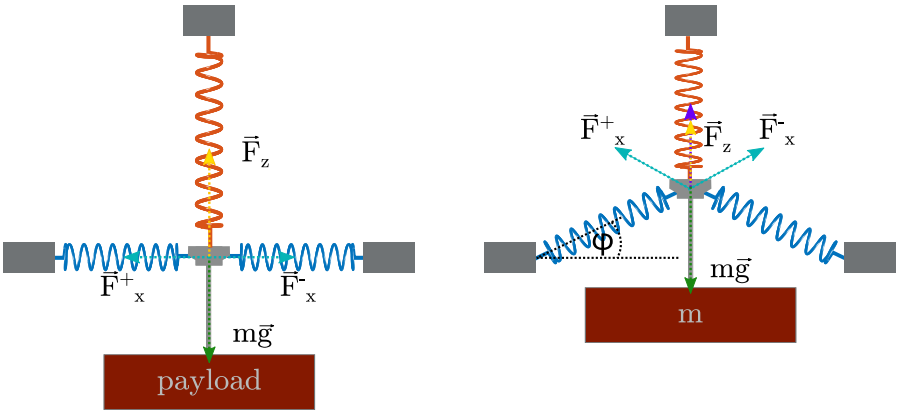


**Figure 47:** Linearized GAS-filter model sketch. The GAS-filter can be modeled as a set of springs. A vertical spring provides the restoring force $\vec{F}_z$ (yellow arrow) which counteracts the gravity force $m\vec{g}$. Two horizontal springs are compressed against each other. The resulting forces $\vec{F}_z^+$ and $\vec{F}_z^-$ (light blue arrows) cancel each other out when the payload is at its vertical working point (left drawing). If the payload is deflected vertically the formally horizontal springs force adds up to a vertical component, the anti-spring force (dark blue arrow). This force counteracts the normal spring force which is the sum of the yellow and the green arrow ($F_z - mg$). This technique theoretically lowers the effective spring constant of the system without lowering the payload mass - working point relation.
In the case in which the horizontal springs are compressed too strongly the absolute value of the anti-spring force exceeds the absolute value of the normal spring force and the system becomes unstable.

Figure 47 shows a sketch of this two dimensional linearized GAS-filter model. At the working point, where $z$ equals zero, the spring force

$$\vec{F}_z = k_z(z_{wp} - l_{oz} - z)\vec{e}_z \tag{66}$$

counteracts the gravity force $-mg$. Here $\vec{e}_z$ is the uni vector in z direction. The parameters used in this calculation are listed in table 8. In

| Parameter | Description |
|---|---|
| $\vec{F}_z$ | Vertical spring force |
| $\vec{F}_x^{\pm}$ | Horizontal spring forces |
| $k_x$ | Horizontal spring constant |
| $k_z$ | Vertical spring constant |
| $k_{eff}$ | Effective vertical GAS-filter spring constant |
| $l_{oz}$ | Vertical spring's rest length |
| $l_{ox}$ | Horizontal spring's rest length |
| $z_{wp}$ | Distance between vertical spring's suspension point and the working point |
| $x_{wp}$ | Distance between horizontal springs' suspension point and the working point i.e. length of the compressed spring. |

**Table 8:** Parameters used in the linearized GAS-filter model.

this position the two compressed springs act only horizontally and the corresponding forces equal each other out. The force of the compressed springs is

$$\vec{F}_x^{\pm} = k_x \left( l_{ox} - \frac{z}{\sin\varphi} \right) \begin{pmatrix} \pm\cos\varphi \\ \\ \sin\varphi \end{pmatrix} \quad . \tag{67}$$

The equation illustrates that if the payload is elongated from its equilibrium position this force has a vertical component. By substituting $\sin\varphi$ by $\frac{z}{\sqrt{x_{wp}^2+z^2}}$ the payload's vertical equation of motion is accordingly [3]

$$\begin{aligned} m\ddot{z} &= k_z(z_{wp} - l_{oz} - z) + k_x \left( \frac{l_{ox}}{\sqrt{z^2 + x_{wp}^2}} - 1 \right) z - mg \\ &\approx k_z(z_{wp} - l_{oz} - z) + k_x \left( \frac{l_{ox}}{x_{wp}} - 1 \right) z - mg \quad . \end{aligned} \tag{68}$$

3 Here the horizontal stiffness $k_x$ represents the combined stiffness of both horizontal springs. This way a factor 2, due to the two springs, can be omitted and the model can be generalized to more than two springs in a three dimensional GAS-filter.

With the small angle approximation $\sin\varphi \approx z/x_{wp}$ the equation of motion of a GAS-filter tuned to its working point is described (second row of equation 68).

Equation 68 shows that in first order the GAS-filter behaves as a harmonic oscillator with an effective spring constant of

$$k_{eff} = k_z - k_x \left( \frac{l_{ox}}{x_{wp}} - 1 \right) \quad . \tag{69}$$

Since the blades are compressed, $l_{ox} \geqslant x_{wp}$. Thus the second summand of equation 69 is positive and $k_{eff}$ is reduced by increasing blade compression. This way the resonance frequency can theoretically be reduced down to a point where the anti-spring stiffness component is equal to or exceeds $k_z$ and $k_{eff}$ equals or is less than zero (In reality material properties limit the resonance frequency tuning).

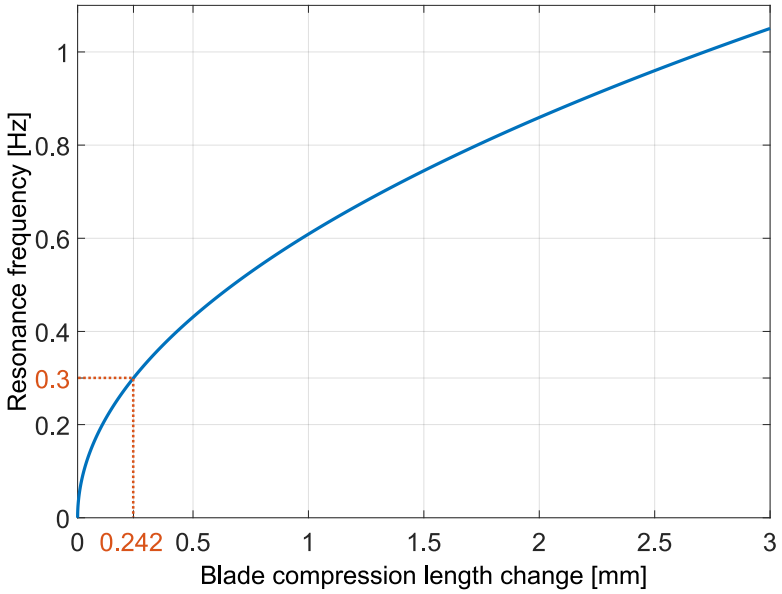


**Figure 48:** Resonance frequency tuning of a GAS-filter. This plot illustrates the compression accuracy necessary to tune the GAS-filters resonance. For the desired $f_0 = 0.3\,\text{Hz}$ the blades are only $0.2373\,\text{mm}$ less compressed than in the state where the GAS-filter is getting unstable. Furthermore, the plot demonstrates that a GAS-filter tuned to low frequencies is strongly susceptible to compression changes as they can be obtained by deformation of the baseplate or fluctuating temperature, as discussed below. The values used for this simulation are shown in table 9.

For the values of the horizontal and vertical stiffness and the vertical spring's rest length, shown in table 9, the critical tuning, causing instability of the system, is achieved at a compressed blade length of $x^c_{wp} = 0.2498\,\text{m}$. Figure 48 illustrates the GAS-filter resonance frequency tuning. At a compression length of $x^c_{wp} + 0.242 \times 10^{-3}\,\text{m}$ the desired resonance frequency of $f_0 = 0.3\,\text{Hz}$ is achieved.

| Parameter | Value |
|---|---|
| $k_x$ | $1.00 \times 10^6\,\mathrm{N/m}$ |
| $k_z$ | $1.01 \times 10^5\,\mathrm{N/m}$ |
| $m$ | $300\,\mathrm{kg}$ |
| $l_{ox}$ | $0.274\,\mathrm{m}$ |
| $x_{wp}$ | $0.249\,\mathrm{m}$ |

**Table 9:** Simplified GAS-filter model values. The numbers chosen for the here presented model are estimates obtained from rough measurements. The distances $l_{ox}$ and $x_{wp}$ were measured in a realistic GAS-filter, tuned to 0.3 Hz. The horizontal stiffness was obtained from measurements of the horizontal spring-box modes. $k_z$ is estimated from these values.

### 8.1.2 *Mass dependance on the equilibrium position*

In a regular spring-mass system the equilibrium position is directly proportional to the payload mass. In the linearized GAS-filter model, the vertical spring alone supports the payload if it is positioned at the working point. However, if it is deflected from this position also the horizontal springs support or push the payload and therefore influence the system's equilibrium position.

When tuning the GAS-filter to the desired resonance frequency its behavior in terms of a variable payload mass is important. Furthermore, this behavior is of interest when the AEI-SAS is equipped with optics and they need to be leveled with respect to each other.

The influence of the payload mass on the equilibrium position can be derived from equation 68. The payload mass is substituted by $m = m_0 + \Delta m$, where $m_0$ is the payload mass at the working point and $\Delta m$ is the change of payload mass. The distance between the vertical spring's suspension point and the working point is then

$$z_{wp} = \frac{m_0 g}{k_z} + l_{oz} \ . \tag{70}$$

This leads to the equilibrium point equation

$$\Delta m(z) = \left[ k_x \left( \frac{l_{ox}}{\sqrt{x_{wp}^2 + z^2}} - 1 \right) - k_z \right] \frac{z}{g} \ . \tag{71}$$

Figure 49 illustrates equation 71 for different compression rates

$$K = 1 - \frac{x_{wp}}{l_{ox}} \ . \tag{72}$$

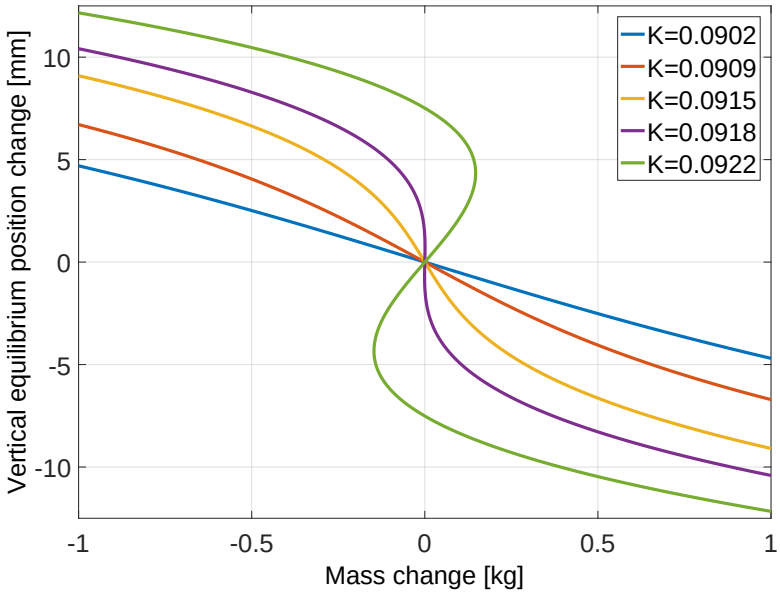


**Figure 49:** Vertical equilibrium position change as a function of the payload mass change. The figure illustrates equitation 71 for three stable (blue, red and yellow) and two instable (purple and green) GAS-filter blade compression states. The compression $K = 0.0918$ corresponds to a critically compressed GAS-filter with a resonance frequency of 0 Hz, thus, the purple curve is vertical in a small range around the working point. The red curve represents the desired 0.3 Hz resonance frequency GAS-filter, with a relatively wide linear dynamic range. The values used for this simulation are shown in table 9.

A stable GAS-filter (blue, red and yellow curve) has a relatively large linear range around the working point. This is favored in the AEI-SAS since it simplifies inter-table alignment. For the critical compression of $K = 0.0918$ (this is where the GAS-filters resonance frequency is 0 Hz) the equilibrium position-mass curve is approximately vertical around the working point. The green curve represents the instabel, overcompressed GAS-filter state.

### 8.1.3 *Resonance frequency dependence on the equilibrium position*

In practice, the vertical equilibrium position of the payload is not necessarily kept at the working point, since the height of all three AEI-SAS units need to be adjusted with respect to each other. Furthermore, an experimental setup might require macroscopic position tuning in the vertical direction.

As shown above, variations of the payload mass influence the equilibrium position linearly only in a defined range around the GAS-filter's working point. This range decreases with higher blade compression i.e. with lower resonance frequency at the working point.

The resonance frequency of a simple harmonic oscillator decreases as the equilibrium position is lowered since it is inversely proportional to the square root of the payload mass, which itself is proportional to the oscillator spring's deflection. However, the GAS-filter behaves differently since the blade compression changes if the payload is displaced away from the working point.

The resonance frequency's dependence on the equilibrium position can be estimated by

$$f_0(z) = \frac{1}{2\pi}\sqrt{\frac{k_{eff}(z)}{m_0 + \Delta m(z)}} \ . \tag{73}$$

Here $k_{eff}(z)$ is the equilibrium point dependent effective spring constant, which can be written as the derivative of the vertical force acting on the payload

$$\begin{aligned} k_{eff}(z) &= \frac{\partial F_z}{\partial z} \\ &= k_z - k_x \left[ \left( \frac{l_{ox}}{\sqrt{x_{wp}^2 + z^2}} - 1 \right) + \frac{l_{ox} z^2}{\left(x_{wp}^2 + z^2\right)^{\frac{3}{2}}} \right] \ . \end{aligned} \tag{74}$$

Equation 73 is illustrated in figure 50 for the same compression rates shown in figure 49. If the keystone is moved below or above the working point the resonance frequency rises since the compression of the blades is reduced. By this means a GAS-filter tuned slightly to instability at the working point (purple and green line) has a positive resonance frequency when mass is reduced or added and thereby the equilibrium position increases or decreases.

### 8.1.4 *Temperature influence*

The working point stability of the GAS-filter is crucial for high precision experiments, especially if these include inter-table measurements, as it is the case for the single arm test, the SQL interferometer, and the frequency reference cavity. Small dynamic changes of the payload's vertical position can be counteracted by the vertical actuators. An estimate of the GAS-filter's thermal stability is necessary to evaluate actuator force and temperature stability requirements.

#### 8.1.4.1 *Modeling the temperature influence*

Temperature influences the GAS-filters equilibrium position in three ways [52, 79]:

- The maraging steel's Young's modulus changes with temperature, which influences the blades spring-constant linearly.

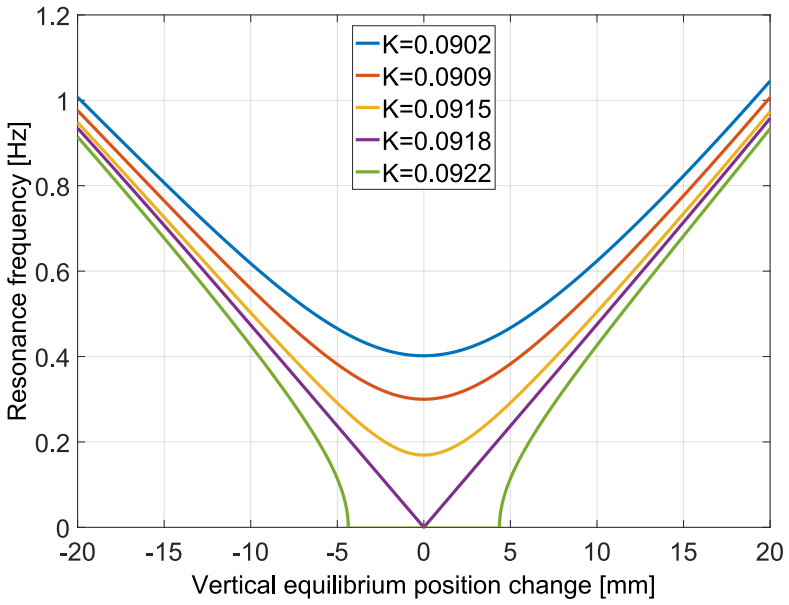


**Figure 50:** Resonance frequency dependence on the equilibrium position. The plots illustrate equation 73 for different blade compressions K. The equilibrium position change described in this simulation is caused by payload mass variations, as it is shown in figure 49. The lowest resonance is achieved at the vertical working point. For a lower or higher payload position the resonance frequency rises. The curves are slightly asymmetric and have a higher slope at positive payload positions.

- The length of the blades changes with temperature, which changes the compression rate.
- The GAS-filter's baseplate dimensions are influenced by temperature. That also influences the blade compression. It counteracts the blade length change.

From equation 69, one can derive that the variation of the effective spring constant is

$$\frac{dk_{eff}}{dT} = \frac{dk_z}{dT} - \left(\frac{l_{ox}}{x_{wp}} - 1\right)\frac{dk_x}{dT} - \frac{k_x}{x_{wp}}\frac{dl_{ox}}{dT} + \frac{k_x l_{ox}}{x_{wp}^2}\frac{dx_{wp}}{dT} \quad , \tag{75}$$

where $d/dT$ is the temperature derivative.

For small temperature changes around room temperature, Young's modulus change and the material expansion are linearly approximated. In the following, $T$ is defined as the difference from room temperature.

The horizontal and vertical stiffness written as a function of the temperature is

$$k_i(T) = k_i(0)(1 + \Delta_E T) \quad . \tag{76}$$

The temperature dependent blade and baseplate length are accordingly

$$l_{ox}(T) = l_{ox}(0)(1 + \Delta_m T) \tag{77}$$

and

$$x_{wp}(T) = x_{wp}(0)(1 + \Delta_a T) \ . \tag{78}$$

The thermal correction coefficients $\Delta_m$, $\Delta_a$ and $\Delta_E$ are listed in table 10. The resulting linearized effective spring constant change for small temperature variations is

$$\frac{dk_{eff}}{dT} = \left(k_z + k_x - \frac{k_x l_{ox}}{x_{wp}}\right)\Delta_E - \frac{k_x l_{ox}}{x_{wp}}(\Delta_m - \Delta_a) \approx 15\,\frac{N}{mK} \ . \tag{79}$$

For a resonance frequency of 300 mHz the corresponding frequency change of about $2\,\mathrm{mHzK}^{-1}$ is negligible, especially since the lab temperature changes only by a fraction of 1 K during experiments.

| Parameter | Value | Description |
|---|---|---|
| $\Delta_a$ | $2.3 \times 10^{-5}\,\mathrm{K}^{-1}$ | Thermal expansion coefficient of aluminum [141] |
| $\Delta_m$ | $1 \times 10^{-5}\,\mathrm{K}^{-1}$ | Thermal expansion coefficient of maraging steel [142] |
| $\Delta_E$ | $2.54 \times 10^{-4}\,\mathrm{K}^{-1}$ | Relative change of Young's modulus of maraging steel with respect to temperature [143, 144] |

**Table 10:** Thermal correction coefficients.

More relevant for the experimental work at the AEI 10 m prototype than the resonance frequency change is the temperature-induced vertical position and vertical tilt change of the payload since this could cause a severe mismatch in inter-table measurements. The position of an idealized GAS-filter, tuned to its working point, is independent of the compression rate K. Thus, it is independent of the thermal expansion of baseplate and blade (compare to figure49). This can be deduced from the GAS-filter's equation of motion (equation 68). The equilibrium position for small temperature changes is given by

$$0 = mg\Delta_E T - k_z(T)z + k_x(T)\left(\frac{l_{ox}(T)}{x_{wp}(T)} - 1\right)z \ , \tag{80}$$

where the vertical working point position is substituted by

$$z_{wp} = \frac{mg}{k_z(0)} + l_{ox} \ . \tag{81}$$

To first order the position change is accordingly

$$\begin{aligned} \frac{dz}{dT} &= \frac{mg\Delta_E}{k_x(0)\left(\frac{l_{ox}(0)}{x_{wp}(0)} - 1\right) - k_z(0)} \\ &= \frac{g\Delta_E}{\omega_0^2} \\ &\approx -6.8 \times 10^{-4} \frac{m}{K} \ , \end{aligned} \tag{82}$$

where $\omega_0$ is the fundamental GAS-filter resonance. The position is only second order dependent on the expansion coefficients of the blade and the baseplate, but depends strongly on the resonance frequency. This is the main reason why the GAS-filters in the AEI-SAS are not tuned to the lowest possible resonance frequency, but to a compromise between good low frequency isolation and usability.

#### 8.1.4.2 *Measuring the temperature influence*

The temperature influence on the GAS-filter's working point position was measured on the central and the south table, as shown in figure 51. The measurement was done after the vacuum system was evacuated and the temperature dropped due to the sudden pressure change. 8 hours of data were recorded at an approximately constant pressure, while the temperature slowly rose back to room temperature. The keystone position was measured by the vertical LVDTs, the temperature by a sensor installed in the optical table. The two AEI-SAS units were velocity-damped and AC-coupled so that the keystone position was dominated by the temperature change. Large deflections by means of the resonance were damped.

Fitting the recorded data linearly shows, that the payload's position change with temperature deviates only by 4 % (central table) and 15 % (south table) from the simplified model (equation 82); however, the individual GAS-filter's temperature drifts differ stronger from the simulation. This is due to a difference in resonance frequency tuning between the GAS-filters. In particular, the first GAS-filter of the central table differs from the others. The corresponding resonance frequency to the temperature induced position change is 265 mHz, according to equation 82. The reason for this is that when the first AEI-SAS unit was assembled, the lowest possible vertical resonance frequency was targeted. Later a more uniform tuning was favored. This reduces vertical

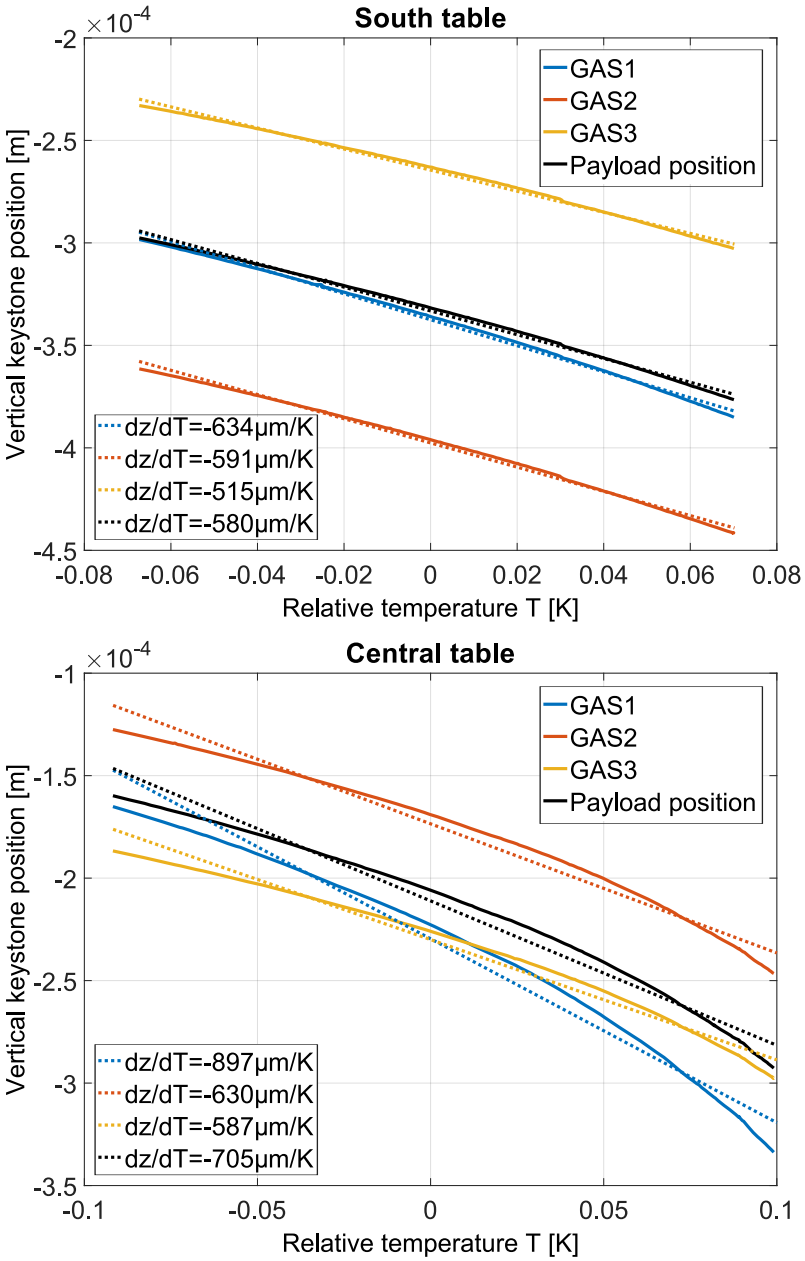


**Figure 51:** Temperature induced GAS-filter equilibrium position change. The blue, red and yellow solid lines represent the keystone position of the south (upper figure) and central (lower figure) table's three GAS-filters. In black the averaged vertical payload position is shown. The data was measured by the vertical LVDTs and temperature sensors installed in the optical tables. The dotted lines represent a linear fit (compare to equation 82).

ground motion to payload tilt coupling, since this way all three filters respond with the same displacement on the vertical ground motion.

However, the results of this measurement can be used to equalize the stiffness of the central table's GAS-filters by carefully changing the blade compression.

Whereas the south table's keystone position changes have a near-linear dependence on temperature, the central table measurement differs from the fit. A possible reason is that the initial keystone position is slightly above the ideal working point. This way the material's thermal expansion-induced reduction of the blade compression would enhance the steepness of the thermal position change.

### 8.1.5 *GAS-filter transimissibility*

As discussed above, a GAS-filter behaves like a harmonic oscillator with the spring constant $k_{eff}$ if deflections around the working point are small. In equation 68 a simplified model with a massless spring is presented. In reality, however, the GAS-filter blades have a nonnegligible mass. The corresponding moment of inertia causes the GAS-filter to oscillate at high frequencies around a stationary point between the keystone and the CoM of the blades, the CoP, as described in section 7.1.4. Thus, the transmissibility function differs at high frequencies from the one of an ideal harmonic oscillator with a massless spring. Similar to the IP-leg with finite mass described in section 7.1.3, the massive GAS-filter's transmissibility is

$$T_{GAS} = \frac{\omega_n^2 + \beta_v \omega^2}{\omega_n^2 - \omega^2} \quad . \tag{83}$$

Here $\omega_n$ is the complex natural frequency

$$\omega_n^2 = \omega_0^2(1 + i\phi) = (2\pi f_0)^2(1 + i\phi) \tag{84}$$

with the resonance frequency $f_0$ and the structural damping factor $\phi$ (see section 6.1). The CoP constant of the vertical stage $\beta_v$ is a function of the GAS-filter blade's dimensions, mass and moment of inertia. The analytical way to model and derive the CoP constant of a GAS-filter is described in detail by Stochino et al [121].

The amplitude of the modeled GAS-filter's transmissibility function (equiation 83) is identical to the one of an IP-leg, shown in figure 39 and 43. It differs from an ideal harmonic oscillator at high frequencies, where the amplitude asymptotes to $|\beta_v|$, the CoP plateau. A CoP constant $\beta_v > 0$ results in an isolation plateau starting at

$$\omega_c = \frac{\omega_o}{\sqrt{\beta_v}} \quad . \tag{85}$$

For $\beta_v < 0$ the transmissibility amplitude forms a notch before plateauing and the GAS-filter is overcompensated. The notch frequency is

$$\omega_{notch} = \frac{\omega_o}{\sqrt{-\beta_v}} \quad . \tag{86}$$

An ideal harmonic oscillator, where the transmissibility amplitude asymptotes to 0, is achieved by $\beta_v = 0$. A close to ideal tuning can be achieved by shifting the CoP of the blades to the horizontal position where they are clamped to the GAS-filter's baseplate. How this can be realized is discussed in the following.

### 8.1.6 *Center of percussion tuning for the GAS-filters*

The first generation's geometry of GAS-filters did not account for adjusting the blade's CoP [52, 136]. By modifying the geometry to a monolithic GAS-filter for the first interferometric gravitational wave detector TAMA300 the CoP plateau was improved due to a modified blade shape [79]. The introduction of CoP compensators, in literature often referred to as magic wand, allows to shift the CoP of the GAS-filter and therefore to increase high frequency isolation. These devices are an integral part of the AEI-SAS's GAS-filters (see figure 45).

The purposes of the CoP compensators is to modify the mass distribution of the GAS-filter, in order to shift the CoP in the position where the blades are clamped to the filter's baseplate. Thus the principle of the vertical CoP compensator is similar to the IP-leg's horizontal CoP tuners discussed in section 7.1.5.

The vertical CoP compensators are basically rigid, horizontally aligned rods which are pivot-mounted to the keystone and to the baseplate (the pivot-mounting is realized by thin blade springs). The outer side of the rod holds a counter mass. It is mounted on a fine pitch thread in order to allow shifting it horizontally in and outwards. Two to four of these structures are mounted on one GAS-filter. Shifting the counter masses manipulates the CoM of the spring-system and therefore allows to move the CoP close to the clamping point. If the mass is shifted too far outwards, the filter is overcompensated and the CoP constant $\beta_v$ is negative. For tuning the GAS-filter's CoP the transmissibility is measured. When it shows a notch at $\omega_{notch}$ the counter mass is moved in the direction of the keystone. If a simple plateau forms, the counter mass is moved outwards. This procedure is described in section 10.2.3.

In the AEI-SAS's original design the CoP compensators' central rods were made from aluminum. The resonances of this assembly were close to the SQL-interferometer's measurement window. Replacing these aluminum rods by very rigid and light silicon carbide tubes shifts those resonances above 300 Hz [23].

## 8.2 HYDROGEN EMBRITTLEMENT IN GAS-FILTER BLADES

During the upgrade to an advanced gravitational wave detector, GAS-filter and Superattenuator filter blades broke spontaneously at the Virgo site. These material failures were associated with hydrogen em-

brittlement. Even though the AEI-SAS GAS-filter blades have not shown any failures yet, there is the potential risk, since they are very similar to the Virgo blades in terms of geometry and manufacturing. In this section, the risk of hydrogen embrittlement in the GAS-filter blades is discussed; however, in order to obtain a full understanding of the process, further investigation is necessary.

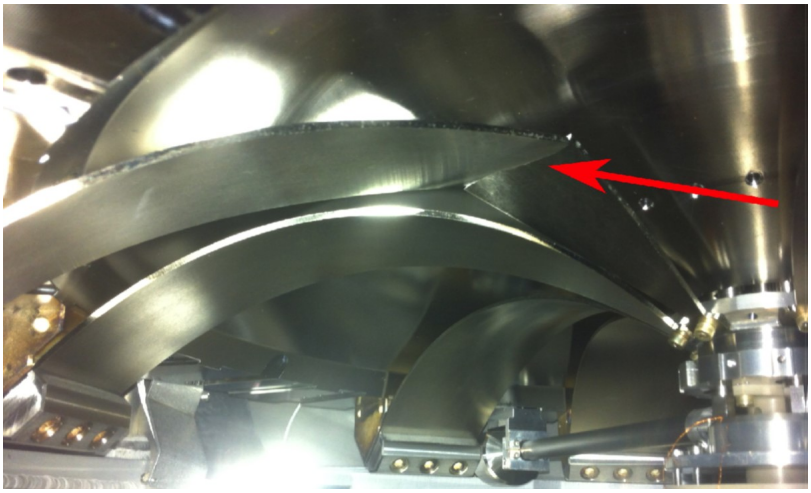

**Figure 52:** Photograph of a blade failure (indicated by the red arrow) in the intermediate filter of Advanced Virgo's SPRB MultiSAS. This figure is taken from [139].

In April 2016 it was noticed that a GAS-filter blade of the Advanced Virgo MultiSAS cracked (see figure 52). Prior to this incident many of the Superattenuator filter blades were found in poor condition or broken after 15 years in operation. All these blades operated under normal conditions before they broke and no defects were found in the nickel plating [139]. Investigations led to the assumption that hydrogen embrittlement caused these spontaneous failures. Hydrogen embrittlement occurs when atomic hydrogen diffuses through the metal surface into the material. Here the atomic hydrogen recombines to molecules and weakens the metal [145]. This process was first described in 1984 by Johnson et al. [146].

As summarized by van Heijningen [139], maraging steel samples, cut from the broken super attenuator blades were tested for their hydrogen content and the corresponding ultimate tensile strength (UTS). A significant decrease of UTS (by about 50 %) was found for maraging steel samples with a hydrogen content of more than 2.5 parts-per-million (ppm) [147]. However, the tested MultiSAS' GAS-filter blade showed a lower average value. The blade fractures in these blades can be explained by the migration of hydrogen towards highly stressed areas in the material. GAS-filter blades are loaded close to their stress limit. Thus, even though the average hydrogen concentration is below the weakening threshold it can very well be exceeded in highly stressed areas [139, 148]. The distinction between trapped and diffusible hydro-

gen needs therefore to be made. Whereas trapped hydrogen is approximately uniformly distributed over the substrate diffusible hydrogen migrates to locations of high stress, thus, is causing hydrogen embrittlement.

Even though the AEI-SAS GAS-filter blades are operating for about 7 years without any failure, the risk of hydrogen embrittlement induced fractures is obvious [149].

Measurements of the diffusible hydrogen content of a spare AEI-SAS GAS-filter blade showed an average concentration of 2.6 ppm [149]. This relatively high value might be due to a relatively thick nickel plating (14.5 µm to 40 µm), due to a production error. This might have prevented hydrogen from defusing out of the material during baking. In comparison, the Advanced LIGO maraging steel blades are coated with a nickel plating thickness of only (0.4 µm to 0.6 µm) [150]. No failures of these blades were observed so far.

This value is already in the critical regime. However, the fact that none of the AEI blades has shown any cracking until now might indicate, that a deeper understanding is necessary [149].

# 9 PASSIVE ISOLATION PERFORMANCE OF THE AEI-SAS

In part II the individual passive isolation components of the AEI-SAS, namely the IP-legs and the GAS-filters are discussed. It is shown that they behave in principle as low frequency massive harmonic oscillators. The isolation system consists of three IP-legs and three GAS-filters, which are interconnected by a complex structure. This structure has the potential to influence the isolation behavior, due to its finite stiffness, and thereby introduced unwanted oscillations. Chapter 11 discusses these internal resonances in detail.

In this chapter, the passive performance of the first two AEI-SAS units is discussed. These results do not reflect the overall isolation performance since the low frequency active isolation is excluded. It rather helps to characterize the mechanical properties of the system. A comparison to a simple massive harmonic oscillator and to a full noise model shows the degree of cross-coupling between the degrees of freedom. Due to internal resonances, the high frequency performance disagrees with the theoretical model. This is the basis and the motivation for the AEI-SAS improvements of all three AEI-SAS units and the modifications of the third AEI-SAS unit. These improvements and modifications are subject of chapter 12 to 15.

Parts of the results presented in this chapter are published in ref. [57].

## 9.1 VERIFICATION OF THE AEI-SAS PERFORMANCE

The horizontal and vertical passive performance of the AEI-SAS is shown in figure 53 and 54 in blue. This measurement is compared to a simple one-dimensional model, which is explained in the following paragraph.

A good measure of isolation performance is the transmissibility, $x_p/x_g$, of ground motion, $x_g$, to payload motion, $x_p$. The transmissibility of a massive harmonic oscillator is derived in section 7.1.3. This is the basis for the one-dimensional models shown in figure 53 and 54.

### 9.1.1 *Vertical isolation performance*

To generate a vertical transmissibility function, the resonance frequency, $f_{ov} = 0.27\,\mathrm{Hz}$, damping factor $\phi_v = \frac{1}{30}$, and CoP factor, $\beta_v = 7 \times 10^{-4}$, were fitted to the measured vertical payload motion (the blue curve in figure 53). The vertical ground motion (the black curve) was then multiplied by the vertical transmissibility function $T_v$

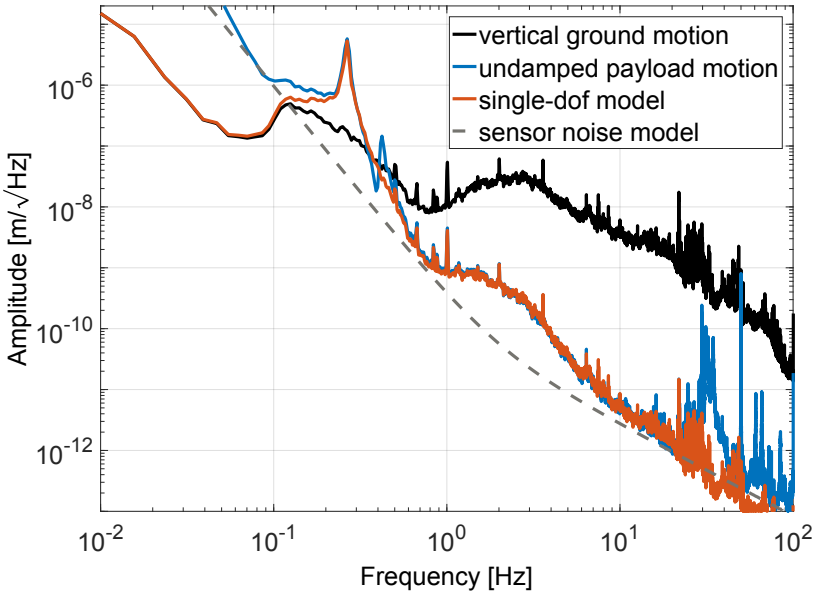


**Figure 53:** Vertical passive AEI-SAS performance: A comparison of the measured table-top motion (blue) and the predicted table-top motion (red) based on the ground motion (black). The model is a simple harmonic oscillator with a fitted resonance frequency, quality factor, and CoP plateau. Above 30 Hz the sensor noise (gray) is dominant in the measurement. The relative deviation of measurement and predicted table motion averaged across all measurement points between 0.1 Hz and 20 Hz is less than 4 %. The internal resonances with the lowest frequencies (described in section 11.3) are the spring-box resonances between 30 and 40 Hz.

to produce the red curve, a single degree of freedom model of the vertical payload motion. The sensor noise of the three vertical L-22D [123] installed in the payload dominates the measurement above $\sim$ 30 Hz. The figure shows the passive performance, free from position control or feedback forces, and it was recorded with the vacuum system pumped down to a pressure below $10^{-5}$ hPa. Up to the first internal resonances above 30 Hz, the measurement matches the predicted payload motion very well. The small peak at 0.4 Hz is due to cross-coupling from the fundamental tilt resonance.

### 9.1.2 *Horizontal isolation performance*

The horizontal payload motion in figure 54 (blue) was measured by an auxiliary horizontal accelerometer placed on the top of the payload. It is compared with the ideal theoretical horizontal table motion (red). The transmissibility of a harmonic oscillator $T_h$ having a fundamental resonance at $f_{oh} = 0.16$ Hz, a damping factor of $\phi_h = \frac{1}{5}$, and a center of percussion factor of $\beta_h = 10^{-4}$ is multiplied by the ground motion (black). At low frequencies, the measurement differs from the model

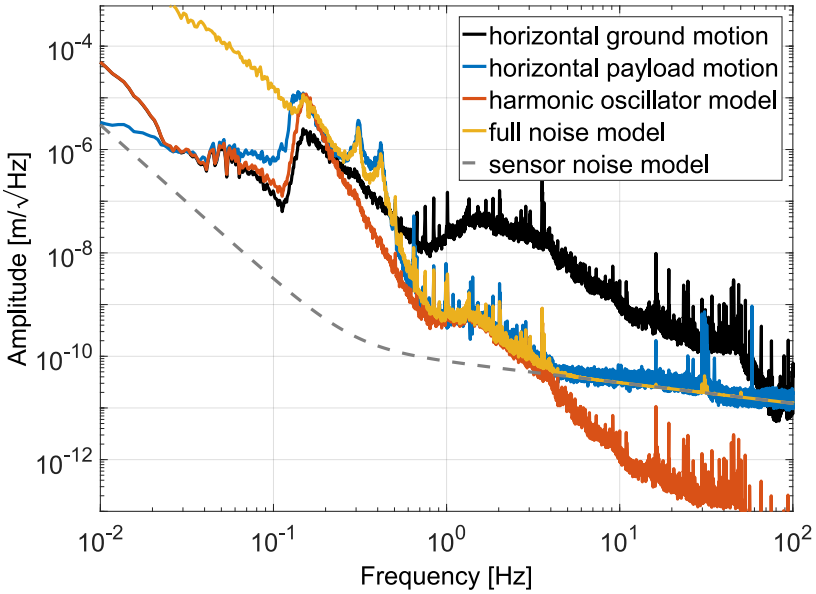


**Figure 54:** Horizontal passive AEI-SAS performance: a comparison of the measured table-top motion (blue), the single-degree of freedom model of the table-top motion (red), and the ground motion (black). The model is again a simple, massive harmonic oscillator model multiplied by the ground motion. A full noise model (yellow) includes cross-coupling from the payload tilt, dominant at low frequencies, and the accelerometer sensor noise, dominant above 5 Hz. A model of the accelerometer noise is shown in gray. The average difference between the measured and predicted motion between 0.1 Hz and 5 Hz is less than 1 %.

due to coupling between payload tilt and the accelerometer readout. The tilt of the payload by an angle $\Theta$ is seen by the accelerometer as a translation of $x_t = \Theta \times g/\omega^2$. That is because of tilt-horizontal coupling, where gravity is assumed constant, and cannot separate tilt and acceleration with a single instrument [151]. This tilt-horizontal coupling at low frequencies as well as the sensor noise $n_s$ is included in the full noise model

$$N^2 = \left(T_h x_g\right)^2 + \left(\Theta_p \frac{g}{(2\pi f)^2}\right)^2 + n_s^2 \ . \tag{87}$$

It is shown in figure 54 in (yellow). The payload tilt motion $\Theta_p$ was measured using differential vertical signals from the L-22D geophones mounted in the payload. Low-frequency noise in the geophones causes the strong deviation of the yellow trace below 0.15 Hz. Above 5 Hz the yellow curve follows the measured sensor noise $n_s$ of the accelerometers. As with the vertical payload motion, internal resonances show up above 30 Hz. These resonances are discussed in more detail in the following section. Note that the measurements in figures 53, figure 54, and fig-

ure 55 were made after the installation of Fluorel pads described in section 12, and as such the 17 Hz resonance is not present in this data.

### 9.1.3 *Vertical and horizontal spectral ratio*

Additional information about the overall passive performance of the AEI-SAS can be obtained by comparing payload motion to ground motion. Figure 55 shows the spectral ratio $|x_p| / |x_g|$. The coherence of $x_p$ and $x_g$ in the lower graph shows in which frequency band the sensor signal is caused by the ground motion in the same direction. The ground motion sensor is not limited by sensor noise at any frequency where the payload sensors provide good signals. In the horizontal direction, the low coherence between 0.3 Hz and 1 Hz is caused by cross-coupling from other degrees of freedom. Below 0.08 Hz and above 4 Hz the payload measurement is limited by sensor noise. Similar to the measurement in figure 53 and figure 54, low-frequency payload tilt couples strongly into the horizontal sensors. In the vertical direction sensor noise limits the measurement below 0.2 Hz and above 9 Hz. The data in figure 55 shows that the payload motion is by a factor of $2.6 \times 10^{-3}$ lower than the ground motion in the horizontal direction at 4 Hz, and is by a factor of $2.4 \times 10^{-3}$ lower than ground motion in the vertical direction at 9 Hz. Above those frequencies, the measurement is limited by measurement noise, but based on prior measurements of the driven transmissibility, we expect more attenuation at higher frequencies. In a shaker test-stand, where the baseplate was excited in the horizontal direction, a peak horizontal isolation of $10^{-4}$ at 7 Hz was achieved. A maximal vertical isolation of $10^{-4}$ above 20 Hz was measured using a single GAS-filter [23].

The lowest horizontal resonance frequency of the mirror suspensions installed on the AEI-SAS is 0.63 Hz. At this frequency, the horizontal payload motion is already 12 times lower than ground motion. At the lowest vertical mirror suspension resonance of 1 Hz, the vertical payload motion is 8 times lower than ground motion.

Advanced LIGO's in-vacuum seismic isolation relies on an active isolation feedback to reduce motion below about 5 Hz. The single-stage HAM-ISI, is most comparable with the AEI-SAS (see section 3.5.2). Compared to the HAM-ISI performance shown in figure 9 and presented in ref. [90]. The passive AEI-SAS transmissibility is better above 2 Hz in the horizontal direction and above 3 Hz in the vertical direction, even though the residual payload motion is higher due to higher ground motion in Hannover. At low frequencies the ground motion attenuation of the active HAM-ISI is significantly higher than the purely passive isolation of the AEI-SAS. The active control and the inter-table motion cancellation by the SPI are not regarded in this comparison. The active feedback will improve the AEI-SAS performance around its fundamental resonances, as discussed in chapter 16.

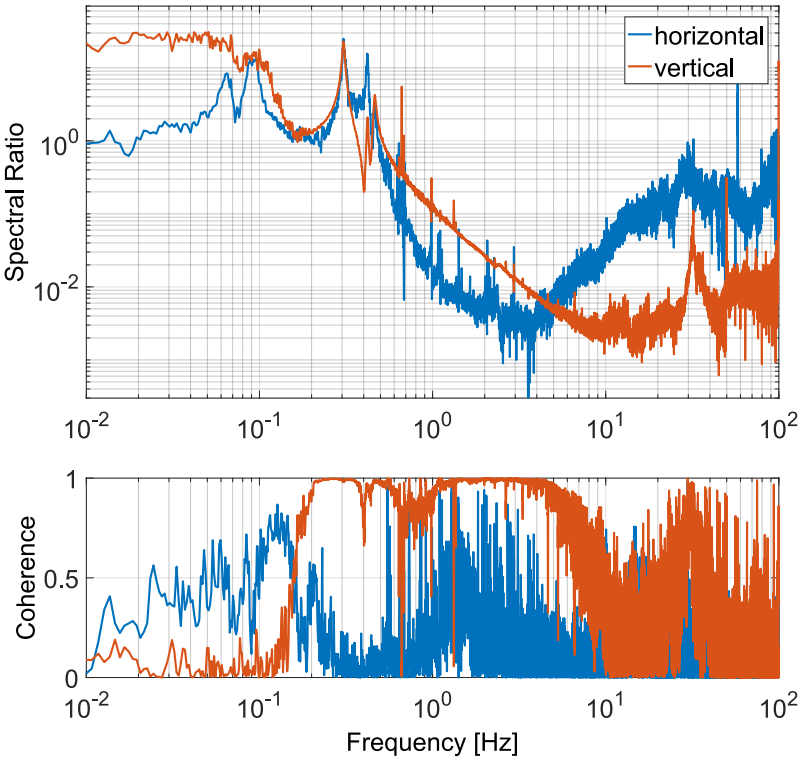


**Figure 55:** Spectral ratio and coherence of ground motion to payload motion: Compared to figure 53, the ground motion at the time of this measurement was lower, so sensor noise is limiting the vertical measurement (red) below ~ 0.2 Hz and above ~ 9 Hz. The horizontal measurement (blue) is limited by sensor noise below ~ 0.08 Hz and above ~ 4 Hz. The sharp peaks around 1 Hz are due to the recoil of the fundamental modes of the mirror suspensions, which were already installed on top of the AEI-SAS at the time of this measurement. At 4 Hz the horizontal payload motion is by a factor of $2.6 \times 10^{-3}$ lower than the ground motion. The vertical payload motion can be measured up to 9 Hz, where it is $2.4 \times 10^{-3}$ lower than the ground motion in this direction. The data in this figure was recorded after the Fluorel pads and the spring-box damper (described in section 12 and 15) were installed.

State of the art commercial isolation systems which can be used in vacuum are made by *Minus k Technology* [152]. The 'SM-1 Low Frequency Vibration Isolator' can support payloads of more than a ton. The design is based on a passive attenuation scheme with a fundamental resonance frequency of 0.5 Hz. Compared to the AEI-SAS this system's typical transmissibility at 9 Hz in the vertical direction is by a factor of about 0.6 higher. In the horizontal direction the AEI-SAS's ground motion suppression is a by factor of about 0.2 higher at 4 Hz than the commercial system. *Minus k Technology* states, that their system offers 10-100 times better isolation than high-performance air tables. The fundamental resonances of the system are, however, in the frequency band of the mirror suspension's fundamental resonances. An

additional active isolation could improve the performance at low frequencies. The better performance of the AEI-SAS over the commercial isolation system justifies the decision to create a customized seismic isolation solution for the AEI 10 m prototype.

## 9.2 COMPARISON OF THE FIRST TWO ISOLATION SYSTEM'S PERFORMANCE

Above the central table's performance in the vertical and one of the horizontal degree of freedom is discussed in detail. In this section, both table's performance in all six degrees of freedom is presented. Figure 56 compares the displacement amplitude of central and south table. The three vertical degrees of freedom represent the payload motion, the horizontal spectra are measured in the spring-box. Comparing the latter to the horizontal payload motion plotted in figure 54 shows, that the cross-coupling of the fundamental tilt modes is weaker in the spring-box measurement. That is because the spring-box's vertical motion is in first-order restricted by the IP-legs, whereas the payload tilts on the GAS-filters. Furthermore, the spring-box modes obviously couple stronger in the spring-box sensors than in the one on the payload.

The measurements were done with the table fully equipped with optics, whereas the performance, shown in section 9.1, was measured earlier when the table top was less populated. Cables and resonances of single arm test, thermal noise interferometer, and frequency reference cavity suspensions have an influence on the AEI-SAS performance.

A group of amplitude peaks between about 15 Hz and 19 Hz is most dominant in the measurement in the z-direction. It is likely that they are caused by the bounce modes of the steering mirrors. These are beam preparation optics are the simplest mirror suspensions in the AEI 10 m prototype. A roughly 1.3 kg mirror mount, inducing the mirror, is suspended from two 0.1 mm thick and about 250 mm long stainless steel wires. A simplified model using these parameters results in a bounce mode of about 16 Hz. Mechanical variations would cause the wider frequency distribution observed in the measurement. The suspension cages are directly bolted to the table top and several of these structures are distributed over south and central table.

At higher frequencies than the steering mirror bounce modes are the differential bounce modes of the test masses and the intermediate masses of the triple suspensions. They are strongly decoupled from the table top by the upper vertical suspension stages, therefore they are hardly identifiable in the measurements.

However, the presence of these mirror suspension modes in the mid frequency range illustrates the importance of widening the isolation window of the AEI-SAS by damping and shifting the AEI-SAS's internal resonances, as it is described in chapters 12 to 15.

The vertical performance of central and south table are relatively similar. In the z-direction mainly the different cross coupling stands out. The fundamental resonance frequency in the rx-direction couples strongly in the central table z-performance, the south table z-performance is dominated by ry cross coupling around 0.45 Hz. Since the orientation of the south AEI-SAS unit is rotated by 90° with respect to the central AEI-SAS, the rx-direction of the central table is geometrically the ry direction of the south table and vice versa. Thus, the dominant cross coupling is in both AEI-SAS units related to rotation about the same geometrical axis. The fundamental resonance frequency difference in the rx-direction is caused by the different payload mass distribution on both tables.

The performance of central and south table in the horizontal directions differs stronger than in the vertical directions. That is because the tuning of the fundamental resonance frequencies is done by adding or removing mass from the spring-box. Since the horizontal stiffness of the first two AEI-SAS units is lower than the design value (see section 7.1), resonance frequency tuning is only possible to a certain extent. The only additional mass in the spring-boxes of the south and central table are the spring-box-damping-units (see section 15). This lack of dummy mass makes increasing the fundamental resonance frequencies hardly possible. Small differences in payload mass and mass distribution cause the difference in frequencies of the fundamental horizontal resonances. Above 1 Hz the central table performance differs from the one of south table, which is probably related the mechanical shortcuts of cables, connecting the table top experiments with the vacuum system feedthroughs. On the central table, several cables connect to components mounted close to the edges of the optical bench. The rz-motion is therefore stronger influenced than other degrees of freedom. Further investigation will clarify the influence of cables on the AEI-SAS performance.

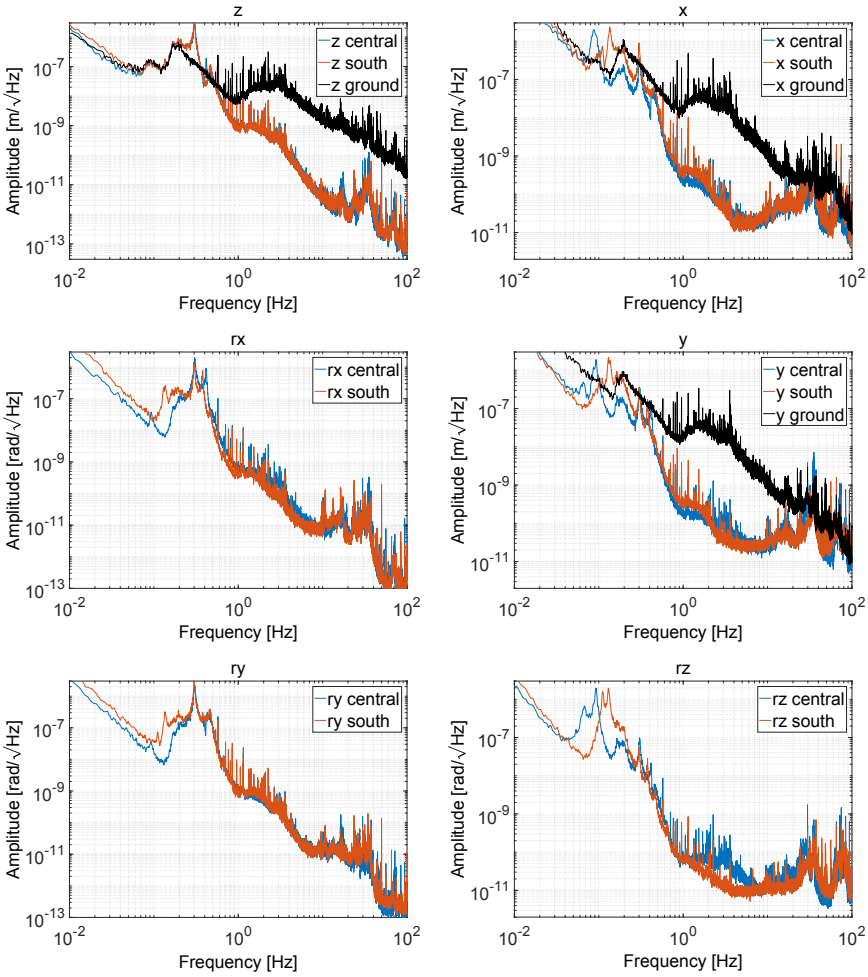


**Figure 56:** Comparison of central (blue) and south (red) table performance. The black curves represent the ground motion. This data was recorded with the STS-2 seismometer which measures solely translational degrees of freedom. The ground motion in the rotational degrees of freedom is not recorded at the AEI 10 m prototype. The vertical degrees of freedom (z, rx, ry) were measured by the L4C geophones located in the optical table (see section 5.2.1). The motion in the horizontal degree of freedom (x, y, rz) was recorded by the monolithic accelerometers (see section 5.2.2). These devices are located in the spring-box. Hence, the spring-box modes appear much stronger in these sensors, than in a horizontal sensor located on top of the payload (compare to figure 54).
The data in this plots was furthermore recorded more than about two years after the performance measurements shown in figure 53 and 54 were done. More optical components introduced additional resonance peaks in the spectrum. Noise is furthermore coupled to the payload by cables connected to components on the table top and to vacuum system feedthroughs.
The two AEI-SAS units behave relatively similar in the vertical degrees of freedom. The fundamental rx resonance frequency is slightly higher in the central table. The reason for that is a different mass-distribution, due to the different optics configuration on the two tables.

# Part III

# IMPROVING THE AEI-SAS

# 10 GAS-FILTER TUNING

## 10.1 INTRODUCTION

Three GAS-filters provide vertical isolation for the AEI-SAS (as discussed in chapter 8). The fundamental resonance frequency and the high frequency isolation performance needs to be adjusted before the GAS-filters are installed in the AEI-SAS. The fundamental resonance frequency is chosen to be 300 mHz for the third AEI-SAS unit. This is a trade-off between a good passive low frequency isolation and a moderate temperature dependance of the equilibrium position (see section 8.1.4). The lack of passive isolation, compared to a GAS-filter system tuned to its limit (about 250 mHz [24]), can be compensated by low frequency active isolation (see section 16).

The CoP plateau of each GAS-filter is tuned as low as possible to obtain good isolation at high frequencies. However, determining the high frequency performance accurately is challenging and has been done insufficiently in the first two AEI-SAS units; also in other attenuation system's GAS-filters, the CoP was specified to a certain extend [95, 121]. The shaker stand therefore was modified for the third table's GAS-filter assembly and testing, in order to obtain more information about the GAS-filter's high frequency performance. As shown below, an isolation plateau of $\beta_v = 1 \times 10^{-5}$ was achieved for one of the third AEI-SAS unit's GAS-filter. That is about an order of magnitude better than the limitations of the first and second AEI-SAS unit's GAS-filter measurements.

Each GAS-filter is individually assembled before the CoP plateau and the resonance frequency are tuned in a shaker stand(see appendix C). The tuning process and the shaker stand improvements are discussed in the following section.

After the tuning procedure, the three GAS-filters are installed in the spring-box and equipped with the vertical LVDTs and the vertical actuators.

This chapter will discuss how the resonances of the three filters for the third AEI-SAS unit were tuned to be as similar to one another as possible and how the high frequency isolation was optimized.

## 10.2 GAS-FILTER TUNING IN THE SHAKER STAND

A GAS-filter's stiffness is critically dependent on the compression of the blades and the equilibrium position of the keystone, which dependents on the payload mass. A careful balancing of those parameters is neces-

sary to achieve a satisfying result. The GAS-filters are therefore tuned in a shaker stand, as shown in figure 57. This way the baseplate of the GAS-filter can be vertically driven and the transmissibility can be measured. The baseplate actuation allows measuring with good coherence even at high frequencies where natural ground motion is attenuated strongly, such that the payload sensor is not sufficiently sensitive to measure. In this setup, the GAS-filters can be accessed from all sides which simplifies the blade tuning. Furthermore, a dummy payload mass, which is suspended from the keystone in this test setup, can be adjusted easily.

### 10.2.1 *Experimental setup*

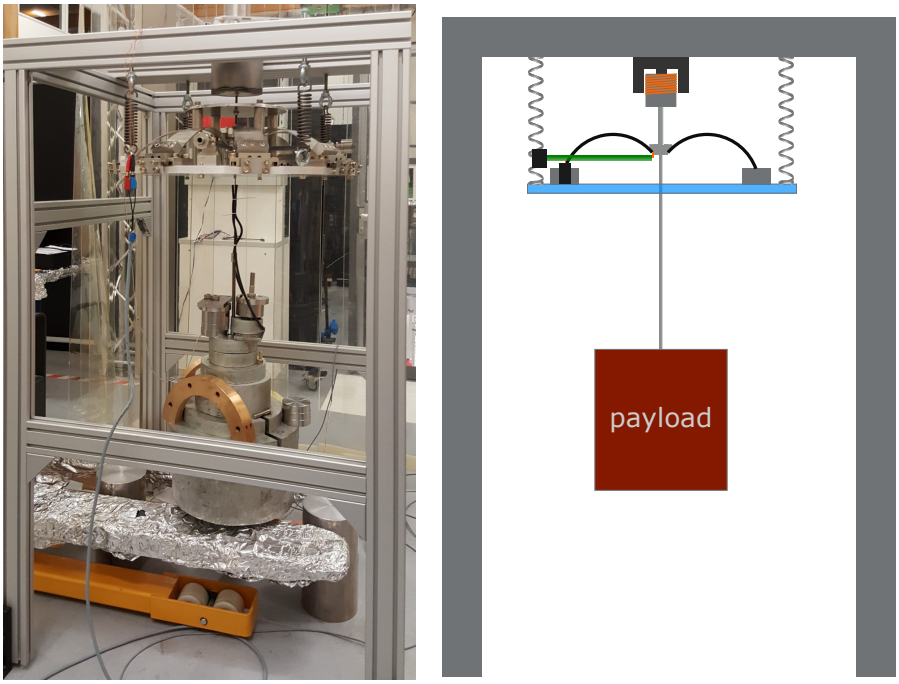


**Figure 57:** Photograph and drawing of the GAS-filter shaker stand: In order to tune the GAS-filters' fundamental resonance frequency and CoP, they are suspended from four extension-springs in a rigid aluminum frame. The GAS-filter's baseplate is driven vertically by a voice-coil actuator. In this test configuration the payload of about 300 kg is suspended from the keystone by a steel wire (the rubber band fixed to the steel wire is used to dampen its resonances). After tuning the equilibrium position and the resonance frequency of the GAS-filter, free tuning masses are bolted to the payload (not shown in this picture). The motion is recorded by one geophone on the GAS-filter baseplate and one geophone mounted to the bottom of the payload. The lower geophone, as well as the actuator coil, are housed in iron boxes in order to prevent magnetic coupling (see section 10.3.2).

Each GAS-filter is tuned individually to the desired resonance frequency and CoP plateau. This is done by using a shaker stand specifically designed for this task. It is shown in figure 57. The GAS-filter baseplate is suspended from four extension-springs, which are hanging from a rigid aluminum profile frame. All four springs can be adjusted in height, and, hence, the roll and pitch angular displacement of the filters baseplate can be balanced. The spring-suspension allows actuation of the baseplate in the vertical direction. A coil is therefore connected to the GAS-filter's baseplate. It moves inside a cylindrical magnet which is mounted to the top of the aluminum frame. An approximately 300 kg dummy mass is suspended from the GAS-filter's keystone in order to simulate the payload.

The GAS-filters are best characterized by measuring their transmissibility. A L-22 geophone is therefore placed on the GAS-filter's baseplate and a second one is mounted to the bottom of the dummy mass.

### 10.2.2 *Tuning the GAS-filter's resonance frequency*

As described in section 8.1 the GAS-filter's resonance frequency is tuned by compressing the blades against each other. In order to maintain the keystone in its vertical working position of about 8.5 cm above the baseplate the dummy mass needs to be adjusted while compressing the blades.

As mentioned above the GAS-filters of the third AEI-SAS unit are tuned to a resonance frequency of 300 mHz. Initially, the vertical fundamental resonance of the AEI-SAS was intended to be as low as possible to obtain maximum passive isolation at low frequencies. below a resonance frequency of about 200 mHz hysteresis increases drastically and fades into a bi-stability of the GAS-filter for an overcompressed filter. Measurements of this effect are described by Wanner et al. [24].

The moderately higher vertical resonance frequency of the third AEI-SAS unit has the advantage that it is in the elastic regime of the blades. Furthermore, the vertical position of the AEI-SAS is less susceptible to temperature change with a higher resonance frequency (compare to section 10). In the first two AEI-SAS unit's temperature changes of less than about 0.5 °C can be compensated by the vertical actuators. The lack of passive low frequency isolation has little effect on the performance of the AEI-SAS. Around the AEI-SAS's fundamental resonance frequencies active isolation dominates the attenuation. Thus, in this frequency regime, is fundamentally limited by sensor noise. Only in the mid-frequency band at a few Hz, above the active isolation frequency band and below the CoP plateau, a lower fundamental GAS-filter resonance frequency increases the attenuation. Here the isolation of a GAS-filter tuned to the limit of about 200 mHz is about 2.3 times better than the isolation of a 300 mHz GAS-filter. It was chosen to sacrifice

this small isolation improvement in favor of a more stable and reliable system.

### 10.2.3 *Tuning the GAS-filter's CoP plateau in the shaker stand*

The high frequency performance of the GAS-filter is dominated by the isolation plateau caused by the CoP effect (see section 8.1.6 and 7.1.4). Once the resonance frequency and the working position is roughly adjusted, the CoP compensators are installed in the GAS-filter. In the first two AEI-SAS units, only two CoP compensators opposing each other were installed per GAS-filter. Improved measurement techniques, discussed below, showed that a better high frequency performance is achieved by three compensators per filter. A significant difference between three and four compensators was not observable. After the CoP compensators are approximately adjusted to the right position, the equilibrium position of the system needs fine adjustment, since a small vertical force from the compensator acts on the keystone.

The high frequency performance is improved by adjusting the counterweights of the CoP compensators. The transmissibility function is then measured. Varying the CoP tuning slightly while keeping the GAS-filter in an overcompensated state helps identifying the overcompensation-dip, since it will shift in frequency, according to equation 86. The CoP tuning was iteratively performed until no improvements were measurable by counterweight variations (discussed in more detail below).

An example for three CoP tunings is shown in figure 58: The GAS-filter's transmissibility amplitude with the CoP-tuning masses shifted as far inside as possible is shown in purple, the green curve represents the transmissibility amplitude of a GAS-filter with the tuning mass shifted far outside and the light blue curve shows an optimized tuning.

All three measurements feature prominent resonances above 70 Hz. These are environmental resonances of, for instance, the shaker stand cage. In the process of operating the shaker stand many parasitic resonances were identified and either damped or stiffened. The status of the shaker stand presented here provides a satisfying measurement window which allows measuring CoP plateau heights down to about $\beta_v = 1 \times 10^{-5}$. The measurements are therefore fitted by the transmissibility amplitude (blue, red and yellow) from the analytic GAS filter model (equation 83).

The undercompensated GAS-filter transmissibility forms a plateau at $\beta_v = 4 \times 10^{-4}$ above the corner frequency $f_c = 15$ Hz. This is already an improvement over old GAS-filter versions without CoP tuning [88].

The overcompensated GAS-filter has a similar plateau height with $\beta_v = 5 \times 10^{-4}$. However, the transmissibility amplitude forms a notch at $f_{notch} = 12.3$ Hz before flattening out. At this notch frequency, the

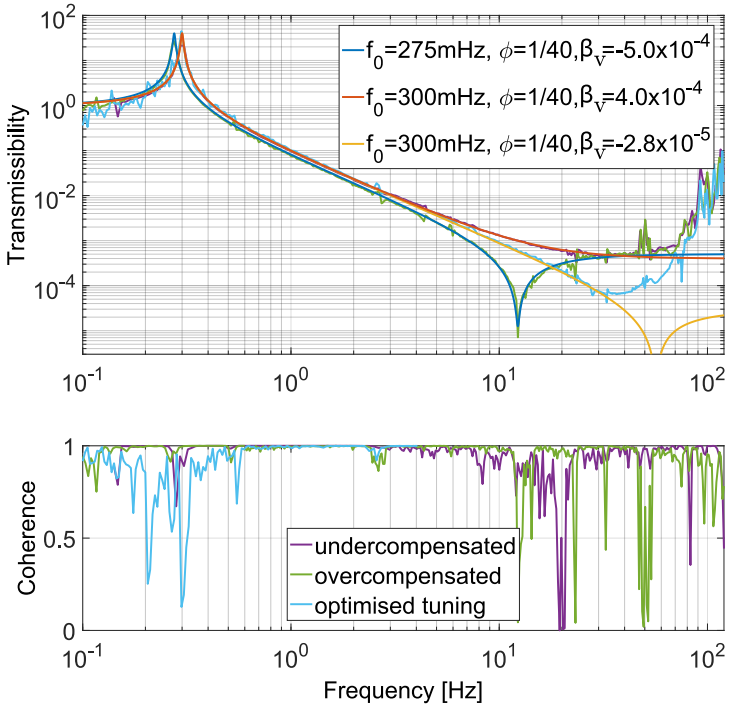


**Figure 58:** CoP tuning of the GAS-filter. The figure shows three plots for different CoP tuning measurements. The purple line is the transmissibility amplitude of an undercompensated GAS-filter. The CoP compensator counterweights are shifted far to the center of the GAS-filter. The green transmissibility plot represents an over-compensated GAS-filter with counterweights shifted far outside. An optimized tuning is shown in light blue. This curve consists of a low frequency (0.1 Hz to 4 Hz) and a high frequency (4 Hz to 120 Hz) measurement. The low frequency part is measured in the conventional way, the high frequency part is post-processed data from two frequency response measurements, one from the actuator to the baseplate geophone and one from the actuator to the payload geophone. Thus the coherence of the optimized configuration is only plotted for low frequencies. This procedure is explained in more detail in section 10.3.1.
The fitted curves (blue, red and yellow) are the transmissibility amplitude from the analytic GAS filter model in equation 83. Resonance frequency $f_0$ and damping factor $\phi$ are fitted to the resonance peak, the CoP plateau constant $\beta_v$ is fitted to the mid-frequency section where the transmissibility either flattens or forms a notch. At high frequencies, the transmissibility is dominated by parasitic resonances.

center of rotation crosses the CoM of the payload, as discussed for the IP-legs in section 7.1.4.

Also the optimized GAS-filter transmissibility is slightly overcompensated, but it has a much lower CoP plateau ($\beta_v = 2.8 \times 10^{-5}$) than the first two examples. The notch frequency is modeled to be at $f_{notch} = 56.5$ Hz. At this frequency, the influence of the parasitic resonances is too high to be measured in the test stand.

## 10.3 IMPROVING THE GAS-FILTER TUNING

Several modifications to the shaker stand were done in order to improve the characterization and tuning of the GAS-filters. A new voice coil actuator and a more rigid dummy payload were implemented to improve the excitation and minimize additional resonances. The most significant improvements resulted from an improved measurement technique and the reduction of the magnetic coupling from the actuator to the geophone.

### 10.3.1 *Improving the CoP tuning*

The performance of the GAS-filter tuning for the first two tables was measured by exciting the filter's baseplate and measuring the transmissibility from the baseplate motion to the suspended mass motion with the two geophones. Due to the limited dynamic range of the geophones, the measurement was only coherent up to a certain frequency. In particular, when tuning the CoP plateau better than a transmissibility of about $3 \times 10^{-4}$, an accurate determination of the isolation performance was not possible in a reasonable time. The GAS-filter's CoP plateaus of the first two AEI-SAS units were therefore not well defined [24]. This is also the case for GAS-filters installed in other isolation systems [95, 121].

By measuring two separate transfer functions, one from the actuator to the baseplate geophone and one from the actuator to the payload geophone, the actuation amplitude can be adjusted separately. Thereby coherence over a much wider spectrum was achieved. The vertical transmissibility $T_{b\to p}$ of the GAS-filter is the ratio of the two frequency responses

$$\frac{R_{a\to p}}{R_{a\to b}} = \frac{z_p F_a}{F_a z_b} = T_{b\to p} \ , \tag{88}$$

Where $R_{a\to p}$ is the frequency response from the actuator to the payload, $R_{a\to b}$ is the frequency response from the actuator to the baseplate, $F_a$ is the actuator force and $z_p$ and $z_b$ are payload and baseplate motion. Figure 59 shows an example of the two separate transfer function. The amplitude of $R_{a\to p}$ is shown in blue, the amplitude of $R_{a\to b}$ is shown in red. While measuring $R_{a\to p}$, the baseplate sensor was saturated, whereas the payload sensor did not show- or need high coherence to the actuation while $R_{a\to b}$ was recorded. Combining those two measurements results in the overall transmissibility, shown in yellow, which enables a high frequency characterization of the GAS-filter.

Below a certain frequency (about 4 Hz) the GAS-filter's attenuation is relatively low. Thus, a direct coherent transmissibility measurement is possible (see for instance light blue curve in figure 58). This is convenient since this way only one-time consuming low frequency measure-

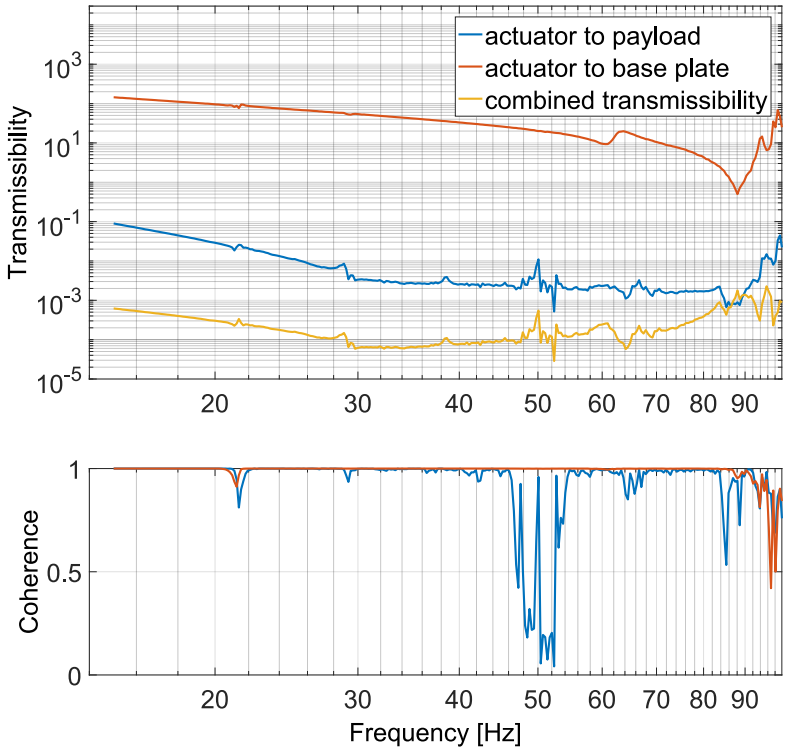


**Figure 59:** Illustration of the high frequency measurement technique used for tuning and characterizing the third AEI-SAS unit's GAS-filters. The limited dynamic range of the geophones does not allow measuring a coherent transmissibility from the baseplate to the payload directly. Therefor first the frequency response from the actuator to the baseplate sensor is measured (red). Only a relatively small actuation amplitude is needed to obtain good coherence. In a second step, the frequency response from the actuator to the payload sensor is measured (blue). For a good coherence the actuation amplitude needs to be high (usually that high that the baseplate sensor is saturated). The transmissibility (yellow) from the baseplate to the payload is the ratio of the two frequency responses, as shown in equation 88.

ment and two rather quick high frequency measurements are necessary to characterize the GAS-filter's isolation performance fully.

With this procedure, isolation plateaus down to about $\beta_v = 1 \times 10^{-5}$ can be determined in a reasonable time. By further elimination of parasitic resonance, the measurement performance could even be enhanced. This could be achieved by redesigning the shaker stand in terms of a stiffer support structure. The shaker stand furthermore could be improved by restricting the GAS-filter baseplate to the purely vertical motion. Even though the actuation is acting centrally on the GAS-filter's baseplate a residual horizontal force from the voice coil actuator causes a tilt motion in the baseplate. This can be enhanced by an unequal tension of the four extension-springs. In the presented measurements this effect was minimized by fine-tuning the coil and magnet position.

A different way of actuation and suspension (for instants by mounting the baseplate on piezo actuators) could even improve this.

### 10.3.2 *Magnetic coupling*

The frequency response from an electromagnetic actuator to a sensor is determined by measuring the induced motion of the component the sensor is connected to e.g. the baseplate or the payload. For high mechanical isolation, the payload motion is so low that magnetic coupling from the actuator coil to the geophone's readout coil dominates the readout signal. As a consequence, the CoP-plateau could only be tuned down to a certain value.

The effect of magnetic coupling was tested by removing the actuator magnet from the shaker stand, thus the current through the actuator coil did not cause a force on the GAS-filter. The frequency response from the actuator to the payload geophone showed good coherence at high frequencies where the payload motion is small and the frequency response amplitude plateaued at the same level as it did with the actuator magnet.

Different shielding methods were tested in order to mitigate the magnetic coupling. Mu-metal, metal with high permeability, would be a good material for efficient shielding. Due to the high costs, tests with simple iron shielding were prioritized and found to be sufficient.

To verify the coupling and to test different shielding configurations, the geophone's test mass was locked by turning it upside down. This way the geophone's readout signal has practically no motion induced part and hence any signal was only due to electromagnetic coupling. The locked geophone was placed of about the same distance below the actuation coil as in the shaker stand configuration. The transfer function from the actuation coil drive to the geophone readout signal was measured for different shielding arrangements, as shown in figure 60.

A satisfyingly lower magnetic transmission is achieved by a shielding configuration where the actuation coil is housed in an iron cup with 1 mm wall thickness. The cup needs to be open to the upper side of the coil where the magnet is inserted. A second magnetic shield is therefore surrounding the payload geophone. This shield is an iron box which in the first attempt had an opening at the bottom (yellow curve). Sealing the geophone fully with an additional lid improved the shielding even further (purple curve).

Even though the baseplate geophone is closer to the actuator coil magnetic coupling to this device does not dominate its readout signal, since the baseplate is directly coupled to the actuator mechanically.

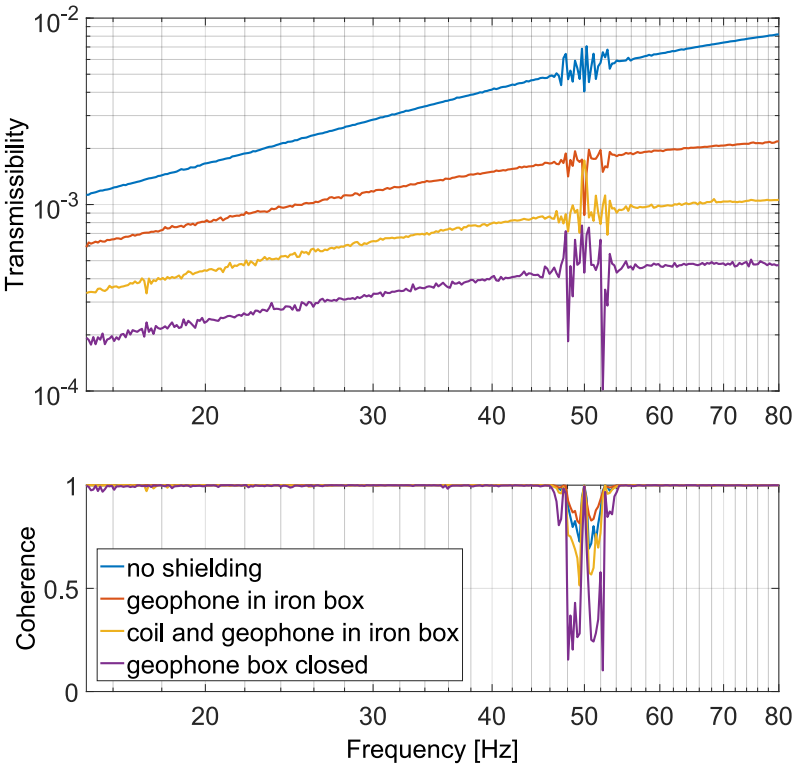


**Figure 60:** Shielding the geophone's sensing coil from the magnetic field of the actuator coil. The shielding was iteratively improved. In a first test only the geophone was shielded in the direction of the actuator coil by a 2 mm wall thickness iron box (red). In a next step, the actuator coil was also housed in a shielding box. A satisfying result was achieved by fully housing the geophone.

## 10.4 CHARACTERIZING THE THIRD AEI-SAS UNIT'S GAS-FILTERS

In order to minimize cross coupling in the AEI-SAS between the vertical and the tilt degrees of freedom, all three filters' vertical stiffness need to be as similar as possible. Figure 61 compares the final transmissibility amplitude measurement fitted by a massive harmonic oscillator model (compare to section 8.1.5). It shows that the resonance frequency of the three filters varies by less than 4 %. This was achieved by repeated careful blade compression tuning, after the CoP was adjusted.

The CoP plateau was tuned, as discussed above, by shifting the counterweight of the CoP compensators. For each GAS-filter the isolation was optimized as good as possible in a reasonable time. Due to the improved measurement techniques the filters could be tuned to CoP plateaus of $5.6 \times 10^{-5}$, $2.8 \times 10^{-5}$, and $1 \times 10^{-5}$. The individual measurements have high coherence up to about 100 Hz.

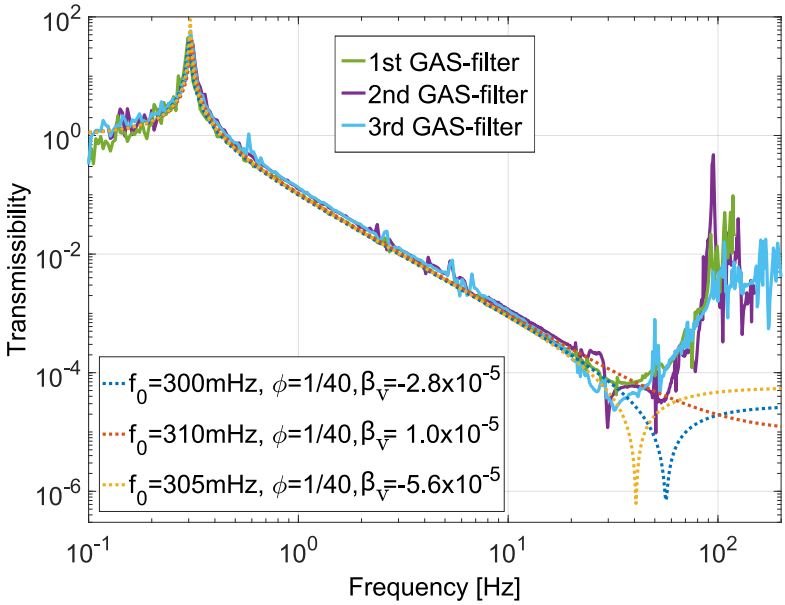


**Figure 61:** Performance of the three third AEI-SAS unit's GAS-filters. In the improved shaker stand the GAS-filters were tuned to the desired 300 mHz resonance frequency. Up to a frequency of 7 Hz the vertical transmissibility was measured directly from a geophone placed on the baseplate to a geophone clamped to the dummy payload. Above this frequency, the transmissibility was derived as described above. In order to determine the GAS-filters' CoP plateau height $\beta_v$ the measurements were fitted by a massive harmonic oscillator model (see section 8.1.5). Even though parasitic resonances dominate the high frequency measurement it can be fitted up to about 30 Hz and therefore a CoP plateau height down to $1 \times 10^{-5}$ can be determined. Note that the amplitude and shape of the parasitic resonances differ in the measurements since different ways of shifting or damping those modes were tested during the GAS-filter tuning phase, in order to improve the shaker stand.

# 11 SPRING-BOX INTERNAL RESONANCES

In contrast to the last chapter, which discussed individual components of the AEI-SAS (namely the GAS-filters), this chapter discusses properties of the entire system. More precisely, the internal resonances of the AEI-SAS with the lowest frequency. These modes are identified and analyzed experimentally with a simple analytical model and finite element simulations.

A solution to mitigate the performance reduction by means of these parasitic resonances, the fluorel stage, is furthermore discussed. Its implementation in the AEI-SAS is described and characterized.

Parts of the results presented in this chapter are published in ref. [57].

## 11.1 PARASITIC SPRING-BOX MODES

The model used to describe the AEI-SAS performance in section 9 is based on the assumption that the spring-box is massless and that horizontal and vertical suspension stages are fully decoupled. It thereby does not describe the internal resonances. A more realistic description of the system must take into account that:

- the CoM of the payload is located well above the CoM of the spring-box. This determines the observed large coupling between the horizontal and the tilt degrees of freedom.
- the IP-legs have a finite vertical compliance.
- the GAS-filters have a finite horizontal compliance.

In particular, the parasitic compliance of the suspension elements, combined with the sizable mass (approximately 300 kg) of the spring-box, is such that the 6 rigid-body modes of the spring-box are in the 10 - 50 Hz frequency band. This affects the overall attenuation performance of the system significantly. The large mass ratio between spring-box and payload (approximately 1 : 3) causes a large transmissibility of ground vibrations in the frequency band around the spring-box's parasitic mode frequencies. In the following sections, the lower three modes are characterized and efforts to mitigate their impact are presented. These modes can be approximated as the two horizontal translational, and the yaw (rotation around the z-axis) oscillation of the spring-box They are therefore referred to as horizontal spring-box modes. For the description of these modes the bending of the spring-box can be neglected.

The three mainly vertical modes, the vertical translational, the roll (rotation around the y-axis) and the pitch (rotation around the x-axis)

oscillations are caused by the elasticity of the spring-box and the vertical compliance of the IP-legs. They are subject to section 11.3.

## 11.2 SPRING-BOX RIGID BODY MODES

The lowest frequency internal resonances of the AEI-SAS are differential oscillations between the spring-box and the payload, both in the horizontal translational direction and the rotation around the vertical axis. These modes show up at approximately 13 Hz and 17 Hz. They were investigated experimentally and by simulations.

### 11.2.1 *Experimental mode analysis*

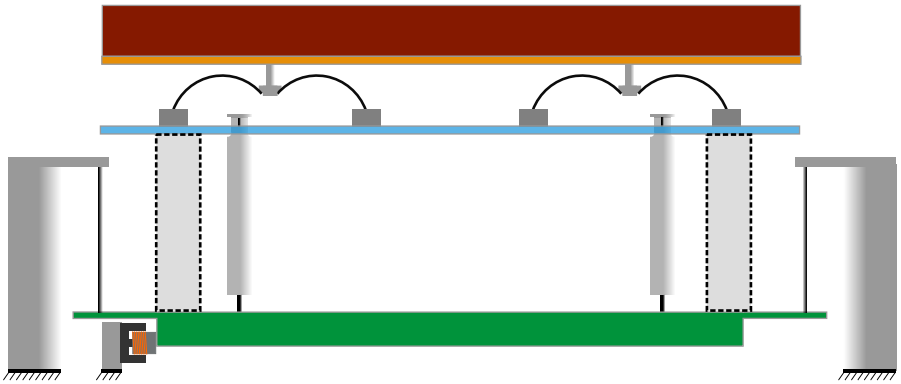

**Figure 62:** Drawing of the AEI-SAS, suspended in a shaker stand. The baseplate is hanging from four thick steel wires, which are connected to rigid posts. A coil-magnet arrangement allows exiting the baseplate in the horizontal direction. This enables measuring the transmissibility from baseplate to tabletop with good coherence. In order to identify the mechanical cause of the lowest frequency internal resonances of the AEI-SAS at approximately 13 Hz and 17 Hz the spring-box was clamped to the baseplate (dashed boxes). This way the GAS-filters are both horizontally and vertically the softest connection between baseplate and payload. the transmissibility was compared to the one of the free AEI-SAS. The corresponding measurement is shown in figure 63. The orange structure represents the intermediate plate which was rigidly connected to the table top in this experiment.

In order to measure and tune the AEI-SAS performance, the whole AEI-SAS was installed in a shaker test-stand. The AEI-SAS's baseplate was suspended from four wires so that it could freely move in the horizontal degrees of freedom. A horizontal voice coil actuator was used to apply a translational force to the baseplate, enabling fast and coherent measurements of the isolation system's transmissibility. Figure 63 shows the horizontal transmissibility from the baseplate to the payload (red). This way the horizontal stage's fundamental resonance and CoP are tuned. For comparison, the transmissibility was re-measured when

the spring-box was clamped to the baseplate. The clamps effectively bypassed the IP-legs. Figure 62 shows a sketch of the AEI-SAS suspended in the shaker stand. the dashed boxes represent the mechanical bypassing of the horizontal stage. In the realistic system, multiple clamping devices were used in order to achieve a rigid connection.

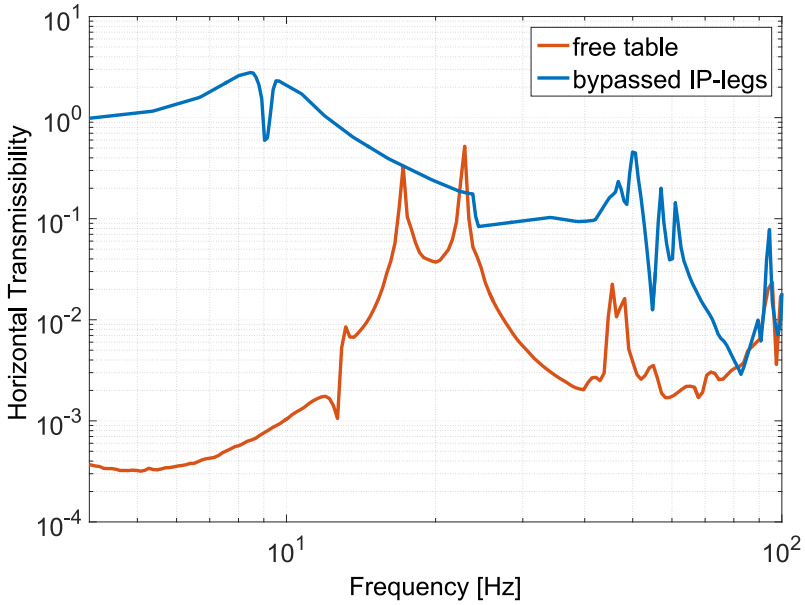


**Figure 63:** Investigation of internal resonances using the test-stand. The AEI-SAS's baseplate is driven horizontally, and the transmissibility from the baseplate to the payload is shown for normal operation (red) and with the horizontal stage clamped (blue). This setup is illustrated in figure 62. The 9 Hz structure in the blue curve is the spring-box mode caused by the horizontal compliance of the GAS-filters. In the free AEI-SAS this mode shifts to 17 Hz. The feature at 13 Hz in the red curve corresponds to the AEI-SAS's yaw internal resonance, also caused by the horizontal compliance of the GAS-filters. The mode above 20 Hz corresponds to the vertical spring-box modes which are discussed in chapter 11.3.

If the spring-box is clamped, the softest connection in the horizontal direction is the horizontal compliance of the three GAS-filters. In a free state, the IP-legs are much softer.

Figure 63 shows in red that the free AEI-SAS has its lowest horizontal internal resonance at 17 Hz (the IP-leg mode is not shown in this graph). For the clamped system it shifts to approximately 9 Hz.

### 11.2.2 *Simplified one-dimensional model*

Considering this setup as a simplified one-dimensional harmonic oscillator, where the 900 kg payload is connected by a spring to the ground, its effective spring constant is, according to equation 13,

$$k_{hGAS}(9\,\mathrm{Hz}) \approx 2.9 \times 10^6\,\mathrm{N/m} \ . \tag{89}$$

This value was confirmed in a separate experiment where a single GAS-filter, suspended in the GAS-filter shaker stand (see figure57) was deflected horizontally.

The free AEI-SAS would correspond to a simplified one-dimensional model, where the payload mass is connected via the same spring to the spring-box mass of 331 kg. The potential of the spring is

$$V_{hGAS} = \frac{1}{2} k_{hGAS} \left(x_{sb} - x_p\right)^2 \ . \tag{90}$$

The parameters used in the model are listed in table 11. In this model the horizontal IP-leg stiffness is neglected. The equations of motion of this simple two mass oscillator follow from equation 34 and equation 38 with the kinetic energy of $m_{sb}$ and $m_p$ to

$$\begin{aligned} 0 &= m_{sb}\ddot{x}_{sb} + k_{hGAS}\left(x_{sb} - x_p\right) \\ \text{and} \\ 0 &= m_p\ddot{x}_p + k_{hGAS}\left(x_{sb} - x_p\right) \ . \end{aligned} \tag{91}$$

This leads to the generalized equation of motion

$$\ddot{x}_{hGAS} = \frac{k_{hGAS}}{m_{red}} x_{hGAS} \tag{92}$$

with the reduced mass $m_{red} = m_{sb}m_p(m_{sb} + m_p)^{-1}$ and the spring deflection $x_{hGAS} = \left(x_{sb} - x_p\right)$. The resonance frequency of this system is according

$$f_{hGAS} = \frac{k_{hGAS}}{2\pi m_{red}} = 17.4\,\mathrm{Hz} \ . \tag{93}$$

Already this greatly simplified one-dimensional model agrees very well with the measurement and confirms the presumption that the horizontal compliance of the GAS-filters is the cause of the parasitic 17 Hz resonance.

### 11.2.3 *Simplified three-dimensional finite element model*

A more realistic description of the differential spring-box-payload dynamics can be deduced from a finite element model. An Ansys Work-

bench simulation (figure 64) shows the resulting mode shapes. The model is a simplified version of the AEI-SAS with the correct horizontal dimensions and masses for both the spring-box and the payload. The model for the IP-legs is close to reality. Vertical dimensions and mass distribution are simplified to produce an efficient mesh. The GAS-filters are modeled as a set of two horizontal springs, using the spring constant $k_{hGAS}$ calculated above. The structure of the finite element simulation is described in more detail in the appendix B. In accordance with the

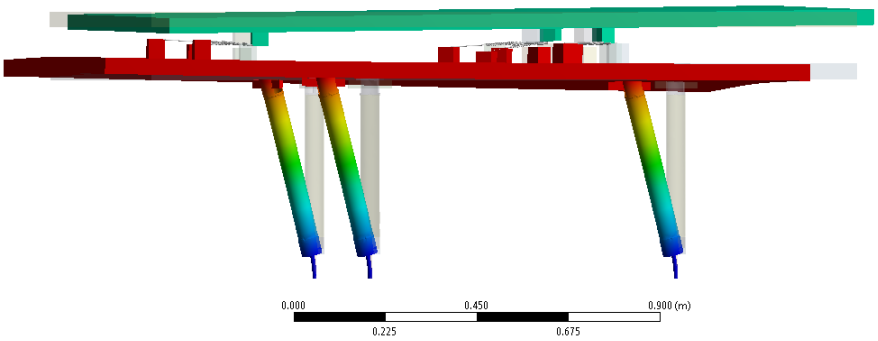


**Figure 64:** Finite element simulation of the horizontal GAS-filter compliance: The spring-box and the payload are represented by stiff plates. The GAS-filters are modeled as a set of springs with the measured horizontal and vertical stiffness. The resulting modes are translational and rotational differential oscillations between spring-box and payload.

one-dimensional analytical model the 17 Hz resonances are lateral differential oscillations between the spring-box and the payload in both horizontal directions. The differential horizontal rotation mode (yaw) is according to the finite element model at 12.8 Hz. This mode is seen at 13 Hz in the horizontal frequency response in figure 63.

## 11.3 SPRING-BOX ELASTIC MODES

In section 11.2 the horizontal spring-box rigid body modes are discussed. They are the lowest internal resonances of the AEI-SAS. Due to the finite vertical compliance of the IP-legs and the spring-box, three additional modes are observable in the system, with the spring-box bouncing vertically, and rotating in pitch and in roll. These modes have natural frequencies between 30 Hz and 50 Hz. The finite element simulation (figure 65) shows the corresponding spring-box mode shapes. It also shows that even though the thin upper flexures (operated in tension) and the thin walls of the IP-legs dominate the vertical compliance, the bending of the spring-box is a significant contribution. Two different approaches are investigated in order to improve the performance in the frequency band above 30 Hz: In the first approach, the geometry of the IP-legs is changed to stiffen them in the vertical direction (see

chapter 13). This, in combination with spring-box stiffening, will shift the vertical spring-box modes to higher frequencies and thereby widen the isolation frequency window (as discussed in the introduction of this part). The second approach is the passively damping of the resonances by installing dedicated inertial damping units (see chapter 15). In this

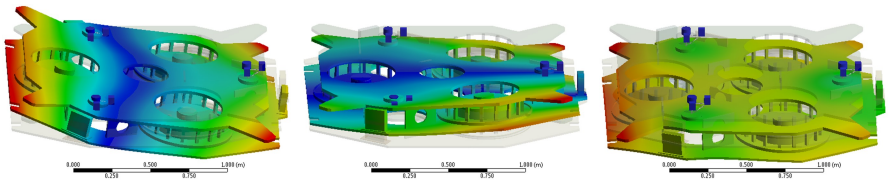

**Figure 65:** Finite element simulation of the spring-box and IP-leg modes. A set of three springs represent each IP-leg's stiffness matrix. These springs are on one end connected to the spring-box, on the other end the connect to nine rigidly supported cubes. The mass and dimensions of the spring-box have realistic values. The color scheme illustrates the total deformation from no displacement (blue) to maximum deformation (red).
The first two modes shown here are primarily rotational oscillations. The third mode is the 'bounce' mode of the IP-legs. All three oscillations are caused by a combination of vertical deformation of the IP-legs and bending of the spring-box. The simulated resonance frequencies are 37.9 Hz, 38.3 Hz and 41.0 Hz. Chapter 15 shows, how inertial dampers can be placed in anti-nodes of the oscillations in order to effectively remove energy from these modes.

chapter, the lowest vertical spring-box modes and the approaches for improvement are discussed.

Parts of the results presented in this chapter are published in ref. [57].

### 11.3.1 *Analysis of vertical spring-box modes*

Above the frequencies of the horizontal spring-box modes, which are discussed in section 11.2, the first two AEI-SAS units show further internal resonances. Their oscillation couples into all motion sensors of the systems and are most prominent in the spring-box. The finite element simulation shown in figure 64shows two tilt modes of the spring-box plate at approximately 30 Hz and a bounce mode of the spring-box plate on the IP-legs at 47 Hz. A more accurate model of the spring-box is necessary to analyze those modes in more detail since the mode frequency is strongly dependent on the stiffness and the geometry of the spring-box.

Figure 65 shows a finite element simulation with a spring-box geometry close to reality. The three GAS-filters, as well as the accelerometers, are modeled as simple geometries with the right mass and footprint in the right position on the lower spring-box plate. The Gas-filters' soft vertical connection to the payload can be neglected for this simulation. A set of three springs represent each IP-leg's stiffness matrix. Their

vertical stiffness is taken from a separate, close to reality IP-leg model (see figure 66) and is $k_v = 1.1 \times 10^7\,\mathrm{N/m}$.

A strongly simplified analytical model shows, that the weakest part of the IP-leg is the aluminum tube. For this approximation, the vertical stiffness is composed of the vertical stiffness of the lower flexure, the upper flexure and the aluminum tube with

$$\begin{aligned} k_v^{flex} &= \frac{\pi E d_{flex}^2}{4 l_{flex}} = 2.3 \times 10^8\,\mathrm{N/m} \\ k_v^{uflex} &= \frac{\pi E d_{uflex}^2}{4 l_{uflex}} = 9.4 \times 10^7\,\mathrm{N/m} \\ k_v^{leg} &= \frac{\pi E_a (d_{leg1}^2 - d_{leg2}^2)}{4 l_{tube}} = 4.2 \times 10^7\,\mathrm{N/m}\ . \end{aligned} \tag{94}$$

with the upper and lower flexure dimensions $d_{flex}$, $l_{flex}$, $d_{uflex}$ and $l_{uflex}$ and the Young's modulus of maraging steel $E$ (see table 6). $d_{leg1} = 0.048\,\mathrm{m}$ and $d_{leg2} = 0.046\,\mathrm{m}$ are the inner and outer diameter of the aluminum tube, the Young's modulus of aluminum is $E_a = 70\,\mathrm{GPa}$.

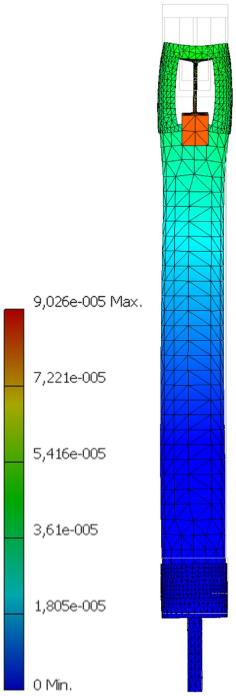


**Figure 66:** Finite element simulation of the vertical stiffness of the IP-leg. The geometry is simplified to the basic components. A force of 1 N is acting on the adapter bar, which is connecting the upper flexure to the upper bell. The exaggerated displacement representation illustrates the weakest parts of the structure. The upper flexure, as well as the aluminum tube, are strongly deformed. The resulting vertical stiffness is $k_v = 1.1 \times 10^7\,\mathrm{N/m}$. The color scale next to the figure is the total deformation in millimeters.

The resulting total vertical stiffness of such a simplified IP-leg is

$$k_v = \frac{k_v^{flex} k_v^{uflex} k_v^{leg}}{k_v^{flex} k_v^{uflex} + k_v^{uflex} k_v^{leg} + k_v^{flex} k_v^{leg}} = 2.6 \times 10^7 \,\mathrm{N/m} \ . \qquad (95)$$

Even though this stiffness is by a factor of approximately 2.4 higher with regard to finite element simulation, this simple calculation shows, that both the tube and the upper flexure limit the vertical stiffness of the IP-leg.[1] These components need to be stiffened in order to shift the vertical spring-box modes to higher frequencies.

As mentioned above, those modes are not only caused by the vertically soft IP-legs, but also by the relatively low bending stiffness of the spring-box itself. The bounce mode frequency of a system with an infinitely stiff spring-box, for instance, would be

$$f_{bounce} = \frac{1}{2\pi}\sqrt{\frac{k_v}{m_{sb}}} = 50.3\,\mathrm{Hz} \ , \qquad (96)$$

1.2 times higher than with a soft spring-box. Furthermore, a finite element simulation with vertically infinitely stiff IP-legs results in resonance frequencies only 1.9 times higher than with realistic IP-legs. That implies, that not only the IP-legs need to be re-designed in order to stiffen the internal resonances, but also the spring-box needs to be stiffened.

The simulated resonance frequencies of the three lowest vertical spring-box modes are at 37.9 Hz, 38.3 Hz and 41.0 Hz. The lowest mode can be approximated as a roll mode around an axis parallel to the y-axis, the second mode is an oscillation around the x-axis and the third mode is mainly a vertical bounce motion.

In order to verify this model, the spring-boxes of both AEI-SASs were excited in the rx, ry and z-direction and the frequency responses to the payload motion were measured (see Figure 67). The vertical actuators, located in between spring-box and GAS-filter-keystone, were therefore used to drive the spring-box in the vertical and vertical-tilt directions. The signal was recorded by a horizontal geophone, mounted on top of the payload. When the spring-box is driven in the z-direction mainly a resonance at 34.6 Hz is excited, when driven in the rx-direction mainly a resonance at 31.2 Hz is excited and when driven in the ry-direction mainly a resonance at 30.5 Hz is excited. Albeit the order of the modes coincides with the simulation, the simulated mode frequencies are up to approximately 1.3 times higher, even though the model accounts for a soft spring-box. This can be explained by the difference in the connection between the single components of the spring-box; in reality, they

1 The difference in finite element simulation and analytical model is mainly due to the geometry of the tube. The two windows at the top of the leg weaken the structure (see figure 66).

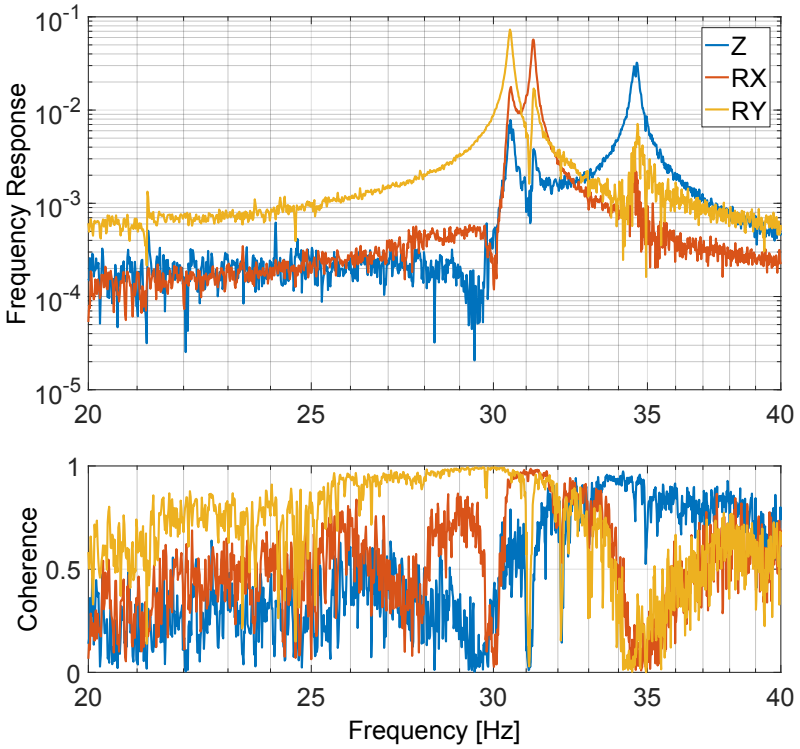


**Figure 67:** Driven vertical spring-box resonances in the south-table. The mode shape and mode frequency were investigated in order to verify the finite element model shown in figure 65 and to characterize the AEI-SAS. For this measurement, the vertical voice coil actuators were used to act on the spring-box. The plot shows the frequency response from the actuation to a horizontal sensor on top of the payload. When actuating the spring-box in the ry-direction, mainly a 30.5 Hz oscillation couples to the payload. rx-direction excitation causes a strong 31.2 Hz resonance, whereas driving the spring-box in the z-direction mainly excites the bounce mode at 34.6 Hz. The ry actuation couples strongest to the sensor since it was aligned with the x-axis. For the other directions, the coherence is only high around the resonances. The same measurement was done in the central table and can be found in the appendix D

are bolted, whereas the model's geometry is monolithic. Section 14.1 discusses this issue in more detail.

# 12 THE FLUOREL STAGE

The 13 Hz and 17 Hz horizontal GAS-filter mode is highly undesirable in the AEI 10 m prototype experiments since some of the mirror suspensions have vertical (bounce) modes very close to this frequency. Any overlap of these resonances would result in strongly enhanced mirror motion. Initially, we attempted to stiffen the GAS-filters in the horizontal direction by installing additional structures. However, this approach was discarded because either the low vertical stiffness of the GAS-filters was compromised or because the functional vertical range of the stiffening structure was too small. A second approach, the inclusion of an additional, well-damped spring-mass stage in the AEI-SAS proved to be very successful. Three vacuum compatible rubber pads (fluorel) were placed between the payload and the 'intermediate plate', a 113 kg aluminum plate mounted on top of the GAS filters, in the position where previously this plate was rigidly connected to the payload.

## 12.1 SIMPLIFIED ONE-DIMENSIONAL MODEL INCLUDING THE FLUOREL STAGE

Figure 68 compares the two configurations using simple one-dimensional models. The model for the original design consists of two horizontal springs. One represents the IP-legs with a stiffness of $k_{ip} \approx 500\,\mathrm{N/m}$ and the other represents the horizontal GAS filter stiffness $k_{hGAS}$. The eigenfrequencies of the coupled system are 0.1 Hz and 17 Hz, as described above in section 11.2.2.

Implementing the Fluorel stage results in a three-spring, three-mass system. Also in the derivation of this model the horizontal IP-leg spring is neglected since its influence on the dynamics of the much stiffer upper part of the AEI-SAS model is small. Accordingly, a system consisting of two springs and two masses is described in the following calculations. The parameters used in the model are listed in table 11.

In analogy equation 90 the potential energy of the fluorel spring is

$$V_{fl} = \frac{1}{2} k_{fl} (x_i - x_{tt})^2 \quad . \tag{97}$$

from the Lagrangian function of the system

$$L = \frac{1}{2} m_{sb} \dot{x}_{sb}^2 + \frac{1}{2} m_i \dot{x}_i^2 + \frac{1}{2} m_{tt} \dot{x}_{tt}^2 - V_{hGAS} - V_{fl} \tag{98}$$

| Parameter | Value | Description |
|---|---|---|
| $k_{hGAS}$ | $2.9 \times 10^6$ N/m | Horizontal GAS-filter stiffness |
| $k_{fl}$ | $1.1 \times 10^6$ N/m | Horizontal fluorel pad stiffness |
| $m_{sb}$ | 331 kg | spring-box mass |
| $m_p = m_{tt} + m_i$ | 900 kg =785 kg+115 kg | payload mass = table top mass + intermediate plate mass |
| $x_{sb}$, $x_p$, $x_{tt}$ and $x_i$ | | spring-box position, payload position, table top position and intermediate plate position |

**Table 11:** horizontal spring-box model coefficients.

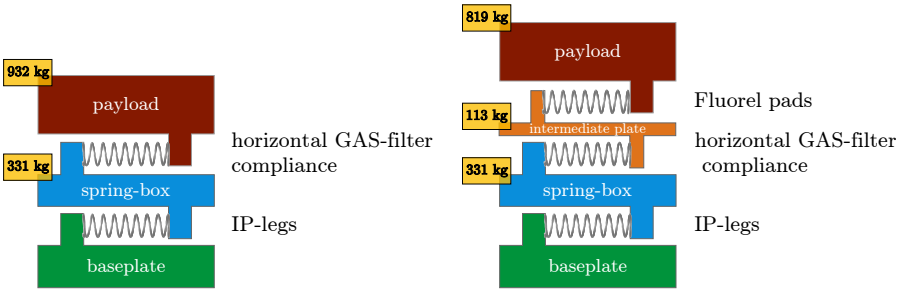


**Figure 68:** Simplified one-dimensional models of the isolation system show how the implementation of a Fluorel stage changes the horizontal eigenfrequencies.
Left: Original system. The IP-leg spring ($k_{ip} \approx 500$ N/m) connects the spring-box (331 kg) to the ground. The horizontal GAS-filter spring $k_{hGAS} = 3 \times 10^6$ N/m connects the spring-box to the 932 kg payload (including the intermediate plate). The common mode of this system is at 0.1 Hz, the differential mode is at 17 Hz.
Right: Fluorel pads are placed between intermediate plate and payload. The horizontal stiffness of this spring is approximately $1.2 \times 10^6$ N/m, resulting in eigenfrequencies of 0.1 Hz, 9 Hz, and 34 Hz. Even though one of the internal resonances is at a lower frequency than before, the lossy Fluorel pads strongly damp these oscillations.

its equation of motion can be derived as

$$\mathcal{M}\ddot{\vec{x}} = -\mathcal{K}\vec{x} \ . \tag{99}$$

Here $\mathcal{M}$ is the mass matrix

$$\mathcal{M} = \begin{pmatrix} m_{sb} & 0 & 0 \\ 0 & m_i & 0 \\ 0 & 0 & m_{tt} \end{pmatrix} , \tag{100}$$

and $\mathcal{K}$ is the stiffness matrix

$$\mathcal{K} = \begin{pmatrix} -k_{hGAS} & k_{hGAS} & 0 \\ k_{hGAS} & -(k_{hGAS} + k_{fl}) & k_{fl} \\ 0 & k_{fl} & -k_{fl} \end{pmatrix} . \tag{101}$$

The squared angular frequency matrix is accordingly $\Omega = \mathcal{M}^{-1}\mathcal{K}$. Diagonalizing $\Omega$ leads to the eigenfrequencies of the system,

$$\begin{aligned} f_1 = -\{ [\, & (k_{hGAS}^2 m_i^2 + (2k_{hGAS}^2 - 2k_{hGAS}k_{fl}) m_{sb} m_i \\ & + (k_{fl}^2 + 2k_{hGAS}k_{fl} + k_{hGAS}^2) m_{sb}^2) m_{tt}^2 \\ & + ((2k_{fl}^2 - 2k_{hGAS}k_{fl}) m_{sb}^2 m_i \\ & - 2k_{hGAS}k_{fl} m_{sb} m_i^2) m_{tt} + k_{fl}^2 m_{sb}^2 m_i^2 \,]^{1/2} \\ & - ((k_{fl} + k_{hGAS}) m_{sb} + k_{hGAS} m_i) m_{tt} \\ & - k_{fl} m_{sb} m_i \}^{1/2} \frac{1}{2\pi\sqrt{2 m_{sb} m_i m_{tt}}} , \end{aligned} \tag{102}$$

$$\begin{aligned} f_2 = -\{ [\, & (k_{hGAS}^2 m_i^2 + (2k_{hGAS}^2 - 2k_{hGAS}k_{fl}) m_{sb} m_i \\ & + (k_{fl}^2 + 2k_{hGAS}k_{fl} + k_{hGAS}^2) m_{sb}^2) m_{tt}^2 \\ & + ((2k_{fl}^2 - 2k_{hGAS}k_{fl}) m_{sb}^2 m_i \\ & - 2k_{hGAS}k_{fl} m_{sb} m_i^2) m_{tt} + k_{fl}^2 m_{sb}^2 m_i^2 \,]^{1/2} \\ & + ((k_{fl} + k_{hGAS}) m_{sb} + k_{hGAS} m_i) m_{tt} \\ & + k_{fl} m_{sb} m_i \}^{1/2} \frac{1}{2\pi\sqrt{2 m_{sb} m_i m_{tt}}} , \end{aligned} \tag{103}$$

and the common DC drifting mode

$$f_3 = 0 . \tag{104}$$

When connecting the system to via the IP-leg spring to the ground, as shown in the left part of figure 68, $f_3$ naturally becomes the IP-leg mode with a resonance frequency of 0.1 Hz.

An approximation of the fluorel pads' stiffness, listed in table 11, was obtained experimentally, by simply measuring the deformation of

the rubber under a defined load. This way the Young's modulus was estimated to

$$E_{fl} \approx 11\,\mathrm{MPa} \ . \tag{105}$$

This value agrees well with a Young's modulus measurement with a similar rubber [153]. Since the fluorel pads are horizontally sheared in the here described modes, not the Young's modulus but rather the Shear Modulus is of interest, which is defined for isotropic materials as

$$G = \frac{E}{2(1+\nu)} \ , \tag{106}$$

where $\nu$ is the material's Poisson's ratio [128]. Most materials have Poisson's ratio values ranging between 0 and 0.5, resulting in a Shear Modulus of $G_{fl} = 4.6 \pm 0.9\,\mathrm{GPa}$. For 3 fluorel pads with an area of $A_{fl} = 50\,\mathrm{mm} \times 16\,\mathrm{mm}$ and a compressed height of approximately $h_{fl} = 10\,\mathrm{mm}$.[1] The corresponding horizontal fluorel stage stiffness of is accordingly

$$k_{fl} = \frac{A_{fl}}{h_{fl}} G_{fl} = 1.10 \pm 0.22\,\frac{\mathrm{N}}{\mathrm{m}} \ . \tag{107}$$

From equation 102 and 103 and the parameters listed in table 11 one can estimate the resonance frequencies of the system displayed in the left part of figure 68.

At $f_1 = 8.94^{+0.64}_{-0.76}\,\mathrm{Hz}$ the spring-box and the intermediate plate oscillate together between the heavy payload and the ground. The resonance at $f_2 = 32.55^{+0.65}_{-0.64}\,\mathrm{Hz}$ corresponds to the oscillation of the intermediate plate between the payload and the spring-box[2]. Since the lossy Fluorel pads' springs are involved in the latter two modes, they are well damped and do not significantly influence the AEI-SAS performance at low frequencies.

## 12.2 SIMPLIFIED THREE-DIMENSIONAL FINITE ELEMENT MODEL INCLUDING THE FLUOREL STAGE

For the AEI-SAS with the fluorel stage the simplified three-dimensional finite element model, introduced in section 11.2.3, is extended by the intermediate plate and the fluorel stage. As well as the GAS-filters the fluorel stage is modeled as three sets of springs (described in more detail in the appendix B). The spring constant of the horizontal springs is $k_{fl}$

1 A more exact measurement and estimation of the fluorel pads elastic properties would be possible, but was postponed due to time limitations. Furthermore, for the model and the application presented here, the stiffness accuracy is sufficient.

2 The high number of fractional pats of the resonance frequencies is displayed to point out that the inaccuracy in the fluorel's elastic properties is rather insignificant for this one-dimensional approximation

(see table 11). The vertical stiffness was determined from the fluorel's Young's modulus (see equation 105). Each of the three vertical springs has accordingly a stiffness of $k_{vfl} = 8.8 \times 10^5$ N/m.

The IP-legs were excluded from this simulation, since the influence of the horizontal the IP-leg stiffness is negligible for the horizontal differential spring-box -intermediate plate - table top dynamics. This way geometry is much simpler and the simulation is more efficient, due to a lower number of elements.

As in the model discussed in section 11.2.3 the spring-box and the table top are modeled as stiff quadratic plates with the right mass and approximately the right horizontal dimensions. This simplifies the model while delivering sufficiently realistic results. However, the intermediate plate's geometry is designed close to reality for this simulation. This way the eigenmodes of this structure, constrained by GAS-filters and fluorel pads can be studied. The discussion of these modes can be found in the section 5.1.3 (they are displayed in figure 26) since they are for the most part bending modes of the structure. In this section only the rigid body modes of the system are discussed, naturally also the compliance of the intermediate plate has a small influence on these mode frequencies. Furthermore, these the bending modes of the intermediate plate have not been experimentally identified. If they will be found to compromise the AEI-SAS's performance, additional damping structures between the intermediate plate and the table top could be easily installed.

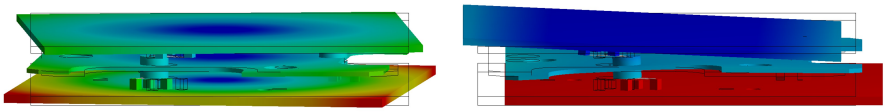

(a) 6.5Hz (b) 8.8Hz

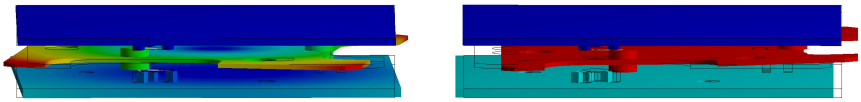

(c) 24.6Hz (d) 29.9Hz

**Figure 69:** Finite element model of the rigid body modes of the AEI-SAS including the fluorel stage. The IP-legs are excluded from the model, instead, the motion of the plate representing the spring-box is restricted to the horizontal direction. Here the yaw ((a) and (c)) and one of each horizontal translational ((b) and (d)) modes are displayed. The two horizontal modes orthogonal to the those displayed have approximately the same shape and resonance frequency. In this simulation, the intermediate plate geometry is close to reality. The simulated bending modes of the intermediate plate are discussed in section 5.1.3.

The mode shapes and the resonance frequencies of the rigid body modes from the finite element simulation are shown in figure 69. Only one of each horizontal transitional modes ((b) and (d)) is displayed

since the second has a very similar shape and frequency. These oscillations correspond to the modes derived in the one-dimensional model in section 12.1. The simulation shows clearly the common oscillation of intermediate plate and spring-box against the relatively still table top (b). In (d) the intermediate plate oscillates between relatively still table top and spring-box. However, the recoil on the lighter spring-box is stronger than on the heavier table top.

The same differential motion can be seen in the rotational degree of freedom ((a) and (c)). However, the resonance frequencies are lower than those of the corresponding translational oscillations.

As mentioned above, the fluorel springs are involved in all these oscillations, thus the modes are all well damped. Furthermore, a second, well-damped isolation stage is introduced in the AEI-SAS.

## 12.3 EXPERIMENTAL COMPARISON OF THE AEI-SAS WITH AND WITHOUT THE FLUOREL STAGE

The substantial performance improvement provided by the additional stage is shown in figure 70. It is clearly visible, that the 17 Hz resonances have vanished. In this final configuration, three fluorel pads were placed

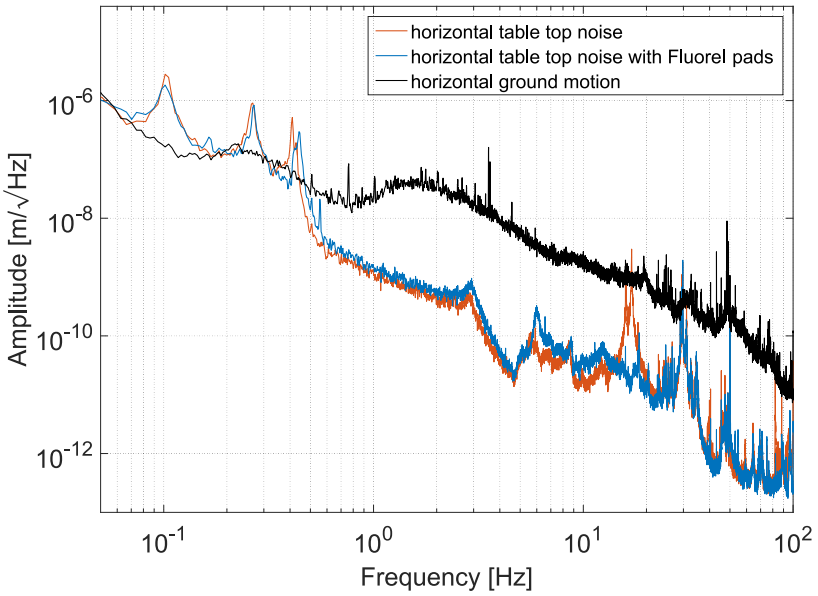


**Figure 70:** A comparison between horizontal payload motion with (blue) and without (red) the additional Fluorel stage. The strong 17 Hz resonance is no longer visible. Unlike the spectrum in figure 54, this measurement was recorded in air, resulting in excess motion between 1 Hz and 10 Hz.

on top of the intermediate plate close to the horizontal position where the GAS-filters are connected to the underside of the plate. This is the same position that was simulated in the finite element model described

above. Different configurations of number, dimensions, and position of the fluorel pads were tested in the shaker stand before the one presented here was found to perform best.

The comparative measurements shown in figure 70 were recorded on the AEI-SAS placed in the vacuum envelope, but in air, resulting in excess motion between 1 Hz and 10 Hz. Hence, the well-damped new modes, described in the models, are not visible in this measurement.

# 13 IMPROVING THE IP-LEG GEOMETRY

As discussed above, a wider isolation window of the AEI-SAS requires stiffer vertical spring-box resonances and therefore, vertically stiffer IP-legs. There are several requirements for such a design:

- substantially higher stiffness in the vertical direction
- a horizontal stiffness close to the design value of the old IP-legs
- compatibility with the existing mechanics and attachment mechanisms
- it should allow a similar range of horizontal motion (about one centimeter)
- it should be made from materials that can be machined and modified in-house
- a CoP compensation system must be able to handle the new mass and mass distribution of the leg.

In the following, a geometry referred to as the 'symmetric IP-leg' is discussed. It has a very simple geometry and meets the requirements itemized above.

Parts of the results presented in this chapter are published in ref. [57].

## 13.1 PRINCIPLE OF THE SYMMETRIC IP-LEG

Starting from a simple IP-leg model with a lower flexure, a rigid leg and an upper flexure one can easily derive the optimal geometry for a high vertical stiffness for a given horizontal stiffness. The horizontal stiffness of an IP-leg with the effective length $l$, where the restoring force is provided by the lower flexure, is

$$k_h = \frac{\kappa}{l^2} \ , \tag{108}$$

where

$$\kappa = E_t I_a / l_{flex} \tag{109}$$

is the angular stiffness of the flexure determined by the Young's modulus of the flexure material, $E_t$, and the flexure length, $l_{flex}$. The second moment of area of a cylinder with diameter $d$ is $I_a = \pi d^4/64$. $k_h$ is the

purely mechanical stiffness. The horizontal stiffness of the AEI-SAS also depends on the gravitational anti spring as $k_{ip} = k_h - Mg/l$.

The stiffness of an IP-leg with one flexure at the top and one at the bottom that both contribute to the total horizontal stiffness can be described as two IP-legs coupled in series, each with half of the total length. The resulting horizontal stiffness is

$$\begin{aligned} k_h &= \frac{4}{l^2}\frac{\kappa_1\kappa_2}{\kappa_1+\kappa_2} \\ &= \frac{\pi E_t}{16 l^2 l_{flex}}\frac{(d_1 d_2)^4}{d_1^4+d_2^4} \quad , \end{aligned} \tag{110}$$

assuming the two flexures have the same length.

The vertical stiffness of such an IP-leg is only dependent on $d^2$, the cross-sectional area. Neglecting the stiffness of the leg itself, the total vertical spring constant is

$$k_v = \frac{\pi E_t}{4 l_{flex}}\frac{(d_1 d_2)^2}{d_1^2+d_2^2} \quad . \tag{111}$$

The ideal thickness of the flexures can be found by solving equation 110 for $d_2$ and inserting it into equation 111

$$d_2 = d_1 \sqrt[4]{\frac{k_h}{B d_1^4 - k_h}} \quad . \tag{112}$$

The new formulation of equation 111 results in

$$k_v(d_1) = \frac{A d_1}{\sqrt{\frac{B d_1^4}{k_h} - 1} + 1} \quad , \tag{113}$$

with $A = \frac{E_t \pi}{4 l_{flex}}$ and $B = \frac{E_y \pi}{64 l_{fl} l^2}$. Finding $d_1$ where $k_h$ is maximal and comparing it to equation 112 shows that the highest vertical stiffness for a given horizontal stiffness is achieved by using flexures with equal thickness at the top and bottom of the leg. This symmetric IP-leg design is discussed in the upcoming sections in more detail.

## 13.2 DESIGN OF THE SYMMETRIC IP-LEG

This section depicts the mechanical design of the symmetric IP-legs. A detailed discussion of the specific choice of the flexures dimensions and calculations of the CoP tuning can be found in the following sections.

The symmetric IP-leg design is much simpler than the original design. As discussed in chapter 3, IP-legs were used in many different systems over time. The older ones did not have CoP tuning. The legs were therefore designed to be as light as possible. Furthermore, the vertical stiffness was not as much an issue as it is in the HAM-SAS, the AEI-

SAS and the EIB-SAS, since in the older systems (the Superattenuator, the LIGO-SAS or the TAMA-SAS) the mass mounted on top of the IP-legs was relatively low and the legs were relatively long. Thus, the lowest IP-leg modes were the bending modes, not the modes caused by its vertical compliance. However, Advanced Virgo's multiSAS's (see section 3.6.1) lowest internal resonances are at frequencies around 50 Hz and associated with tilt and bounce modes of the upper stage on the IP-legs [59]. These kind of systems also could potentially benefit from vertically stiffer IP-legs.

As shown in figure 71, it mainly consists of two identical flexures, a 48 mm diameter stainless steel tube, an upper and lower cap, and an adapter bar. This bar connects directly to the adapter bell of the old design, from which the spring-box is suspended (see figure 44). The center of the bar is bolted to the upper flexure. This, in turn, is bolted to the upper cap. The upper and lower cap are welded to the stainless steel tube. The flexure's threads are fine pitch threads, in order to increase the rigidity of the leg-flexure connections. The lower flexure is the link between the lower cap and the connection to the AEI-SAS's baseplate.

The lower cap features a rim on which the CoP tuning bell from the old design is installed. Due to the shorter new flexures, the new design includes a shimming ring to account for the lower height of the rim (see figure 72). Furthermore, the position of the eddy current damper unit (see figure 44 and section 13.3.2) inside the upper bell needed to be lowered, whereby the magnets are aligned with the stainless steel tube. Otherwise, the original AEI-SAS design remains unchanged. The distance from the bar to the bottom of the lower flexure therefore needs to be 508 mm. That leads to the component dimensions shown in table 12.

The original IP-leg flexures were made from maraging steel, a material chosen because it combines very high strength (1.94 GPa ultimate tensile strength), very low creep, and a low loss angle [68, 69]. However, maraging steel has a long lead-time for procurement. For the new design, this material was substituted with Titanium grade 5. This material is easy to machine, has a low internal loss and high strength [154, 155]. The leg itself is made from a stainless steel tube with 2 mm wall thickness, making it much stiffer than the original 1 mm wall thickness aluminum leg.

The symmetric IP-legs are designed to carry a load which is closer to the design value derived in ref. [24]. Each of the old IP-legs carries about 75 kg less than originally intended. Hence, the requirement on additional mass in the spring-box is relatively tight so that the maximum mass of the spring-box damper design was limited (see section 15.1.3). Furthermore, auxiliary stiffening structures cannot be retrofitted into the spring-box due to the mass limit.

**Figure 71:** Mechanical design and photograph of the symmetric IP-leg. The new IP-leg consists of an identical upper and lower flexure made from titanium grade 5 and a stainless steel leg. An upper and a lower cap are welded to the stainless steel tube with 2 mm wall thickness. The bottom cap features a rim on which the original CoP tuning structure can be installed. The hole in the steel tube, visible in the photograph, is for venting the structure during the evacuation of the vacuum system.

The horizontal design stiffness of the symmetric IP-legs was chosen to carry about 35 kg more mass than the old IP-legs. That provides the freedom to design efficient stiffening and damping structures.

## 13.3 MODELING THE SYMMETRIC IP-LEG

| Parameter | Value | Description |
|---|---|---|
| $E_t$ | $\sim 115\,\mathrm{GPa}$ | Young's modulus of Titanium Grade 5 [156] |
| $d$ | $0.0083\,\mathrm{m}$ | thickness of the flexures |
| $l_{flex}$ | $0.025\,\mathrm{m}$ | flexure length |
| $k_h$ | $\sim 10000\,\mathrm{N/m}$ | horizontal stiffness of a single symmetric IP-leg |
| $\kappa$ | $1072\,\mathrm{N\,m}$ | horizontal stiffness of a single symmetric IP-leg |
| $l_{leg}$ | $0.405\,\mathrm{m}$ | length of the steel tube and the IP-leg caps |
| $l$ | $0.4533\,\mathrm{m}$ | effective length of the symmetric IP-leg |
| $l_{b1}$ | $0.1001\,\mathrm{m}$ | distance from pivot point of the IP-leg to counter weight |
| $l_{b2}$ | $0.0413\,\mathrm{m}$ | distance from pivot point of the IP-leg to the effective CoM of the bell |
| $m_{b2}$ | $0.216\,\mathrm{kg}$ | effective bell mass |
| $m^*$ | $1.72\,\mathrm{kg}$ | effective leg mass |
| $M_{cw}$ | variable | counter weight mass |

**Table 12:** symmetric IP-leg parameters. (compare to figure 72)

### 13.3.1 *Horizontal transmissibility of the symmetric IP-leg*

The thickness and the length of the two flexures was chosen to be $d_{flex} = 8.3\,\mathrm{mm}$ and $l_{flex} = 25\,\mathrm{mm}$. That leads to a horizontal stiffness of

$$k_h = \frac{\pi E_t d^4}{32 l^2 l_{flex}} \approx 10000\,\mathrm{N/m} \ . \tag{114}$$

The resulting maximum payload mass of a single symmetric IP-leg is, according to equation 28,

$$M_{max} = 462\,kg \ . \tag{115}$$

A resonance frequency of 0.1 Hz is achieved by a payload mass of

$$M_{0.1} = \frac{k_h}{(2\pi \cdot 0.1)^2 + \frac{g}{l}} = 454\,kg \ , \tag{116}$$

that is 35 kg more than the payload mass of the old IP-legs.

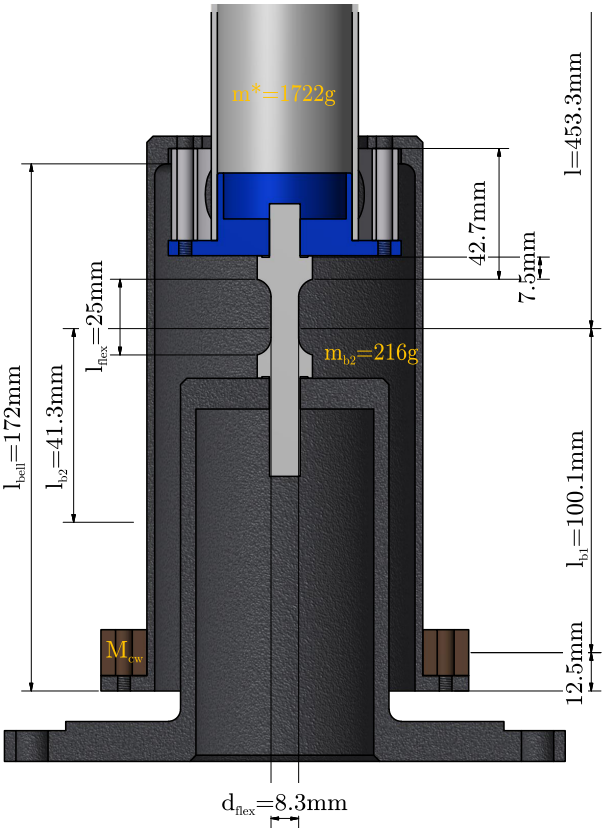


**Figure 72:** Geometry and dimension of the CoP tuning structure of the symmetric IP-leg. This figure shows the lower part of the IP-leg (compare to figure 41). The CoP tuning structure as well as the foot the IP-leg is resting on are identical to the old IP-leg's geometry. The unintuitive choice of dimensions $(l, l_{b1}, l_{b1})$ and masses $(m^*, m_{b2})$ is chosen with respect to the IP-leg's pivot point, which is at $\frac{1}{3}$ of the flexure height.

A simple model of the horizontal isolation capabilities of the symmetric IP-legs can be developed in analogy to the model of the old IP-legs shown in section 7.1.5. The dimensions of the symmetric IP-leg and its

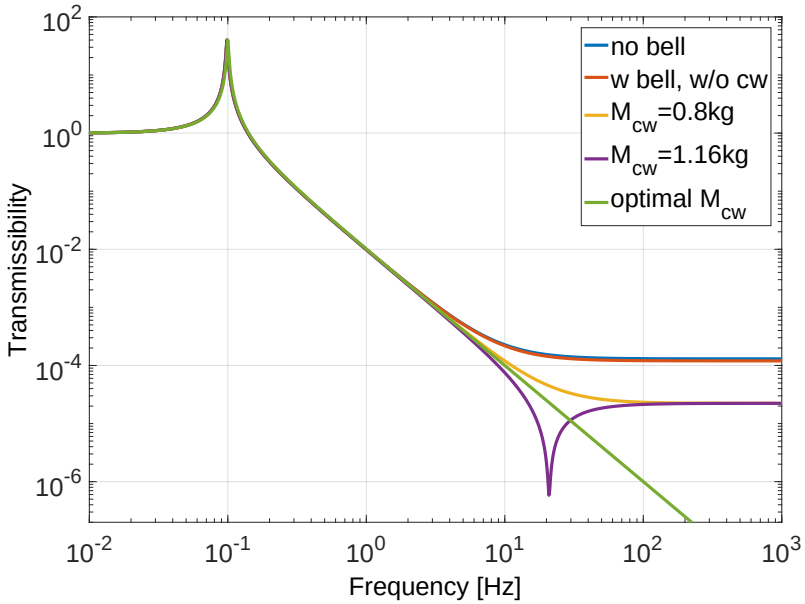


**Figure 73:** Amplitude of the symmetric IP-leg's transmissibility with CoP tuning (compare to figure 43 and equation 59). The transmissibility is plotted for different tuning settings. The configuration without any CoP tuning (blue) results in an already quite good isolation performance at higher frequencies of $\beta_h = 2.7 \times 10^{-5}$. By attaching the bell to the IP-leg, the CoP plateau does change only marginally (red). The ideal tuning is achieved by a counterweight mass of approximately 0.98 kg (green). Examples of satisfying realistic tunings are shown in yellow and purple. A CoP plateau height of $\beta_h = 4.6 \times 10^{-6}$ is achieved by counterweight masses of 0.8 kg or 1.16 kg.

CoP tuning structure are displayed in figure 71. The length of the rigid part of the IP-leg is

$$l = l_{leg} + 2 \times \left(7.5 \times 10^{-3} + \frac{2}{3} l_{flex}\right) = 0.4533\,\mathrm{m} \ . \tag{117}$$

It is composed of the stainless steel tube's length with the upper and lower cap and the distance from the cap to the bending point of the upper and lower flexure (see section 7.1.2). The effective counter weight and bell lengths $l_{b1}$ and $l_{b2}$ and the effective bell and leg mass $m_{b2}$ and $m^*$ are derived in the same way as in equation 56 and 57. The additional reduction of the lengths is due to the 30 mm high adapter piece between leg and bell (see figure 71). The amplitude of the transmissibility of the symmetric IP-leg is derived as in section 7.1.5. It is plotted in figure 73 for different CoP tuning adjustments. The ideal tuning mass is

$$M_{cw}^{ideal} = \frac{l^2 m^* - 6 m_{b2}\left(l_{b2} l + \frac{4}{3} l_{b2}^2\right)}{6 l_{b1}(l + l_{b1})} \approx 0.98\,\mathrm{kg} \ . \tag{118}$$

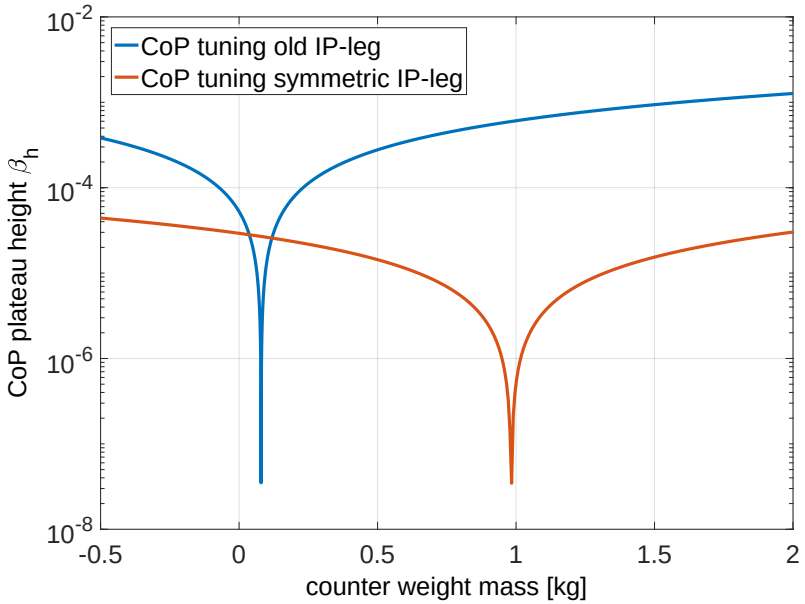


**Figure 74:** Comparison of the old and new IP-leg's CoP tuning. The plot shows the absolute value of CoP plateau height $\beta_h$ as a function of the counterweight mass. The steep roll-off on a logarithmic scale illustrates the difficulties in CoP tuning. The slope of the symmetric IP-leg's tuning curve is much lower than the curve of the old design. Furthermore, the symmetric IP-leg without counterweights (and bell) has already a much lower isolation plateau than the old IP-leg. That simplifies achieving a good CoP tuning.

This can easily be achieved by a ring of four slightly enlarged counter weights and a set of smaller tuning masses.

The process of CoP tuning is illustrated in figure 74. It shows the strong influence of the payload mass on the CoP plateau height. Even though the symmetric IP-leg is heavier than the old IP-leg, $\beta_h$ is lower without any CoP tuning. The slope of the new IP-legs' tuning curve is also lower, which simplifies the CoP adjustment.

### 13.3.2 *Internal resonances of the symmetric IP-leg*

Internal resonances of single components of the AEI-SAS can compromise the isolation performance. They are potentially harmful, particularly when their eigenfrequency is close to the measurement window at 200 Hz. Here the internal resonances of the old and the new IP-leg are investigated and compared. Figure 75 shows finite element simulations of the four lowest IP-leg mode shapes and frequencies. In this model, the upper and lower flexure are regarded rigidly fixed in the position where they are connected to the baseplate and the spring-box. The lowest internal resonances of the old IP-leg are horizontal oscillations of its top. Due to their mode shapes, they can couple strongly to the

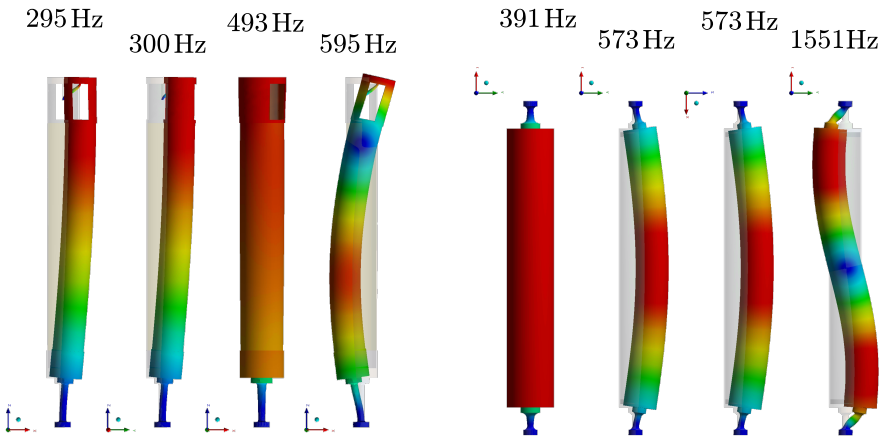


(a) old IP-leg (b) symmetric IP-leg

**Figure 75:** Finite element simulation of the internal resonances of the old (a) and new (b) IP-leg. The lowest modes of the old IP-leg are horizontal oscillations of its top part, due to the soft upper flexure. The symmetric IP-leg's lowest mode is a rotation around its long axis and approximately 100 Hz higher.

upper parts of the AEI-SAS. The AEI-SAS design includes therefore an eddy current damper unit. It consists of a set of neodymium magnets located inside the upper bell (see figure 44). With this setup, the leg modes can be efficiently damped.

The symmetric IP-leg's structure is much stiffer and its lowest internal resonance is approximately 100 Hz higher than the one of the old IP-leg. It is a rotational mode around the leg's long axis. Due to the higher mass of the 2 mm wall thickness stainless steel tube the mode frequency is lower than the old IP-leg's equivalent at 493 Hz. Even though this mode does not couple strongly to the spring-box, the eddy current damper unit is included in the design of the new IP-legs.

The anti-node of the two neighboring higher internal resonances is in the vertical center of the IP-leg. Hence, they are hardly influenced by the damping unit. However, their resonance frequency is relatively high and retrofitting of a damping unit is uncomplicated.

### 13.3.3 *Symmetric IP-leg stress model*

The bending stress in the symmetric IP-leg's flexures is higher than in the old ones since the new flexures are much shorter. Finite element simulations helped to design the new flexures with a tolerable maximum stress. In order to reduce the peak stress, the transition from the flexible cylindrical part to bottom and top were smoothed. The finite element simulations of the new IP-leg design (figur 76) show that displacing the payload by 10 mm results in a maximum bending stress of approximately 60 % of the yield [157]. Although this is much closer to yield than equivalent maraging steel flexures (which were at approx-

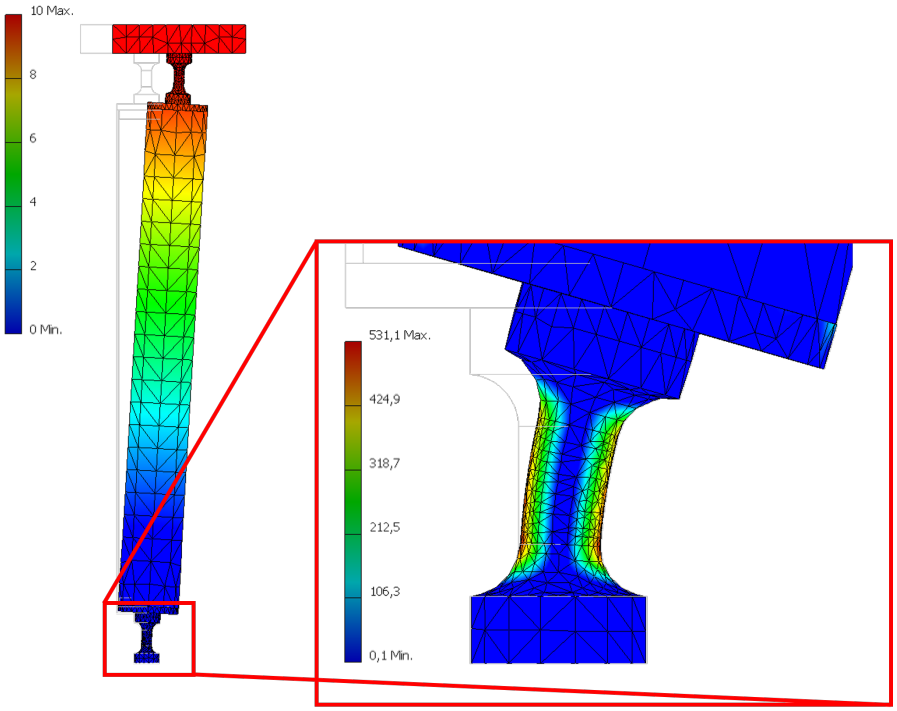


**Figure 76:** Finite element simulation of the maximum equivalent tensile stress in the new IP-leg's flexures. The IP-leg was deflected by 1 cm, while keeping the adapter bar parallel to the ground, in order to simulate the realistic deformation in the AEI-SAS. The left part of the figure shows a finite element simulation of the IP-leg's deformation, the right part represents the stress in the lower flexure. It is identical to the stress in the upper flexure. The color scale on the left represents the total deformation in millimeters, the one on the right is the stress in MPa. The simulation illustrates, that the rounded corners at top and bottom of the flexure distribute the stress equally on the bending part.

imately 20 % of yield), the margin is still sufficient considering that in normal operation the payload translates less than 1 mm. In order to prevent any damage, the horizontal AEI-SAS motion is limited to 0.8 mm.

## 13.4 HORIZONTAL AND VERTICAL STIFFNESS OF THE SYMMETRIC IP-LEG

The properties of the new IP-legs were modeled and tested experimentally before installing them in the AEI-SAS.

### 13.4.1 *Horizontal stiffness*

The symmetric IP-leg's flexures were designed to be modifiable in terms of horizontal stiffness by changing their thickness. The design procedure

of the flexures started with values from the simplified analytical model (see section 13.3.1). The stiffness and the maximum stress were then evaluated in finite element simulations of a more realistic CAD-model shown in figure 76. The difference between simulation and reality can be relatively large. Not only inaccuracies in the meshing of the model, the machining of the real part or inhomogeneities in the material can have an influence, but already the uncertainty of the material property definition can make a difference between reality and simulation. The Young's modulus of titanium grade 5, for instance, is defined between 110 and 119 GPa [156]. The flexures were therefore designed to be slightly thicker than required. By this means the stiffness could be adjusted after it was measured experimentally by reducing the flexures diameter.

The angular stiffness of each flexure was measured individually. Therefor the symmetric IP-legs were installed on the AEI-SAS's baseplate. A defined horizontal force was applied to the structure at the position where the upper flexure is connected to the leg. Simultaneously the resulting deflection was measured at the same position. This way the stiffness $k_h^{test}$ was determined. The angular stiffness of this configuration is of the order of

$$\kappa = k_h^{test} l_{test}^2 = \frac{\pi E_t d^4}{64 l_{flex}} \approx 1071.6\,\mathrm{Nm} \ , \tag{119}$$

where $l_{test} = 0.4292\,\mathrm{m}$ is the length from the IP-leg's pivot point to the position where the force is acting. The results of this measurement are presented in table 13 and the results of a finite element simulation of this experiment are shown in figure 77. The latter differs strongly from the measurement. Reasons for that could be, as mentioned above, due to the uncertainty of the material properties. Furthermore, the mounting of the leg is not included in the simulation. Whereas the adapter foot between flexure and baseplate is relatively stiff, the baseplate itself is more likely to cause a decrease of the bending stiffness of the IP-leg.

Due to the strong difference between simulation and reality, the flexures were first produced with a diameter of 9 mm, which was then iteratively reduced until the satisfying stiffness was achieved.

The horizontal stiffness of the entire IP-leg, when implemented in the AEI-SAS, follows from equation 110 and 115

$$k_h = \frac{2\kappa}{l^2} \approx 10578\,\mathrm{N/m} \ . \tag{120}$$

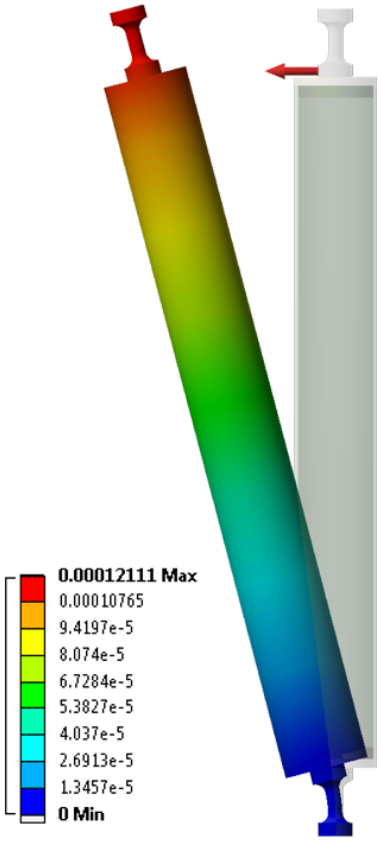


**Figure 77:** Finite element simulation of the experimental setup for measuring the horizontal bending stiffness of the IP-leg. A force of 1 N is applied to the foot of the upper flexure and the displacement is measured at the same position. The minimum level of Young's modulus of titanium grade 5 results in a stiffness of 6545 N/m. The upper limit of the stiffness is at 11167 N/m. Respectively, the angular stiffness of the flexure is between 1206 Nm and 2057 Nm. The scale in the figure shows the displacement in meter for $E_t = 115$ GPa.

### 13.4.2 *Vertical stiffness*

The vertical stiffness of the symmetric IP-legs can be approximated by the vertical stiffness of two cylinders with the parameters of the flexures and one tube with the dimenions of the leg;

$$\begin{aligned} k_v^{flex} &= \frac{\pi E_t d^2}{4 l_{flex}} = 2.5 \times 10^8 \,\mathrm{N/m} \\ k_v^{leg} &= \frac{\pi E_s (d_{leg1}^2 - d_{leg2}^2)}{4 l_{tube}} = 5.1 \times 10^8 \,\mathrm{N/m} \ , \end{aligned} \tag{121}$$

with the Young's modulus of stainless steel $E_s = 193$ GPa [158] and $d_{leg1} = 0.048$ m and $d_{leg2} = 0.044$ m the inner and outer diameter of the stainless steel tube $d_{leg1}$ and $d_{leg2}$.

The resulting total vertical stiffness of the symmetric IP-leg is

$$k_v = \frac{k_v^{flex} k_v^{leg}}{k_v^{flex} + 2 k_v^{leg}} = 5.1 \times 10^7 \,\mathrm{N/m} \ . \tag{122}$$

The vertical stiffness of the new IP-legs was also measured in an auxiliary experiment. As a measure for the vertical stiffness the vertical bounce mode was measured after loading both legs individually with the same mass (see figure 80). The mass was chosen to be lower than the

| Flexure # | Stiffness in N/m | Angular stiffness in Nm |
|---|---|---|
| 1 | $5846.3 \pm 340.5$ | $1077.0 \pm 62.7$ |
| 2 | $6040.9 \pm 285.9$ | $1112.8 \pm 52.7$ |
| 3 | $5629.2 \pm 80.5$ | $1037.0 \pm 14.8$ |
| 4 | $5665.9 \pm 65.3$ | $1043.7 \pm 12.0$ |
| 5 | $6310.9 \pm 242.6$ | $1162.5 \pm 44.7$ |
| 6 | $5904.8 \pm 190.5$ | $1087.7 \pm 35.1$ |
| Average | $5899.7 \pm 304.5$ | $1086.8 \pm 72.2$ |

**Table 13:** Horizontal bending stiffness and angular stiffness of the symmetric IP-leg. The table shows the results of the experiment determining the new IP-leg flexure's stiffness. All six flexures needed for the three IP-legs were measured individually to detect possible irregularities. The values correspond to the final version of the flexures. The structure was mounted on the AEI-SAS baseplate and the force was applied to the foot of the upper flexure.The stiffness and the standard deviation of each flexure results from several measurements in which the pulling force was varied and the corresponding horizontal displacement was measured at the position where the force was applied. The last row of this table shows the average stiffness of all measurements. The stiffest flexure is less than 8 % stiffer than the softest flexure.

final payload mass, in order to keep the experimental setup simple and stable. The vertical transmissibility was measured by placing one geophone on the ground and one on the suspended mass. Figure 79 shows the vertical transmissibility of both IP-leg designs. The bounce mode of the old and new legs are 76 Hz and 164 Hz respectively. The resulting vertical spring constant of the old IP-leg is $9.1 \times 10^6$ N/m. Comparing this to the finite element simulation in figure 66, the simulated stiffness is approximately 17 % higher than the measured one. That difference could be explained by the relatively complicated designed setup, containing many individual parts. Whereas the geometry is simulated with rigid connections the assembly's connections base on bolting or simply friction in the realistic system. The vertical stiffness also depends on where the force is acting on the structure. Whereas the simulated force is uniformly distributed over the adapter bar, it is acting on confined areas in the real setup.

The new symmetric IP-leg is with $42.4 \times 10^6$ N/m more than 4 times stiffer than the old design. That is close to the simulated value. The measured stiffness is only approximately 8 % lower. In combination with the

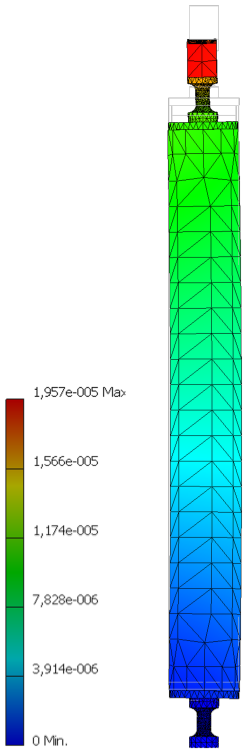


**Figure 78:** Finite element simulation of the symmetric IP-leg's vertical stiffness. A force of 1 N is acting on the adapter bar, connecting the upper flexure and the upper bell. In comparison to the old IP-leg, the symmetric IP-leg deforms uniformly over its whole length, due to its simpler structure (compare to figure 66). The resulting vertical stiffness is $k_v = 5.1 \times 10^7$ N/m. The color scale in the figure is the total deformation in millimeters.

stiffening of the spring-box, this increases the frequency of the spring-box modes greatly. If the spring-box was assumed to be a rigid body, the bounce mode on the new IP-legs would be at approximately 100 Hz, although the bending of the spring-box will lower the mode frequency. As discussed in section 14.4.2.3 a bounce mode as high as 70 Hz was achieved with the symmetric IP-legs and a stiffened spring-box.

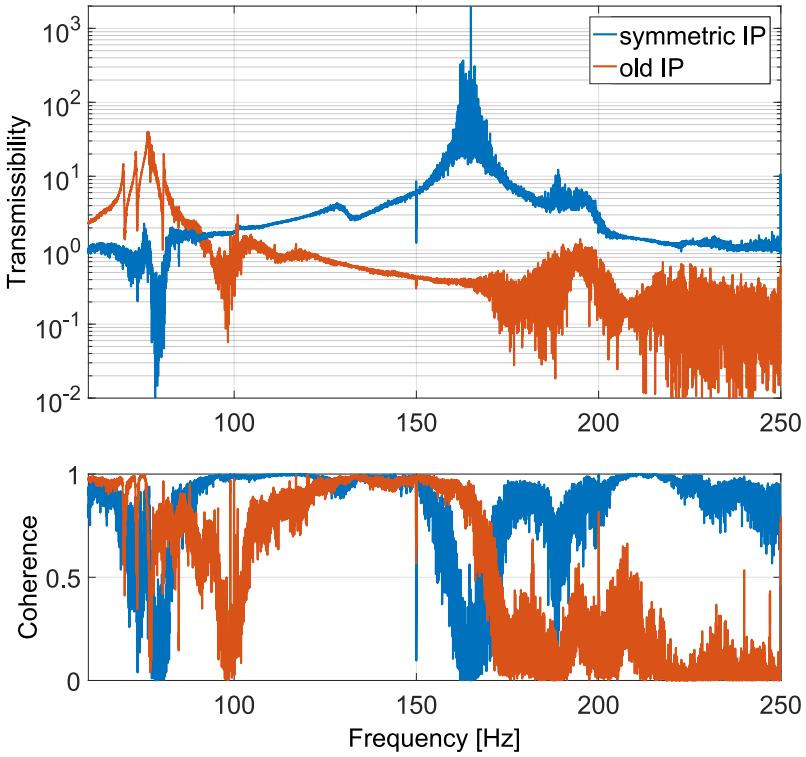


**Figure 79:** Vertical transmissibility of old and new IP-legs: The improvement in vertical stiffness from the new design was experimentally tested by measuring the fundamental bounce mode of both IP-legs. Each leg was loaded with a 40 kg mass and the transmissibility was measured. The measurement result shows that the stiffness of the new design is more than four times higher than the original design. The dip in the symmetric IP-leg curve at 80 Hz and in the old IP-leg curve at 98 Hz is caused by the tilt of the suspended mass. The experimental setup is shown in figure 80.

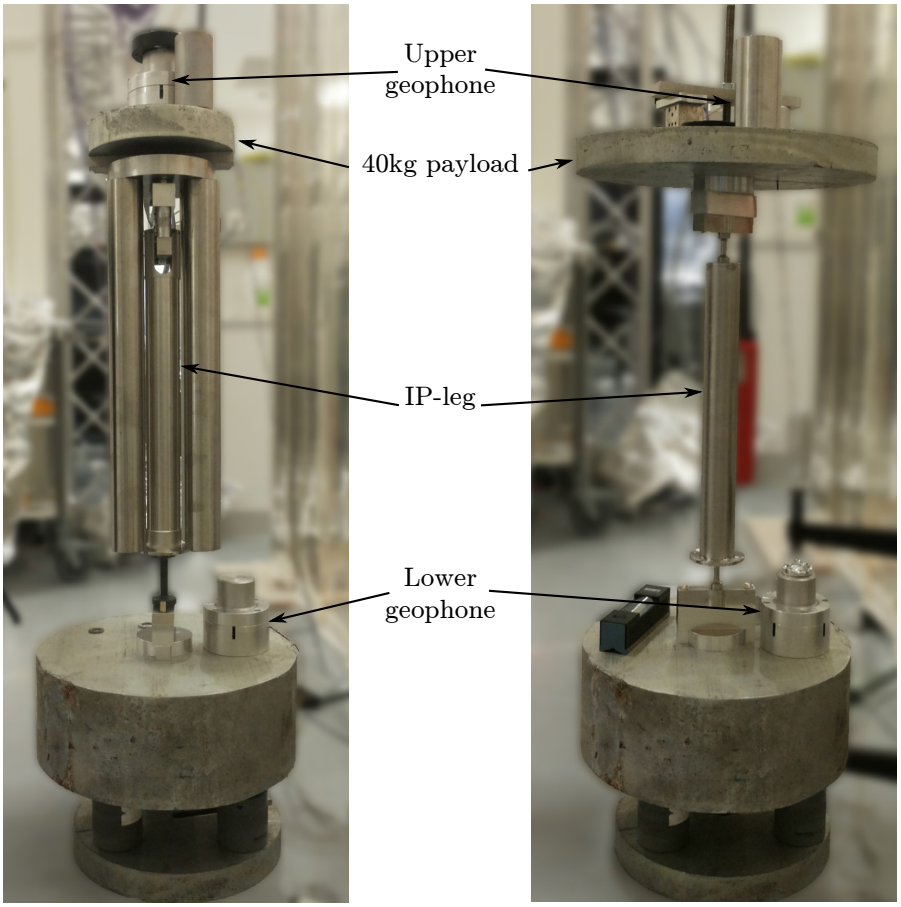


**Figure 80:** Photographs of the experimental setup for measuring the vertical stiffness of the old (left) and the symmetric (right) IP-leg. Both IP-legs were loaded with a 40 kg mass. Due to geometric constraints, the mass was mounted in two different ways. A movable mass on top of the construction was used to level the payload. The IP-legs were mounted on top of a heavy block of steel, which was resting on three vertically adjustable feed. The vertical transmissibility of ground motion was measured by two L-22D geophones. One was placed on the steel block, the other one on top of the payload. The results of the measurements are shown in figure 79

# 14

# SPRING-BOX STIFFENING

As discussed in the chapter above, the vertical spring-box resonances limit the isolation window to high frequencies. Shifting those modes to higher frequencies would widen the low frequency isolation window and reduce the rms-motion of the payload since ground motion declines with increasing frequency.

The vertical spring-box modes are caused by a combination of the old IP-leg's low vertical spring constant and the soft bending stiffness of the spring-box itself (see section 11.3). Additionally to the new IP-legs, discussed above, a spring-box reinforcement was designed to shift the vertical spring-box modes to higher frequencies. This section discusses the principles, the design, the implementation and the verification of this stiffening structure.

Without any stiffening structure, the upper and lower spring-box would only be interconnected by the GAS-filter reinforcements. The modes resulting from such a geometry are shown in the lower part of figure 89. The original stiffening plates (see figure 23) have a relatively small effect. The first two AEI-SAS units show the lowest three spring-box resonances between 30 Hz and 35 Hz (see figure refsbdriven-res). The goal of the spring-box stiffening is to shift those modes to as high frequencies as possible, without compromising the AEI-SAS's performance or influencing its functionality. Starting from the original design's insufficient stiffening plates, additional reinforcement structures were simulated, optimized and implemented in the third AEI-SAS unit.

As described in section 11.3, the 'monolithically' simulated spring-box modes differ from the measured resonance frequencies in the real system with bolted connections. In order to test the influence of the contact between the individual components of a system, a side-experiment was performed. Here the stiffness of a bolted aluminum structure is compared to the stiffness of the same structure with glued and bolted connections. This experiment is described in the following section, followed by a discussion of the spring-box stiffening structure.

As well as the new IP-legs, the here introduced stiffening method is only suitable for the third AEI-SAS unit. Since the first two tables are operating in the vacuum system, populated with optics, disassembling the systems would hardly be feasible without severely delaying the 10 m prototype experiments. In order to reduce the rms motion in the first two AEI-SAS units, the internal resonances are inertially damped, as described in section 15.

In the following, the spring-box design without the new auxiliary stiffening is referred to as original design.

## 14.1 GLUE-BOLTING EXPERIMENTS

Complex mechanical systems such as the AEI-SAS often suffer from the finite stiffness of their individual components. Internal resonances can disturb measurements and in the case of the AEI-SAS can limit the seismic isolation performance.
The bending stiffness of the AEI-SAS's spring-box in combination with the low vertical stiffness of the IP-legs are currently causing the lowest undamped internal resonances of the AEI-SAS. FEM simulations imply a much stiffer spring-box than the measurements of the real system show. The FEM model assumes rigid connections, however, in reality, there are bolted contacts. In a simple experiment the bending mode frequency of a bolted I-beam shaped aluminum assembly at 690 Hz could be increased to 1133 Hz by both gluing and bolting metal surfaces together.

These results are also summarized in a LIGO document [159]

## 14.2 BOLTING VS. GLUE-BOLTING

The bending stiffness of a simple rod is proportional to the third power of its thickness, which explains, why a monolithic rod of the thickness $d$ is much stiffer in bending than two parallel bars, each of the thickness $d/2$. Bolting a structure increases the contact area, but does not provide a rigid connection. Welding is in many cases, not an option, due to deformations or practicality. A simple experiment should show, if glue-bolting can provide a rigid connection and make composite systems behave monolithic in a sub 3 kHz frequency range. It will provide an indication whether glue-bolting the spring-box could improve the AEI-SAS´s performance.

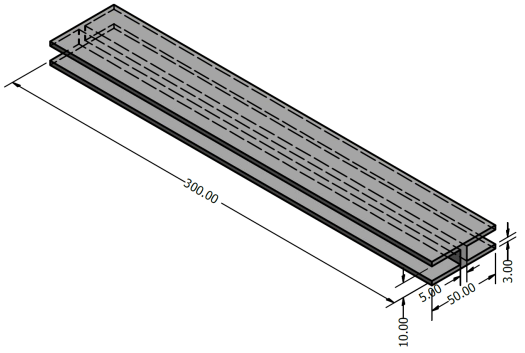


**Figure 81:** Outline and dimensions (in units of millimeter) of the experimental assembly. (the 6 M3 bolts and the bolt holes are excluded)

In this simple experiment, we chose a structure which resembles a single segment of the spring-box´s stiffening structure: An I-beam shaped aluminum assembly (see figure 81) was first bolted-only and later glue-bolted. The fundamental bending mode frequencies were compared to verify an increase in rigidity, due to glue-bolting the structure. FEM simulations of the structures supported the experiment.

## 14.3 EXPERIMENT, SIMULATIONS AND RESULTS

### 14.3.1 *Experimental setup*

At first, the aluminum I-beam was bolted tightly. The structure was suspended from a single thin wire in its center. The wire was coiled in order to lower the influence of its vertical stiffness (see figure 82). The oscillations were exited by tapping the short edges of the I-beam (in order to excite the bending mode) and measured using a microphone.

**Figure 82:** Experimental setup to measure the resonance frequencies. The I-beam was suspended in its center from a steel wire. In order to reduce the vertical stiffness of the wire, and therefore its influence on the structure's resonance frequencies, it was curled. The modes were excited by tapping the edges of the structure. The beam's vibration was measured with a microphone.

The frequencies of the two lowest resonances were measured at 649 Hz and 690 Hz. Due to the mechanical mode shape, the amplitude of the peak and the direction of excitation, the 690 Hz resonance could be iden-

tified as the bending mode, and the 649 Hz resonance as the twisting mode (for comparison see figure 85).

The same structure was disassembled and the full contact surfaces were covered with a thin layer of two component epoxy glue. The structure was then bolted tightly together so that only a thin film of glue was left in between the plates. After the glue was cured, the twisting mode shifted to 730 Hz and the bending mode shifted to 1133 Hz. A third resonance peak was excited at 2472 Hz.

### 14.3.2 *Simulations*

The results from the glue-bolted structure fit remarkably well to the FEM simulations. As shown in figure 83, a free-floating monolithic I-beam was modeled. The lowest mode is the twisting mode at 755 Hz, the modeled bending mode at 1132 Hz is only 0.09 % higher than the measurement. The third measured resonance presumably corresponds to the horizontal bending mode (figure 83 right) with a modeled frequency of 2464 Hz.

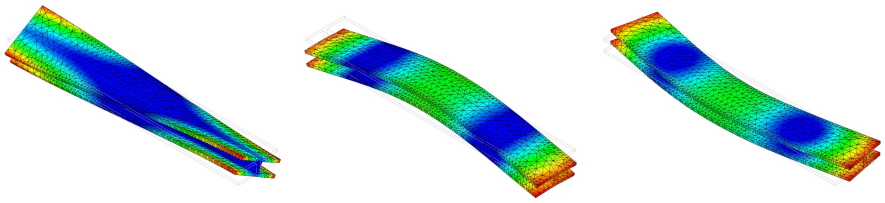

**Figure 83:** FEM simulation of the glue-bolted structure. left: twisting mode at 755 Hz, center: vertical bending mode at 1132 Hz, right: horizontal bending mode at 2464 Hz

A second FEM simulation helps to understand the behavior of the 'bolted-only' structure. The surfaces are not connected over the whole connection area, but only in the areas, where the bolts are located. In order to keep the simulation and the mesh simple, 0.5 mm high cuboids connect the middle bar with the upper and lower plate, as shown in figure 84. (Reducing the cuboids height to the half had a negligible influence on the resonance frequencies).

**Figure 84:** Simplified 'bolted-only' model: The upper and lower plate are connected only in the positions where the bolts are.

This model represents the minimal contact area and is not the realistic case where the contact area is undefined. The simulation shows

a bending mode at 518 Hz and a twisting mode at 624 Hz (figure 85). The bending resonance frequency is strongly influenced by the contact area. Also, the number of low frequency modes is much higher for the 'bolted-only' model. The monolithic model has only 5 eigenmodes below 3 kHz, whereas the 'bolted-only' model has 28. Those are mainly the oscillations of the individual plates. These results suggest that bolting provides rigid contact only in a limited area.

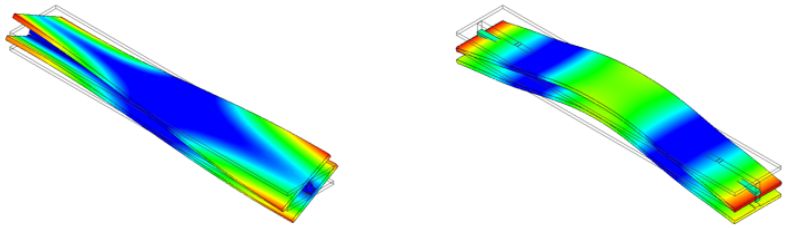

**Figure 85:** FEM simulation of the bolted structure. left: twisting mode at 518 Hz, right: vertical bending mode at 624 Hz

### 14.3.3 *Results*

Increasing the contact area of a bolted structure significantly increases its stiffness. In this experiment, glue-bolting made the structure's bending mode close to equal to the simulated bending mode of a monolithic structure. The results of the experiment compared to the simulation of the monolithic structure is shown in table 14.

| mode # | bolted only [Hz] | glue-bolted [Hz] | simulation [Hz] |
|---|---|---|---|
| 1 | 649 | 730 | 755 |
| 2 | 690 | 1133 | 1132 |
| 3 | not measurable | 2472 | 2472 |

**Table 14:** Resonance frequency measured in the glue-bolting experiment compared to the simulation of the monolithic structure. Glue bolting increased the resonance frequency of the structure by a factor of 1.12 (twisting mode) and 1.64 (vertical bending mode). The glue bolted structure's mode frequencies are remarkably close to the simulation.

A model with reduced contact area showed a significantly lower bending resonance frequency and a much higher number of low frequency eigenmodes. The quality factor change of the resonances was not investigated in this experiment, but from the ringdown time of the modes

in the acoustic band, the glue-bolted structure seemed to have significantly less internal damping.
These results suggest that glue-bolting the spring-box's stiffening structure could have a positive effect on the AEI-SAS's isolation performance.

## 14.4 DESIGNING THE SPRING-BOX STIFFENING STRUCTURE

The spring-box consist of two relatively soft aluminum plates. Three GAS-filters, the motorized springs, the horizontal accelerometers and the blades of the tilt stabilization are connected to the lower plate. Particularly the approximately 50 kg GAS-filters lower the bending resonance frequencies of the system. Three stiffening plates around the central spring-box hole and six additional plates frame the three IP-legs (see figure 23). These plates and the reinforcement structure surrounding the GAS-filters interconnect the upper and lower spring-box plate. Unfortunately, these original stiffening plates are hardly oriented in the mode's bending curvature direction of a spring-box without stiffening (see the lower part of figure 89).

In figure 65 the three lowest spring-box modes are illustrated. Ideally one would implement additional stiffening plates, following the bending curve of the upper and lower spring-box plate. Since the mode shape is strongly influenced by the GAS-filters, they are naturally in the way of such an ideal stiffening. Also, the other components located in the spring-box limit space for additional stiffening structures.

The performance of different stiffening structures was studied with the aid of finite element simulations or experiments. These included I-beams-like reinforcement structures which were mounted below the lower spring-box plate, viton-aluminum structures which were clamped between the two spring-box plates, and additional stiffening plates, which simulated to be rigidly connected to upper and lower spring-box plate. The latter system showed the most promising results. As discussed above, the assembly needs to be glue-bolted to achieve a close to simulation stiffness.

Various stiffening plate configurations were analyzed for their feasibility and reinforcement properties. The geometry introduced in the following increased the vertical spring-box resonance frequencies the most, while it does not interfere with the subsystems installed in the spring-box.

Figure 86 shows a CAD-drawing of the spring-box including the new stiffening structure (red). These plates are made of aluminum and are 12 mm thick. That allows them to fit in the tight spaces between original stiffening plates and GAS-filter baseplates. Holes were placed in the plates in positions where they do not compromise the stiffness, but allow limited maintenance of the inner components of the spring-box.

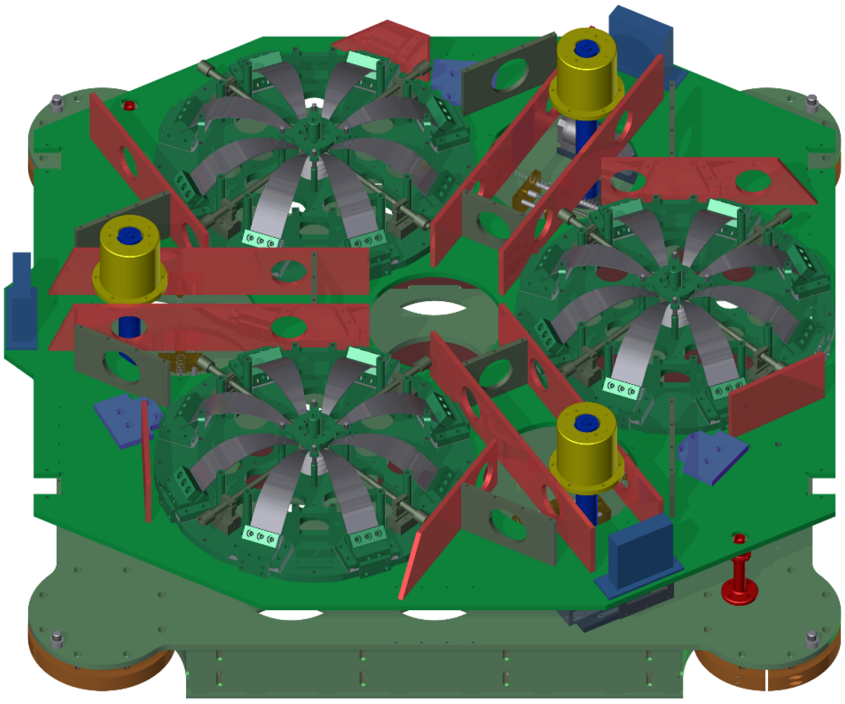

**Figure 86:** CAD-drawing of the spring-box including the new stiffening structure (red). The new stiffening structure is designed to increase the bending rigidity of the spring-box. Since space is constrained by various components, this unsymmetrical geometry was chosen. Holes in the stiffening plates ensure visibility of the inner components and make them reachable from the outside.

Since the upper spring-box plate does not cover all of the lower plate, the sides of the stiffening plates in those positions are chamfered.

### 14.4.1 *Stiffening structure simulations*

In order to analyze the performance of the new stiffening structure, it was included in the simplified spring-box model, which is discussed in section 11.3.1. The IP-leg stiffness matrix (represented by three sets of springs) was changed to the symmetric IP-leg's measured vertical stiffness values (see section 13.4.2). Resonance frequencies of the four lowest resonances with and without the stiffening structure were compared. Figure 87 shows the mode shape of these resonances. The pictures are overlaid with the stiffening structure to illustrate the choice of their positioning. The six long plates stiffen the region between the IP-leg - spring-box connection and the spring-box center. The shorter plates reinforce the corners of the spring-box by surrounding the GAS-filters. The relative mode shapes of the stiffened spring-box's lowest three resonances are similar to the mode shapes of the original design (compare to figure 65). The reason for this is that these two lowest resonances

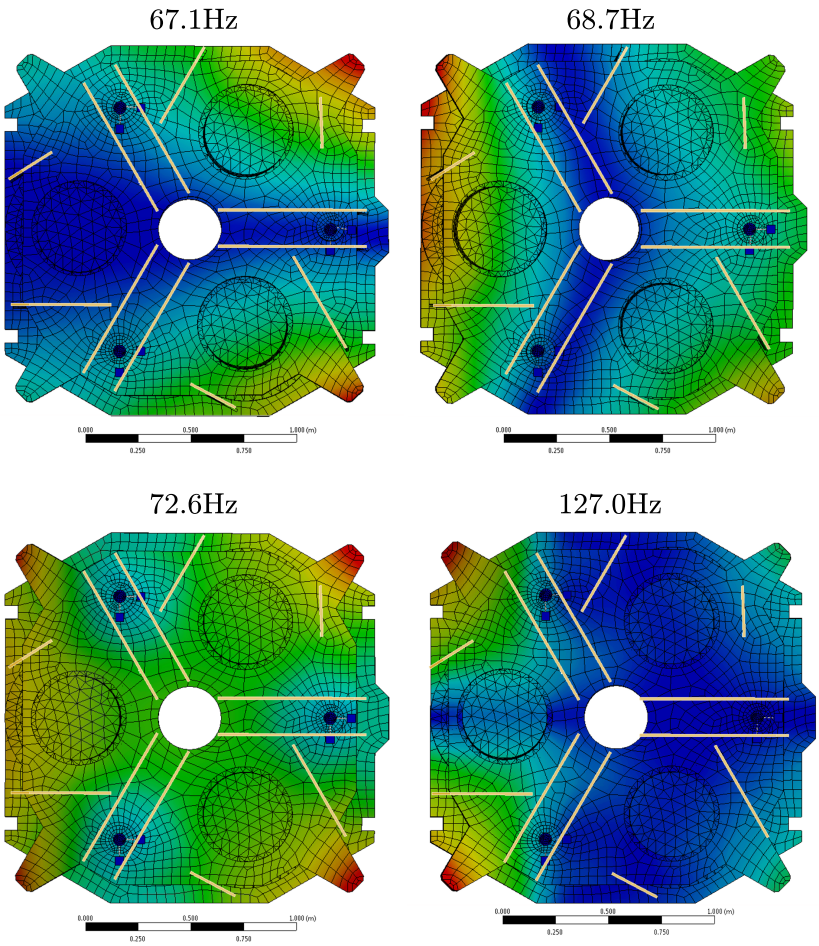


**Figure 87:** Mode shape of the four spring-box modes with the lowest resonance frequency. The first two modes are oscillations around the two horizontal axes, the third mode is the bounce mode of the spring-box. The influence of the spring-box bending is significantly reduced with respect to the old design. The fourth mode is an alternating bending oscillation of the spring-box about its two diagonal axes. The color scheme represents the total deflection from no deflection (blue) to maximal deflection (red). In order to visualize the choice of stiffening plate's positions, it is highlighted in the geometry.

are mainly oscillations around the two horizontal axes, and the third mode is similar to the bounce mode of a rigid spring-box. The bending stiffness has less influence in the mode shape than in the resonance frequency.

Table 15 shows the results of the stiffening study. The second column shows the simulated resonance frequencies of the spring-box, suspended from the symmetric IP-legs. The new IP-legs alone increases the lowest two resonance frequencies by approximately 25 % and the bounce mode by approximately 35 % with respect to the system where the spring-box is suspended from the old IP-legs (compare to figure 65).

| mode # | w/o stiffening resonance frequency [Hz] | w stiffening resonance frequency[Hz] | frequency shift factor |
|---|---|---|---|
| 1 | 50.2 | 67.1 | 1.34 |
| 2 | 50.8 | 69.0 | 1.36 |
| 3 | 61.5 | 77.8 | 1.26 |
| 4 | 97.7 | 127.0 | 1.30 |

**Table 15:** Results from the finite element stiffening study. The table shows the four lowest resonance frequencies of the spring-box model suspended from springs imitating the symmetric IP-leg stiffness matrix. Here the measured stiffness values of the IP-leg are used (compare to section 13.4.2). The second column shows the mode frequency of the spring-box without axillary stiffing, the second column shows the values of the spring-box including the new stiffening structure. In the last column the gain in frequency shift is displayed.

The 2nd column of the table shows the results of the spring-box model without additional stiffening. The corresponding mode shapes are shown in figure 87. As displayed in the last column, the 1st, and 2nd modes are strongest influenced by the stiffening structure. The 3rd mode is stronger influenced by the increased vertical IP-leg stiffness since it is mainly a vertical bounce motion of the whole spring-box.

The here presented structure caused the largest frequency shift of the tested geometries. If, for instance, the six central stiffening plates are excluded from the model, and only the outer six plates provide additional rigidity, the average frequency shift of the lowest four modes would only be 9 %. The influence of the only the inner six plates is slightly larger with an average frequency shift of 16 %.

In addition to table 15, table 16 compares the resonance frequencies of the original design's model (without stiffening and with the old IP-legs) with the improved configuration. The bounce mode is stiffened the most, with an almost doubled resonance frequency. These promising results justify major changes in the AEI-SAS's design in order to improve its mid-frequency isolation performance. The experimental validation of these design changes is discussed in the following.

### 14.4.2 *Experimental verification*

Even though results from finite element simulations of such complex assemblies as the spring-box vary from the reality, They do give a good idea of how changing this geometry will affect its behavior.

| mode # | original design resonance frequency [Hz] | improved design resonance frequency [Hz] | frequency shift factor |
|---|---|---|---|
| 1 | 37.6 | 67.1 | 1.78 |
| 2 | 38.0 | 69.0 | 1.82 |
| 3 | 39.9 | 77.8 | 1.95 |
| 4 | 86.2 | 127.0 | 1.47 |

**Table 16:** Comparison of the old spring-box's simulated resonance frequencies with the improved design. The original design is a model of the first two AEI-SAS units, featuring the old IP-legs and original spring-box design. The new design improves the resonance frequencies by up to almost double of the old design. In both simulations the measured IP-leg stiffness values were used.

In order to have a good reference on how well the auxiliary spring-box reinforcements stiffens the vertical spring-box modes the here presented measurements were all done in a system, mounted on the symmetric IP-legs. Just like the simulations, the vertical spring-box modes were measured without stiffening and these results are then compared to a reinforced system. The reinforced system is characterized in a state where all component connections are bolted, here referred to as bolted only, and in a state where the whole spring-box assembly is bolted after all contact areas were covers with glue, here referred to as glue-bolted.

#### 14.4.2.1 *Reference measurement*

Figure 88 shows the reference measurement without stiffening structure. These plots represent the transmissibility from baseplate motion to spring-box motion. The data was recorded by two vertical L-22D geophones. One was placed on the baseplate, one on the spring-box. In order to be able to assign the three modes to the simulated mode shapes the geophone was placed in different locations on the spring-box. They are named after their cardinal directions, as shown in figure 88. The north-west corner has a large vertical amplitude in all three resonances, therefore they are all dominant in the measurement. The center of the south edge is a point on the rotation axis of the lowest mode. The second and the third mode have an amplitude maximum at this position. The measurements in these two positions allow distinguishing between the two lowest modes: The unstiffened spring-box oscillates around the south-north axis at 33.5 Hz and around the east-west axis at 35 Hz. The slight resonance frequency shifts between the measurement are caused by shifting the geophone in different positions

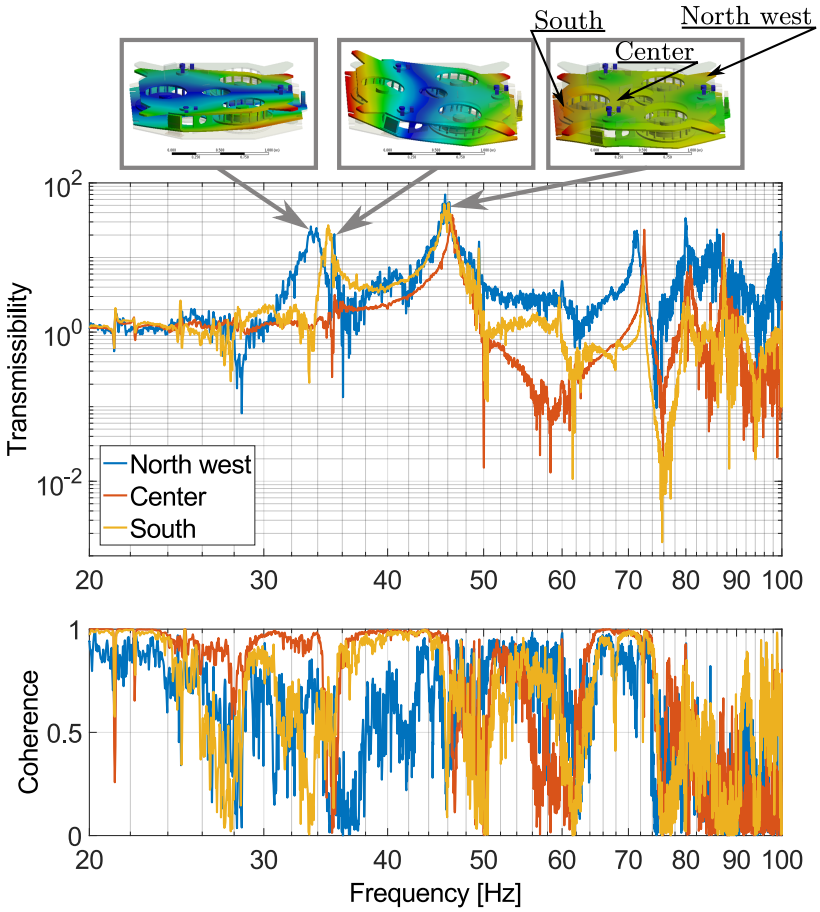


**Figure 88:** Original spring-box design's vertical resonances. The plot shows the transmissibility of baseplate motion to three locations on the spring-box. The baseplate was driven by ground motion. The three measurements in combination with the simulated mode shapes enable identifying the lowest three resonances. The lowest mode is the oscillation around the spring-box's south-north axis at 33.5 Hz. Rotated by 90° is the second mode at 35 Hz. The bounce mode has a resonance frequency of 46 Hz. Note that compared to the measurement in figure 67, where the spring-box was suspended from the old IP-legs, here the system is mounted on the symmetric IP-legs. That increases the mode frequencies by an average factor of approximately 1.2.

and thereby changing the mass distribution. The measurement where the geophone is placed in the center of the spring-box confirms the first two. The lowest prominent resonance in this transmissibility amplitude is the bounce mode at 46 Hz. This mode has a high amplitude in all three positions. Even though the measured resonance frequencies are lower than in the simulation, the mode shapes and the mode order is consistent with the simulation. The following results show, that finite element simulations supported the reinforcement procedure strongly.

These measured resonance frequencies are about an averaged factor of 0.7 lower than the simulation. As mentioned above, the reason for

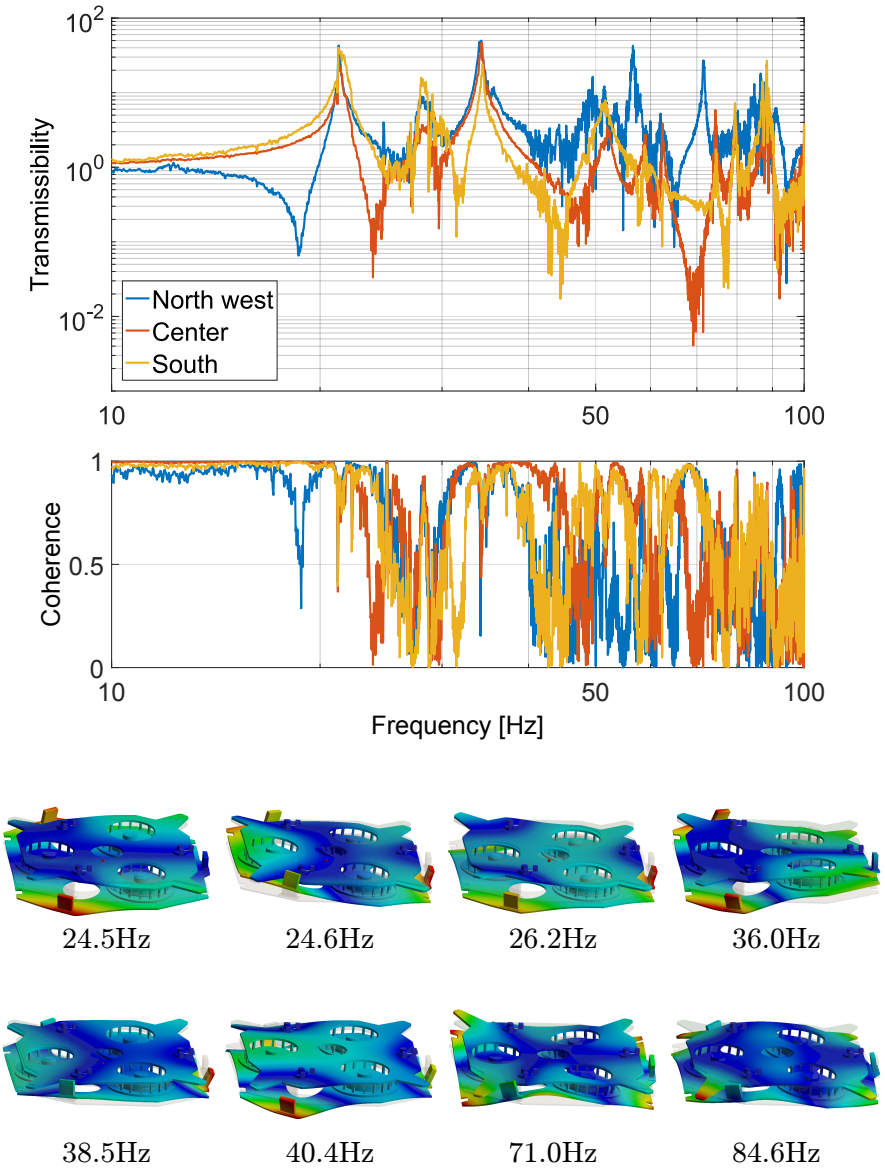


**Figure 89:** Vertical spring-box resonances with a bad component connection. This experiment shows the influence of loose bolt joints. The bolts connecting the original stiffening plates with the upper spring-box plate were therefore slightly loosened but not removed. The bolts in the stiffening structure around the GAS-filters were still tight. The measurement of the transmissibility in the same locations as before shows much lower mode frequencies. A finite element simulation of the spring-box where the original stiffening plates are removed gives an idea of possible mode shapes.

that is mainly the less rigid assembly connections of the real spring-box with respect to the simulation. An additional experiment illustrates the strong influence of component contact: For the measurements shown in figure 88 the identical setup and geophone positions as in the reference measurement (figure 88) were used. Only the bolts which connect the upper plate to the original stiffening structure were loosened by ap-

proximately half a bolt turn. As expected, this has a strong influence on the spring-box modes. The lowest resonance is with 21 Hz is approximately 0.6 times lower than in the case where the bolts were tightened. Furthermore, numerous resonance peaks were measured below 100 Hz. A finite element simulation of the spring-box without the original stiffening structure gives an idea of how those modes are shaped (see the lower part of figure 89 ). Naturally, the presented simulation is only a rough approximation since a correct model of the contact areas in the loose bold case is hardly possible.

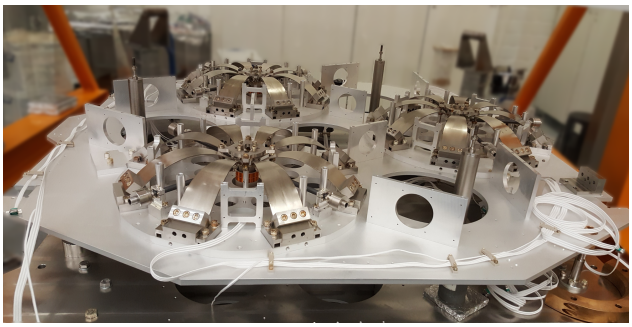

a) original stiffening design

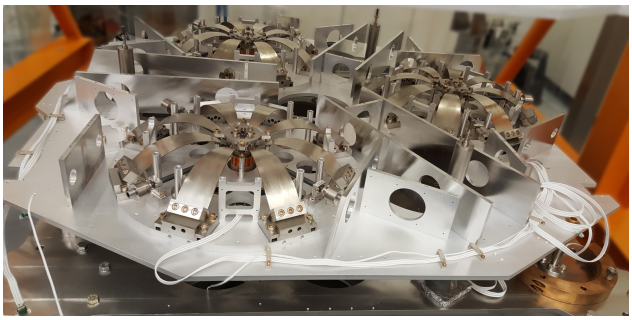

b) with new auxiliarys tiffening plates

**Figure 90:** Spring-box with (b) and without (a) stiffening structure. The photograph shows the spring-box without the upper spring-box plate during the assembly of the third AEI-SAS unit. In the lower picture 12 additional stiffening plates are bolted (not glued yet) to the lower spring-box plate (compare to figure 86).

#### 14.4.2.2 *Bolted only measurement*

The results from the bolted only measurement are shown in figure 91. 12 additional stiffening plates were installed in the spring-box. Figure 90 shows a photograph of the spring-box equipped with the new stiffening structure compared to a photograph of the old design.

Two to three bold connections at the top and bottom side of each plate join them with the upper and the lower spring-box plate. Those bolt connections were fastened tightly. The mode frequencies and mode shifts with respect to the reference measurement are shown in table 17. The unglued stiffening structure increases the vertical spring-

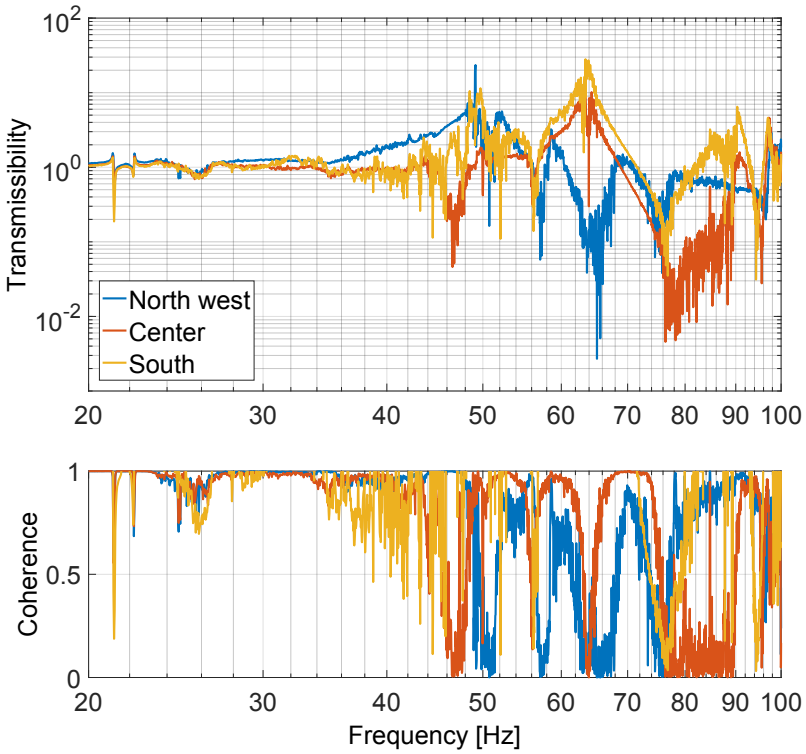


**Figure 91:** Vertical resonances of bolted only spring-box. Already the bolted (unglued) stiffening structure increases the lowest three spring-box modes by a factor of approximately 1.4. The resonance frequencies are compared to the reference measurement in table 17.

box modes already by a factor of approximately 1.4 with respect to the reference measurement. Compared to the original spring-box design suspended from the old IP-legs the resonance frequencies even shifted by an averaged factor of 1.66 [(compare to figure 67).

#### 14.4.2.3 *Final design: the glue-bolted spring-box*

The results of the final stiffening configuration are shown in figure 92, 93 and 94. All contact surfaces between original/auxiliary stiffening plates and the upper and lower spring-box plates were coated with tra-bond 2151 epoxy glue [160] before bolting the assembly tightly together. After the glue was cured the transmissibility from baseplate to spring-box was measured. In figure 92, 93 and 94 the measurements are separated in the three geophone locations and each is compared with the corresponding reference measurement. This highlights the stiffening improvement. Clearly visible is that not only the resonances were shifted to higher frequencies, but also the peak height is reduced with respect to the reference. That is probably due to the glue layer between the plates, which has a lower mechanical quality than the aluminum. This

| mode # | reference w/o stiffening resonance frequency [Hz] | bolted only resonance frequency [Hz] | frequency shift factor, reference-bolted only |
|---|---|---|---|
| 1 | 34 | 47 | 1.38 |
| 2 | 35 | 50 | 1.43 |
| 3 | 46 | 64 | 1.39 |

**Table 17:** Results from spring-box stiffening experiment: bolted only. The table shows the three lowest measured resonance frequencies of the bolted only experiment (see figure91) compared to the reference measurement (see figure 88). Also the frequency increase is displayed. Note that all three measurements were done with the system suspended from the new IP-legs, thus the numbers do not include the symmetric IP-leg stiffening gain.

is a positive side effect, since reducing the rms-motion using spring-box dampers is planned anyway (see chapter 15).

Due to the low resonance amplitude, the identification of the single modes is hardly possible with the transmissibility alone. Additional information about the resonance frequencies can be gained from the power spectral density (lower plots in figure 92, 93 and 94). The results from the glue-bolted measurement are summarized in table 18 and table 20. In table 18 the resonance frequencies of the glue-bolted spring-box are compared to those of the reference experiment. Stiffening the spring-box increased the three lowest resonances by up to a factor of 1.67. Glue bolting with respect to just bolting the assembly improved the three lowest resonance frequencies by an average factor of 1.14.

Glue bolting the spring-box increased the rigidity of the assembly connections strongly. Even though the resonance frequencies predicted in the monolithic model are not exceeded, the finial spring-box designs resonance frequencies are only about a factor of 0.85 lower than those simulated. The three lowest resonance frequencies are compared to the simulation in table 19.

The improvement gained from the whole re-design, including the symmetric IP-legs and the spring-box stiffening is shown in table 20. With respect to the original design, on which the first two AEI-SAS units are based, the re-design increased the vertical spring-box modes up to double the old resonance frequencies. Furthermore one can see from the plots that the number of resonances below 100 Hz is reduced.

| mode # | reference w/o stiffening resonance frequency [Hz] | glue-bolted resonance frequency [Hz] | frequency shift factor, reference glue-bolted |
|---|---|---|---|
| 1 | 34 | 54 | 1.59 |
| 2 | 35 | 58.5 | 1.67 |
| 3 | 46 | 70 | 1.52 |

**Table 18:** Results from spring-box stiffening experiment: glue-bolted. The table shows the three lowest measured resonance frequencies of the final glue-bolted spring-box configuration (compare to figure 92, 93 and 94) compared to the reference measurement (see figure 88).

| mode # | simulation resonance frequency [Hz] | glue-bolted resonance frequency [Hz] | frequency shift factor, measurement-simulation |
|---|---|---|---|
| 1 | 67.1 | 54.0 | 0.80 |
| 2 | 69.0 | 58.5 | 0.85 |
| 3 | 77.8 | 70 | 0.90 |

**Table 19:** Results from spring-box stiffening experiment compared to finite element simulation of a monolithic spring-box (compare to section 14.4.1).

| mode # | original design resonance frequency [Hz] | glue-bolted resonance frequency [Hz] | frequency shift factor, original design -glue-bolted |
|---|---|---|---|
| 1 | 30.5 | 54 | 1.77 |
| 2 | 31.2 | 58.5 | 1.88 |
| 3 | 34.6 | 70 | 2.02 |

**Table 20:** Results from spring-box stiffening experiment: Final glue-bolted spring-box configuration compared to the original spring-box design (compare to section 11.3.1)

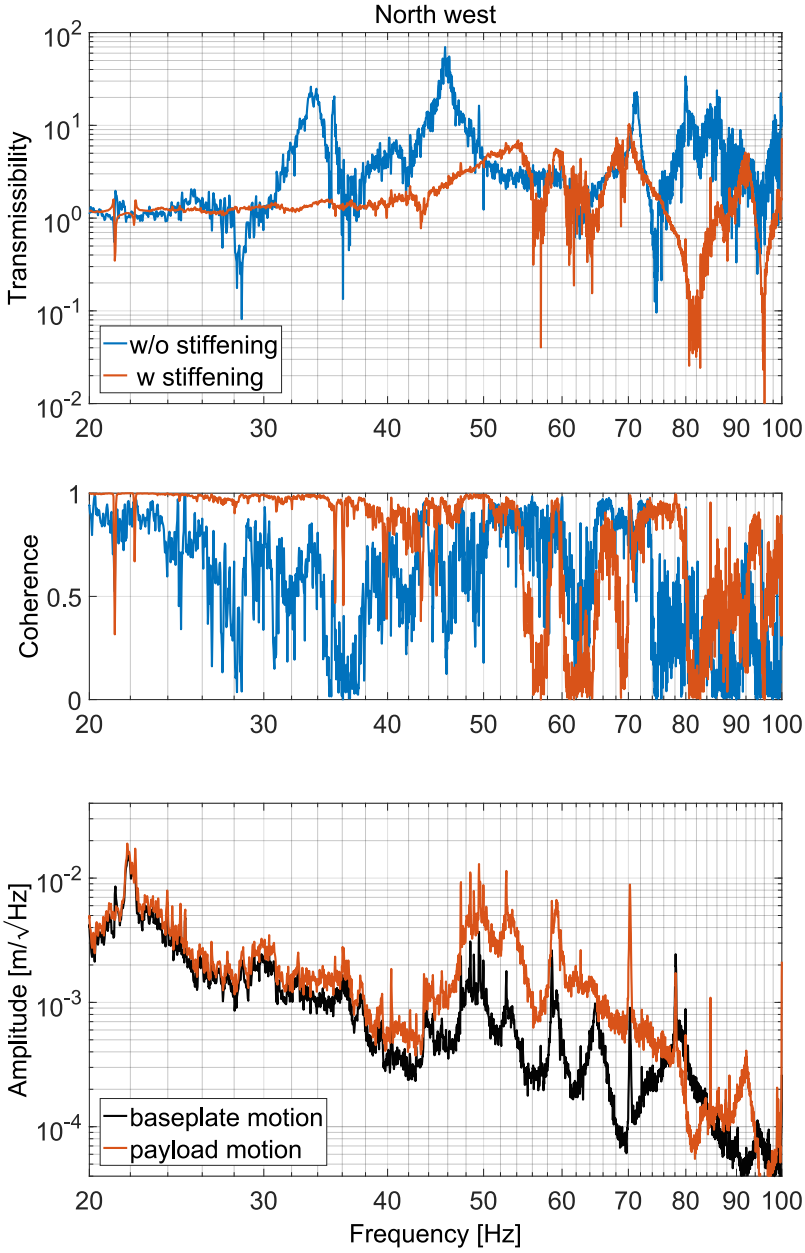


**Figure 92:** Results from glue-bolted spring-box north west corner measurement. In this and the two following figures (figure 93 and 94) the performance of the final (glue-bolted) improved spring-box design (red) is compared to the reference measurement (blue). Table reftab:stiffeningexp1 summarizes the frequency shifts. The combination of the transmissibility plots (upper two graphs) and the power spectral density of the vertical spring-box motion and the baseplate motion allows identifying the three lowest vertical spring-box modes. This additional information is necessary, since glue bolting the spring-box not only stiffens the system, but also introduces damping. Thus the resonance amplitude is lower.

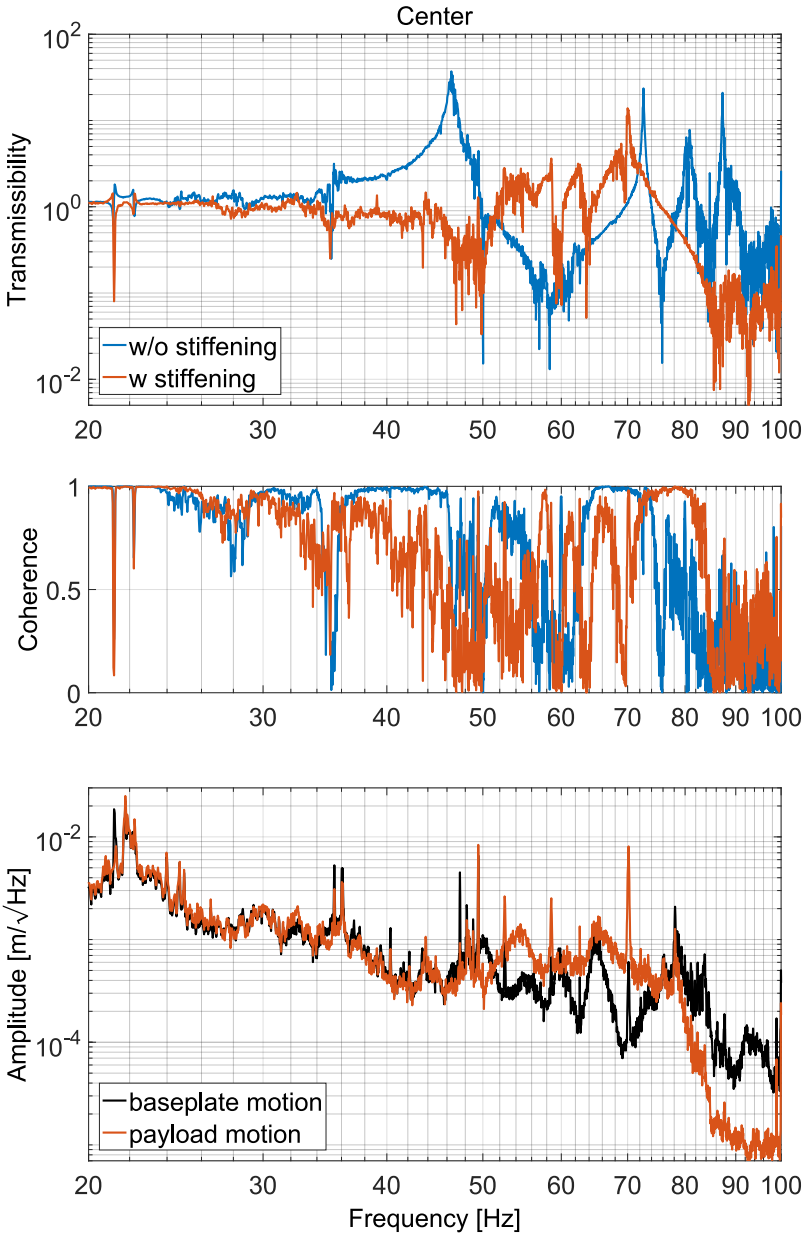


**Figure 93:** Results from glue-bolted spring-box north central position measurement. The figure description can be found in the caption of figure 92

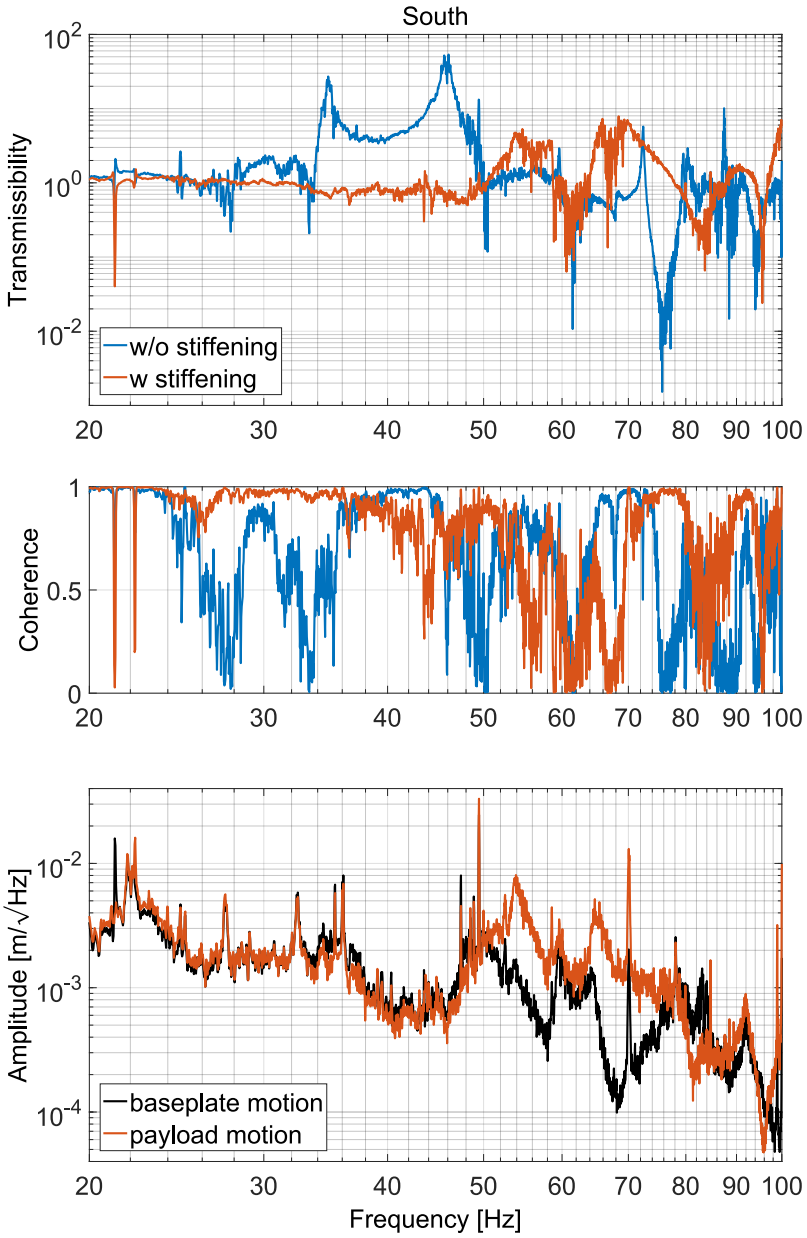


**Figure 94:** Results from glue-bolted spring-box south edge measurement. The figure description can be found in the caption of figure 92

# 15 SPRING-BOX DAMPING

The previous chapter describes, how the isolation window of the AEI-SAS can be broadened to higher frequencies by stiffening the whole system, except its springy parts, e.i. the IP-leg flexures and the GAS-filter blades. This stiffening shifts unavoidable internal resonances to higher frequencies. In the frequency band of these resonances, the ground motion's amplitude is relatively low and the mirror suspension systems provide sufficient isolation for the high precision measurements of the AEI 10 m prototype experiments.

The first two AEI-SAS units are already installed in the vacuum system and populated with electronics and optics. Replacing the old IP-legs and stiffening the spring-box is not feasible. However, the effect of the vertical spring-box modes can be mitigated by means of tuned dampers. These spring-box dampers are discussed in this chapter.

Even though the shifted higher frequency spring-box resonances are less critical than the low frequency ones of the original AEI-SAS design, high resonance amplitude still can be harmful for the active control. Thus, the spring-box dampers will be implemented in the third improved AEI-SAS unit, too.

Parts of the results presented in this chapter are published in ref. [57].

## 15.1 TUNED MASS DAMPERS

Tuned mass dampers are generally used to reduce the mechanical vibration amplitude of certain structures. They provide efficient inertial damping and are used in a variety of applications, such as damping vibrations in the flapwise direction of wind turbine blades [161], or reducing the amplitude of the fundamental modes of sky scrapers [162]. In the field of gravitational physics tuned mass dampers are proposed for the reduction of the Q factor of the coupling from optical to mechanical energy in the test masses. They thereby increase the threshold for parametric instabilities [163]. For this purpose also multi-stage damper systems are proposed, which are supposed to damp resonances over a wide spectral range [164].

Resonant damper structures were also tested in the AEI-SAS [24] and are employed in the EIB-SAS [165]. Here a new, much simpler system for broadband damping is discussed.

### 15.1.1 *Principles of tuned mass dampers*

In principle, a tuned mass damper is a mass (here referred to as secondary oscillator) which is connected via a spring to an oscillating object (here referred to as primary oscillator). The goal is to reduce the primary mass oscillation amplitude (see figure 95). In general, the secondary mass is much lighter than the primary mass.

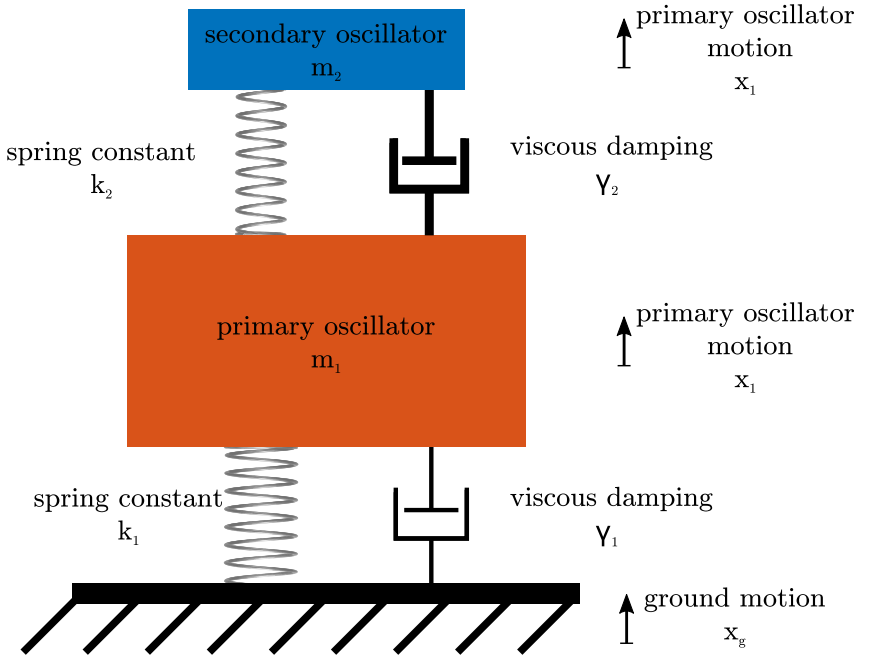


**Figure 95:** Simple one dimensional model of a tuned mass damper system. A primary mass is connected via a spring-damping system to the ground. The resulting resonance frequency of this system is to be damped. A secondary, lighter mass is therefore coupled through a damped spring to the primary mass. The resonance frequency of this damper is matched to the one of the primary oscillator. This way energy from the primary oscillator mode is transferred to the secondary oscillator, where it is dissipated via damping. In the case of the AEI-SAS, the primary oscillator represents the spring-box. The vertical spring-box modes are the resonances to be damped.

A special case of a tuned mass damper is the resonant damper. Here the secondary oscillator is tuned to the eigenfrequency of the primary oscillator. The energy of the primary mass oscillation is thereby transferred to an oscillation of the secondary oscillator. Due to the high mass ratio, the secondary oscillator motion is much larger than the primary oscillator motion. By damping the secondary oscillator, the energy is dissipated. In the following paragraphs a simplified, one dimensional tuned mass damper model is analyzed.

The transmissibility from ground motion $x_g$ to primary mass motion $x_1$ of the system shown in figure 95 is derived from its equations of motion[1]:

$$0 = k_1(x_1 - x_g) + k_2(x_1 - x_2) + \gamma_1(\dot{x}_1 - \dot{x}_g) + \gamma_2(\dot{x}_1 - \dot{x}_2) + m_1\ddot{x}_1 \tag{123}$$

and

$$0 = k_2(x_1 - x_2) + \gamma_2(\dot{x}_1 - \dot{x}_2) - m_2\ddot{x}_2 \ . \tag{124}$$

Here $x_1$ and $x_2$ are the positions of the primary and secondary masses and $x_g$ is the ground motion. $\gamma_1$ and $\gamma_2$ are the viscous damping factors of the primary and secondary oscillators and $k_1$ and $k_2$ are the corresponding spring constants. Analogous to the method discussed in section 6.1 the transmissibility function is obtained by converting the equations of motion into the frequency domain. Eliminating $x_2$ leads to

$$\frac{x_1}{x_g} = \frac{A}{B + CD} \ , \tag{125}$$

with

$$\begin{aligned} A(f) &= -f_1^2 - i\frac{\gamma_1}{2\pi m_1} f \ , \\ B(f) &= f^2 - f_1^2 - \frac{m_2}{m_1} f_2^2 - i\frac{\gamma_1 + \gamma_2}{2\pi m_1} f \ , \\ C(f) &= \frac{m_2}{m_1} f_2^2 + i\frac{\gamma_2}{2\pi m_1} f \ , \\ &\text{and} \\ D(f) &= \frac{f_2^2 + i\frac{\gamma_2}{2\pi m_2} f}{f_2^2 - f^2 + i\frac{\gamma_2}{2\pi m_2} f} \ . \end{aligned} \tag{126}$$

Here $k_j$ $(j = 1, 2)$ is substituted by

$$k_j = (2\pi f_j)^2 m_j \ . \tag{127}$$

Comparing $D(f)$ to equation 12 shows, that this parameter is the transmissibility of the primary mass motion to the secondary mass motion.

Figure 96 illustrates the gain from employing tuned mass dampers. The plot compares the transmissibility amplitude of the primary oscillator with (yellow line) and without (red dotted line) resonant damping. In the illustrated case the resonance frequency of the secondary oscil-

1 The equation of motion and the transmissibility of the system without the damper, i.e. a single stage harmonic oscillator is discussed in section 6.1

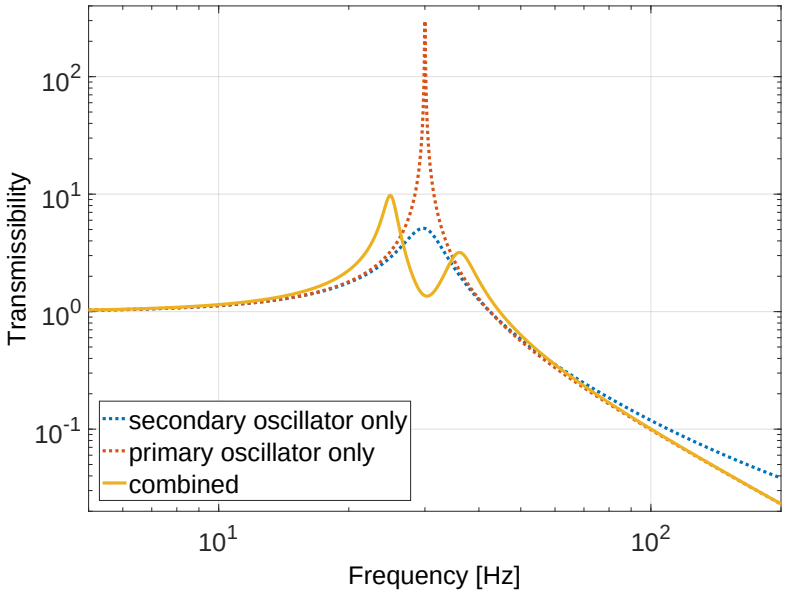


**Figure 96:** Simple model of the tuned mass damper performance. This figure shows the transmissibility amplitude $\frac{x_1}{x_g}$ from ground motion to primary oscillator motion with (yellow) and without (red dotted) tuned mass damper. The blue dotted line represents the transmissibility of the tuned mass damper itself ($D(f)$ in equation 126). The resonance frequency of the secondary oscillator matches the resonance frequency of the primary oscillator (30 Hz). This way two resonances with a lower amplitude form. The here presented primary oscillator has a quality factor of $Q_1 = m_1 2\pi f_1/\gamma_1 = 300$ and a mass of $m_2 = 35\,\mathrm{kg}$. These parameters and the secondary mass ($m_2 = 5\,\mathrm{kg}$) have approximately the realistic values of the lowest vertical spring-box mode and the assigned damper. Only the secondary quality factor $Q_2 = m_2 2\pi f_2/\gamma_2 = 5$ was chosen to be higher, in order to illustrate the interaction of the two oscillators more clearly. A variation of the quality factor is shown in figure 97. Already in this simple configuration, a peak amplitude reduction by a factor of 30 is achieved.

lator is matched to the one of the primary oscillator. It is chosen to be 30 Hz, which is approximately the lowest vertical spring-box mode frequency. A low secondary damping factor $\gamma_2$ reduces the combined amplitude on resonance strongly, while two resonances above and below the original resonance frequency with a relatively high-quality factor appear. The lower frequency resonance corresponds to the common mode of the primary and the secondary oscillator, the higher frequency resonance is the differential oscillation of the two masses. A strongly damped secondary oscillator reduces the amplitudes of these modes, in particular the one corresponding to the differential oscillation. If instead a relatively low damping of the secondary oscillator is applied, the two new modes are strongly enhanced, however, the amplitude at

the frequency of the original mode is relatively low. Such a configuration would be applied if a particular refined frequency band requires a superior noise performance.

Below a quality factor of $Q_2 = 2$ the higher frequency mode amplitude is negligible and the lower frequency mode amplitude is minimal. Figure 97 illustrates this transmissibility's dependency on the secondary quality factor.

In terms of the AEI-SAS, a low (broadband) rms-motion is favored over an extremely low amplitude at a certain frequency. A spring-box damper design with a low quality factor was therefore developed.

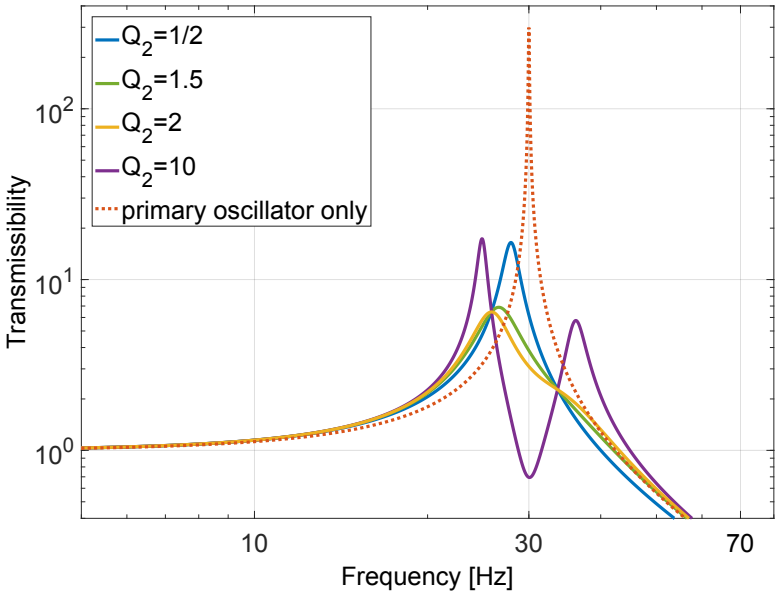


**Figure 97:** Simple model of the tuned mass damper performance for varying quality factors. The dotted red line represents the primary oscillator without a tuned mass damper. The primary mass in this simulation is $m_1$=35 kg and the secondary mass is $m_2$=5 kg. The other colors show the transmissibility from ground motion to the primary mass motion for a system with resonant damper. A relatively high-quality factor of the secondary damper reduces the amplitude at the primary resonance frequency, though the two new resonance peaks are strongly enhanced (purple). A low Q factor couples the primary and the secondary mass strongly and the common mode is dominant (blue). The lowest rms-motion is achieved with a Q factor of approximately 2 (yellow).

In the case of a highly damped secondary spring, a further improvement of the overall damping performance can be achieved by the variation of the secondary oscillator's resonance frequency. As shown in figure 33 in secion 6, the phase roll-off above and below the resonance frequency of a highly damped system is less steep than in a system with low damping. The suppression of the relative motion between primary and secondary mass is therefore not necessarily largest if the two resonance frequencies are matched. Figure 98 illustrates the influence of

the secondary resonance frequency on the primary oscillators transmissibility amplitude. It shows that in the modeled system the maximal amplitude suppression is achieved with a secondary oscillator tuned to a slightly lower resonance frequency with respect to the primary oscillator

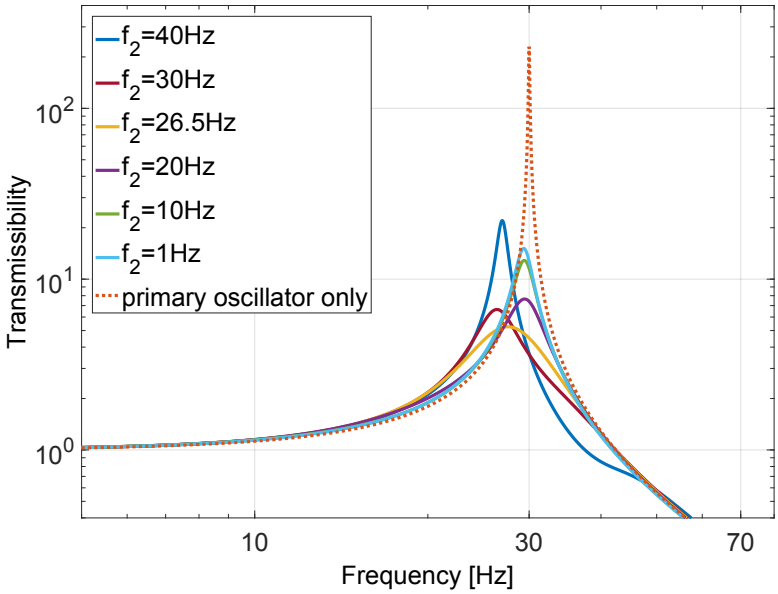


**Figure 98:** Influence of the secondary oscillator's resonance frequency on the transmissibility amplitude of the primary oscillator. In this simulation, the damping factors of the system are kept constant at $\gamma_2$ =580 s/kg. This is approximately the value measured for the spring-box dampers. The simulation shows, that a secondary resonance frequency slightly lower than the primary provides the larges amplitude suppression (yellow). Tuning the secondary resonance frequency even lower still provides a fairly high damping. This illustrates that broadband damping can be achieved by means of well damped secondary oscillators. The masses used in this simulation are the same as in the model shown in figure 97.

In the case that the secondary oscillator frequency is small compared to the primary oscillator frequency, the amplitude reduction remains approximately constant for a varying secondary oscillator frequency (see green and light blue line in figure 98). This is due to the fact that the secondary mass is strongly decoupled from the primary mass motion at the primary resonance frequency. The relative motion of primary and secondary mass equals approximately the primary resonance frequency amplitude, while the phase lag in between the two masses is approximately −90° (compare to figure 33). This means, that a highly damped tuned mass damper serves not only as a resonant damper but also as a broadband damper. Higher frequency modes can be damped with devices that are tuned to a certain lower frequency mode. The damping performance is, in this case, only dependent on the secondary damping

factor and the mass ratio of the two oscillators. This effect is experimentally shown below in the damping performance measurements.

### 15.1.2 *Determining the spring-box mode parameters*

As we have seen above, the parameters describing the modeled primary oscillator mode are the resonance frequency, the damping factor, and the mass. The resonance frequencies and the quality factors of the three lowest vertical spring-box modes can be deduced from the measurements described in section 11.3.1. Figure 99 shows this driven spring-box mode measurement fitted by a simple damped harmonic oscillator model.

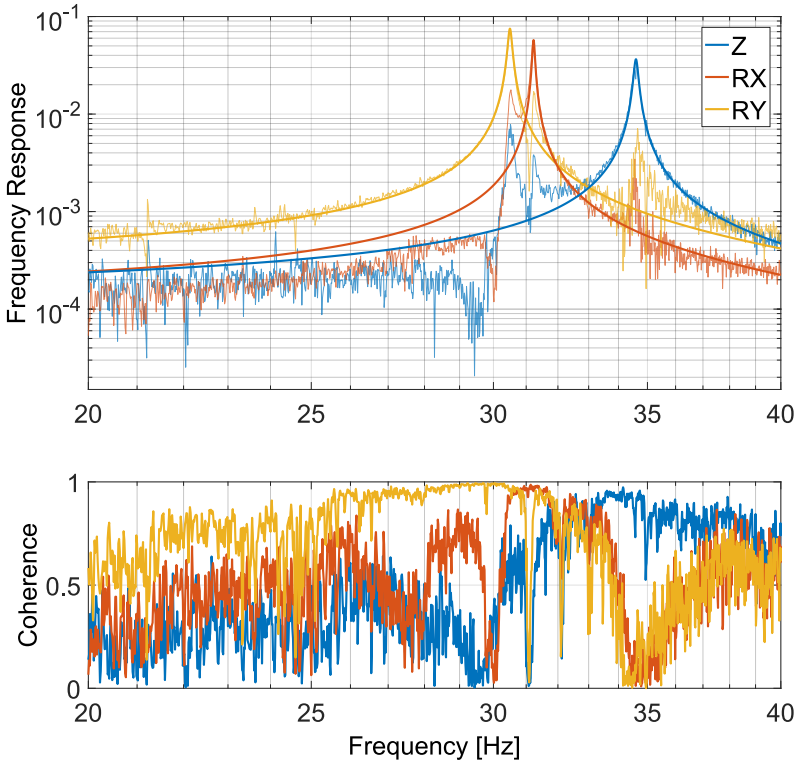


**Figure 99:** Fitted driven vertical spring-box resonances (south table). In order to determine the parameters of the modes to be damped by the spring-box dampers, the measured data is fitted by a simple damped harmonic oscillator model. The parameters of the fit are shown in table 21. The measurement and fit for the central table spring-box modes is shown in the appendix in figure 129.

The parameters resulting from these fits are displayed in table 21.

The primary oscillator mass $m_1$ (here referred to as effective mode mass) strongly depends on the position in which the spring-box damper is placed on the spring-box. The reason for that is that the oscillations are all partly rotational motions. Thus, positioning the damper in the anti-node of the mode results in the lowest primary oscillator mass, the

| | Mode direction | Resonance frequency | Quality factor |
|---|---|---|---|
| South | Z | 34.6 Hz | 230 |
| | RX | 31.2 Hz | 400 |
| | RY | 30.5 Hz | 250 |
| Central | Z | 34.9 Hz | 210 |
| | RX | 31.7 Hz | 415 |
| | RY | 30.6 Hz | 230 |

**Table 21:** Vertical spring-box mode parameters. The table shows the results from fitting a damped harmonic oscillator model to the driven vertical spring-box resonances (see figure 99 and figure 129).

strongest coupling between the two oscillators and the most efficient damping.

Various positions on the spring-box were tested for their effective mode mass. The finite element simulation of the vertical spring-box modes (see figure 65) aided pre-selecting the locations.

The effective mode mass was experimentally determined by placing a probe mass ($m_p = 3.8\,\mathrm{kg}$) in a potential damper position. Then the mode frequencies with and without the mass were measured and compared. From equation 13 follows the effective mass

$$m_1 = \frac{m_p}{\frac{f_a^2}{f_b^2} - 1} \,, \tag{128}$$

where $f_a$ is the mode frequency without and $f_b$ is the mode frequency with the probe mass added.

The three positions chosen for damping the three lowest vertical spring-box modes of the central table are displayed in figure 100. In the case of the south table, the ideal B position was found to be shifted about 60 cm to the left. Position A and C are identical in both AEI-SAS units. The effective mass of the three lowest vertical spring-box modes in the three (per AEI-SAS unit) chosen damper positions are listed in table 22. The significant difference between the south and the central table's mode masses is due to the different mass distribution in the spring-boxes and the slightly different positions in which the probe mass was placed. The criteria for the position choice were, on the one hand, a low effective mass of one of the modes, since that allows the highest damping. On the other hand, a low effective masses of at least

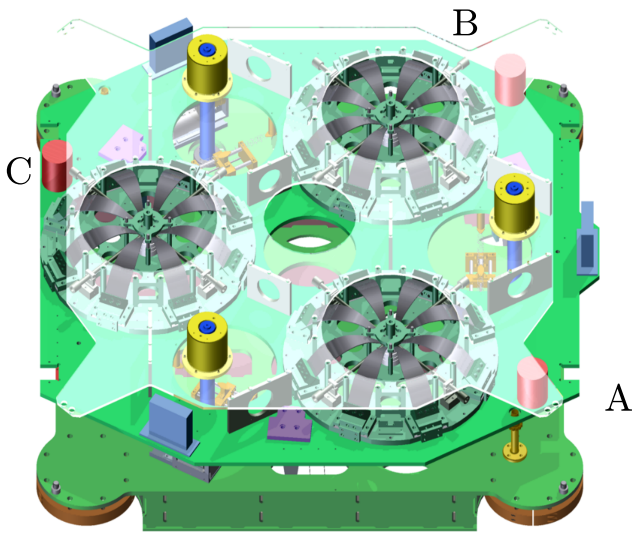


**Figure 100:** Position of tuned mass dampers in the spring-box of the central table. The three red cylinders represent the spring-box dampers. Their positions (A, B and C) are chosen with the aid of finite element mode shape simulations and experimental measurements of the effective mode mass. The upper spring-box plate is displayed transparently.

two modes allows efficient damping of more than one mode. The latter is the case for position C in the south table and position B in the central table.

Printed in bold are the masses corresponding to the modes the dampers are tuned to in that position.

### 15.1.3 *Spring-box damper design*

The design of the AEI-SAS spring-box dampers is fairly simple. Originally they were built as a test version, but due to their remarkable performance, the dampers were installed permanently.

**Figure 101:** Photograph of an AEI-SAS spring-box damper. The damper consist of a 5 kg stainless steel mass mounted on three cylindrical viton rubber legs. For tuning purpose the upper part of the mass can be replaced by a geophone. The circular plate stabilizes the viton feet.

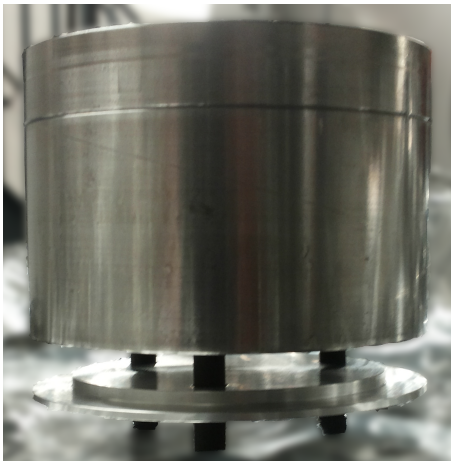

| | Position | 1st mode mass [kg] | 2nd mode mass [kg] | 3rd mode mass [kg] |
|---|---|---|---|---|
| South | A | **35** | 235 | 162 |
| | B | -- | **59** | 322 |
| | C | 48 | -- | **99** |
| Central | A | **65** | 135 | 230 |
| | B | 65 | **93** | 247 |
| | C | 99 | 241 | **172** |

**Table 22:** Effective mode masses of the central and the south table. The mode mass is indirectly measured in the way explained above. The positions A, B and C in the spring-box are displayed in figure 100 (note that position B in the south table varies from the position shown in the figure). The effective masses printed in bold correspond to the mode to be damped in that position. For two mode masses (marked with '--') the frequency shift was not measurable.

Figure 101 shows a photograph of a spring-box damper. It consists of a 5 kg mass mounted on three cylindrical viton rubber legs. These legs were cut from a 7 mm diameter viton o-ring. They are hold in place by tight intakes in the mass. The length of those viton cylinders determines the vertical resonance frequency of the damper. The mass was chosen to be 5 kg, since that was the maximum additional mass that can be loaded on the spring-box (compare to section 13.2).

In order to stabilize the rubber legs, an aluminum plate with three holes at the position of the feet is mounted at half the heights of the legs to interconnect them. Without this structure, the damper system would be unstable in the horizontal direction, since the three legs would bend independently or buckle.

### 15.1.4 *Tuning the spring-box damper*

As mentioned above, the vertical resonance frequency of the spring-box dampers depends on the length of its legs. The Q factor and the resonance frequency of the dampers are determined by measuring its transmissibility. The upper part of the damper mass is therefore replaced by a vertical geophone with the same mass. A second geophone is placed right next to the damper on a rigid plate. The plate is driven by ground motion, which is sufficient for this purpose.

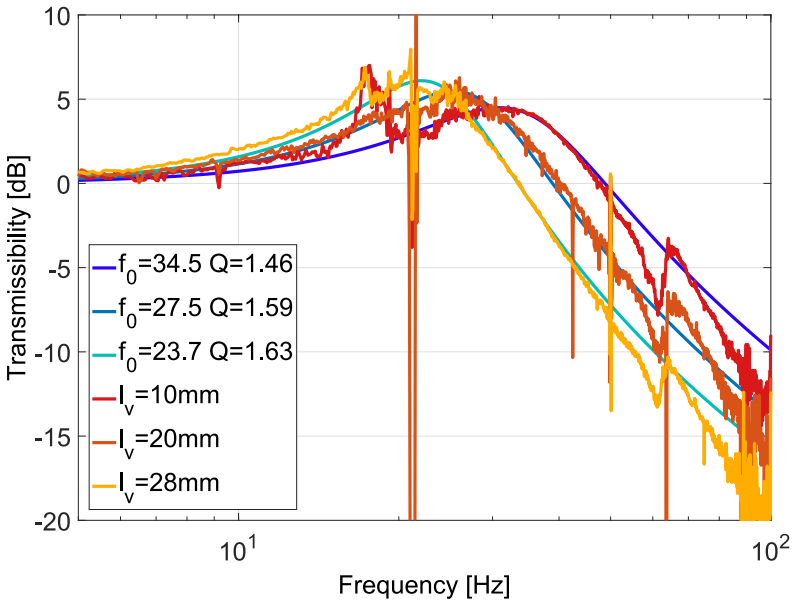


**Figure 102:** Spring-box damper characterization. The transmissibility amplitude (shades of red) is fitted with a simple harmonic oscillator model (shades of blue). This way, the resonance frequency and the Q factor are determined. The three dampers for the three selected positions have been tuned to different resonance frequencies by varying the lengths $l_v$ of the viton leg.

Figure 102 show the damper's transmissibility amplitudes fitted by a simple damped harmonic oscillator model. The highest resonance frequency damper with a viton leg length of $l_v = 10\,\mathrm{mm}$ is placed in the position C to damp mainly the third highest vertical spring-box mode. Accordingly, the damper with a leg length of $l_v = 20\,\mathrm{mm}$ damps mainly the second mode in position B and the $l_v = 28\,\mathrm{mm}$ damper is placed in position A to reduce the lowest resonance frequency mode amplitude.

From the simplified model shown above the damper in position A would reduce the first mode's amplitude of the south table by a factor of 38. The second mode's amplitude would be lowered by a factor of 43 by placing a damper in position B. The third mode has a much higher effective mass, thus is only reduced by a factor of 16.[2] These values are close to the ideal amplitude reduction with a 5 kg damper. An even higher damping can be achieved by a heavier damper mass. This was not feasible in the first two AEI-SAS units since they are loaded close to their maximum payload. The new symmetric IP-legs for the third AEI-SAS unit, however, are designed to carry a higher payload in the spring-box, thus more efficient dampers can be designed for this system.

2 This simplified model does not take into account, that all three dampers have an effect on the mode amplitude, thus a higher damping performance is expected in reality.

### 15.1.5 *Spring-box damper performance*

Three spring-box dampers were implemented in the first two AEI-SAS units. The dampers for the third improved AEI-SAS unit will be designed and implemented when the system is installed in the vacuum system.

The improvement in the AEI-SAS performance is shown in figure 103 and 104. As an example of the damping of the spring-box modes, figure 103 shows the transmissibility from the ground to the spring-box in the horizontal direction. The transmissibility amplitude is reduced by a factor of up to 75 for the third mode. This is more than predicted by the simplified single damper model but can be explained by the influence of all three dampers on this mode.

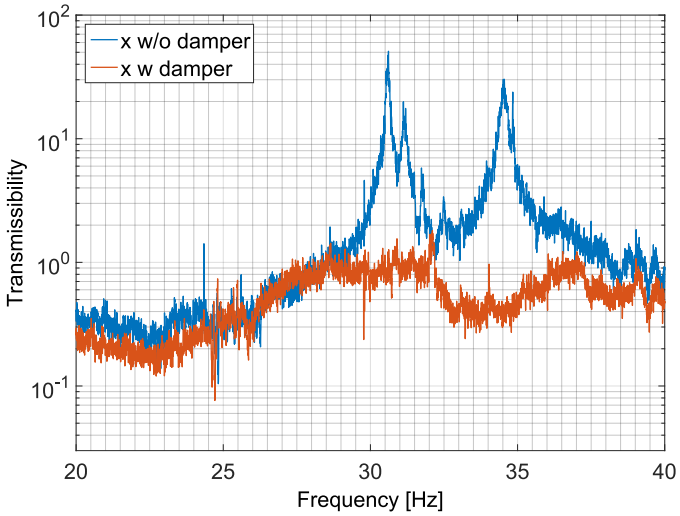


**Figure 103:** The transmissibility of horizontal ground motion to horizontal payload motion with (red) and without (blue) spring-box dampers. The payload motion was measured with an auxiliary accelerometer mounted directly on the payload. By placing three damping structures inside the spring-box, the three lowest spring-box modes were strongly damped.

Resonances at higher frequencies are also strongly damped due to the damper's broadband damping characteristics, discussed above. Figure 104 shows the payload motion (z, rx, ry degrees of freedom) and the spring-box motion (x, y, rz degrees of freedom). The rms-motion is substantially reduced over a wide frequency band in all degrees of freedom.

This remarkable performance of this first damper design led to the decision to keep it as a permanent part of the AEI-SAS. Further improvements were not necessary, for now. Nevertheless, the damper performance could slightly be improved by a more accurate tuning of the resonance frequencies. Furthermore, an analysis of the additional modes of the damper structure could enable tuning one damper to different

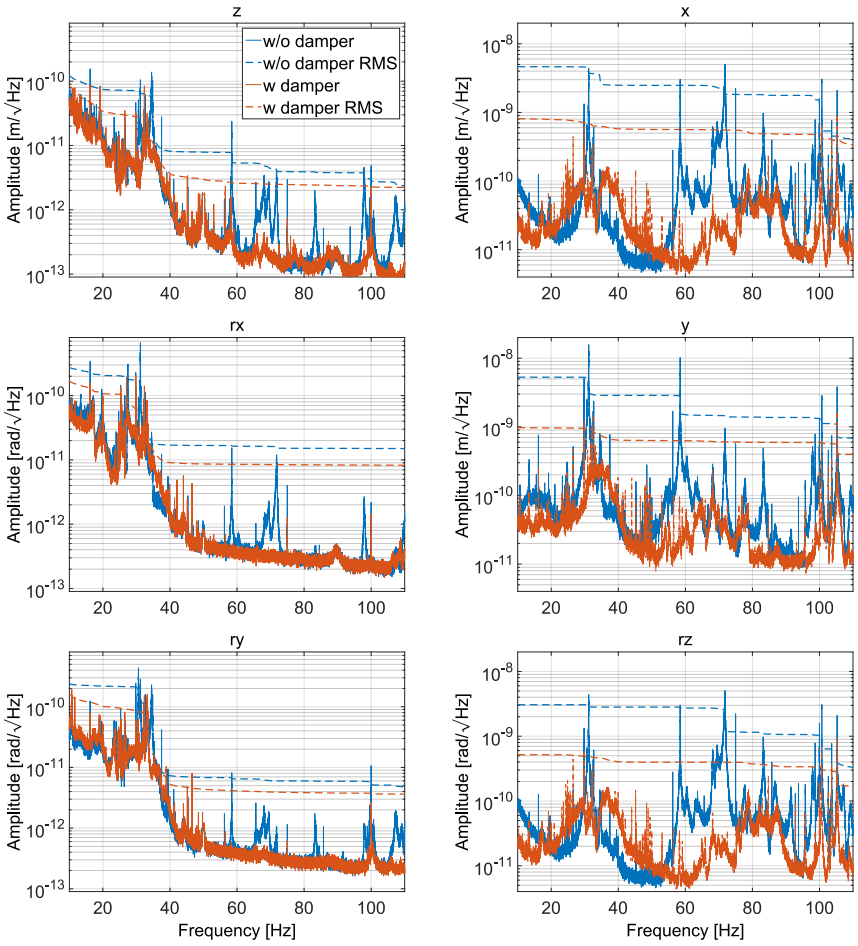


**Figure 104:** Spring-box damper performance in all 6 degrees of freedom. The plots on the left of this figure show the vertical payload motion (measured with the payload geophones) with (red) and without (blue) spring-box dampers. The plots on the right show the horizontal spring-box motion (measured with the three spring-box accelerometers) again with (red) and without (blue) spring-box dampers. Not only are the three fundamental spring-box modes between 30 Hz and 35 Hz damped, but higher frequency resonances are also significantly reduced. The rms-motion, integrated from high frequencies to low frequencies (dashed lines), is substantially reduced over a large frequency band.

mode frequencies by adjusting the geometry (for instance the tilt modes of the current spring-box damper design might already have an influence on their performance). Also, the position of the dampers in the spring-box could be further improved. A damper, suspended from the corners of the upper spring-box plate could be considered.

Moreover, the damping factor matching could be improved. Different spring materials or tunable damping methods as, for instant eddy current damping, used for the EIB-SAS dampers could be applied [95]. As mentioned above, increasing the damper mass would improve their performance strongly. This is possible in the third AEI-SAS unit since

its maximum payload is higher than the one of the first two AEI-SAS units.

# 16 ACTIVE CONTROL FOR THE AEI-SAS

In the previous chapters, characterization and improvements of the AEI-SAS's passive high frequency performance were discussed. In this frequency regime (above a few Hz) the system attenuates ambient vibrations purely due to its mechanical inertia. Such a passive isolation has the disadvantage that ground motion is strongly enhanced at and around the fundamental resonance frequencies of the system (see section 6). This is certainly unfavorable since the fundamental resonances of the AEI-SAS are in the frequency band of the microseismic peak.

In order to improve the AEI-SAS's low frequency performance, it is actively controlled in this frequency band while maintaining purely passive vibration isolation at high frequencies. The individual SASs are locally controlled using the sensors and actuators described in section 5.2. The longitudinal differential payload motion is sensed by the SPI, and most payload tilt degrees of freedoms are red out by OLs (see section 4.3) The resulting error signal is used to imprint the central table motion in the directions of the interferometer arms on the two other tables. This strongly reduces the inter-table motion.

In this chapter, the control scheme of the AEI-SAS is introduced and preliminary results are shown. A detailed analysis of the active isolation is expected to be published in 2018.

## 16.1 CONTROL SCHEME

The basic principle of active isolation is to read out the inertial payload motion and to minimize this signal by actuating on the payload. Ideally, this would result in a motionless payload. In reality occurring limitations are listed below in section 16.1.1.

The basic idea of the control scheme applied in the AEI-SAS is depicted as a block diagram in figure 105. Each box represents a matrix of frequency response functions. $\mathsf{P}$ is the plant which is to be stabilized. This means, that the output signal is to be minimized; therefore the output signal is measured by a sensor which has a response $\mathsf{S}$. The resulting error signal is fed to the controller. Its response $\mathsf{C}$ is usually the part of the control loop that is modified in order to control the system. After the error signal is filtered by the controller it is sent to the actuator which provides the actuation signal. The actuator has the strength $\mathsf{A}$. Both, actuation signal and input signal drive the plant. By means of the former, the effect of the latter is minimized.

$\mathsf{P}$,$\mathsf{S}$,$\mathsf{C}$ and $\mathsf{A}$ are the open loop transfer functions of the corresponding devices. These transfer functions can be multi-dimensional for multi-

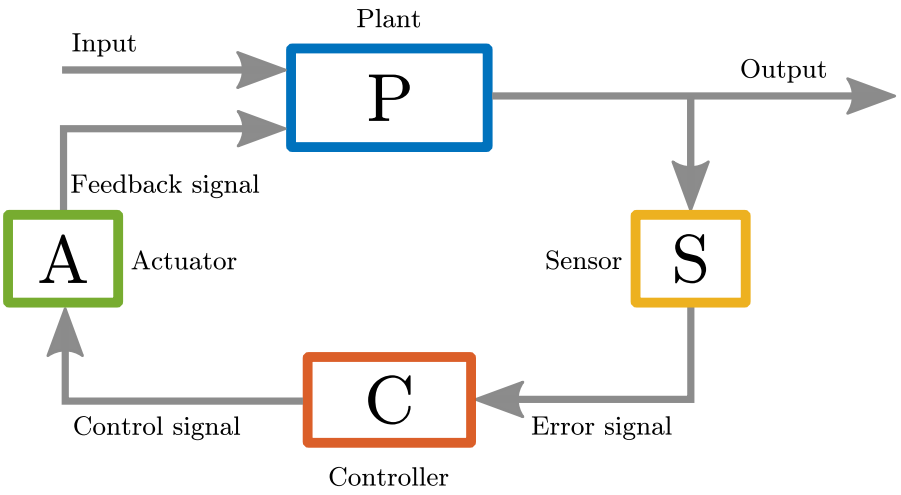


**Figure 105:** Illustration of the principle of the control scheme applied in the AEI-SAS.

dimensional systems and they are usually frequency depended. In a vibration cancellation feedback system, negative feedback is applied. It means, that a positive feedback signal is subtracted from the input signal.

From the block diagram shown in figure 105 one can obtain the closed loop transfer function of the plant,

$$\mathrm{TF_{cl}} = \frac{\mathrm{Output}}{\mathrm{Input}} = \frac{\mathsf{P}}{1 + \mathsf{PACS}} \ . \tag{129}$$

This illustrates, that the system is instable when $\mathsf{PACS}$, the open loop transfer function of the feedback system, equals $1$ while having a phase shift of $-180°$ [166]. A robust system has therefore high amplitude or phase margin to this values. This way small perturbations of the system do not cause instability.

### 16.1.1 *Limitations of active isolation performance*

The idealized system discussed above, which neglects the signal processing delay, could completely cancel the output signal. However, the noise reduction is determined, among other things, by the limitations itemized below.

- The actuator gain is finite, also sensors and actuators are limited by their individual accuracy (see section 5.2). Furthermore, the data acquisition system's noise floor can limit the control performance.
- In a realistic mechanical system which is to be stabilized in 6 degrees of freedom, these are rarely entirely decoupled. The most intuitive example for cross-coupling is the transfer from ground

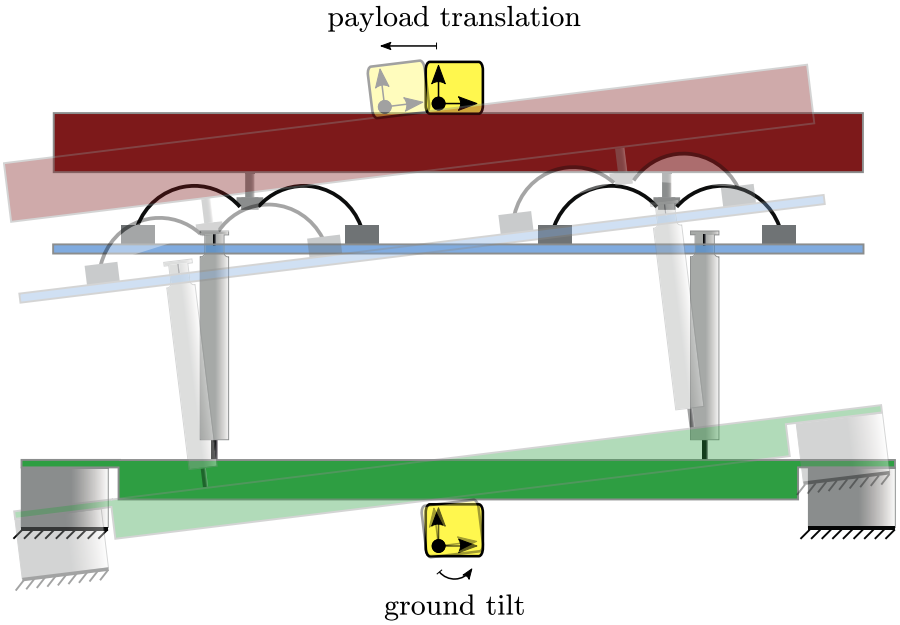


**Figure 106:** Tilt to horizontal coupling. The figure illustrates an example of a fundamental cross-coupling between different degrees of freedom. Ground tilt causes not only payload tilt but also horizontal translation. The coupling scales with the distance of the payload to the ground tilt rotation axis.

tilt to horizontal payload translation if the payload's center of mass does not coincide with the rotation point of the ground tilt. This is illustrated in figure 106.

- The influence of low frequency tilt on inertial horizontal sensors, as it is briefly discussed in section 9.1.2, limits the low frequency performance. Tilt sensors could mitigate this performance loss [151].
- Not only fundamental mechanics cause cross-coupling, also an imperfect alignment of sensors and actuators causes degree of freedom interaction. In terms of the model shown in figure 105 this would mean that the matrices $\mathsf{G}$, $\mathsf{A}$ and $\mathsf{S}$ have off-diagonal entries.
- The design of efficient filters and unity gain frequency is limited by internal resonances, as summarized in section 2.1.2.

The first and the last item are the reasons why the active control of the AEI-SAS is applied exclusively below a few Hz. At high frequencies, the passive isolation attenuates the ground motion below the sensor noise floor. Thus, feeding back this noise to the actuators would compromise the high frequency AEI-SAS performance.

The cut off frequency for the control filter, however, cannot be set to where the noise starts limiting since the AEI-SAS's internal resonance amplitudes are much higher than the sensors noise floor; therefore the

amplitude of the control filters needs to be reasonably low in the internal resonance frequency band in order to prevent causing instabilities. This way mitigating the high frequency performance, as it is described in the chapters above, influences the low frequency isolation ability of the AEI-SAS.

### 16.1.2 *The AEI-SAS control scheme*

The results presented in this section were obtained together with C. M. Mow-Lowry, R. Kirchhoff, and S. M. Köhlenbeck. Some of them are subject of R. Kirchhoff's master's thesis [124]. Results from SPI and OL control will not be discussed here. They will be subject of S. M. Köhlenbeck's thesis.

The AEI-SAS's control scheme relies on the set of sensors and actuators introduced in section 5.2. A simple and robust way to damp the fundamental resonances is to exclusively use the LVDT signals in a feedback loop. By choosing the control filter such that the feedback signal is proportional to the velocity this damping scheme is equivalent to a viscous damping dash-pot as it is described in section 6.1. This damping scheme is used in the AEI-SAS as a safety mode or during (manual) modifications on the payload. For instance when optics are adjusted. For such tasks, a robust system with a short ring-down time is preferable[1]. Both can be provided by this damping approach.

The drawback of this relative velocity damping is, that the reference of the measurement is the moving ground; therefore, the payload motion can be at best reduced to the ground motion amplitude in the frequency regime around and below the fundamental resonance frequencies. Above the fundamental resonance frequencies, the AEI-SAS isolation performance is compromised by the $f^{-1}$ roll-off, due to viscous damping (discussed in section 6.1). This could certainly be partially mitigated by limiting the feedback to a certain frequency range around the fundamental resonance frequencies.

Instead of using the relative sensors for payload motion cancellation one can control the system with inertial sensor signals. Using an inertial reference instead of the moving ground ideally lowers the payload motion in the entire control band with respect to the uncontrolled system. However, also this control scheme has the limitations listed at the beginning of this section. In order to obtain the best control signal possible with the available sensors for each degree of freedom in the frequency band of interest the different sensor signals are combined. The principle of this sensor correction and sensor blending is summarized in the following section.

1 The exponential decay time of the uncontrolled AEI-SAS is approximately $\tau = 2Q_v\omega_0^{-1} \approx 42\,\mathrm{s}$ for the vertical fundamental resonance.

### 16.1.3 *Sensor correction and sensor blending*

The AEI-SAS's horizontal accelerometers and the vertical geophones provide an inertial payload motion signal, though, as mentioned above, the sensors have individual performance limitations. The L-4C geophones with newly designed amplifier electronics are already a great improvement over the originally used L-22D geophones (see section 5.2.1). However, even their noise floor is limiting payload motion measurements at low frequencies, below approximately 0.07 Hz in the uncontrolled AEI-SAS [167].

The horizontal accelerometer's signal deviates from the horizontal payload motion at low frequencies (below approximately 0.3 Hz in the uncontrolled AEI-SAS) due to the tilt to the horizontal coupling of the sensor (compare to section 9.1.2 and [151]).

The LVDTs are relatively good low frequency sensors and they provide a DC signal, that can be used to control the position of the payload. However, they measure the differential motion between ground and payload[2] and not the inertial payload motion. A way to obtain an inertial signal from this relative signal is the sensor correction.

#### 16.1.3.1 *Sensor correction*

Since the LVDT sensors signal is proportional to displacement they have good sensitivity at low frequencies and DC. Furthermore, the horizontal relative sensors themselves are, in contrast to the horizontal inertial sensors, not sensitive to tilt. However, they measure the horizontal motion of the payload which is at low frequencies induced by ground tilt.

The differential signal $S_r$ the LVDTs measure can be described as the inertial payload motion $x_p$ minus the ground motion $x_g$. The ground motion is recorded by the STS2. Thus, adding the STS2 signal to the LVDT signal results in the inertial payload motion.

$$x_p = S_r + x_g \ . \tag{130}$$

This sensor correction is depicted as a part of the AEI-SAS control scheme block diagram in figure 107.

Unfortunately, at the AEI 10 m prototype, the ground motion is only recorded in the three translational degrees of freedom. This sensor correction can therefore only be applied in these three directions. The for the AEI 10 m prototype experiments most relevant of the rotational degrees of freedom, however, are inertially controlled via the OL signals, as shown in table 23.

2 this is certainly simplified, in reality, the horizontal differential sensors measure the differential motion between spring-box and ground, the vertical differential sensors measure the differential motion between the individual GAS-filter baseplates and the keystones.

#### 16.1.3.2 *Sensor blending*

The inertial control signals consist of up to three different parts, depending on the degree of freedom.

- At DC the AEI-SAS is integrated to a certain LVDT signal value in all 6 degrees of freedom.
- In the mid frequency band, the sensor corrected LVDTs provide the control signal.
- At high frequencies, the AEI-SAS is controlled by the inertial sensors.

The mid and high frequency band boundaries differ between the individual degrees of freedom and are listed in table 23. In some of the rotational degrees of freedom, the payload motion is sensed by OL. They provide the control signal for the entire frequency band. In the other rotational degrees of freedom LVDT and geophone signals are used, due to a lack of a tilt sensor correction signal. Currently, this is the case for the ry degree of freedom of the central and south table. In the final AEI-SAS configuration, which includes the west table, only the south table's ry and the west table's rx degree of freedom motion will not be controlled by OLs. The control signals for the different frequency bands in the individual degrees of freedom are summarized in table 23.

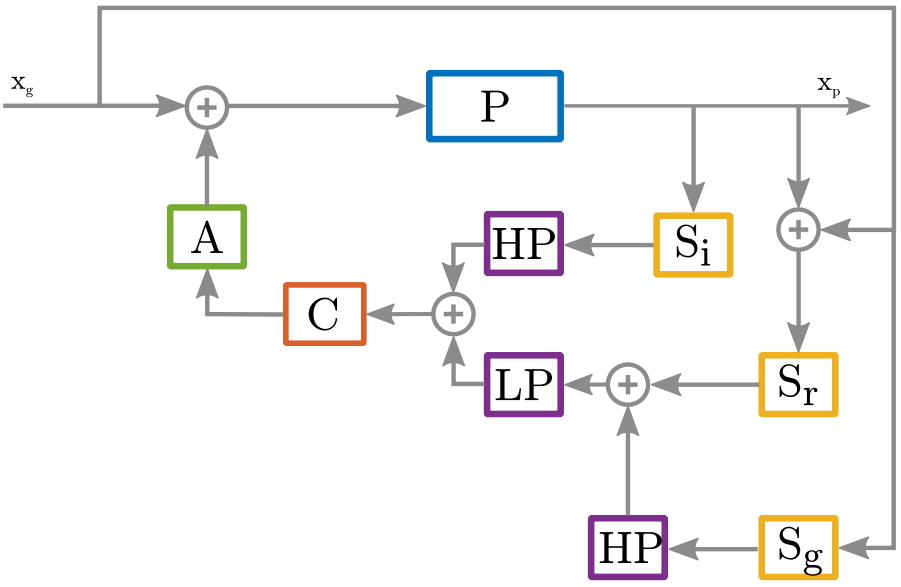


**Figure 107:** AEI-SAS local control block diagram. The scheme represents the local control strategy in the translational degrees of freedom, including sensor correction and sensor blending. The SPI control scheme is not included in this figure.

In order to combine the different sensor signals in each degree of freedom, they need to be filtered by high pass (HP) and low pass (LP)

| Degree of freedom | DC | Mid frequencies | High frequencies | Blending frequency |
|---|---|---|---|---|
| x | LVDT | SC | ACC | 0.1 Hz |
| y | LVDT | SC | ACC | 0.1 Hz |
| rz | OL | OL | OL | |
| z | LVDT | SC | L-4C | 0.55 Hz |
| rx | OL | OL | OL | |
| ry | LVDT | LVDT | L-4C | 0.8 Hz |

**Table 23:** Current central table control signals. Shown are the signals used for the different frequency bands in the individual degrees of freedom. SC represents the signal from the sensor corrected LVDTs, OL the optical lever signal and ACC the signal from the accelerometers. The blending frequency marks the transition between mid and high frequency control signal.
Displayed is the current status where no OL links to a west table exist. In the south table the control signal for the entire frequency band of the y degree of freedom is provided by the SPI, in the west table the SPI will take over the control in the x-direction. As mentioned above, the west table OL will control the central and west table's ry degree of freedom ones it is installed (compare to section 4.3).

blending filters. The resulting combined control signal is called super sensor. HP and LP are complementary high and low pass filters. That means they add up to 1 and therefore form a uniform transition from one sensor to the other. A simple example for such a blended super sensor signal of the vertical degree of freedom is

$$\begin{aligned} S_s &= \mathrm{LP\ LVDT} + \mathrm{HP\ L\text{-}4C} \\ &= \frac{s_0^5 + 5s_0^4 s + 10 s_0^3 s^2}{(s+s_0)^5}\mathrm{LVDT} + \frac{s^5 + 5s_0 s^4 + 10 s_0^2 s^3}{(s+s_0)^5}\mathrm{L\text{-}4C}\ . \end{aligned} \tag{131}$$

Here s is the Laplace frequency $s = \sigma + i\omega$ and $s_0$ is the corresponding blending frequency. The example shows a third order filter pair. The HP and LP filters applied in the AEI-SAS are more complex. They are expanded by additional filters in order to increase the super sensor's signal to noise ratio and to account for internal resonances and cross coupling.

Figure 107 shows a block diagram of the AEI-SAS's local control scheme. Here one of the transverse degrees of freedom is depicted, where LVDT, sensor corrected LVDT and inertial sensor are forming the control signal. The principle of the feedback system is the same as shown

in figure 105. However, here the sensor S is divided into the inertial sensor $S_i$ and the relative sensor $S_r$. In order to obtain a low frequency inertial signal the LVDT signal is corrected by the ground motion sensor signal $S_g$. This signal is filtered by a high pass filter so that only the relative sensor signal controls the DC position. As discussed above, corrected relative sensor signal and inertial sensor signal are combined via LP and HP blending filters. The blended signal is then fed through the controller to the AEI-SAS's actuators.

As mentioned above, this block diagram is only valid for some degrees of freedom of the AEI-SAS. In the final configuration, these are the x, y and z-directions of the central table, the south table's x and z-directions and the west tables y and z-directions. The block diagram for the rotational degrees of freedom that are not red out by an OL is identical to the one shown in figure 107, excluding the ground motion sensor path. In the final configuration, these are the south table's ry and the west table's rx degree of freedom. Currently, the ry degree of freedom of the central table is controlled this way as well.

#### 16.1.3.3 *Preliminary results*

The control scheme described above is applied in the AEI-SAS and provides sufficient vibration isolation for the single arm test currently being commissioned in the AEI 10 m prototype. However, the active noise cancellation is still being improved. Figure 108 shows the vertical translational and the vertical tilt performance of the actively controlled south table. The data was recorded by three auxiliary L-4C geophones placed on the optical table. They function as witness sensors and are therefore not involved in the payload control. So far only the south table is equipped with vertical witness sensors. Vertical out of loop performance measurements are therefore exclusively available for the south table.

In the horizontal directions, only one out of loop sensor is currently available. This witness sensor is a spare monolithic accelerometer and it is located on the central table. The sensor is aligned in the y-direction, however, it is placed on the north edge of the optical table, far away from the payloads rotation axis. Naturally, the amplitudes of ry and rz-motion are higher in this position than if they were measured in the payload's center of mass. More horizontal sensors on the payload will help to characterize and improve the active isolation of the AEI-SAS. Measurements with the central table auxiliary accelerometer are shown in figure 109.

The z and ry measurements clearly show the benefits of the active control. Not only the fundamental resonances of the system are damped, but the payload motion amplitude is reduced significantly below the performance of the uncontrolled AEI-SAS. The ry degree of freedom was controlled by the geophone signal blended with the LVDT signal.

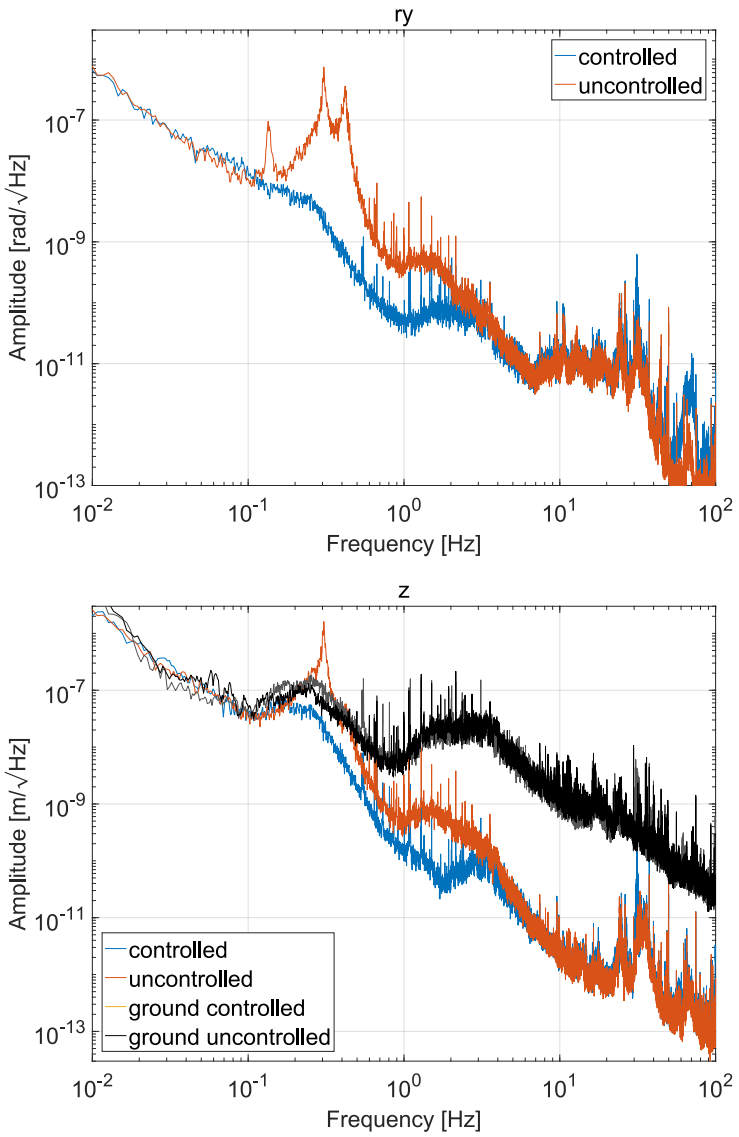


**Figure 108:** Comparison of the controlled (blue) and uncontrolled (red) vertical translational and vertical tilt south table payload noise. The data was recorded by three witness sensors (L-4C geophones) installed on the table top. Above 20 Hz the measurements are (partly) limited by the sensor noise floor.

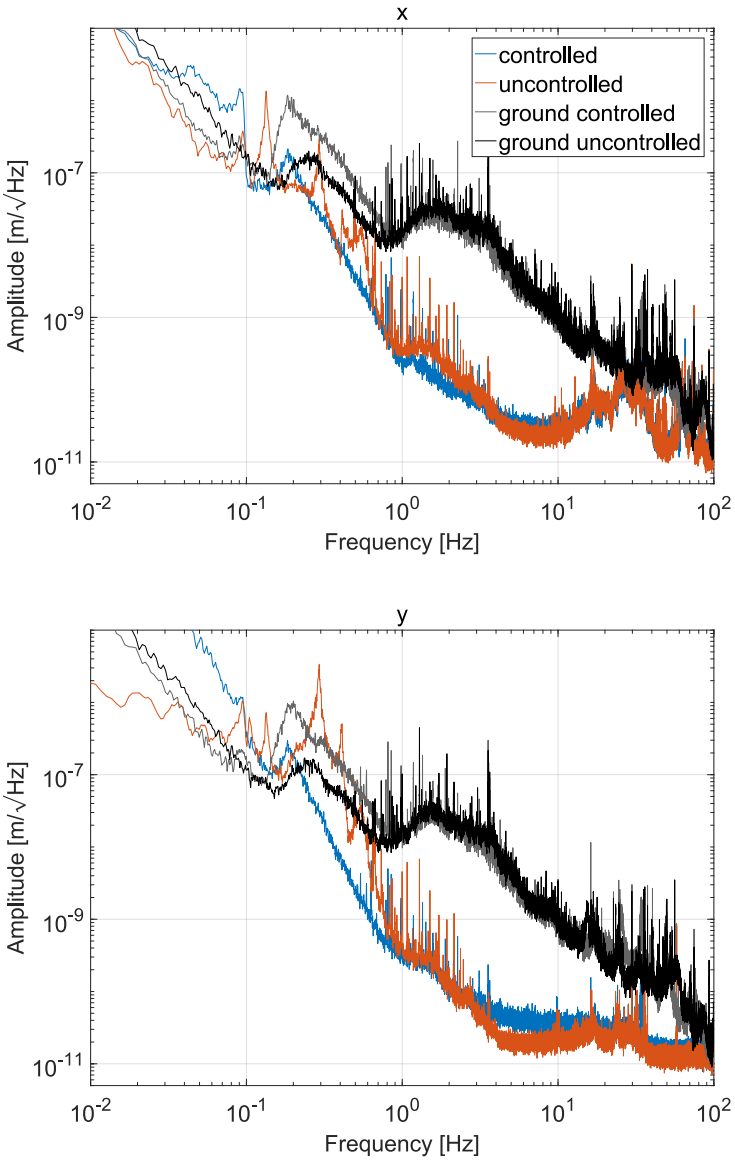


**Figure 109:** Comparison of the controlled (blue) and uncontrolled (red) horizontal central table payload noise. The upper figure shows data recorded with the three in loop accelerometers, the lower plot shows an out of loop measurement. Note that the ground motion in the frequency band of the microseismic peak during the controlled measurement (gray) is higher than during the uncontrolled measurement (black). Further modifications of the active control will improve the AEI-SAS performance.

In Z the control signal was provided by geophones and sensor corrected LVDTs, as depicted in the block diagram in figure 107.

In figure 109 the y-direction out of loop payload measurement also shows a strong reduction of payload motion around the AEI-SAS's fundamental resonances. The microseismic peak amplitude was much larger during the controlled measurement than during the uncontrolled measurement. However, in the frequency band at a few Hertz, the controlled payload motion has a larger amplitude than in the uncontrolled measurement. This is probably because the noise floor of the combined signal of the three in loop accelerometers is higher than the noise floor of the out of loop accelerometer. This noise is partly fed back to the payload. Furthermore, below 0.1 Hz noise is fed back to the payload due to not sufficiently steep blending filters and sensitivity limitations of the sensors. However, further analysis of the control system is needed in order to optimize the noise cancellation.

First measurements by R. Kirchhoff suggest, that the accelerometers and its data acquisition's noise floor limit the active control of the AEI-SAS over a wide frequency range [167]. It is planned to improve the horizontal and rz performance of the AEI-SAS by installing additional horizontal L-4C geophones on the payload. These geophones have a sensitivity comparable to the vertical L-4Cs (see section 5.2.1 ).

The data in the upper plot in figure 109 is recorded by the in-loop accelerometers since no further witness sensors are available at present. The AEI-SAS's internal resonances have a much larger amplitude in this x-direction measurement compared to the y-direction measurement recorded by the witness accelerometer, since the in loop accelerometers are located in the spring-box and not, as the witness accelerometer, on the table top. This is a further reason for placing additional geophones on the table top in order to improve the active isolation performance.

Further active isolation performance measurements, including the OL and SPI performance, are expected to be published in 2018. They will be subject of S. M. Köhlenbeck's thesis.

# 17

# HOW TO PROCEED IN THE CASE OF A GAS-FILTER FAILURE

As discussed in section 8.2, hydrogen embrittlement might cause damage in the GAS-filter blades. The AEI-SAS is not designed for exchanging individual components, such as GAS-filter blades. Hence, this would be a major setback of the AEI 10 m prototype's experimental progress. Procedures to follow in case of GAS-filter failure should be considered in advance in order to lose as little time as possible. In this chapter, two possible scenarios for such an incident are briefly discussed.

The first scenario is less work consuming and less time-consuming. It is limited to the replacement of the broken GAS-filter blade. In the second scenario, the whole AEI-SAS would be replaced by a newly designed, improved isolation system. A third option, which could be a hybrid of the two discussed below, certainly would be possible as well.

## 17.1 REPLACING A BROKEN GAS-FILTER BLADE

Section 8.2 showed that blade damage due to hydrogen embrittlement is related to the material treatment and coating. The nickel plating of new GAS-filter blades should be much thinner than on the current blades, and the heat treatment should be executed accordingly. This process would need to be controlled and the quality of the coating would need to be tested before the blade installation.

However, replacing a broken blade requires careful preparation. Parts of the AEI-SAS need to be disassembled, therefore the table top must be removed from the isolation system. Since the optical tables are populated with delicate optics and their suspension systems they have to be (at least partly) removed beforehand. The Intermediate plate and the upper spring-box plate would need to be removed from the system. This is only possible when the GAS-filters are vertically locked. This requires the disassembly of the vertical LVDT and actuator units. If payload, intermediate plate and upper spring-box plate can be kept inside the vacuum system while the GAS-filter blades are exchanged, and if this would be less time consuming than removing them safely from the system would need to be carefully judged.

The broken GAS-filter would be removed and the new blades would need to be installed as described in the appendix C. For this process, the GAS-filter would need to be taken out of the vacuum system and to be suspended in the shaker stand. This would include the time-consuming tuning of the resonance frequency and the CoP plateau (see

section 10.2). Depending on the number of experienced people involved in this process it could take on the order of months.

Building a spare GAS-filter in advance would reduce the downtime of the AEI 10 m prototype in case of a GAS-filter failure. This way the time-consuming assembly and tuning would be done beforehand and broken and new GAS-filters could be exchanged immediately after the incident.

## 17.2 ALTERNATIVE ISOLATION SYSTEM DESIGN

An alternative to just exchanging the broken components of the system would be to design and build an improved isolation system. If this would be done in advance the downtime of the 10 m prototype would be limited by moving the components from the old optical table to the new one. If one of the first two AEI-SAS units breaks one could simply replace it with an improved version similar to the third AEI-SAS unit. This requires a minimum of designing and testing; however, if a new system would be built one could learn from the experiences with the AEI-SAS and other isolation systems and design a new system.

Adapting a high natural resonant frequencies, high active control bandwidth system such as LIGO's HAM-ISI (see section 3.5.2) is an option. The high performance of the active system due to a long experience would benefit the AEI 10 m prototype. However, a high dynamic range such as it is provided by the AEI-SAS is favorable for a versatile test facility such as the AEI 10 m prototype. This cannot be provided by an ISI like system alone but would require an additional stage, such as the HEPI (see section 3.5).

Employing a commercial system should be considered as an alternative, too. The *Minus k Technology* products do not provide an isolation performance comparable to the AEI-SAS (discussed in section 9.1.3), they could, however, potentially be stacked to a multi-stage system. This would certainly require extensive feasibility and performance tests. Active low frequency isolation would be needed in order to reduce the payload motion around the system's fundamental resonance frequencies at 0.5 Hz. A further application of such commercial devices would be the incorporation of a custom designed isolation system. This is briefly discussed below.

In the following paragraphs an alternative low fundamental resonance frequencies, low active bandwidth isolation system design is proposed. This will not be a detailed analysis of the system but rather a rough outline. This system has a high dynamic range and consists of components tested and improved in the AEI-SAS.

An isolation system that supports the optical table from below has the advantage of being compact. Furthermore, the whole surface of the optical table is free of obstacles and can be populated with experimental

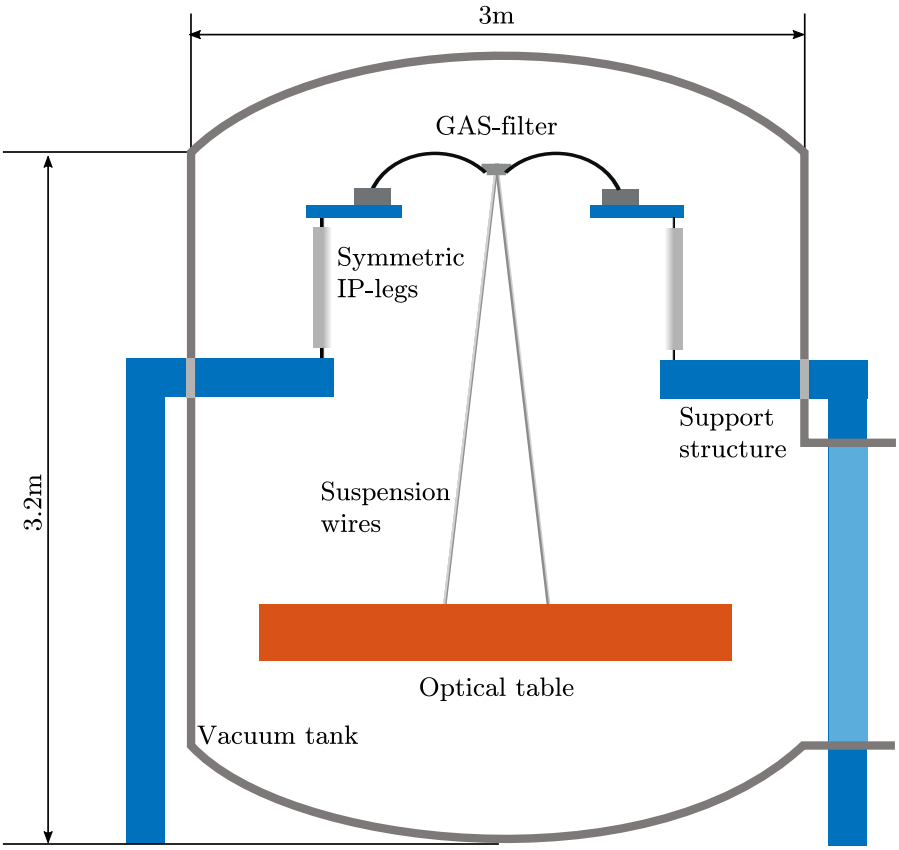


**Figure 110:** Basic concept of the new isolation system design. The optical bench is suspended from a single GAS-filter, which is mounted on top of three symmetric IP-legs. The IP-legs are supported by a rigid structure which is connected to the ground. This structure could be located outside the vacuum tank and reach through soft feedthroughs to the inside. The spacious vacuum tank allows a low resonance frequency pendulum suspension and provides sufficient room for modifications and a support structure for the active components.

setups. However, mitigation of internal resonances and cross-coupling is challenging, as seen in the AEI-SAS.

Suspending the payload from the isolation system, on the other hand, has the potential to reduce the complexity of the system. Furthermore, high internal resonances can be achieved with such a design. This way the system can provide low frequency noise cancellation and good isolation at high frequencies. Figure 110 shows the basic concept of such a system. The optical table is suspended from a single GAS-filter which is supported by three symmetric IP-legs. The large vacuum chamber would allow a relatively large GAS-filter design. This way the stress in the blades and thereby the risk of a failure could be reduced. However, internal resonance frequencies of the blades usually decline with size. Furthermore, the higher mass of the larger system reduces the vertical bounce mode frequencies on the IP-legs, as discussed below. A trade-off in size would need to be made.

The IP-legs would need to be mounted on a rigid structure of a certain height. Such a structure could be built around the vacuum chambers in order to save space inside the vacuum system. Stable arms could reach through soft feedthroughs inside the tanks. This way the support structure would be well decoupled from vacuum system vibrations.

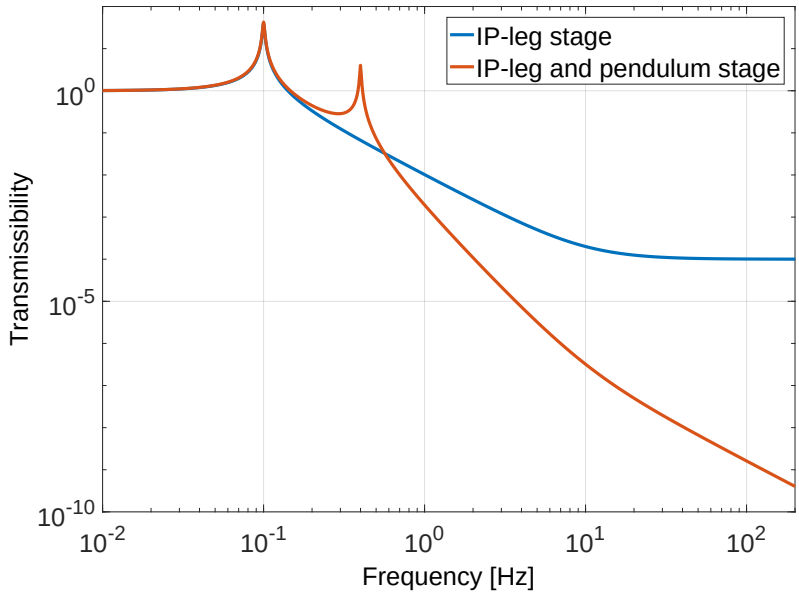


**Figure 111:** Simplified horizontal passive performance of the new isolation system design compared to a single IP-leg stage. The parameters used in single IP-leg stage model are realistic values and therefore illustrate a simplified model of the AEI-SAS.

In the vertical direction, the passive performance of the system is determined by the GAS-filter resonance frequency and the CoP tuning. The resonance frequencies of the rotational degrees of freedom depend on the way the optical table is suspended from the GAS-filter. This is briefly discussed below. In the horizontal directions, the payload is isolated by two stages, the IP-leg stage, and the pendulum stage. Figure 111 shows the simplified, purely passive, transmissibility of the new isolation system compared to the performance of an AEI-SAS type single IP-leg stage. The IP-leg stage is modeled with a resonance frequency of 0.1 Hz and a CoP parameter of $\beta_h = 10^{-4}$. These are realistic values which can be easily achieved with an IP-leg stage. The pendulum stage's CoP effect is neglected. A 1.5 m long pendulum wire results in a resonance frequency of 0.4 Hz. This provides reasonably low frequency isolation by the second horizontal stage. Compared to the IP-leg stage the transmissibility of the new design is lower above 0.57 Hz. A better passive isolation at the fundamental resonance frequencies of the mirror suspension is therefore provided by the two-stage system. At mid frequencies the new design's transmissibility amplitude rolls off with $f^{-4}$ and flattens to $f^{-2}$ where the CoP plateau of the IP-leg stage starts.

Internal resonances are not regarded in this model. They are discussed in the following section.

### 17.2.1 *Internal resonances of the new design*

A major subject of this thesis is the mitigation of the effect of the AEI-SAS's internal resonances. A new isolation system should be designed carefully in order to avoid performance loss due to parasitic vibrations. In this section, a rough estimate of such oscillations is discussed. For a realistic design, finite element simulations, as well as experimental tests, will be indispensable.

In the AEI-SAS, internal resonances below 20 Hz are caused by the horizontal compliance of the GAS-filters and the high mass mounted to the keystones (see section 11.2). The fluorel stage improves the performance in this frequency band strongly. However, the modified system introduces new resonances in the frequency band of the suspension's fundamental resonances, even though they are well damped (see section 12).

In the new isolation system design, the horizontal GAS-filter compliance would not be an issue, since the suspended mass is horizontally decoupled from the keystone. Assuming the same horizontal GAS-filter stiffness as it is provided by the three AEI-SAS GAS-filters and a keystone mass of 5 kg results in a horizontal mode frequency of approximately 133 Hz.

A system with some similarities to the one proposed here is the Advanced Virgo MultiSAS. The lowest frequency internal resonances of this structure are at aproximately 50 Hz and caused by the vertical compliance of the IP-legs (see [59] and section 3.6.1). The MulitSAS features an IP-leg design close to the original AEI-SAS IP-leg design. The new symmetric IP-legs are vertically approximately 4 times stiffer than the old ones, as shown in section 13.4.2. In the AEI-SAS the bounce and roll mode frequencies on the IP-legs are lowered by the flexibility of the spring-box. This should not be a major issue in the new isolation system design since the GAS-filter could be supported by a rather compact, rigid and light structure. It should be easily possible to design such a horizontal stage which weights less than 50 kg. With the new AEI-SAS symmetric IP-legs this would result in a bounce mode frequency higher than 200 Hz.

In the new isolation system design, the optical table is suspended from the GAS filter. Assuming the payload of the AEI-SAS with a weight of approximately 900 kg would be recycled for the new design, a suspension wire would need to be at least 2 mm thick. This assumes a music wire material (304V, Hyten, SLT) as it is used in the reference cavity suspensions [28]. Naturally one would aim for a high safety margin for suspending the optical table. Furthermore, suspending the table from a single wire is rather unpractical for the experimental setups of

the AEI 10 m prototype, as discussed below. Furthermore, multiple suspension wires with the same cross-sectional area as a single wire are stressed equally but their violin mode frequency is higher since the stress in the suspension wire is proportional to load-area ratio and the violin mode frequency is inversely proportional to the square root of the load-area ratio. Four 1.5 m long wires with a thickness of 2 mm each, for instance, have fundamental violin modes of approximately 100 Hz. Proper engineering of the wires' profile should enable a safe system with even higher wire mode frequencies.

### 17.2.2 *Design remarks*

As mentioned above, suspending the optical table from three or four wires would have the advantage of higher violin mode frequencies. This would furthermore allow populating the center of the optical table, as it is currently the case. Beam splitter suspension and SPI baseplate, for instance, are located in the center of the central table. By distributing the connection points of multiple wires around the center of the table they leave space for optical components. The beam splitter suspension cage is about 1 m high and about 0.16 m wide. This requires a minimum wire separation of 0.5 m on the table surface in case of a four-wire solution. Multiple wires furthermore allow the adjustment of the second stage's yaw mode frequency. The pitch and the roll mode are also influenced by the position of the connection between suspension wires and the payload.

A possible modification of the new isolation system design would be the implementation of regular blade springs instead of GAS-filters. A set of pre-stressed blades, as used in the suspension systems, could be installed on top of the IP-leg stage, such that they are horizontally flat when under load. This way they provide a high horizontal stiffness and the stress in the blades would be lower than in the GAS-filter blades. This reduces the risk of blade failures. In such a configuration the single suspension wires could be connected to the tips of each blade. Moderately low vertical fundamental resonance frequencies could be achieved since the large diameter of the vacuum system allows the use of relatively long blade springs. A resonance frequency of 0.6 Hz would be feasible which could be achieved by a pre-bent blade that deflects approximately 0.7 m. Such a system would be less prone to temperature changes (see section 8.1.4). Temperature chance induced GAS-filter stiffness change limits the long-term stability of the AEI-SAS. Due to active control, the low frequency performance would not degrade due to the higher fundamental resonance frequencies.

The high frequency performance of such a system would be limited by the CoP effect. CoP compensators similar to those used for the GAS-filter could be implemented in such a system. This way the blade

springs have a high frequency performance comparable to the GAS-filter. The passive isolation performance in the mid-frequency range, however, is approximately proportional to the square of the resonance frequencies. Hence, the mid-frequency isolation factor of a GAS-filter resonance frequency of 0.3 Hz would be by a factor of 4 better than the isolation performance of the blade springs. This mid frequency range is between the unity gain frequency of the active isolation and the CoP plateau. In case of the AEI-SAS, this would be between a few hertz and a few ten hertz. Higher internal resonances and stronger actuators would allow shifting unity gain to higher frequencies.

However, such a system requires further investigation of advantages and disadvantages of the blade springs and the GAS-filters. Internal resonances of the blades, as well as the way the suspension wire is connected to the blade springs in order to minimize vertical to tilt coupling need to be analyzed.

A further design option would be the incorporation of a commercial isolation system in a custom-made structure. Compact devices, such as the 'SM-1 Low Frequency Vibration Isolator' (briefly discussed in section 9.1.3) could be fitted in the new SAS design as an additional stage. Certainly, the benefitand feasibility need to be evaluated. Testing such a configuration could, however, benefit the design of potential future isolation systems.

Actuators, relative and inertial sensors can be implemented in a similar way as in the AEI-SAS. Horizontal LVDTs and actuators can be mounted in between the support structure and the horizontal stage, a single vertical actuator LVDT pair can be mounted to the keystone and the horizontal stage.

Tilt control could either be realized by actuating against an additional recoil mass, which could be suspended below the optical table, or by actuating against the ground. The recoil mass type requires a more complex design, but a quasi-inertial tilt signal and actuation would be gained. Furthermore, the horizontal displacement does not influence the sensing and actuation signal. Actuation against a rigid structure connected to feet inside the vacuum system requires a less complex suspension system. However, a system for actuating and sensing tilt independent of the horizontal position of the optical table would be required. Motorized blades as well as safety and locking structure could be attached to the in vacuum feet.

Summarized, the advantages of this new suspended system compared to the AEI-SAS would be:

- A wide isolation window due to high internal resonances.

- A better isolation performance in the horizontal directions and in yaw due to two low resonance frequency isolation stages.
- The individual components are better accessible, therefore maintenance and modifications of the system are possible.
- Vertical to tilt coupling is reduced if the system is suspended from a single vertical filter.
- If the vertical filter consists of regular blade springs instead of a GAS-filter the system is less temperature sensitive. A higher bandwidth active isolation in the vertical degree of freedom would minimize the performance disadvantages due to the higher resonance frequency.

However, designing, building, and testing would be costly and require a high amount of resources and time. Based on the experience with the AEI-SAS, this process could take of the order of years, depending on the number of experienced people involved. Further studies are needed to decide how to prepare for and how to proceed in the case of a GAS-filter failure.

# Part IV

# SUMMARY AND OUTLOOK

# SUMMARY AND OUTLOOK

In the scope of this thesis, the AEI 10 m prototype Seismic Attenuation System (AEI-SAS) has been constructed, analyzed, improved and tested. Two out of three AEI-SAS units were successfully implemented in the AEI 10 m prototype, where they are in constant operation. They provide pre-isolation at low frequencies for the subsystems and experiments that are currently being commissioned, such as the single arm test and the thermal noise interferometer (see section 4).

During construction and characterization the first two AEI-SAS units highlighted design aspects that could be improved. Improvements that could be retrofitted in the first two AEI-SAS units have been developed, implemented and characterized.

More invasive performance improving modifications have not been implemented in the first two AEI-SAS units that are already installed in the vacuum system, as they would have to be disassembled to a large extent. This would have delayed the operation of the AEI 10 m prototype considerably. The current experiments of the AEI 10 m prototype require only two isolated platforms, therefore novel improvements were developed and tested on the third AEI-SAS unit outside the vacuum system. The third AEI-SAS unit now features all improvements and geometry changes discussed in this thesis. It will be installed in the AEI 10 m prototype in spring 2018, and together with the first two AEI-SAS units it will provide vibration isolation for the SQL interferometer (see section 4.1) and further experiments to come.

The studies and improvements presented in this thesis do not only increase the AEI-SAS performance, but they could be adapted for other isolation systems and benefit future designs. Beyond the field of GW detection these devices have applications other high precision experimental setups such as atom interferometers (see chapter2).

Improving the GW observatory's sensitivity and developing of novel techniques for future GW detectors will allow more precise measurements of additional GW sources at greater distances. These improvements are developed in test facilities such as the AEI 10 m prototype. An overview of this system and the SQL-interferometer in chapter 4 emphasized the need for seismic isolation.

Part I furthermore discussed the necessity and benefits of performance improvements of the AEI-SAS. It showed, that the system's isolation frequency band is expanded to high frequencies by shifting or damping its internal resonances. At low frequencies, the table top motion is reduced by active isolation. All fundamental resonances of the AEI 10 m prototype suspension systems are pre-isolated this way. Without the discussed improvements, low frequency internal resonances of

the AEI-SAS would have excited suspension resonances. The improved high frequency performance of the AEI-SAS furthermore enables an enhanced low frequency active noise cancellation.

Finite element simulations of the AEI-SAS elastic behavior of the baseplate, the intermediate and the table top, discussed in section 5, aid the evaluation of the AEI-SAS's limitations. So far, these components have not influenced the AEI-SAS performance. The improved isolation of the third AEI-SAS unit, however, might be limited by their elastic behavior.

An analytical model of the Inverted Pendulum (IP)-legs was derived in chapter 7. Methods described in the literature are insufficient to analyze the properties of the IP-legs, therefore a refined analytical model was developed and discussed. The required payload mass estimated this way differed only by approximately 2% from the experimentally determined value. This model was applied for designing the new symmetric IP-legs, described in chapter 13.

The principle of the Geometric Anti-Spring (GAS)-filters was briefly discussed in chapter 8. Since it is highly important for the experiment in practice, the temperature influence on the GAS-filter stiffness and therefore the vertical payload position was derived with a simplified analytical model. The results were confirmed by experimental data. It shows that the vertical payload position decreases by approximately 600 µm/K, depending on the resonance frequency of the individual GAS-filters. These analyses can be used in the future for determining thermal stability requirements for the AEI 10 m prototype. They were furthermore regarded for the fine-tuning of in the AEI-SAS installed GAS-filters' resonance frequencies. Such fine tuning reduces the coupling from vertical ground motion to payload tilt.

Due to recent incidents involving the GAS-filters and superattenuator blade defects at Virgo, the potential risk of GAS-filter blade failure in the AEI-SAS caused by hydrogen embrittlement was discussed. Current measurements are inconclusive. Possible strategies in the case of a failure, however, need to be regarded, as described in chapter 17 and at the end of this chapter.

The second part of this thesis ended with a discussion of the first two AEI-SAS units' passive performance. It matches ideal models very well up to the frequency of first internal resonances (which are not included in the ideal model). A peak isolation performance of $2.6 \times 10^{-3}$ was measured at 4 Hz in the horizontal direction. In the vertical direction, the ground motion is attenuated by a factor of $2.4 \times 10^{-3}$ at 9 Hz. The improved third AEI-SAS unit is supposed to provide even better isolation at higher frequencies, where the first two AEI-SAS units are limited by vertical spring-box resonances. A horizontal fundamental resonance of the AEI-SAS at 0.1 Hz enables a substantial reduction in motion in the frequency band near the mirror suspension resonances.

At the lowest suspension resonance, 0.63 Hz, the horizontal payload motion is approximately 12 times lower than ground motion. Active low frequency isolation results in even better performance. This enabled a suspension design with low force actuators and passive eddy-current damping.

Despite the difference in design philosophies and performance requirements, the AEI-SAS has comparable performance to Advanced LIGO's HAM-ISI. The active control of the HAM-ISI was optimized for low frequency noise cancellation. In this frequency band the system performs better than the AEI-SAS. Above 2 Hz in the horizontal direction and 3 Hz in the vertical direction, the passive isolation of the AEI-SAS provides lower payload motion. Upgrading the active control will further improve the AEI-SAS's low frequency performance, potentially reducing the performance gap below 3 Hz between HAM-SAS and AEI-SAS.

The *Minus k Technology* SM-1 is a state of the art commercial isolation system. It provides 10-100 times better isolation than commercial high-performance air tables. The AEI-SAS, however, provides a significantly higher vibration isolation, justifying the decision to create a customized seismic isolation solution for the AEI 10 m prototype.

The refined GAS-filter tuning in a revised shaker stand was discussed in chapter 10. The high frequency performance of the GAS-filters is determined by the Center of Percussion (CoP) plateau, which was adjusted by a dedicated tuning structure. In the first two tables, as well as in the other isolation systems that employ GAS-filters, the high frequency performance measurements were limited by the sensitivity and dynamic range of the geophones, and by limitations of the test assembly. An improved shaker stand and a refined measurement technique allowed determining GAS-filter CoP plateaus down to an isolation factor of $\beta_v = 1 \times 10^{-5}$. This is about an order of magnitude better than the measurement limits of the first and second AEI-SAS unit's GAS-filters.

The oscillations of the spring-box limits the isolation frequency window of the AEI-SAS at high frequencies. These internal resonances were discussed in section 11. They were subdivided into rigid body spring-box modes and elastic spring-box modes. The rigid body modes are at frequencies between 10 Hz and 20 Hz; their oscillation direction is aligned mostly horizontally and caused by the horizontal compliance of the GAS-filters. The elastic modes are at frequencies between 30 Hz and 40 Hz. They are mostly vertical oscillations of the spring-box. The vertical compliances of the IP-legs soften these modes.

The internal resonances of the system were characterized by a combination of measurements, analytical modeling, and finite-element analysis. The following means of mitigating the effect of these resonances were proposed and tested:

- Fluorel pads to decouple the spring-box and the payload.

- Spring-box dampers to improve isolation performance between 10 and 100 Hz significantly.
- Novel symmetric IP-legs, which are vertically 4 times stiffer than the old design.
- Auxiliary reinforcement structures to stiffen the spring-box. The rigidity of the contacts between the individual spring-box components is enhanced by a combination of adhering and bolting the assembly.

The first two design changes were suitable to be retrofitted into the first two AEI-SAS units. All four presented improvements are incorporated in the third one. The improvements to the third AEI-SAS unit's IP-legs and spring-box shifted the vertical spring-box mode with the lowest resonance frequency from 30.5 Hz to 54 Hz. The third lowest mode frequency has even doubled. By shifting and damping the internal resonances, all mirror suspension resonances are now well isolated from ground motion.

Chapter 16 summarized the active control strategy of the AEI-SAS and showed preliminary performance results. The fundamental resonances of the AEI-SAS was efficiently damped and the payload motion was suppressed below the uncontrolled tabletop noise level over a wide frequency range.

The AEI-SAS provides a low noise environment that allows a SQL-interferometer test mass actuation by means of an ESD which is directly mounted on the table top. The discussion of this system's realization is not directly related to the main part of this thesis and therefore subject of Appendix A. On the bases of finite element analyzes the new ESD concept was found to be suitable for a low noise actuation of low mass mirrors in one horizontal direction. Experimental tests with this system are underway.

Building on the work presented in this thesis, the seismic isolation for the AEI 10 m prototype will be further improved.

Improvements to the low frequency active isolation are still underway. New horizontal L4C geophones with better noise performance and greater robustness than the currently used monolithic accelerometers will be implemented in all three AEI-SAS units. This will improve the low frequency performance of the system.

Measurements of the first two AEI-SAS units show a different behavior at a few hertz (discussed in section 9.2). Relatively stiff cables connecting payload electronics with the environment could be the reason for this; however, further investigations are necessary in order to improve the central table's performance at those frequencies.

After the third improved AEI-SAS unit will be installed in the AEI 10 m prototype, the full system's in vacuum performance will be mea-

sured and analyzed. Spring-box dampers will be assembled and tuned to the system's internal resonances. The active isolation will be adapted for the third AEI-SAS unit. Its performance will likely be enhanced with respect to the first two AEI-SAS units since higher internal resonance frequencies allow a higher control loop unity gain frequency.

For global control, the Suspension Platform Interferometer (see section 4.3) will be expanded to the west table. Optical Levers (see section 4.3) between west and central tank will furthermore be implemented.

As discussed in section 8.2, hydrogen embrittlement might cause damage in the GAS-filter blades. This would mean a major setback of the AEI 10 m prototype's experimental progress, since the AEI-SAS and its payload would need to be partly disassembled. An outlook of possible scenarios on how to prepare for such an incident is given in chapter 17. A promising option would be to develop a new improved isolation system. The experience with the AEI-SAS and its limitations lead to a design where the payload is suspended from an isolation system instead of being supported from below. The system discussed in section 17.2 has the potential to have lowest internal resonances above 100 Hz. The resulting isolation window would thereby be far wider than that one of the AEI-SAS. This, furthermore, allows a broader active isolation band. A second horizontal isolation stage would improve the passive isolation by a factor of $f^{-2}$ above the fundamental resonance frequency. In contrast to the AEI-SAS the individual components of such a system would be accessible which would allow modifications and maintenance; however, further investigations will show if replacing the AEI-SAS is reasonable and feasible. The studies and improvements discussed in this thesis certainly will benefit the design of future vibration isolation systems.

# Part V

# APPENDIX

# A

# THE ELECTRO-STATIC DRIVE

As briefly discussed in section 4.1.3, a new concept for electrostatic test mass actuation was proposed for the SQL interferometer [168]. It will be used for fast and direct test mass actuation. Due to the low noise environment provided by the AEI-SAS these Electrostatic drives (ESDs) can be mounted directly on the optical table.

ESDs were first employed in gravitational wave detectors in 2001 to actuate GEO 600's interferometer mirrors without contact and with extremely low noise [169]. In Advanced LIGO similar systems were implemented based on the positive experience at GEO 600 [85]. As shown in figure 112 such ESDs consists of four quadrants of comb-shaped electrode pairs coated onto a reaction mass, which is suspended behind the test masses. This enables electrostatic actuation in pitch, yaw and the longitudinal direction.

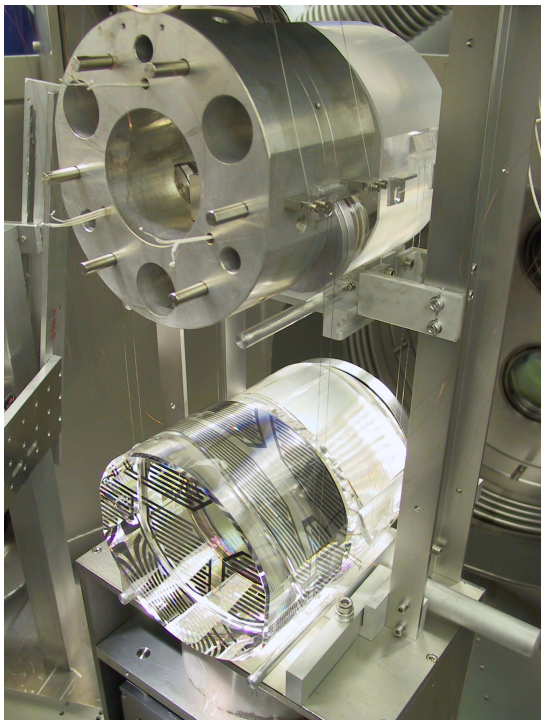

**Figure 112:** GEO 600 ESD. Four comb shaped electrode pair quadrants are coated on the surface of a reaction mass. It is suspended behind the test mass. Advanced LIGO's ESD is an adapted version of the one shown here.

The basic working principle of an ESD is that a force is acting on a dielectric medium when it is located in an asymmetric inhomogeneous electric field. The force is directed towards higher intensity of the field.

Hence, the mirrors are pulled towards the ESDs up to a point where the restoring forces of the test mass and reaction mass pendulums match the ESD force. The variation of the ESD voltage, therefore, induces mirror motion.

For the SQL interferometer at the AEI 10 m prototype the design used in GEO 600 and Advanced LIGO is not applicable. As mentioned in section 4.1, the low coating thermal noise performance of the interferometer relies on large beam sizes on the mirror surfaces. A tiny fraction of the light is transmitted through the optics and sensed by a photodiode. A large free aperture therefore is required. The electrodes of the GEO 600/Advanced LIGO design cover a large part of the optics' surface. A second aspect why this design is not suitable for the SQL interferometer is that such an ESD requires a vibration isolation with a performance comparable to the test masses, in order to avoid coupling to the table top motion.

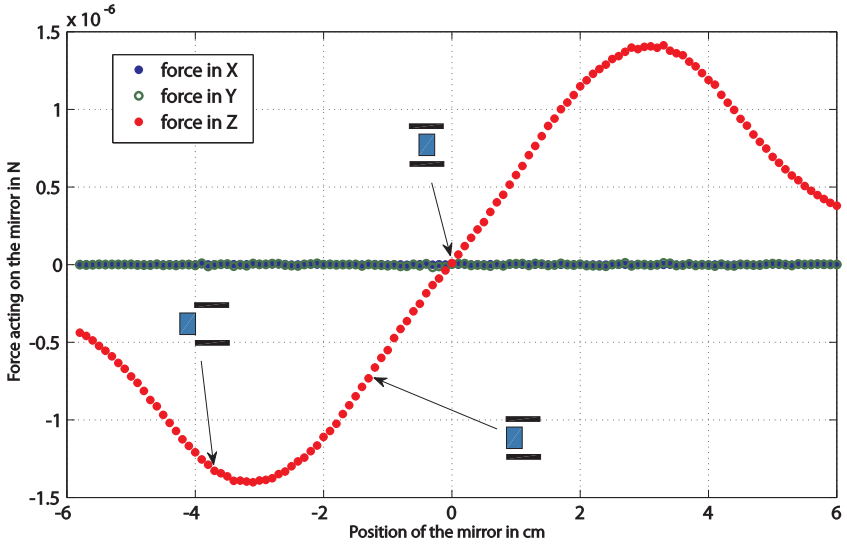


**Figure 113:** Longitudinal force on the mirror, versus relative longitudinal position of mirror and ESD. The x-axis shows the relative distance between the mirror center and the center of the capacitor plates. The mirror-plate position is depicted for clarification. The position of choice is at one of the extrema of the longitudinal (z) force. There the force is in first order independent of the relative distance between mirror and plates.
This figure is taken from [170]

The new ESD design for the AEI 10 m prototype is rather simple. A plate capacitor with one plate above and one plate below the test mass generates the electric field. This structure provides a clear aperture. Furthermore, simulations show, that around a certain relative mirror-plate position such a system provides a force that is in first order independent of the longitudinal plate position. This is illustrated in figure 113. Proof of principle simulations of this new concept show

that the vibration isolation provided by the AEI-SAS is sufficient to neglect coupling from capacitor plate motion [170].

For the realization of the AEI 10 m prototype ESD the proof of principle simulation structure needs to be modified and fitted to the SQL-interferometer suspension design; furthermore, the influence of the surrounding structure on the actuation needs to be regarded. Particularly the fiber guards, which are aluminum structures surrounding the suspension fibers, have the potential to influence the ESD permanence since they are located relatively close to the mirrors. They furthermore restrict the capacitor plate dimensions.

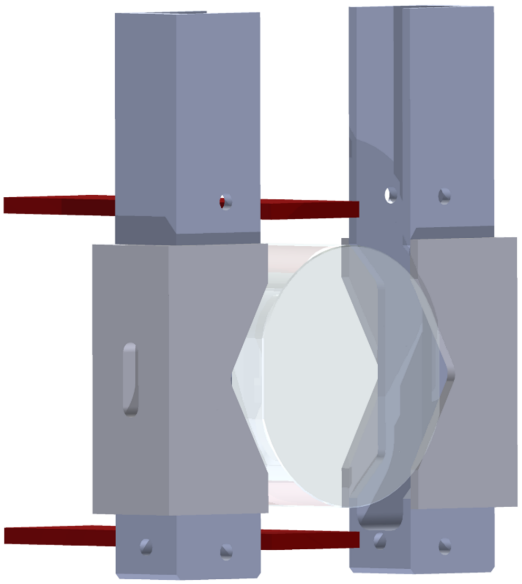

**Figure 114:** Illustration of the test mass, the fiber guards, and the ESD capacitor plates. The fiber guards are made of aluminum. The lower two pieces surrounding the mirror and attached to the fiber guards are made from polyether ether ketone (PEEK), It serves as a safety structure for the test mass and can be moved in order to clamp the mirror.

A 23 mm wide, 3 mm high and 70 mm long capacitor plate design fits between the fiber guards with sufficient clearance to avoid electric sparks. A CAD drawing of the ESD-plates, the fiber guards, and the test mass is shown in figure 114. The thickness provides a high bending stiffness and the length allows to mount the plate far away from the optic, as discussed below. The force provided by these plates, however, is lower than in the proof of principle simulation, where the plates were modeled to be 50 mm wide.

## A.1 ESD FORCE SIMULATION

In order to achieve the required longitudinal force of about 1 µN with the narrower plate design with respect to the proof of principle model, the gap between mirror and plate was reduced. In the proof of principle version, the distance between mirror's rim and inner capacitor plate surface is 10.5 mm. This distance was reduced to 4.75 mm in the new version. The new dimensions were determined by means of finite element simulations of a close to reality model.

In order to verify the quality of the ESD finite element simulation technique a greatly simplified geometry was modeled. This model's geometry resembles a system that can be approximated analytically. It consists of two large capacitor plates filled with glass. The force acting on the glass body is given by [171]:

$$F_{ESD} = \frac{l U_{ESD}^2}{2d} \left(\epsilon_g - \epsilon_0\right) \quad . \tag{132}$$

Here $l$ is the plate's width, $d$ is the plates' separation, $U_{ESD}$ is the voltage difference between the two plates, $\epsilon_g$ is the dielectric constant of glass, and $\epsilon_0$ is the vacuum permittivity. The results from the finite element simulation and the analytic approximation were compared and the simulation was adjusted accordingly before the more complex ESD structure was computed.

The geometry used in the simulation features capacitor plates which were set to a certain voltage, the fiber guards, and the test mass. The aluminum parts of the fiber guards were set to 0 V. The force on the mirror was computed. Figure 115 shows the simulated electric field in the structure. From this, the force acting on the mirror is computed.

An ESD voltage is provided by a custom made high voltage source [172]. About ±350 V will be available for the maximum mirror actuation. According to the finite element simulation, this results in a longitudinal force on the mirror of 0.9 µN. Such a force allows a maximal DC displacement of 315 nm of the 100 g mirror suspended from the triple suspension. No significant influence of the fiber guards was observed in the simulations.

Preliminary experimental ESD tests as part of the single arm test resulted in a maximal longitudinal mirror displacement of 350 nm [173]. With a 10 % deviation, this result agrees relatively well with the simulation. Further experiments will verify the influence of the relative longitudinal mirror-plate position, the vertical plate position and the plate separation. Furthermore, the possibility and the influence of test mass charging will be investigated. If an influence will be determined, techniques for the mitigating it will be tested. Ultimately, the ESD control of the single arm cavity will be characterized and optimized.

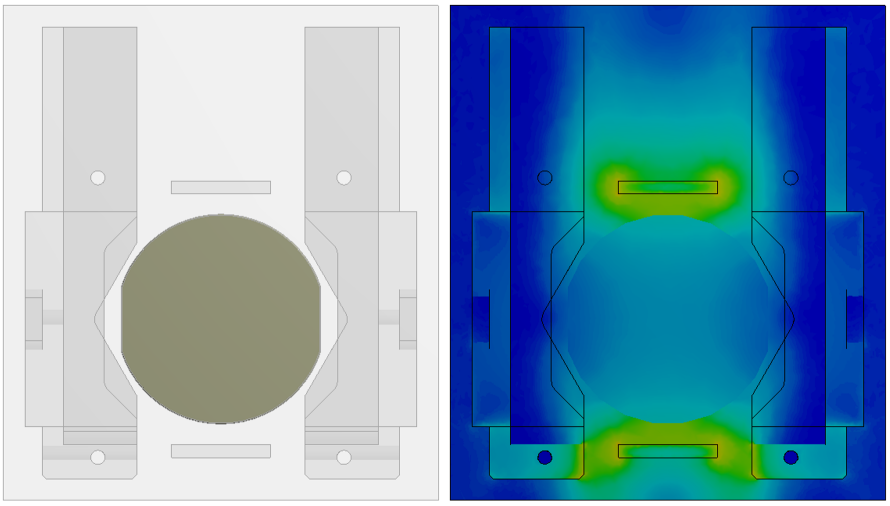

**Figure 115:** Illustration of the ESD finite element model. The left part of the figure shows the modeled geometry. The upper capacitor plate is set to +350 V, the lower plate is set to −350 V, and the fiber guards are set to 0 V. The right part of the figure shows a section view of the structure. The electric field intensity is displayed as a color scheme. The force on the test mass is computed from the electric field.

An ESD design similar to the one discussed in this chapter is currently being tested for the speedmeter proof of principle experiment in Glasgow [174].

## A.2 MECHANICAL ESD DESIGN

For the realization of the ESD the following design criteria were regarded:

- The ESD post needs to be compatible with the suspension cage and the suspension itself.
- The ESD plates need to be electrically insulated from the ESD post.
- Sufficient clearance between capacitor plates and post needs to be ensured.
- The capacitor plates should be adjustable in all three translational degrees of freedom.
- The capacitor plates and the ESD post should be designed relatively stiff, such that internal resonances of the structure are as high as possible and do not influence the interferometric measurements.

A possible mechanical ESD design is shown in figure 116. This post is made from aluminum, only the yellow cylinders are commercial ceramic

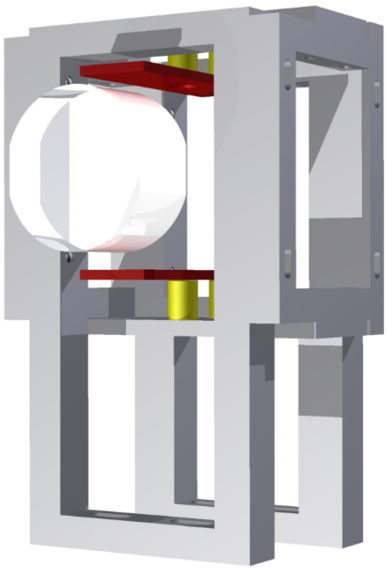

**Figure 116:** CAD drawing of an ESD post. The design fulfills the requirements itemized above. The structure is made from aluminum. the yellow cylinders, which separates the capacitor plates (red) from the post, are commercial ceramic insulators. The mechanical resonances of this system are shown in figure 117.

insulators. The cables are bolted directly to the capacitor plates. The plate position is adjustable in the three translational degrees of freedom. If needed, earthquake stops for the test mass can be added to the frame.

The ESD post was designed to be relatively stiff. Figure 117 shows a finite element simulation of the system's four lowest frequency internal resonances. In this model, the base of the post is fixed and the individual components of the assembly are rigidly connected. In reality, The lowest frequency internal resonances of the system are the bending and torsion modes at frequencies between 521 Hz and 533 Hz. This is above the SQL measurement frequency band and far higher than the control unity gain frequencies currently tested; furthermore, the simulated capacitor blade motion will not couple to the longitudinal mirror motion in first order. The lowest frequency plate bending mode is at 1221 Hz this will not limit any SQL interferometer measurement.

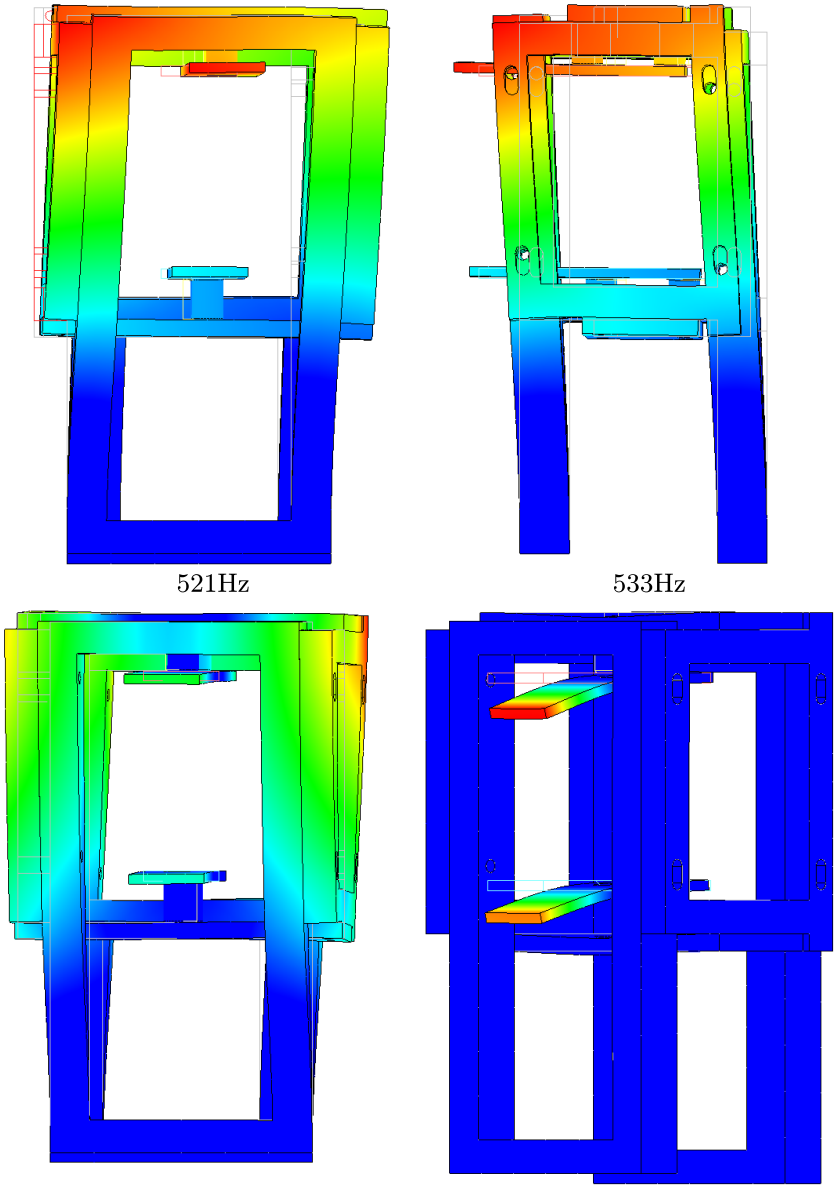


**Figure 117:** Finite element simulation of an ESD post mechanical resonances. Mode shape and frequency of this structure should not limit the SQL-interferometer.

# B

# FINITE ELEMENT SIMULATION PROCEDURE

Finite element simulations are a helpful tool to solve physical problems which are too complex to be treated analytically. In the scope of this thesis they were used as a tool for analyzing the mechanical behavior of the AEI-SAS and its components; furthermore, the improvements of the system were partly tested and optimized by means of these models.

The finite element simulations discussed in this thesis were mostly computed with *Ansys Workbench*. However, some of the simpler models were simulated with *Autodesk Inventor*.

In principle, finite element simulations were approached in the itemized steps:

- The problem to be solved is simplified in a way that it is analytically solvable. In general, these simplified models are one-dimensional, linear and they consist of point masses rather than volumes. That means, however, that the results of these models only provide limited information about the reality.
- The results from the analytically solved simplified model are then compared to a finite element simulation of a similar problem. This way the modeling methods and results are validated.
- If the results match, the model can be evolved to a closer to reality version. In general, that means, that geometries become three-dimensional, and match the realistic shapes. Furthermore, material properties, as for instance the elasticity, can be regarded.
- The geometry should, however, be kept as simple as possible in order to achieve an efficient finite element meshing and to facilitate analyzing possible modeling issues.
- For each finite element model, the convergence of the results with higher mesh density needs to be studied.
- The results naturally need to be validated and compared to reality.

A technique for simplifying geometries, and thereby making the meshing more efficient is shown in figure 118. It was often applied in simulations presented in this thesis. This spring matrix is used for substituting elastic components of a geometry. In terms of analyzing the AEI-SAS dynamics it is used to model the GAS-filter stiffness matrix (see for instance section 11.2.3), the IP-leg stiffness matrix (see for instance section 11.3) and the fluorel stage stiffness matrix (see for instance

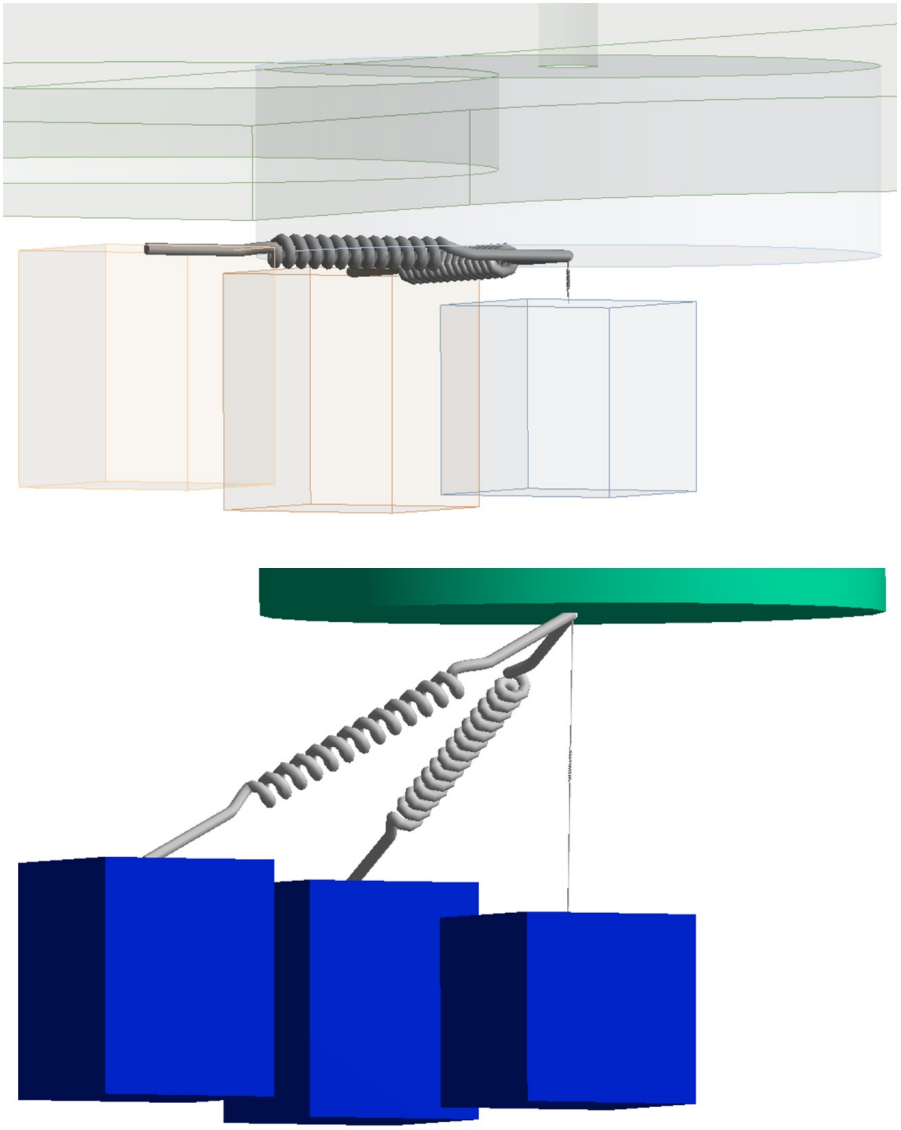

**Figure 118:** Illustration of a stiffness matrix for finite element simulations. The displayed technique is used to simulate spring components such as the GAS-filters, the IP-legs, or the fluorel stage. Three springs are interconnecting two blocks. One block is rigidly connected to an upper geometry, three blocks are connected to a lower one. Spring constant and damping factor can be assigned to the individual springs. The springs only have these two properties and are not part of the meshed geometry. They, therefore, simplify simulations strongly. The figure shows an example in which the spring matrix is used. The upper part shows the assembly at its resting position, the lower part in a deflected state.

section 12.2). If the main focus of a simulation is not on the dynamics or the static behavior of the spring components, but of the overall geometry, this technique can greatly simplify the model.

The spring matrix consists of three springs, one in the vertical direction and two horizontal directions. The directions in which the three springs are oriented are linearly independent. Each spring connects to an upper and a lower body. The stiffness and the damping factor can be assigned to the springs. These properties of a single spring are unidirectional in the direction given by the two connecting points.

# C

# GAS-FILTER ASSEMBLY

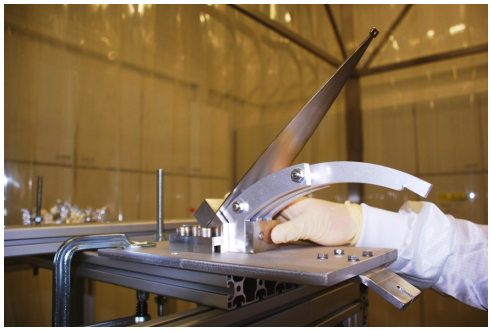

**Figure 119:** The bottom of the blade is bolted into the clamp and mounted on the bending jig.

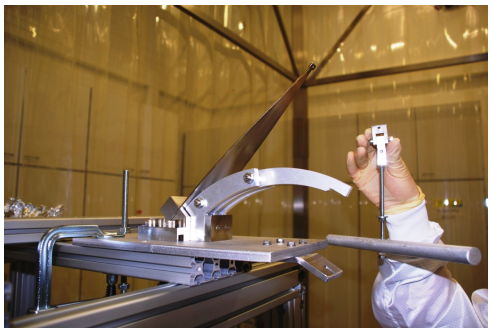

**Figure 120:** This figure shows the tool for bending the blades.

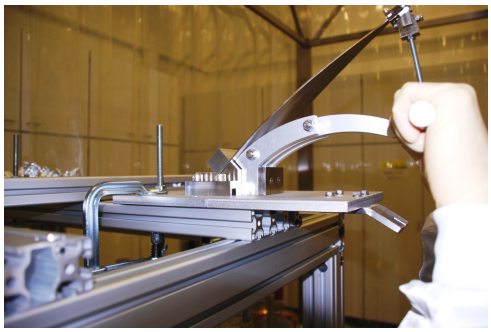

**Figure 121:** The bending tool is clamped to the top of the blade...

This chapter describes the GAS-filter blade assembly. The photographs on the left show the single stages of the blade preparation and the implementation in the filter. After the blades are installed on the filter's baseplate they are compressed against each other. That introduces the anti-spring force which lowers the resonance frequency. The filters are tuned to 0.3 Hz. Subsequently the center of percussion is tuned (see section 10.3.1).
This procedure was documented together with Robin Kirchhoff and is part of his bachelor thesis [175].
In order to bend the straight GAS-filter blade to the right position, it is mounted in a jig, exclusively designed for this task.

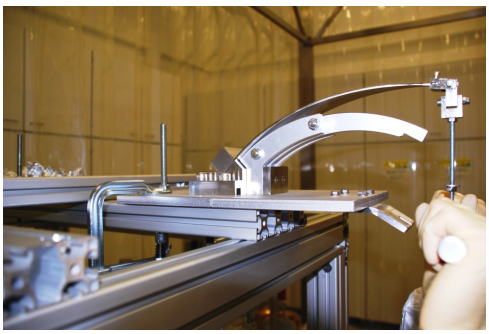

**Figure 122:** ... and the blade is bent over the bending-jig.

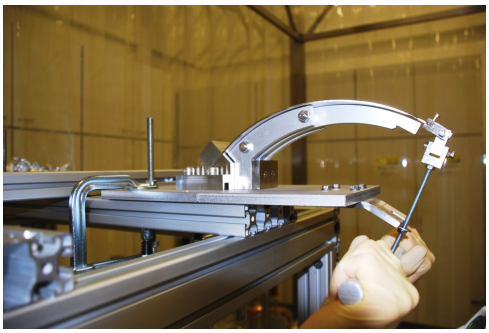

**Figure 123:** Hooking the bending tool in a dedicated notch in the jig keeps the blade in place.

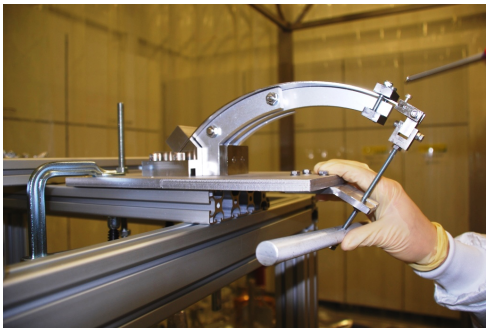

**Figure 124:** An additional clamp fixes the blade to the jig.

The blade is bent over the jig by pulling its tip down by hand. The bending tool is hooked in the jig to secure its position. Before the bending tool is taken off, two plates are clamped around the blade and the jig to keep the blade in place.

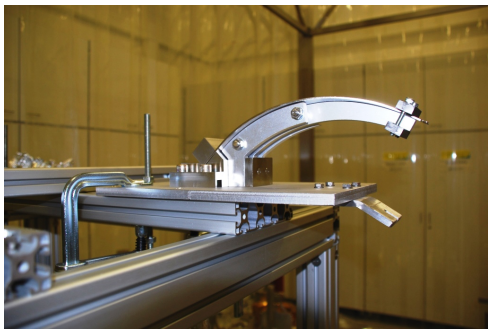

**Figure 125:** The bending tool is taken off the blade, while the clamp holds it in place.

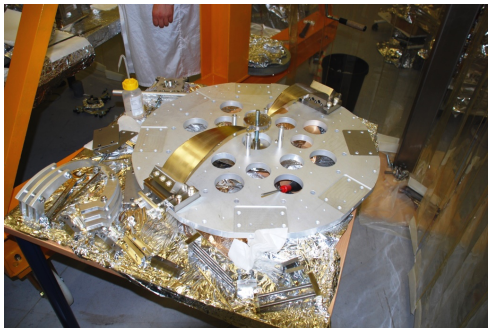

**Figure 126:** The blade, the bending profile, and the lower clamp are taken from the jig and mounted on the GAS-filter baseplate. Two blades are always opposing each other. The blade's tip is bolted to the keystone. It is held in place by a threaded rod from the bottom of the baseplate.

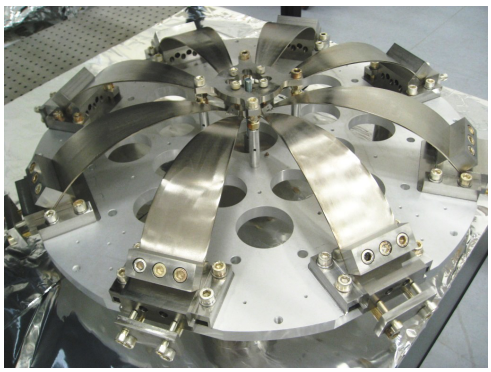

**Figure 127:** All eight blades are bend and installed on the baseplate. Eight plates with four bolts each are mounted to the outside of the filter, in order to compress the blades against each other and, thus, tune the GAS-filters resonance frequency.

The blades are prepared one by one before they are mounted on the filter's baseplate. The blade's tip is bolted to the keystone from below. A threaded rod is holding the keystone in place. The foot of the blade is clamped to the baseplate in a way that it can be shifted in- an outwards. This enables the resonance frequency tuning of the GAS-filters by compressing the blades against each other. For this purpose, a plate is bolted to the outside of the baseplate. Two horizontal bolts in the upper part of this plate force the foot of the blade inwards or outwards. This way the compression of the blades against each other can be fine-tuned.

Before tuning the resonance frequency, all blades are installed in a crown-shaped assembly on the filter baseplate, the filter is suspended in a shaker stand and the keystone is loaded with an about 300 kg dummy mass (see section 10.2). After the resonance frequency is tuned to 0.3 Hz the CoP of the GAS-filters is tuned.

# D

## COMPARISON OF THE CENTRAL AND SOUTH TABLE'S VERTICAL SPRING-BOX MODES

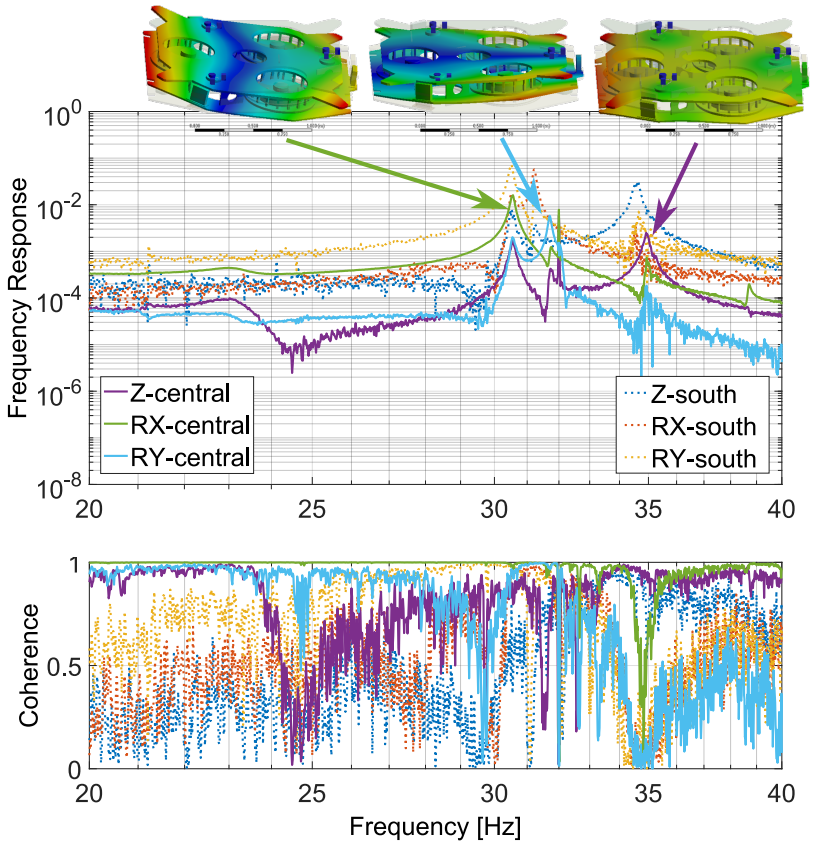


**Figure 128:** Comparison of driven three lowest vertical spring-box modes in central and south table. The system was actuated by the vertical actuators, located between the spring-box and the GAS-filter's key-stones. Even though the resonance frequency is lower than simulated (see section 11.3.1), the order and the shape of the modes coincides. The mode frequencies in the two AEI-SAS units differ only by less than 1 Hz.

As described in chapter 11.3, the low vertical spring-box modes in the first two AEI-SAS units are caused by the relatively low vertical stiffenss of the old IP-legs and the bending of the spring-box. For the sake of completeness the internal resonances of the both tables are compared in figure 128. The dotted lines are identical with the plot shown in figure 67. The central table measurement was done in a similar way as it was done at the south table. The difference in frequency response gain is due to a different sensor position in both AEI-SAS units. The mode frequencies of both systems are lower than simulated.

This is because the real components are bolted, where as the simulated system is monolithic. Nevertheless the shape and the order of the modes coincides with the finite element simulation. The internal resonance frequencies of the two AEI-SAS units differ only by less then 1 Hz.

Figure 129 shows the central table measurement with a simple damped harmonic oscillator model fitted to it. This provides information about the modes' quality factors and resonance frequencies, which is needed for designing efficient spring-box dampers (see section 15.1.2).

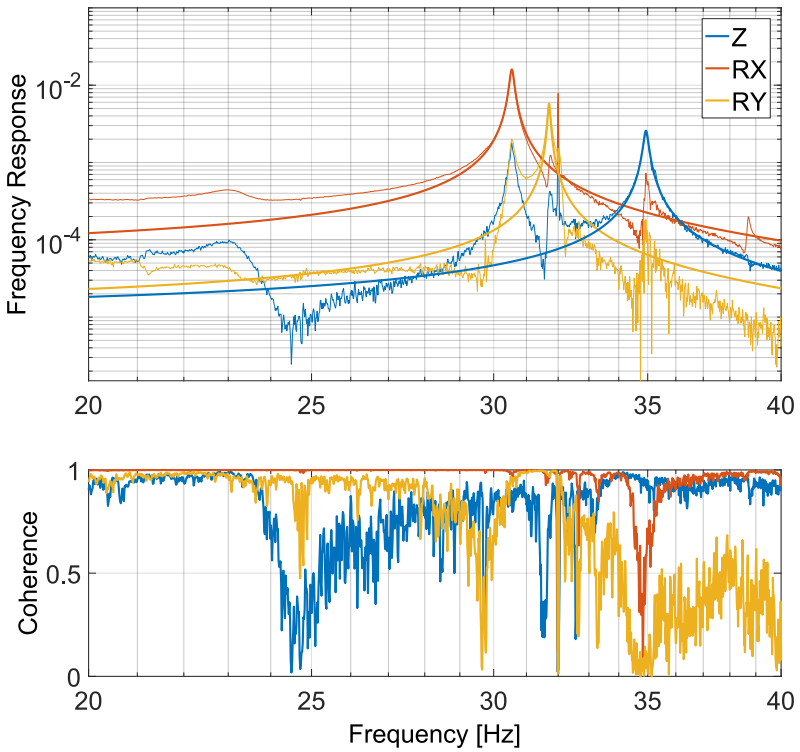


**Figure 129:** Fitted driven vertical spring-box resonances (central table). In order to determine the parameters of the modes to be damped by the spring-box dampers the measured data is fitted by a simple damped harmonic oscillator model. The parameters of the fit are shown in table 21. The measurement and fit for the south table spring-box modes is shown in figure 99.

# BIBLIOGRAPHY


[1] B. P. Abbott, R. Abbott, T. Abbott, M. Abernathy, F. Acernese, K. Ackley, C. Adams, T. Adams, P. Addesso, R. Adhikari, et al. "Observation of gravitational waves from a binary black hole merger." In: *Physical review letters* 116.6 (2016), p. 061102.

[2] A. Einstein. *Näherungsweise integration der feldgleichungen der gravitation*. Wiley Online Library, 1916.

[3] P. R. Saulson. *Fundamentals of interferometric gravitational wave detectors*. World scientific, 1994.

[4] B. P. Abbott, R Abbott, T. Abbott, F Acernese, K Ackley, C Adams, T Adams, P Addesso, R. Adhikari, V. Adya, et al. "GW170814: A three-detector observation of gravitational waves from a binary black hole coalescence." In: *Physical Review Letters* 119.14 (2017), p. 141101.

[5] Caltech 40m and prototype. URL: https://labcit.ligo.caltech.edu/ajw/40m/40m_upgrade.html.

[6] D Shoemaker, R Schilling, L Schnupp, W Winkler, K Maischberger, and A Rüdiger. "Noise behavior of the Garching 30-meter prototype gravitational-wave detector." In: *Physical Review D* 38.2 (1988), p. 423.

[7] K. Skeldon, D. Clubley, B. Barr, M. Casey, J Hough, S. Killbourn, P. McNamara, G. Newton, M. Plissi, D. Robertson, et al. "Performance of the Glasgow 10 m prototype gravitational wave detector operating at λ= 1064 nm." In: *Physics Letters A* 273.5 (2000), pp. 277–284.

[8] D. Castelvecchi. *Hunt for gravitational waves to resume after massive upgrade*. Nature News. 2015.

[9] B. Abbott, R Abbott, T. Abbott, M. Abernathy, F Acernese, K Ackley, C Adams, T Adams, P Addesso, R. Adhikari, et al. "Observing gravitational-wave transient GW150914 with minimal assumptions." In: *Physical Review D* 93.12 (2016), p. 122004.

[10] B. P. Abbott, R Abbott, T. Abbott, M. Abernathy, F Acernese, K Ackley, M Adamo, C Adams, T Adams, P Addesso, et al. "Characterization of transient noise in Advanced LIGO relevant to gravitational wave signal GW150914." In: *Classical and Quantum Gravity* 33.13 (2016), p. 134001.

[11] B. P. Abbott, R Abbott, T. Abbott, M. Abernathy, F Acernese, K Ackley, C Adams, T Adams, P Addesso, R. Adhikari, et al. "Properties of the binary black hole merger GW150914." In: *Physical review letters* 116.24 (2016), p. 241102.

[12] N. J. Cornish and T. B. Littenberg. "Bayeswave: Bayesian inference for gravitational wave bursts and instrument glitches." In: *Classical and Quantum Gravity* 32.13 (2015), p. 135012.

[13] *The Nobel Prize in Physics*. The Nobel Foundation, 2017.

[14] B. Abbott, R Abbott, T. Abbott, M. Abernathy, F Acernese, K Ackley, C Adams, T Adams, P Addesso, R. Adhikari, et al. "Binary black hole mergers in the first advanced LIGO observing run." In: *Physical Review X* 6.4 (2016), p. 041015.

[15] Hughey et al. "GW151226: observation of gravitational waves from a 22-solar-mass binary black hole coalescence." In: *Phys Rev Lett* 116 (2016), p. 241103.

[16] B. Abbott, R Abbott, T. Abbott, F Acernese, K Ackley, C Adams, T Adams, P Addesso, R. Adhikari, et al. "GW170104: observation of a 50-solar-mass binary black hole coalescence at redshift 0.2." In: *Physical Review Letters* 118.22 (2017), p. 221101.

[17] B. Abbott, R Abbott, T. Abbott, F Acernese, K Ackley, C Adams, T Adams, P Addesso, R. Adhikari, V. Adya, et al. "GW170608: Observation of a 19 solar-mass binary black hole coalescence." In: *The Astrophysical Journal Letters* 851.2 (2017), p. L35.

[18] B. P. Abbott, R. Abbott, T. Abbott, F. Acernese, K. Ackley, C. Adams, T. Adams, P. Addesso, R. Adhikari, V. Adya, et al. "GW170817: observation of gravitational waves from a binary neutron star inspiral." In: *Physical Review Letters* 119.16 (2017), p. 161101.

[19] B. Abbott, R Abbott, T. Abbott, F Acernese, K Ackley, C Adams, T Adams, P Addesso, R. Adhikari, V. Adya, et al. "Gravitational waves and gamma-rays from a binary neutron star merger: GW170817 and GRB 170817A." In: *The Astrophysical Journal Letters* 848.2 (2017), p. L13.

[20] B. Abbott, R Abbott, R. Adhikari, A Ananyeva, S. Anderson, S Appert, K Arai, M. Araya, J. Barayoga, B. Barish, et al. "Multi-messenger observations of a binary neutron star merger." In: *Astrophysical Journal Letters* 848.2 (2017), p. L12.

[21] A Albert, M. Andre, M. Anghinolfi, S Sarkar, V. Scientific Ligo and Collaborations, Antares Collaboration, IceCube Collaboration, Pierre Auger Collaboration, et al. "Search for high-energy neutrinos from binary neutron star merger GW170817 with ANTARES, IceCube, and the Pierre Auger Observatory." In: (2017).

[22] LIGO Scientific Collaboration, Virgo Collaboration, 1M2H Collaboration, Dark Energy Camera GW-EM Collaboration, DES Collaboration, DLT40 Collaboration, Las Cumbres Observatory Collaboration, VINROUGE Collaboration, MASTER Collaboration, et al. "A gravitational-wave standard siren measurement of the Hubble constant." In: *Nature* 551.7678 (2017), pp. 85–88.

[23] A Wanner, G Bergmann, A Bertolini, T Fricke, H Lück, C. Mow-Lowry, K. Strain, S Goßler, and K Danzmann. "Seismic attenuation system for the AEI 10 meter Prototype." In: *Classical and quantum gravity* 29.24 (2012), p. 245007.

[24] A Wanner. "Seismic Attenuation System (AEI-SAS) for the AEI 10 m prototype." PhD thesis. Technische Informationsbibliothek und Universitätsbibliothek Hannover (TIB), 2013.

[25] M. Abernathy, F Acernese, P Ajith, B Allen, P Amaro-Seoane, et al. "Einstein gravitational wave Telescope conceptual design study." In: *available from European Gravitational Observatory, document number ET-0106A-10* (2011).

[26] Gravity sensing with very long baseline atom interferometry. URL: https://www.geoq.uni-hannover.de/a02.html.

[27] D. R. Crooks. "Mechanical loss and its significance in the test mass mirrors of gravitational wave detectors." PhD thesis. University of Glasgow, 2002.

[28] T. Westphal. "A coating thermal noise interferometer for the AEI 10 m prototype facility." PhD thesis. Gottfried Wilhelm Leibniz Universität Hannover, 2016.

[29] K. Strain, G. Hammond, L MacKenzie, and A. Cumming. "Modelling of the AEI 10m Suspension." In: *internal logbook page 296* (2010).

[30] M. Ando, TAMA collaboration, et al. "Current status of the TAMA300 gravitational-wave detector." In: *Classical and Quantum Gravity* 22.18 (2005), S881.

[31] H. Grote, LIGO Scientific Collaboration, et al. "The GEO 600 status." In: *Classical and Quantum Gravity* 27.8 (2010), p. 084003.

[32] GEO 600. URL: http://www.geo600.org/.

[33] LIGO. URL: https://www.ligo.caltech.edu/.

[34] J Aasi, B. Abbott, R Abbott, T Abbott, M. Abernathy, K Ackley, C Adams, T Adams, P Addesso, R. Adhikari, et al. "Advanced LIGO." In: *Classical and quantum gravity* 32.7 (2015), p. 074001.

[35] Virgo. URL: http://www.virgo-gw.eu/.

[36] J Abadie, B. Abbott, R Abbott, M Abernathy, T Accadia, F Acernese, C Adams, R Adhikari, P Ajith, B Allen, et al. "Search for gravitational waves from compact binary coalescence in LIGO and Virgo data from S5 and VSR1." In: *Physical Review D* 82.10 (2010), p. 102001.

[37] KAGRA. URL: http://gwcenter.icrr.u-tokyo.ac.jp/.

[38] T Akutsu, M Ando, A Araya, N Aritomi, H Asada, Y Aso, S Atsuta, K Awai, M. Barton, K Cannon, et al. "The status of KAGRA underground cryogenic gravitational wave telescope." In: *arXiv preprint arXiv:1710.04823* (2017).

[39] B Iyer, T Souradeep, C. Unnikrishnan, S Dhurandhar, S Raja, and A Sengupta. *LIGO-India: proposal of the consortium for Indian initiative in gravitational-wave observations (IndIGO)*. Tech. rep. LIGO Tech. Rep. LIGO-M1100296-v2 https://dcc. ligo. org/LIGO-M1100296-v2/public, 2013.

[40] M Punturo, M Abernathy, F Acernese, B Allen, N. Andersson, K Arun, F Barone, B Barr, M Barsuglia, M Beker, et al. "The Einstein Telescope: a third-generation gravitational wave observatory." In: *Classical and Quantum Gravity* 27.19 (2010), p. 194002.

[41] A. Stochino, B. Abbot, Y. Aso, M. Barton, A. Bertolini, V. Boschi, D. Coyne, R. DeSalvo, C. Galli, Y. Huang, et al. "The Seismic Attenuation System (SAS) for the Advanced LIGO gravitational wave interferometric detectors." In: *Nuclear Instruments and Methods in Physics Research Section A: Accelerators, Spectrometers, Detectors and Associated Equipment* 598.3 (2009), pp. 737–753.

[42] N. Kanda, M. A. Barton, and K. Kuroda. "Transfer function of a crossed wire pendulum isolation system." In: *Review of scientific instruments* 65.12 (1994), pp. 3780–3783.

[43] D. G. Blair, J. Liu, E. F. Moghaddam, and L. Ju. "Performance of an ultra low-frequency folded pendulum." In: *Physics letters A* 193.3 (1994), pp. 223–226.

[44] J Winterflood and D. Blair. "A long-period conical pendulum for vibration isolation." In: *Physics Letters A* 222.3 (1996), pp. 141–147.

[45] J Winterflood and D. Blair. "A long-period vertical vibration isolator for gravitational wave detection." In: *Physics Letters A* 243.1-2 (1998), pp. 1–6.

[46] E. Chin, J. Dumas, C Zhao, L Ju, and D. Blair. "AIGO High Performance Compact Vibration Isolation System." In: *Journal of Physics: Conference Series*. Vol. 32. 1. IOP Publishing. 2006, p. 111.

[47] M Pinoli, D. Blair, and L Ju. "Tests on a low-frequency inverted pendulum system." In: *Measurement Science and Technology* 4.9 (1993), p. 995.

[48] M Beccaria et al. "Extending the VIRGO gravitational wave detection band down to a few Hz: metal blade springs and magnetic antisprings." In: *Nuclear Instruments and Methods in Physics Research Section A: Accelerators, Spectrometers, Detectors and Associated Equipment* 394.3 (1997), pp. 397–408.

[49] S Braccini, L Barsotti, C Bradaschia, G Cella, A Di Virgilio, I Ferrante, F Fidecaro, I Fiori, F Frasconi, A Gennai, et al. "Measurement of the seismic attenuation performance of the VIRGO Superattenuator." In: *Astroparticle Physics* 23.6 (2005), pp. 557–565.

[50] R Del Fabbro, A Di Virgilio, A Giazotto, H Kautzky, V Montelatici, and D Passuello. "Three-dimensional seismic superattenuator for low frequency gravitational wave detection." In: *Physics Letters A* 124.4-5 (1987), pp. 253–257.

[51] M Barton, A Bertolini, E Black, G Cella, E Cowan, E D ambrosio, R DeSalvo, K Libbrecht, V Sannibale, A Takamori, et al. "Proposal of a seismic attenuation system (SAS) for the LIGO advanced configuration (LIGO-II)." In: *T990075-00* (1999).

[52] A Bertolini, G Cella, R DeSalvo, and V Sannibale. "Seismic noise filters, vertical resonance frequency reduction with geometric anti-springs: a feasibility study." In: *Nuclear Instruments and Methods in Physics Research Section A: Accelerators, Spectrometers, Detectors and Associated Equipment* 435.3 (1999), pp. 475–483.

[53] A. Bertolini, G. Cella, E. D Ambrosio, R. DeSalvo, V. Sannibale, A. Takamori, and H. Yamamoto. "New seismic attenuation system (SAS) for the advanced LIGO configurations (LIGO2)." In: *AIP Conference Proceedings*. Vol. 523. 1. AIP. 2000, pp. 320–324.

[54] A. Takamori, M. Ando, A. Bertolini, G. Cella, R. DeSalvo, M. Fukushima, Y. Iida, F. Jacquier, S. Kawamura, S. Márka, et al. "Mirror suspension system for the TAMA SAS." In: *Classical and Quantum Gravity* 19.7 (2002), p. 1615.

[55] V. Boschi. "Modeling and Simulation of Seismic Attenuation Systems for Gravitational Wave Interferometers." PhD thesis. 2010.

[56] A. Bertolini, R. DeSalvo, C Galli, G Gennaro, M Mantovani, S. Márka, V. Sannibale, A Takamori, and C Torrie. "Design and prototype tests of a seismic attenuation system for the advanced-LIGO output mode cleaner." In: *Classical and Quantum Gravity* 23.8 (2006), S111.

[57] G Bergmann, C. Mow-Lowry, V. Adya, A Bertolini, M. Hanke, R Kirchhoff, S. Köhlenbeck, G Kühn, P Oppermann, A Wanner, et al. "Passive-performance, analysis, and upgrades of a 1-ton seismic attenuation system." In: *Classical and Quantum Gravity* 34.6 (2017), p. 065002.

[58] M. Beker, M Blom, J. van den Brand, H. Bulten, E Hennes, and D. Rabeling. "Seismic attenuation technology for the Advanced Virgo gravitational wave detector." In: *Physics Procedia* 37 (2012), pp. 1389–1397.

[59] M. G. Beker. "Low-frequency sensitivity of next generation gravitational wave detectors." PhD thesis. 2013.

[60] T Sekiguchi. "Study of Low Frequency Vibration Isolation System for Large Scale Gravitational Wave Detectors." In: (2016).

[61] S. Marka, A. Takamori, M. Ando, A. Bertolini, G. Cella, R. DeSalvo, M. Fukushima, Y. Iida, F. Jacquier, S. Kawamura, et al. "Anatomy of the TAMA SAS seismic attenuation system." In: *Classical and Quantum Gravity* 19.7 (2002), p. 1605.

[62] L. Holloway. "The Superattenuator: a mirror suspension system for reducing seismic induced noise in the VIRGO gravitational wave interferometer." In: *Nuclear Physics B-Proceedings Supplements* 54.3 (1997), pp. 176–178.

[63] J. Giaime, P. Saha, D. Shoemaker, and L. Sievers. "A passive vibration isolation stack for LIGO: design, modeling, and testing." In: *Review of scientific instruments* 67.1 (1996), pp. 208–214.

[64] S Goßler, A Bertolini, M Born, Y Chen, K Dahl, D Gering, C Gräf, G Heinzel, S Hild, F Kawazoe, et al. "The AEI 10 m prototype interferometer." In: *Classical and Quantum Gravity* 27.8 (2010), p. 084023.

[65] T. Accadia, F Acernese, M Alshourbagy, P Amico, F Antonucci, S Aoudia, N Arnaud, C Arnault, K. Arun, P Astone, et al. "Virgo: a laser interferometer to detect gravitational waves." In: *Journal of Instrumentation* 7.03 (2012), P03012.

[66] R Del Fabbro, A Di Virgilio, A Giazotto, H Kautzky, V Montelatici, and D Passuello. "First results from the Pisa seismic noise super-attenuator for low frequency gravitational wave detection." In: *Physics Letters A* 132.5 (1988), pp. 237–240.

[67] S Braccini, C Bradaschia, M Cobal, R Del Fabbro, A Di Virgilio, R Flaminio, A Giazotto, H Kautzky, M Morganti, D Passuello, et al. "An improvement in the VIRGO Super Attenuator for interferometric detection of gravitational waves: The use of a magnetic antispring." In: *Review of scientific instruments* 64.2 (1993), pp. 310–313.

[68] G Losurdo, M Bernardini, S Braccini, C Bradaschia, C Casciano, V Dattilo, R De Salvo, A Di Virgilio, F Frasconi, A Gaddi, et al. "An inverted pendulum preisolator stage for the VIRGO suspension system." In: *Review of scientific instruments* 70.5 (1999), pp. 2507–2515.

[69] M Beccaria, M Bernardini, S Braccini, C Bradaschia, G Cagnoli, C Casciano, G Cella, E Cuoco, V Dattilo, G De Carolis, et al. "The creep problem in the VIRGO suspensions: a possible solution using Maraging steel." In: *Nuclear Instruments and Methods in Physics Research Section A: Accelerators, Spectrometers, Detectors and Associated Equipment* 404.2 (1998), pp. 455–469.

[70] S Braccini, C Casciano, F Cordero, F Corvace, M De Sanctis, R Franco, F Frasconi, E Majorana, G Paparo, R Passaquieti, et al. "The maraging-steel blades of the Virgo super attenuator." In: *Measurement Science and Technology* 11.5 (2000), p. 467.

[71] G Losurdo, G Calamai, E Cuoco, L Fabbroni, G Guidi, M Mazzoni, R Stanga, F Vetrano, L Holloway, D Passuello, et al. "Inertial control of the mirror suspensions of the VIRGO interferometer for gravitational wave detection." In: *Review of Scientific Instruments* 72.9 (2001), pp. 3653–3661.

[72] F. Acernese et al. "Advanced Virgo: a second-generation interferometric gravitational wave detector." In: *Class. Quant. Grav.* 32.2 (2015), p. 024001. DOI: 10.1088/0264-9381/32/2/024001. arXiv: 1408.3978 [gr-qc].

[73] Virgo Collaboration et al. "Advanced Virgo technical design report." In: (2012).

[74] M. Plissi, C. Torrie, M. Husman, N. Robertson, K. Strain, H Ward, H Lück, and J Hough. "GEO 600 triple pendulum suspension system: Seismic isolation and control." In: *Review of scientific instruments* 71.6 (2000), pp. 2539–2545.

[75] M. Husman, C. Torrie, M. Plissi, N. Robertson, K. Strain, and J Hough. "Modeling of multistage pendulums: Triple pendulum suspension for GEO 600." In: *Review of Scientific Instruments* 71.6 (2000), pp. 2546–2551.

[76] R Takahashi, F Kuwahara, E Majorana, M. A. Barton, T Uchiyama, K Kuroda, A Araya, K Arai, A Takamori, M Ando, et al. "Vacuum-compatible vibration isolation stack for an interferometric gravitational wave detector TAMA300." In: *Review of scientific instruments* 73.6 (2002), pp. 2428–2433.

[77] M. A. Barton, T. Uchiyama, K. Kuroda, N. Kanda, and H. Ishizuka. "Two-dimensional X pendulum vibration isolation table." In: *Review of scientific instruments* 70.4 (1999), pp. 2150–2154.

[78] K. Arai, TAMA collaboration, et al. "Recent progress of TAMA 300." In: *Journal of Physics: Conference Series*. Vol. 120. IOP Publishing. 2008, p. 032010.

[79] A Takamori. "Low frequency seismic isolation for gravitational wave detectors." PhD thesis. Ph. D. thesis, 2002.

[80] G Cella, V Sannibale, R DeSalvo, S Marka, and A Takamori. "Monolithic geometric anti-spring blades." In: *Nuclear Instruments and Methods in Physics Research Section A: Accelerators, Spectrometers, Detectors and Associated Equipment* 540.2 (2005), pp. 502–519.

[81] R. Takahashi, K Arai, D Tatsumi, M Fukushima, T Yamazaki, M. Fujimoto, K Agatsuma, Y Arase, N Nakagawa, A Takamori, et al. "Operational status of TAMA300 with the seismic attenuation system (SAS)." In: *Classical and quantum gravity* 25.11 (2008), p. 114036.

[82] C. Hardham, B Abbott, R Abbott, G Allen, R Bork, C Campbell, K Carter, D Coyne, D DeBra, T Evans, et al. "Quiet hydraulic actuators for LIGO." In: *IFAC Proceedings Volumes* 39.16 (2006), pp. 259–265.

[83] S Wen, R Mittleman, K Mason, J Giaime, R Abbott, J Kern, B OReilly, R Bork, M Hammond, C Hardham, et al. "Hydraulic external pre-isolator system for LIGO." In: *Classical and Quantum Gravity* 31.23 (2014), p. 235001.

[84] D. Shoemaker. "Consideration of HAM SAS for Advanced LIGO." In: *LIGO Document G070284-00* (2007).

[85] S. Aston, M. Barton, A. Bell, N Beveridge, B Bland, A. Brummitt, G Cagnoli, C. Cantley, L Carbone, A. Cumming, et al. "Update on quadruple suspension design for Advanced LIGO." In: *Classical and Quantum Gravity* 29.23 (2012), p. 235004.

[86] LIGO Scientific Collaboration et al. "Advanced ligo." In: *arXiv preprint arXiv:1411.4547* (2014).

[87] R Abbott, R Adhikari, G Allen, S Cowley, E Daw, D DeBra, J Giaime, G Hammond, M Hammond, C Hardham, et al. "Seismic isolation for Advanced LIGO." In: *Classical and Quantum Gravity* 19.7 (2002), p. 1591.

[88] A. Stochino. "The HAM-SAS Seismic Isolation System for the Advanced LIGO Gravitational Wave Interferometer." PhD thesis. 2007.

[89] J. S. Kissel. "Calibrating and Improving the Sensitivity of the LIGO Detectors." PhD thesis. 2010.

[90] F Matichard, B Lantz, R Mittleman, K Mason, J Kissel, B Abbott, S Biscans, J McIver, R Abbott, S Abbott, et al. "Seismic isolation of Advanced LIGO: Review of strategy, instrumentation and performance." In: *Classical and Quantum Gravity* 32.18 (2015), p. 185003.

[91] B Lantz. "Lessons from the ETF technology demonstrator." In: *LIGO document G050271* 50271 (2005).

[92] D. Newell, S. Richman, P. Nelson, R. Stebbins, P. Bender, J. Faller, and J Mason. "An ultra-low-noise, low-frequency, six degrees of freedom active vibration isolator." In: *Review of scientific instruments* 68.8 (1997), pp. 3211–3219.

[93] M. Beker, A Bertolini, J. van den Brand, H. Bulten, E Hennes, and D. Rabeling. "State observers and Kalman filtering for high performance vibration isolation systems." In: *Review of Scientific Instruments* 85.3 (2014), p. 034501.

[94] J. van Heijningen, A Bertolini, and J. van den Brand. "Interferometric readout of a monolithic accelerometer, towards the resolution." In: *Nuclear Instruments and Methods in Physics Research Section A: Accelerators, Spectrometers, Detectors and Associated Equipment* 824 (2016), pp. 665–669.

[95] M. R. Blom. "Seismic Attenuation for Advanced Virgo: Vibration Isolation for the External Injection Bench." PhD thesis. Uitgeverij BOXPress, 2015.

[96] M. Blom, M. Beker, A Bertolini, J. van den Brand, H. Bulten, E Hennes, F. Mul, D. Rabeling, and A Schimmel. "Seismic attenuation system for the external injection bench of the Advanced Virgo gravitational wave detector." In: *Nuclear Instruments and Methods in Physics Research Section A: Accelerators, Spectrometers, Detectors and Associated Equipment* 718 (2013), pp. 466–470.

[97] T. Sekiguchi. "Modeling and simulation of vibration isolation system for large-scale cryogenic gravitational-wave telescope (LCGT)." PhD thesis. Masters thesis (University of Tokyo, 2012), 2012.

[98] R. X. Adhikari. *personal communication.*

[99] T Accadia, F Acernese, F Antonucci, P Astone, G Ballardin, F Barone, M Barsuglia, A Basti, T. S. Bauer, M. Beker, et al. "Performance of the Virgo interferometer longitudinal control system during the second science run." In: *Astroparticle Physics* 34.7 (2011), pp. 521–527.

[100] F Acernese, F Antonucci, S Aoudia, K. Arun, P Astone, G Ballardin, F Barone, M Barsuglia, T. S. Bauer, M. Beker, et al. "Measurements of Superattenuator seismic isolation by Virgo interferometer." In: *Astroparticle Physics* 33.3 (2010), pp. 182–189.

[101] G Ballardin, L Bracci, S Braccini, C Bradaschia, C Casciano, G Calamai, R Cavalieri, R Cecchi, G Cella, E Cuoco, et al. "Measurement of the VIRGO superattenuator performance for seismic noise suppression." In: *Review of Scientific Instruments* 72.9 (2001), pp. 3643–3652.

[102] H. Grote. "Making it Work: Second Generation Interferometry in GEO600!" In: (2003).

[103] M. Plissi, K. Strain, C. Torrie, N. Robertson, S Killbourn, S Rowan, S. Twyford, H Ward, K. Skeldon, and J Hough. "Aspects of the suspension system for GEO 600." In: *Review of scientific instruments* 69.8 (1998), pp. 3055–3061.

[104] K. Somiya. "Detector configuration of KAGRA– the Japanese cryogenic gravitational-wave detector." In: *Classical and Quantum Gravity* 29.12 (2012), p. 124007.

[105] R. X. Adhikari. "Gravitational radiation detection with laser interferometry." In: *Reviews of Modern Physics* 86.1 (2014), p. 121.

[106] K. Yamamoto, T Uchiyama, S Miyoki, M Ohashi, K Kuroda, H Ishitsuka, T Akutsu, S Telada, T Tomaru, T Suzuki, et al. "Current status of the CLIO project." In: *Journal of Physics: Conference Series*. Vol. 122. 1. IOP Publishing. 2008, p. 012002.

[107] H. J. Kimble, Y. Levin, A. B. Matsko, K. S. Thorne, and S. P. Vyatchanin. "Conversion of conventional gravitational-wave interferometers into quantum nondemolition interferometers by modifying their input and/or output optics." In: *Physical Review D* 65.2 (2001), p. 022002.

[108] R Kirchhoff, C. Mow-Lowry, V. Adya, G Bergmann, S Cooper, M. Hanke, P Koch, S. Köhlenbeck, J Lehmann, P Oppermann, et al. "Huddle test measurement of a near Johnson noise limited geophone." In: *Review of Scientific Instruments* 88.11 (2017), p. 115008.

[109] A. Buonanno and Y. Chen. "Optical noise correlations and beating the standard quantum limit in advanced gravitational-wave detectors." In: *Classical and Quantum Gravity* 18.15 (2001), p. L95.

[110] T Westphal, G Bergmann, A Bertolini, M Born, Y Chen, A. Cumming, L Cunningham, K Dahl, C Gräf, G Hammond, et al. "Design of the 10 m AEI prototype facility for interferometry studies." In: *Applied Physics B* 106.3 (2012), pp. 551–557.

[111] C. Gräf. "Optical design and numerical modeling of the AEI 10m Prototype sub-SQL interferometer." In: (2013).

[112] D. Wu. "Sub-SQL interferometer noise budget." In: *internal logbook page 2961* (2018).

[113] P Bormann. "Conversion and comparability of data presentations on seismic background noise." In: *Journal of Seismology* 2.1 (1998), pp. 37–45.

[114] G. D. Cole, W. Zhang, M. J. Martin, J. Ye, and M. Aspelmeyer. "Tenfold reduction of Brownian noise in high-reflectivity optical coatings." In: *Nature Photonics* 7.8 (2013), pp. 644–650.

[115] M. Frede, B. Schulz, R. Wilhelm, P. Kwee, F. Seifert, B. Willke, and D. Kracht. "Fundamental mode, single-frequency laser amplifier for gravitational wave detectors." In: *optics express* 15.2 (2007), pp. 459–465.

[116] T. Alig. "Charakterisierung und Unterdrückung der Strahlgeometriefluktuationen des fasergekoppelten 35W Lasers für das AEI 10m Prototypinterferometer." In: (2013).

[117] P. Oppermann. "Characterization and stabilization of a high power fiber amplifier laser." PhD thesis. Gottfried Wilhelm Leibniz Universität Hannover, 2017.

[118] J. Junker, P. Oppermann, and B. Willke. "Shot-noise-limited laser power stabilization for the AEI 10 m Prototype interferometer." In: *Optics Letters* 42.4 (2017), pp. 755–758.

[119] K. Dahl, G Heinzel, B Willke, K. Strain, S Goßler, and K Danzmann. "Suspension platform interferometer for the AEI 10 m prototype: concept, design and optical layout." In: *Classical and quantum gravity* 29.9 (2012), p. 095024.

[120] A Bertolini, R DeSalvo, F Fidecaro, M Francesconi, S Marka, V Sannibale, D Simonetti, A Takamori, and H Tariq. "Mechanical design of a single-axis monolithic accelerometer for advanced seismic attenuation systems." In: *Nuclear Instruments and Methods in Physics Research Section A: Accelerators, Spectrometers, Detectors and Associated Equipment* 556.2 (2006), pp. 616–623.

[121] A Stochino, R DeSalvo, Y. Huang, and V Sannibale. "Improvement of the seismic noise attenuation performance of the Monolithic Geometric Anti-Spring filters for gravitational wave interferometric detectors." In: *Nuclear Instruments and Methods in Physics Research Section A: Accelerators, Spectrometers, Detectors and Associated Equipment* 580.3 (2007), pp. 1559–1564.

[122] Y Nakayama, T Ito, S Matsui, R Sugahara, S Takeda, H Yamaoka, and S Yamashita. "Performances test of STS-2 seismometers with various data loggers." In: *Proc. IWAA2004* (2004).

[123] Sercel. URL: http://www.sercel.com/.

[124] R. Kirchhoff. "Verbesserung der aktiven Seismikisolation für die seismische Isolationsplattform AEI-SAS." In: *Gottfried Wilhelm Leibniz Universität Hannover* (2016).

[125] R Kirchhoff. "Accelerometer huddle test." In: *LIGO Document T1700493* (2017).

[126] H Tariq, A Takamori, F Vetrano, C Wang, A Bertolini, G Calamai, R DeSalvo, A Gennai, L Holloway, G Losurdo, et al. "The linear variable differential transformer (LVDT) position sensor for gravitational wave interferometer low-frequency controls." In: *Nuclear Instruments and Methods in Physics Research Section A: Accelerators, Spectrometers, Detectors and Associated Equipment* 489.1 (2002), pp. 570–576.

[127] C. Wang, H. Tariq, R. DeSalvo, Y. Iida, S. Marka, Y. Nishi, V. Sannibale, and A. Takamori. "Constant force actuator for gravitational wave detector's seismic attenuation systems (SAS)." In: *Nuclear Instruments and Methods in Physics Research Section A: Accelerators, Spectrometers, Detectors and Associated Equipment* 489.1 (2002), pp. 563–569.

[128] W. Demtröder. *Experimentalphysik 1: Mechanik und Wärme*. Springer-Verlag, 2015.

[129] P Raffai, A Takamori, S Márka, S DeSalvo, V Sannibali, H Tariq, A Bertolini, G Cella, N Viboud, K Numata, et al. "Inverted pendulum as low frequency pre-isolation for advanced gravitational wave detectors." In: *submitted to LSC* (2002).

[130] H. Dubbel, W. Beitz, and K.-H. Küttner. *Dubbel: Taschenbuch für den Maschinenbau*. Springer-Verlag, 2013.

[131] J. M. Gere and S. P. Timoshenko. *Mechanics of materials PWS*. KENT Publishing Company, Elsevier Science BV, Amsterdam, 1990.

[132] W. Nolting. *Grundkurs Theoretische Physik*. Vol. 6. Springer, 2010.

[133] R. Cross. "Center of percussion of hand-held implements." In: *American Journal of Physics* 72.5 (2004), pp. 622–630.

[134] Aubert&Duval. *supplier for steel and alloys*. URL: http://www.aubertduval.com.

[135] H. A. Sodano, J.-S. Bae, D. J. Inman, and W. K. Belvin. "Concept and model of eddy current damper for vibration suppression of a beam." In: *Journal of Sound and Vibration* 288.4 (2005), pp. 1177–1196.

[136] G Cella, R DeSalvo, V Sannibale, H Tariq, N Viboud, and A Takamori. "Seismic attenuation performance of the first prototype of a geometric anti-spring filter." In: *Nuclear Instruments and Methods in Physics Research Section A: Accelerators, Spectrometers, Detectors and Associated Equipment* 487.3 (2002), pp. 652–660.

[137] B. Boom, A Bertolini, E Hennes, R. Brookhuis, R. Wiegerink, J. van den Brand, M. Beker, A Oner, and D van Wees. "Nano-G accelerometer using geometric anti-springs." In: *Micro Electro Mechanical Systems (MEMS), 2017 IEEE 30th International Conference on*. IEEE. 2017, pp. 33–36.

[138] K. S. Hardman, P. J. Everitt, G. D. McDonald, P. Manju, P. B. Wigley, M. Sooriyabandara, C. C. Kuhn, J. E. Debs, J. D. Close, and N. P. Robins. "Simultaneous precision gravimetry and magnetic gradiometry with a Bose-Einstein condensate: a high precision, quantum sensor." In: *Physical review letters* 117.13 (2016), p. 138501.

[139] J. V. van Heijningen. "Low-frequency Performance Improvement of Seismic Attenuation Systems and Vibration Sensors for Next Generation Gravitational Wave Detectors." PhD thesis. 2018.

[140] S Braccini, C Bradaschia, R Del Fabbro, A Di Virgilio, I Ferrante, F Fidecaro, R Flaminio, A Gennai, A Giassi, A Giazotto, et al. "Seismic vibrations mechanical filters for the gravitational waves detector VIRGO." In: *Review of scientific instruments* 67.8 (1996), pp. 2899–2902.

[141] P. Hidnert and H. Krider. "Thermal expansion of aluminum and some aluminum alloys." In: *Journal of research of the national bureau of standards* 48.3 (1952), pp. 209–220.

[142] D Gerlich, R. Roberts, G. White, and R Tainsh. "Thermoelastic properties of 350 grade maraging steel." In: *Journal of materials Science* 25.4 (1990), pp. 2249–2252.

[143] F Cordero, F Corvasce, R Franco, G Paparo, E Maiorana, P Rapagnani, F Ricci, S Braccini, C Casciano, R De Salvo, et al. "Elastic and anelastic properties of Marval 18 steel." In: *Journal of alloys and compounds* 310.1 (2000), pp. 400–404.

[144] H. Ledbetter and D. Read. "Low-temperature elastic properties of a 300-grade maraging steel." In: *Metallurgical Transactions A* 8.11 (1977), pp. 1805–1808.

[145] H. K.D. H. Bhadeshia. "Prevention of hydrogen embrittlement in steels." In: *ISIJ international* 56.1 (2016), pp. 24–36.

[146] W. H. Johnson. "On Some Remarkable Changes Produced in Iron and Steel by the Action of Hydrogen and Acids." In: *Proceedings of the Royal Society of London* 23 (1874), pp. 168–179. ISSN: 03701662. URL: http://www.jstor.org/stable/113285.

[147] R. Valentini et al. "Fractographic analysis and hydrogen measurement in Maraging Steel Blades (Virgo project)." In: *Dipartemento di Ingegneria Civile e Industriale, Universita di Pisa, Virgo note VIR-0191A-16* ().

[148] M. Wang, E. Akiyama, and K. Tsuzaki. "Determination of the critical hydrogen concentration for delayed fracture of high strength steel by constant load test and numerical calculation." In: *Corrosion science* 48.8 (2006), pp. 2189–2202.

[149] A Bertolini. *personal communication*.

[150] C Calum Torrie, Mason, D K Coyne, J Romie, and N. Robertson. "Manufacturing Process for Cantilever Spring Blades for Advanced LIGO." In: *LIGO-E0900023* (2010).

[151] F Matichard and M Evans. "Review: Tilt-Free Low-Noise Seismometry." In: *Bulletin of the Seismological Society of America* 105.2A (2015), pp. 497–510.

[152] Minus K Technology. URL: https://www.minusk.com.

[153] H. Wittel. "Young's Modulus of Fluorel/Vitro." In: *internal logbook page 3219* (2012).

[154] ASM Aerospace Specification Metals. URL: http://asm.matweb.com/.

[155] International Molybdenum Association. URL: http://www.imoa.info/.

[156] AZO Materials. URL: http://www.azom.com.

[157] Maryland Metrics. URL: https://mdmetric.com.

[158] A. Inventor. "Mechanical library." In: (2015).

[159] G Bergmann. "Increasing mechanical stiffness by both gluing and bolting metal surfaces together." In: *LIGO Document T1600375* (2016).

[160] *TRA-BOND 2151 Thermal Conductive electrical insulating compound*. www.tra-con.com.

[161] D. Hrovat, P. Barak, and M. Rabins. "Semi-active versus passive or active tuned mass dampers for structural control." In: *Journal of Engineering Mechanics* 109.3 (1983), pp. 691–705.

[162] I. Kourakis. "Structural systems and tuned mass dampers of super-tall buildings: case study of Taipei 101." PhD thesis. Massachusetts Institute of Technology, 2007.

[163] S. Gras, P. Fritschel, L. Barsotti, and M. Evans. "Resonant dampers for parametric instabilities in gravitational wave detectors." In: *Physical Review D* 92.8 (2015), p. 082001.

[164] L. Ju. "Multi-stage Dampers for Parametric Instability Suppression." In: *LIGO-G1700852* (2017).

[165] M. Blom, A. Bertolini, E. Hennes, A. Schimmel, H. Bulten, M. Beker, F. Mul, M. Doets, and J. van den Brand. "Performance of the Advanced Virgo External Injection Bench Seismic Attenuation System." In: *LVC meeting 2013 Hannover* ().

[166] A. Abramovici and J. Chapsky. *Feedback control systems: A fast-track guide for scientists and engineers*. Springer Science & Business Media, 2012.

[167] R Kirchhoff. "Accelerometer huddle test." In: *internal logbook page 2773* (2017).

[168] H. Wittel, S Hild, and K. Strain. "Design ideas for the electrostatic drives of the AEI 10 m." In: *internal logbook page 693* (2012).

[169] M. Hewitson, K. Danzmann, H. Grote, S. Hild, J Hough, H. Lück, S Rowan, J. Smith, K. A. Strain, and B. Willke. "Charge measurement and mitigation for the main test masses of the GEO 600 gravitational wave observatory." In: *Classical and Quantum Gravity* 24.24 (2007), p. 6379.

[170] H Wittel, S. Hild, G. Bergmann, K. Danzmann, and K. A. Strain. "New design of electrostatic mirror actuators for application in high-precision interferometry." In: *Classical and Quantum Gravity* 32.17 (2015), p. 175021.

[171] S Margulies. "Force on a dielectric slab inserted into a parallel-plate capacitor." In: *American Journal of Physics* 52.6 (1984), pp. 515–518.

[172] C. Mow-Lowry. "ESD HV amplifier." In: *internal logbook page 1187* (2013).

[173] J Lehmann. *personal communication*.

[174] ERC Sagnac Speed-Meter Project. URL: www.speed-meter.eu.

[175] R. Kirchhoff. "Aufbau und Test der Seismischen Isolationsplattform (AEI-SAS)." In: *Gottfried Wilhelm Leibniz Universität Hannover* (2014).

# ACKNOWLEDGMENTS

This work would not have been possible without the support I received from my supervisors, colleagues, friends, and family.
First of all I would like to thank Karsten Danzmann for giving me the opportunity to spend my time as a doctoral student at the AEI in such exciting times. The friendly and supportive approach in the institute, as well as in the LVC- and I am grateful that I have been part of them- is not a matter of course.
I particularly enjoyed being part of AEI 10 m prototype team and I appreciated that I could benefit from the experience of the group members while participating in great science.
I want to thank Harald and Ken for the exceptional supervision and the experimental and scientific support. The numerous discussions in the meetings, over lunch or in the office were a tremendous help.
I also want to thank all the other past and present members of the AEI 10 m prototype team I had the pleasure to work with.
A special thanks goes to Vaishali for sharing tee and the thesis writing experience.
I want to thank Sina for being a great office mate. She made stress due to deadlines, problems with my measurements or lab equipment much more endurable.
With Alex, Conor, and Robin I shared a few great, and many frustrating moments while working together on the AEI-SAS. For the great teamwork, the discussions and the shared experiences I want to thank them.
I am especially grateful to Alex, Alessandro, and Conor for their help and support in working on the AEI-SAS, even after they have left the AEI.
For proofreading parts of this many pages I am truly thankful to Alessandro, Alex, Anna, Daniel, David, Dirk, Emil, François, Fu, Harald, Jan, Jan, Johannes, Michèle, Patrick, Robin, Sean, Sina, Suresh, Timo, and Vaishali.
Without my friends and roommates, the time of writing would have been far more difficult. I want to thank them for keeping me mostly sane.
Finally, I want to thank my family for their support. They have enabled me to follow my way throughout my education.

# CURRICULUM VITÆ

| | |
|---|---|
| **Zur Person** | |
| Name | **Gerald Bergmann** |
| Geburtstag | 31. Mai 1984 |
| Geburtsort | Detmold |
| Staatsangehörigkeit | deutsch |
| **Berufserfahrung** | |
| 04/2011 - 04/2018 | **Promotion** am Max-Planck-Institut für Gravitationsphysik (Albert-Einstein-Institut) |
| 01/2011 - 03/2011 | **Wissenschaftliche Hilfskraft** am Max-Planck-Institut für Gravitationsphysik (Albert-Einstein-Institut) |
| 10/2010 - 12/2010 | **Wissenschaftliche Hilfskraft** am Laserzentrum Hannover |
| 07/2010 - 09/2010 | **Praktikum** an der University of St. Andrews, Schottland |
| 03/2006 - 09/2007 | **Wissenschaftliche Hilfskraft** am Institut für Quantenoptik, Hannover |
| 07/2003 - 04/2004 | **Zivildienst** im Krankenhaus Porz am Rhein, Köln |
| **Studium** | |
| 05/2009 - 05/2010 | **Diplomand** am Laserzentrum Hannover |
| 09/2007 - 03/2008 | **Auslandssemester** im Erasmus-Programm an der Universidad de Salamanca, Spanien |
| Seit 10/2004 | **Physikstudium** an der Leibniz Universität Hannover |
| **Schulische Ausbildung** | |
| 08/2000 - 06/2003 | **Gymnasium** Stadtgymnasium Detmold |
| 08/1994 - 06/2000 | **Realschule** Städtische Realschule I Detmold |
| 08/1990 - 06/1994 | **Grundschule** Heiligenkirchen Detmold |

[1] Wolfgang A. Ertmer, ..., G. Bergmann, ..., Alexander Heisterkamp. Optical forces in biophotonics: transfection and cell sorting. In Enrique J. Galvez, David L. Andrews, and Jesper Glückstad, editors, *Complex Light and Optical Forces IV*. SPIE, feb 2010.

[2] K Dahl, ..., G. Bergmann, ..., K Danzmann. Status of the AEI 10 m prototype. *Classical and Quantum Gravity*, 29(14):145005, jun 2012.

[3] Fumiko Kawazoe, ..., G. Bergmann, ..., K Danzmann. The AEI 10 m prototype interferometer frequency control using the reference cavity and its angular control. *Journal of Physics: Conference Series*, 363:012012, jun 2012.

[4] Helen A. Rendall, Robert F. Marchington, Bavishna B. Praveen, Gerald Bergmann, Yoshihiko Arita, Alexander Heisterkamp, Frank J. Gunn-Moore, and Kishan Dholakia. High-throughput optical injection of mammalian cells using a bessel light beam. *Lab on a Chip*, 12(22):4816, mar 2012.

[5] A Wanner, G Bergmann, A Bertolini, T Fricke, H Lück, C M Mow-Lowry, K A Strain, S Goßler, and K Danzmann. Seismic attenuation system for the AEI 10 meter prototype. *Classical and Quantum Gravity*, 29(24):245007, nov 2012.

[6] T. Westphal,..., G. Bergmann, ..., K. Danzmann. Design of the 10 m AEI prototype facility for interferometry studies. *Applied Physics B*, 106(3):551–557, feb 2012.

[7] Helen A. Rendall, Robert F. Marchington, Bavishna B. Praveen, Gerald Bergmann, Yoshihiko Arita, Alexander Heisterkamp, Frank J. Gunn-Moore, and Kishan Dholakia. High-throughput optical injection of mammalian cells using a non-diffracting beam in a microfluidic platform. In Alexander Heisterkamp, Peter R. Herman, Michel Meunier, and Stefan Nolte, editors, *Frontiers in Ultrafast Optics: Biomedical, Scientific, and Industrial Applications XIII*. SPIE, mar 2013.

[8] G Hofmann, ..., G. Bergmann, ..., and K Yamamoto. Indium joints for cryogenic gravitational wave detectors. *Classical and Quantum Gravity*, 32(24):245013, dec 2015.

[9] H Wittel, S Hild, G Bergmann, K Danzmann, and K A Strain. New design of electrostatic mirror actuators for application in

high-precision interferometry. *Classical and Quantum Gravity*, 32(17):175021, aug 2015.

[10] G Bergmann, et al. Passive-performance, analysis, and upgrades of a 1-ton seismic attenuation system. *Classical and Quantum Gravity*, 34(6):065002, feb 2017.

[11] R. Kirchhoff, ..., G. Bergmann, ..., K. A. Strain. Huddle test measurement of a near johnson noise limited geophone. *Review of Scientific Instruments*, 88(11):115008, nov 2017.

[1] J. Aasi et al. Directed search for continuous gravitational waves from the galactic center. *Physical Review D*, 88(10), nov 2013.

[2] J. Aasi et al. Enhanced sensitivity of the LIGO gravitational wave detector by using squeezed states of light. *Nature Photonics*, 7(8):613–619, jul 2013.

[3] J. Aasi et al. Search for long-lived gravitational-wave transients coincident with long gamma-ray bursts. *Physical Review D*, 88(12), dec 2013.

[4] M. G. Aartsen et al. Multimessenger search for sources of gravitational waves and high-energy neutrinos: Initial results for LIGO-virgo and IceCube. *Physical Review D*, 90(10), nov 2014.

[5] J. Aasi, , et al. Search for gravitational waves associated withγ-ray bursts detected by the interplanetary network. *Physical Review Letters*, 113(1), jun 2014.

[6] J Aasi et al. Application of a hough search for continuous gravitational waves on data from the fifth LIGO science run. *Classical and Quantum Gravity*, 31(8):085014, apr 2014.

[7] J. Aasi et al. Constraints on cosmic strings from the LIGO-virgo gravitational-wave detectors. *Physical Review Letters*, 112(13), apr 2014.

[8] J. Aasi et al. First all-sky search for continuous gravitational waves from unknown sources in binary systems. *Physical Review D*, 90(6), sep 2014.

[9] J. Aasi et al. First searches for optical counterparts to gravitational-wave candidate events. *The Astrophysical Journal Supplement Series*, 211(1):7, feb 2014.

[10] J. Aasi et al. Gravitational waves from known pulsars: Results from the initial detector era. *The Astrophysical Journal*, 785(2):119, apr 2014.

[11] J Aasi et al. Implementation of an $\mathcal{f}$-statistic all-sky search for continuous gravitational waves in virgo VSR1 data. *Classical and Quantum Gravity*, 31(16):165014, aug 2014.

[12] J. Aasi et al. Improved upper limits on the stochastic gravitational-wave background from 2009–2010 LIGO and virgo data. *Physical Review Letters*, 113(23), dec 2014.

[13] J. Aasi et al. Methods and results of a search for gravitational waves associated with gamma-ray bursts using the GEO 600, LIGO, and virgo detectors. *Physical Review D*, 89(12), jun 2014.

[14] J. Aasi et al. The NINJA-2 project: detecting and characterizing gravitational waveforms modelled using numerical binary black hole simulations. *Classical and Quantum Gravity*, 31(11):115004, may 2014.

[15] J. Aasi et al. Search for gravitational radiation from intermediate mass black hole binaries in data from the second LIGO-virgo joint science run. *Physical Review D*, 89(12), jun 2014.

[16] J. Aasi et al. Search for gravitational radiation from intermediate mass black hole binaries in data from the second LIGO-virgo joint science run. *Physical Review D*, 89(12), jun 2014.

[17] J. Aasi et al. Search for gravitational wave ringdowns from perturbed intermediate mass black holes in LIGO-virgo data from 2005–2010. *Physical Review D*, 89(10), may 2014.

[18] F. Acernese et al. Concepts and research for future detectors. *General Relativity and Gravitation*, 46(5), apr 2014.

[19] J. Aasi et al. Advanced LIGO. *Classical and Quantum Gravity*, 32(7):074001, mar 2015.

[20] J Aasi et al. Characterization of the LIGO detectors during their sixth science run. *Classical and Quantum Gravity*, 32(11):115012, may 2015.

[21] J Aasi et al. Characterization of the LIGO detectors during their sixth science run. *Classical and Quantum Gravity*, 32(11):115012, may 2015.

[22] J. Aasi et al. Directed search for gravitational waves from scorpius x-1 with initial LIGO data. *Physical Review D*, 91(6), mar 2015.

[23] J. Aasi et al. Narrow-band search of continuous gravitational-wave signals from crab and vela pulsars in virgo VSR4 data. *Physical Review D*, 91(2), jan 2015.

[24] J. Aasi et al. Searches for continuous gravitational waves from nine young supernova remnants. *The Astrophysical Journal*, 813(1):39, oct 2015.

[25] J. Aasi et al. Searching for stochastic gravitational waves using data from the two colocated LIGO hanford detectors. *Physical Review D*, 91(2), jan 2015.

[26] J. Aasi et al. Searching for stochastic gravitational waves using data from the two colocated LIGO hanford detectors. *Physical Review D*, 91(2), jan 2015.

[27] J. Aasi et al. First low frequency all-sky search for continuous gravitational wave signals. *Physical Review D*, 93(4), feb 2016.

[28] J. Aasi et al. Search of the orion spur for continuous gravitational waves using a loosely coherent algorithm on data from LIGO interferometers. *Physical Review D*, 93(4), feb 2016.

[29] B. P. Abbott et al. Astrophysical implications of the binary black hole merger gw150914. *The Astrophysical Journal*, 818(2):L22, feb 2016.

[30] B P Abbott et al. Characterization of transient noise in advanced LIGO relevant to gravitational wave signal GW150914. *Classical and Quantum Gravity*, 33(13):134001, jun 2016.

[31] B. P. Abbott et al. Localization and broadband followup of the gravitational-wave transient gw150914. *The Astrophysical Journal*, 826(1):L13, jul 2016.

[32] B. P. Abbott et al. Prospects for observing and localizing gravitational-wave transients with advanced LIGO and advanced virgo. *Living Reviews in Relativity*, 19(1), feb 2016.

[33] B. P. Abbott et al. Supplement: "localization and broadband follow-up of the gravitational-wave transient gw150914". *The Astrophysical Journal Supplement Series*, 225(1):8, jul 2016.

[34] B. P. Abbott et al. The rate of binary black hole mergers inferred from advanced ligo observations surrounding gw150914. *The Astrophysical Journal*, 833(1):L1, nov 2016.

[35] B. P. Abbott et al. Upper limits on the rates of binary neutron star and neutron star black hole mergers from advanced ligos first observing run. *The Astrophysical Journal*, 832(2):L21, nov 2016.

[36] B. P. Abbott et al. All-sky search for long-duration gravitational wave transients with initial LIGO. *Physical Review D*, 93(4), feb 2016.

[37] B. P. Abbott et al. Binary black hole mergers in the first advanced LIGO observing run. *Physical Review X*, 6(4), oct 2016.

[38] B. P. Abbott et al. Comprehensive all-sky search for periodic gravitational waves in the sixth science run LIGO data. *Physical Review D*, 94(4), aug 2016.

[39] B. P. Abbott et al. Directly comparing GW150914 with numerical solutions of einstein's equations for binary black hole coalescence. *Physical Review D*, 94(6), sep 2016.

[40] B. P. Abbott et al. First targeted search for gravitational-wave bursts from core-collapse supernovae in data of first-generation laser interferometer detectors. *Physical Review D*, 94(10), nov 2016.

[41] B. P. Abbott et al. GW150914: First results from the search for binary black hole coalescence with advanced LIGO. *Physical Review D*, 93(12), jun 2016.

[42] B. P. Abbott et al. GW150914: Implications for the stochastic gravitational-wave background from binary black holes. *Physical Review Letters*, 116(13), mar 2016.

[43] B. P. Abbott et al. GW150914: The advanced LIGO detectors in the era of first discoveries. *Physical Review Letters*, 116(13), mar 2016.

[44] B. P. Abbott et al. GW151226: Observation of gravitational waves from a 22-solar-mass binary black hole coalescence. *Physical Review Letters*, 116(24), jun 2016.

[45] B. P. Abbott et al. GW151226: Observation of gravitational waves from a 22-solar-mass binary black hole coalescence. *Physical Review Letters*, 116(24), jun 2016.

[46] B. P. Abbott et al. Improved analysis of GW150914 using a fully spin-precessing waveform model. *Physical Review X*, 6(4), oct 2016.

[47] B. P. Abbott et al. Observation of gravitational waves from a binary black hole merger. *Physical Review Letters*, 116(6), feb 2016.

[48] B. P. Abbott et al. Observing gravitational-wave transient GW150914 with minimal assumptions. *Physical Review D*, 93(12), jun 2016.

[49] B. P. Abbott et al. Properties of the binary black hole merger GW150914. *Physical Review Letters*, 116(24), jun 2016.

[50] B. P. Abbott et al. Properties of the binary black hole merger GW150914. *Physical Review Letters*, 116(24), jun 2016.

[51] B. P. Abbott et al. Results of the deepest all-sky survey for continuous gravitational waves on LIGO s6 data running on the einstein@home volunteer distributed computing project. *Physical Review D*, 94(10), nov 2016.

[52] B. P. Abbott et al. Search for transient gravitational waves in coincidence with short-duration radio transients during 2007–2013. *Physical Review D*, 93(12), jun 2016.

[53] B. P. Abbott et al. Tests of general relativity with GW150914. *Physical Review Letters*, 116(22), may 2016.

[54] S. Adrián-Martínez, , et al. High-energy neutrino follow-up search of gravitational wave event GW150914 with ANTARES and IceCube. *Physical Review D*, 93(12), jun 2016.

[55] and B. P. Abbott et al. The basic physics of the binary black hole merger GW150914. *Annalen der Physik*, 529(1-2):1600209, oct 2016.

[56] B P Abbott, , et al. Effects of waveform model systematics on the interpretation of GW150914. *Classical and Quantum Gravity*, 34(10):104002, apr 2017.

[57] B. P. Abbott, , et al. First search for gravitational waves from known pulsars with advanced LIGO. *The Astrophysical Journal*, 839(1):12, apr 2017.

[58] B. P. Abbott et al. Erratum: "first search for gravitational waves from known pulsars with advanced LIGO" (2017, ApJ, 839, 12). *The Astrophysical Journal*, 851(1):71, dec 2017.

[59] B. P. Abbott et al. Estimating the contribution of dynamical ejecta in the kilonova associated with GW170817. *The Astrophysical Journal*, 850(2):L39, dec 2017.

[60] B P Abbott et al. Exploring the sensitivity of next generation gravitational wave detectors. *Classical and Quantum Gravity*, 34(4):044001, jan 2017.

[61] B. P. Abbott et al. A gravitational-wave standard siren measurement of the hubble constant. *Nature*, oct 2017.

[62] B. P. Abbott et al. Gravitational waves and gamma-rays from a binary neutron star merger: GW170817 and GRB 170817a. *The Astrophysical Journal*, 848(2):L13, oct 2017.

[63] B. P. Abbott et al. Gravitational waves and gamma-rays from a binary neutron star merger: GW170817 and GRB 170817a. *The Astrophysical Journal*, 848(2):L13, oct 2017.

[64] B. P. Abbott et al. GW170608: Observation of a 19 solar-mass binary black hole coalescence. *The Astrophysical Journal*, 851(2):L35, dec 2017.

[65] B. P. Abbott et al. Multi-messenger observations of a binary neutron star merger. *The Astrophysical Journal*, 848(2):L12, oct 2017.

[66] B. P. Abbott et al. On the progenitor of binary neutron star merger GW170817. *The Astrophysical Journal*, 850(2):L40, dec 2017.

[67] B. P. Abbott et al. Search for gravitational waves associated with gamma-ray bursts during the first advanced LIGO observing run and implications for the origin of GRB 150906b. *The Astrophysical Journal*, 841(2):89, may 2017.

[68] B. P. Abbott et al. Search for gravitational waves associated with gamma-ray bursts during the first advanced LIGO observing run and implications for the origin of GRB 150906b. *The Astrophysical Journal*, 841(2):89, may 2017.

[69] B. P. Abbott et al. Search for post-merger gravitational waves from the remnant of the binary neutron star merger GW170817. *The Astrophysical Journal*, 851(1):L16, dec 2017.

[70] B. P. Abbott et al. Upper limits on gravitational waves from scorpius x-1 from a model-based cross-correlation search in advanced LIGO data. *The Astrophysical Journal*, 847(1):47, sep 2017.

[71] B. P. Abbott et al. All-sky search for periodic gravitational waves in the o1 LIGO data. *Physical Review D*, 96(6), sep 2017.

[72] B. P. Abbott et al. All-sky search for short gravitational-wave bursts in the first advanced LIGO run. *Physical Review D*, 95(4), feb 2017.

[73] B. P. Abbott et al. All-sky search for short gravitational-wave bursts in the first advanced LIGO run. *Physical Review D*, 95(4), feb 2017.

[74] B. P. Abbott et al. Directional limits on persistent gravitational waves from advanced LIGO's first observing run. *Physical Review Letters*, 118(12), mar 2017.

[75] B. P. Abbott et al. First low-frequency einstein@home all-sky search for continuous gravitational waves in advanced LIGO data. *Physical Review D*, 96(12), dec 2017.

[76] B. P. Abbott et al. First low-frequency einstein@home all-sky search for continuous gravitational waves in advanced LIGO data. *Physical Review D*, 96(12), dec 2017.

[77] B. P. Abbott et al. First narrow-band search for continuous gravitational waves from known pulsars in advanced detector data. *Physical Review D*, 96(12), dec 2017.

[78] B. P. Abbott et al. First narrow-band search for continuous gravitational waves from known pulsars in advanced detector data. *Physical Review D*, 96(12), dec 2017.

[79] B. P. Abbott et al. GW170104: Observation of a 50-solar-mass binary black hole coalescence at redshift 0.2. *Physical Review Letters*, 118(22), jun 2017.

[80] B. P. Abbott et al. GW170814: A three-detector observation of gravitational waves from a binary black hole coalescence. *Physical Review Letters*, 119(14), oct 2017.

[81] B. P. Abbott et al. GW170817: Observation of gravitational waves from a binary neutron star inspiral. *Physical Review Letters*, 119(16), oct 2017.

[82] B. P. Abbott et al. Search for continuous gravitational waves from neutron stars in globular cluster NGC 6544. *Physical Review D*, 95(8), apr 2017.

[83] B. P. Abbott et al. Search for gravitational waves from scorpius x-1 in the first advanced LIGO observing run with a hidden markov model. *Physical Review D*, 95(12), jun 2017.

[84] B. P. Abbott et al. Search for intermediate mass black hole binaries in the first observing run of advanced LIGO. *Physical Review D*, 96(2), jul 2017.

[85] B. P. Abbott et al. Upper limits on the stochastic gravitational-wave background from advanced LIGO's first observing run. *Physical Review Letters*, 118(12), mar 2017.

[86] Benjamin P Abbott et al. The basic physics of the binary black hole merger gw150914. *Annalen der Physik*, 529(1-2), 2017.

[87] A. Albert et al. Search for high-energy neutrinos from binary neutron star merger GW170817 with ANTARES, IceCube, and the pierre auger observatory. *The Astrophysical Journal*, 850(2):L35, nov 2017.

[88] A. Albert et al. Search for high-energy neutrinos from gravitational wave event GW151226 and candidate LVT151012 with ANTARES and IceCube. *Physical Review D*, 96(2), jul 2017.

[89] A. Albert et al. Search for high-energy neutrinos from gravitational wave event GW151226 and candidate LVT151012 with ANTARES and IceCube. *Physical Review D*, 96(2), jul 2017.

[90] B P Abbott et al. All-sky search for long-duration gravitational wave transients in the first advanced LIGO observing run. *Classical and Quantum Gravity*, 35(6):065009, feb 2018.

[91] B. P. Abbott et al. First search for nontensorial gravitational waves from known pulsars. *Physical Review Letters*, 120(3), jan 2018.

[92] BP Abbott et al. Localization and broadband follow-up of the gravitational-wave transient gw150914. pages –, 2018.